AMMONIA SPLITTING FOR RENEWABLE ENERGY CONVERSION

By

Reza Ghazfar

A DISSERTATION

Submitted to
Michigan State University
in partial fulfillment of the requirements
for the degree of

Chemistry – Doctor of Philosophy

2023

ABSTRACT

Due to the intermittent nature of renewable energy sources like wind and solar, efficient energy storage and distribution is essential when these sources are dormant. Among potential candidates for chemical energy storage, ammonia is gaining more attention, owing to its zero-carbon footprint, relatively efficient synthesis on a global scale, and well-established transportation infrastructure. If ammonia is synthesized via renewable energy sources, the efficient conversion of NH_3 to N_2 and H_2 would complete an energy cycle where H_2 stored as NH_3 can fuel hydrogen/hybrid vehicles that are being commercialized. The efficiency of ammonia electrolysis to N_2 and H_2 can be improved by catalysts designed to lower the high overpotentials for oxidation and reduction at conventional electrodes.

This work first describes the synthesis of tris and mono(ammine) iron complexes with tridentate phosphine ligands and their role in increasing current densities for NH_3 oxidation relative to current densities generated using standard anodes. Electrocatalytic ammonia oxidation by a mononuclear ruthenium ammine complex supported by an isoindole-based tridentate ligand has been investigated next and its oxidation potential has been compared to previously reported mononuclear ruthenium ammine catalysts. At the end, a dinuclear polypyridine ruthenium bis(ammine) complex was reported in which ruthenium centers are held in close proximity by a bridging ligand in a way two NH_3 ligands have a syn relationship, allowing the possibility of intramolecular oxidative N–N coupling.

NULLIUS IN VERBA

ACKNOWLEDGMENTS

First, I would like to thank Prof. Milton R. Smith for accepting me into his research group and supporting me during the Ph.D. program. I need to acknowledge Prof. Thomas W. Hamann for his valuable suggestions on the electrochemical aspects of my project. Also, I would like to thank Dr. Amrendra K. Singh for his contributions to the synthesis of some iron complexes. I am thankful to Dr. Daniel Holmes for his assistance in NMR experiments, Dr. Richard J. Staples for X-Ray crystallography, and Prof. John McCracken for EPR spectroscopy.

I owe a lot of gratitude to my lab mates – Mona Maleka Ashtiani, Po-Jen Hsiao, Alex O'Connell, Pauline Mansour, Tim Shannon – and ammonia project members – Dan Little, Susanne Miller, Geletu Quing, Chenjia Mi, Arianna Savini – for being always happy to help.

TABLE OF CONTENTS

LIST OF ABBREVIATIONS

AO	Ammonia Oxidation
BDD	Boron-doped diamond
BE	Bulk electrolysis
C	Columb
CE	Counter electrode
cm	Centimeters (1×10^{-2} meters)
CV	Cyclic Voltammogram, or Cyclic Voltammetry
D	Diffusion coefficient (cm^2s^{-1})
DCM	Dichloromethane
DFT	Density Functional Theory
dmpe	1,2-Bis(dimethylphosphino)ethane
DMSO	Dimethyl sulfoxide
e^-	Electron
$E_{1/2}$	Half-wave potential
E_p	Peak potential
F	Faraday constant (96485.3321233100184 C mol^{-1})
Fc	Ferrocene
Fc^+	Ferrocenium
Fc*	Decamethylferrocene
Fc^{*+}	Decamethylferrocenium
GC	Glassy carbon
J	Joule

K	Kelvin
kg	Kilogram (1×10^3 grams)
L	Liters
mA	Milliamps (1×10^{-3} amps)
mL	Milliliters (1×10^{-3} Liters)
n	Integer number of electrons
NHE	Normal Hydrogen Electrode
NMR	Nuclear magnetic resonance
M	Molar (moles solute divided by liters solvent)
MeCN	Acetonitrile
mM	Millimolar (millimoles of solute divided by liters of solvent)
mV	Millivolts (1×10^{-3} volts)
NBO	Natural Bond Orbital
OTf^-	Trifluoromethanesulfonate (triflate) anion
pH	Negative base ten logarithm of the molar concentration of protons
ppm	Part Per Million
RE	Reference Electrode
s	Seconds
T	Temperature
TBAOTf	Tetrabutylammonium trifluoromethanesulfonate
$TBAPF_6$	Tetrabutylammonium hexafluorophosphate
THF	Tetrahydrofuran
Triflate	Trifluoromethanesulfonate

Trpy	2,2’:6’,2”–terpyridine
UV	Ultraviolet
V	Volts
Vis	Visible
vs.	Versus
WE	Working Electrode
XPS	X-ray Photoelectron Spectroscopy
°C	Degrees Celsius
$^{298.15\ \mathrm{K}}\Delta G_{\mathrm{rxn}}$	Change in Gibbs free energy for a chemical reaction at 298.15 K

Abbreviation	**Chemical Structure**
bid	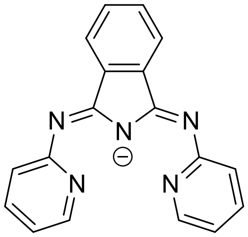
bpp	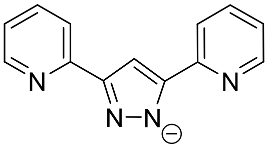
bpy	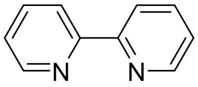
bpy'	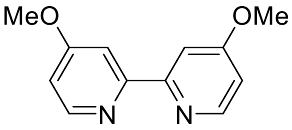
dmpe	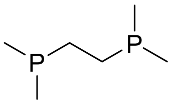
trpy	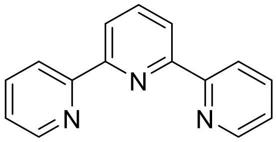
^{t}SiP$_3$	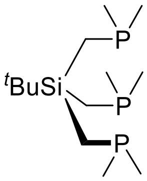

Chapter 1. AMMONIA AS A CARBON-NEUTRAL FUEL

1.1. Consumption of Fossil Fuels and Global Warming

Global warming due to anthropogenic greenhouse gasses released into the atmosphere remains one of the challenges for today's world to overcome.[1] On the other side, a progressive increase in the planet's human population results in high demand for energy production. Fossil fuels constitute a major part of the world's energy consumption. According to BP's annual statistical review of world energy, fossil fuels provided 83.2% of the global energy supply in 2020 whereas for renewable energies this number reaches 5.7% (Figure 1.1).[2]

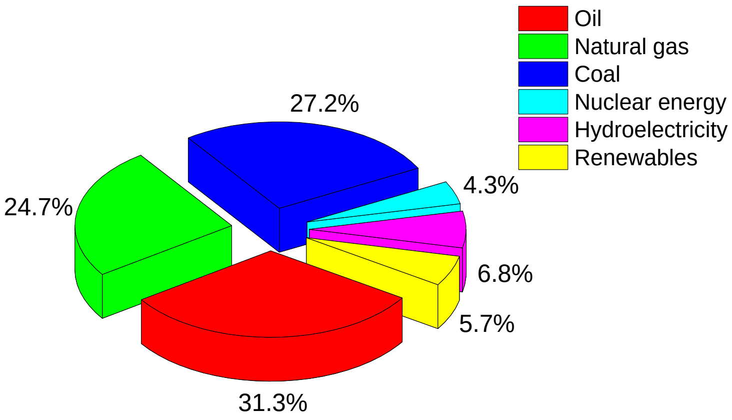

Figure 1.1 World's energy consumption by fuel in 2020

The emission of CO_2 is an inevitable consequence of fossil fuel combustion that is still rising worldwide, mainly due to the high energy demand in transportation sectors and increases in the standard of living (Figure 1.2).[3] Although oil, natural gas, and coal resources are limited, new technology continues to make unexploited deposits accessible reserves, and by adding up the discoveries of new reservoirs, fossil fuels will sustain for centuries.

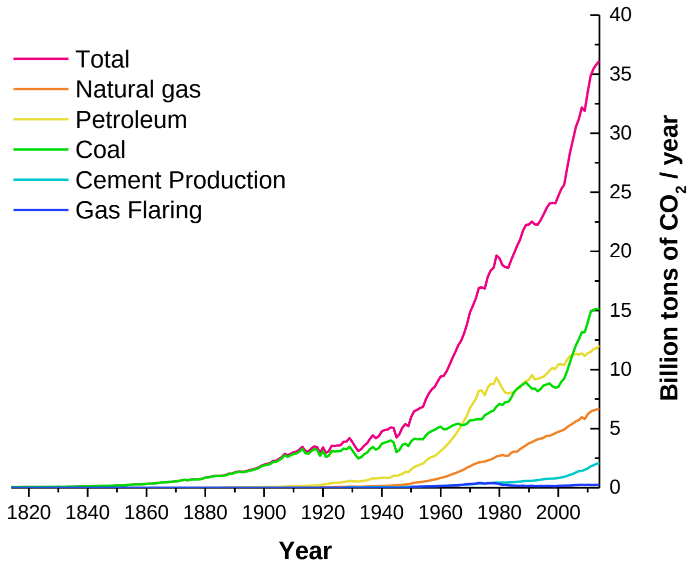

Figure 1.2 Increase in CO_2 emission due to the consumption of fossil fuels

Extraction and employment of new carbon-based fuel deposits regardless of considering the consequences of CO_2 emission into the atmosphere will eventuate in a 1.5°C temperature increase for the northern hemisphere by 2050 based on the current trend of energy consumption. The accelerated rise of sea level, changes in precipitation patterns, droughts, and heat waves are the most significant outcomes of global warming.[4]

1.2. Hydrogen Economy: Removing Carbon Out of Fuel Cycle

An alternative for decreasing the emission from the combustion of fossil fuels can be achieved by utilizing non-carbon-based energy carriers. Hydrogen, as a sustainable and green energy carrier, has gained extensive consideration around the world due to its high energy density per mass and taking carbon out of the fuel cycle. Natural gas reforming and coal gasification are the most common industrial processes for massive hydrogen production that generate CO_2 emission.[5] So,

H_2 can be regarded as a renewable fuel only if produced directly from renewable energy sources such as wind, solar, and hydropower.[6]

H_2 has higher energy density per mass but lower energy density per volume among the common fuels which makes its transportation costly. Liquefaction of H_2 increases its volumetric energy density from 4.5 MJ/L (at 700 bar) to 8.5 MJ/L but consumes ~35% of hydrogen's energy content.[7] Even the volumetric energy density of liquefied hydrogen is 1/4 of gasoline, and this is not a solution due to the high-energy-consuming process of hydrogen liquefaction. Moreover, even a cryogenic liquid hydrogen tank with good thermal insulation has a continuous boil-off at a rate of up to 1% per day which makes long-term storage challenging.[8] All of these difficulties and safety concerns regarding hydrogen storage suggest an alternative hydrogen carrier.

1.3. Ammonia as Hydrogen Carrier

Among the compounds that store hydrogen chemically, ammonia has attracted a significant amount of consideration due to its low-cost, large-scale production, and carbon-free emission when being used as a fuel. In 2016, 175 million metric tons of ammonia were produced worldwide and more than half of it was used in agriculture.[9] Unlike hydrogen which requires carbon fiber-reinforced composite tanks for storage at 700 bar, ammonia liquefies at 10 bar and thus can be stored in stainless steel tanks. Moreover, there is a safe storage and transportation infrastructure due to the large-scale industrial production of ammonia, which is one of the prerequisites for a chemical to be considered as a worldwide fuel.

Vehicles can be powered by ammonia in three different ways: internal combustion engines (ICEs), ammonia fuel cells, and onboard conversion of NH_3 to N_2 and H_2, by thermal cracking or NH_3 electrolysis and then feeding the produced H_2 into a hydrogen fuel cell. Since the activity of ammonia toward combustion is 1/6 of gasoline[10], in internal combustion engines ammonia must be mixed with some portion of a combustion enhancer like gasoline, diesel, or H_2 to burn and release enough energy to propel the car.[11,12] There are some challenges to be solved regarding ammonia ICEs such as a relatively high NH_3:gasoline ratio (3:7) in 1400 rpm engine speeds, ammonia's high auto-ignition (651°C compared to 440 °C for gasoline), low flame temperature, corrosion of the engine parts and potential NOx emissions.[13]

The prototype of an ammonia fuel cell was first examined in the late 1960s based on alkaline fuel cells (AFCs) using a KOH electrolyte with an operating temperature range of 50-200 °C.[14] The net reaction in an alkaline fuel cell is shown in the Scheme 1.1:

Scheme 1.1 Overall reactions in an ammonia alkaline fuel cell

Cathode: $$3\ O_2 + 6\ H_2O + 12\ e^- \longrightarrow 12\ OH^-$$

Anode: $$4\ NH_3 + 12\ OH^- \longrightarrow 2\ N_2 + 12\ H_2O + 12\ e^-$$

Net: $$4\ NH_3 + 3\ O_2 \longrightarrow 2\ N_2 + 6\ H_2O$$

Based on today's technology, it is hard to develop a good low-temperature direct ammonia fuel cell with high power density. They are not suitable for transport applications due to the slow start-up and brittleness of their ceramic components.[15] Low-temperature proton exchange membrane fuel cells (PEMFCs) using hydrogen as fuel have been developed for various applications including electric vehicles. Toyota Mirai which is commercially available to purchase uses PEMFC as an energy source. The car stores 6 kg of hydrogen at 700 bar in two tanks which can provide enough energy to drive 845 miles.

Utilizing ammonia in PEMFCs poisons the Pt/C anode catalyst and reacts with the acidic Nafion membrane; therefore, it is not a suitable fuel for PEMFCs by itself. However, ammonia can be used as a source for hydrogen production and the produced hydrogen can be fed into PEMFC for power generation.[16]

1.4. Splitting NH_3 to H_2 and N_2

Two methods can be considered for NH_3 splitting to H_2 and N_2: thermal cracking and electrolysis. Thermal cracking of ammonia occurs at temperatures ~500 °C in the presence of a heterogeneous catalyst. Ru is the most used catalyst for this process due to its high activity toward NH_3 decomposition. The catalytic activity of Ru is support-dependent, which means the support facilitates the electron transfer and helps the recombination desorption of N atoms from the Ru surface, the rate-determining step in the heterogeneous catalytic cycle. It also enhances the dispersion and increases the effective area of the active catalyst.[17] Utilizing carbon materials such as activated carbon, carbon nanotubes (CNTs), and CNTs-MgO as support shows the highest catalytic activity in ammonia decomposition. However, the reaction to produce H_2 with a carbon support at high temperatures eventuates in the production of methane and decreases the efficiency of the catalyst over time.[18] Investigating the new supports for Ru-based catalysts is the subject of ongoing research. Ru/graphene nanocomposites and Ru catalysts on non-carbon-based supports (MgO, SiO_2, Al_2O_3, TiO_2, ZrO_2, and Cr_2O_3) have demonstrated high activity for ammonia dehydrogenation.[19] In addition to Ru-based heterogeneous catalysts, the catalytic activity of main group compounds, including $LiNH_2$ and $NaNH_2$, also have been investigated, and it was shown that they could be effective ammonia decomposition catalysts.[20]

Electrolysis or electro-oxidation is another method for splitting ammonia into H_2 and N_2. The scalability and ability to operate in on-demand mode and at moderate temperature are the advantages of electrolysis over thermal cracking methods.[21] The thermodynamic potential for ammonia electrolysis in aqueous alkaline media is –0.06 V compared with –1.223 V for the electrolysis of water. The theoretical thermodynamic energy consumption is 1.55 Wh/g of H_2 from the electrolysis of NH_3 compared to 33 Wh/g of H_2 from the electrolysis of H_2O assuming that there are no kinetic limitations. This means that, theoretically, ammonia electrolysis consumes 95% less energy to produce the same quantity of hydrogen than water electrolysis.[21] Electrolysis of ammonia is favorable thermodynamically; however, kinetics limits the rate of reaction requiring higher voltages to be applied.

1.5. Catalysis for Reducing the Overpotential of NH_3 Oxidation

In the search for electrodes that reduce the overpotential of NH_3 oxidation in aqueous media, Pt alloys show effective catalytic properties. Pt/Ir, Pt/Ru, and Pt/Rh alloys are the most efficient catalysts for the dehydrogenation of NH_3 in lower potentials. The electrocatalytic activity of Pt alloys decreases with the trend Pt/Ir > Pt/Rh > Pt/Ru.[22] A significant amount of effort has been devoted to the development of electrocatalysts for the anode since ammonia oxidation has been identified as the limiting reaction.[23] The efficiency of Pt/Ir electrodes for ammonia oxidation range from 80% at 10 mA/cm^2 to 60% at 400 mA/cm^2 in alkaline media.[24] There are still some challenges with ammonia–alkaline electrolytic cells. The commercialization of the technology demands the development of more efficient electrodes with low–cost metals for future large–scale production. Moreover, the hydrogen capacity is limited to 6.1 mass%, because the ammonia concentration in saturated ammonia aqueous solution is 34.2 mass% at 20 °C.[25] Unlike the electrolysis of NH_3 in aqueous media, electrolysis of liquid NH_3 has attracted less attention. In 2010 Hanada *et al.*, reported the current density of 7.2 mA/cm^2 from the electrolysis of liquid ammonia with 2.0 V applied potential between two Pt electrodes using 1 M KNH_2 as the supporting electrolyte.[26] They proposed that oxidation of amide at the anode and reduction of ammonia at the cathode generates nitrogen and hydrogen respectively. Because of the application of a potential between the working and counter electrodes and not using a reference electrode for measuring the exact potential of each electrode, the overpotential of the anodic and cathodic reactions was not reported. In 2015 a revised mechanism was proposed.[27] It was suggested that the cathodic reaction proceeds via initial one–electron reduction of NH_4^+ to $NH_4^{\bullet}$ rather than NH_4^+ dissociation to NH_3 and H^+ followed by H^+ reduction. Also, by using a three-electrode system, overpotentials at the anode and cathode were determined to be 1000 mV and 600 mV, respectively. Finally, it was shown that Pt electrodes get poisoned in NH_3(l) due to nitride formation.

Even after resolving the problem of electrode poisoning, employing a suitable catalyst that lowers the overpotential of ammonia oxidation for efficient H_2 generation is necessary. One possible solution is the use of a homogeneous catalyst. A catalyst should be designed to be oxidized, and then, in turn, oxidize NH_3 in the bulk solution. In this project, we focus on the synthesis of Fe and Ru complexes to reduce the anodic overpotential of ammonia oxidation.

Chapter 2. GENERAL EXPERIMENTAL PROCEDURES

2.1. Electrochemistry

2.1.1. Instrument

All electrochemical experiments were performed with a Metrohm Autolab PGSTA128N potentiostat using the Nova 2.1 software package.

2.1.2. Reference Electrode

For accurate and precise control of the potential of a working electrode and obtaining reliable electrochemical data, an ideally non-polarized electrode, i.e., reference electrode, should be utilized. The potential of the reference electrode should remain practically constant upon current flow through the electrochemical cell. In previously reported papers, silver-based non-aqueous reference electrodes ($Ag/AgNO_3$, Ag/AgOTf, $Ag/AgClO_4$) have been used for electrochemical measurement in the presence of NH_3. It will be shown here that the potential of these reference electrodes shifts due to the reaction of NH_3 with silver to yield $[Ag(NH_3)_2]^+$. This potential shift can result in serious experimental errors, especially during controlled potential electrolysis.

Figure 2.1 shows the CV of 1 mM decamethylferrocene (Fc*) in THF containing 2 M of NH_4OTf as a supporting electrolyte. Glassy carbon (GC) was used as the working electrode, Pt disk as the counter electrode and for preparing the reference electrode a 1/4 inch diameter glass tube with a Pt fused tip was filled with THF containing 5 mM of AgOTf. Although the CV of Fc* in the absence of NH_3 was stable and no potential drift was observed after 200 scans, upon bubbling NH_3 to make a saturated solution (3.24 M NH_4 measured by titration and NMR spectroscopy), reference electrode potential started to drift. After ~150 scans, potential of the reference electrode became stable, however, ~100 mV drift was observed.

Due to the assumption that the formation of $[Ag(NH_3)_2]^+$ in the reference electrode after introducing NH_3 to the solution results in drifting its potential, it was devised that instead of

$Ag(OTf)_2$ in the reference electrode, $[Ag(NH_3)_2]^+$to be used. For this purpose, $[Ag(NH_3)_2]^+$was easily prepared by bubbling NH_3 into AgOTf solution in THF. Upon removing the solvent, white solids of $[Ag(NH_3)_2][OTf]$ were collected.

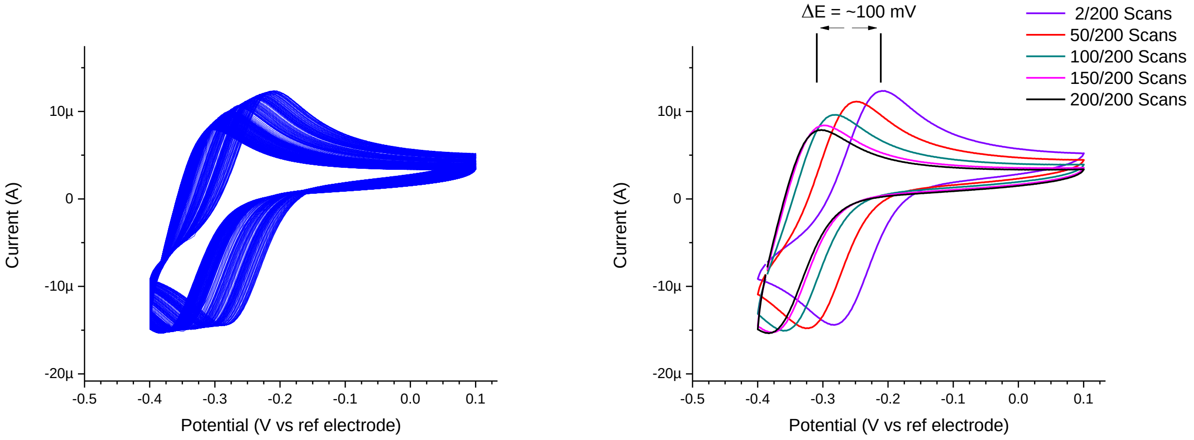

Figure 2.1 Left: CV of 1 mM of Fc* in THF with 200 scans containing 2 M NH_4OTf as supporting electrolyte right after bubbling NH_3 for 5 min to get a saturated NH_3 solution (3.24 M of NH_3). Right: Same CV in which only scans #2, 50, 100, 150, and 200 are plotted for clarity. Working electrode: GC; counter electrode: Pt disk; reference electrode: Ag wire immersed in THF containing 2 M NH_4OTf, and 5 mM AgOTf with Pt fused tip; scan rate: 100 mV/s

Although $Ag/[Ag(NH_3)_2]^+$ reference electrode was stable after bubbling NH_3 and no potential drifting was observed, $E_{1/2}$ of ferrocene (Fc) shifted upon the addition of 1 mM of Fc* into the solution (Figure 2.2). This pattern was observed in different solvents with different supporting electrolytes, so it was assigned to the intrinsic property of the reference electrode.

In addition to Fc, $E_{1/2}$ of other inorganic complexes was also shifted upon the addition of Fc*. For these reasons, a new reference electrode was realized for electrochemical experiments in presence of NH_3 to eliminate silver. A previously reported reference electrode with a Pt wire immersed in a 1:1 ratio of Fc^*/Fc^{*+} was chosen for this purpose due to the inertness of Fc* toward NH_3.[28–31]

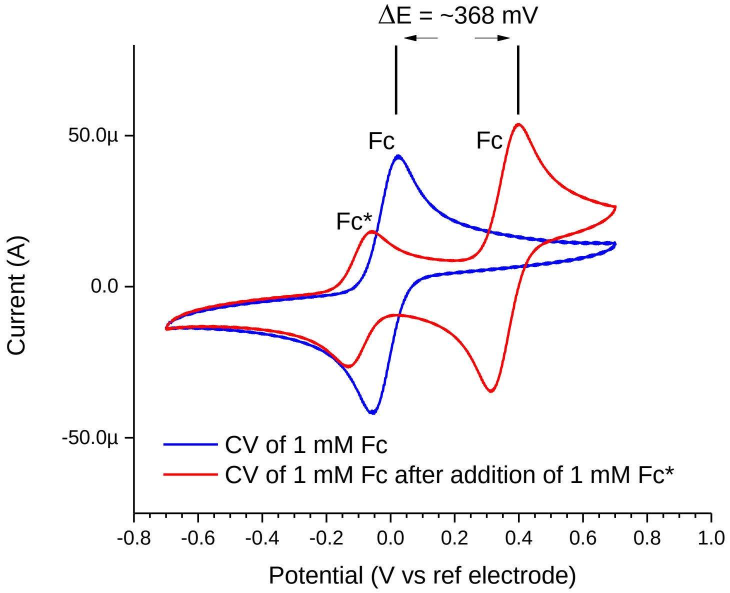

Figure 2.2 $E_{1/2}$ of 1 mM Fc after the addition of 1 mM of Fc* with Ag/$[Ag(NH_3)_2]^+$ reference electrode in THF containing 2 M of NH_4OTf shifts 368 mV to more anodic potential. Working electrode: GC; counter electrode: Pt disk; reference electrode: Ag wire immersed in THF containing 2 M NH_4OTf, and 5 mM $[Ag(NH_3)_2][OTf]$ with Pt fused tip; scan rate: 100 mV/s

Fc*/$Fc*^+$ reference electrode was prepared by immersing a Pt wire into a 1/4 inch glass tube with CoralPor tip containing THF, 1 M of NH_4OTf as supporting electrolyte, 3 mM of Fc*, and 3 mM of Fc*OTf. Because Fc*OTf is not soluble in THF but dissolves in the presence of NH_4OTf and Fc* is highly soluble in THF but dissolves very slowly in the presence of NH_4OTf, it’s better to prepare Fc*OTf in THF with 1 M NH_4OTf and Fc* in pure THF and then mix both. Due to the oxidation of Fc* solutions upon exposure to air, the reference electrode should be prepared under an inert atmosphere (glovebox) and sealed properly.

To test the leaking of Fc* and/or Fc*OTf into the solution from the reference electrode through CoralPor membrane, CV of blank THF containing 1 M of NH_4OTf was taken with the Fc*/$Fc*^+$ reference electrode. A very small peak at 0 V vs Fc*/$Fc*^+$ reference electrode can be observed in the SQW which indicates a small leak of Fc* and/or Fc*OTf into the solution from the reference electrode through CoralPor membrane, which is reasonable (Figure 2.3).

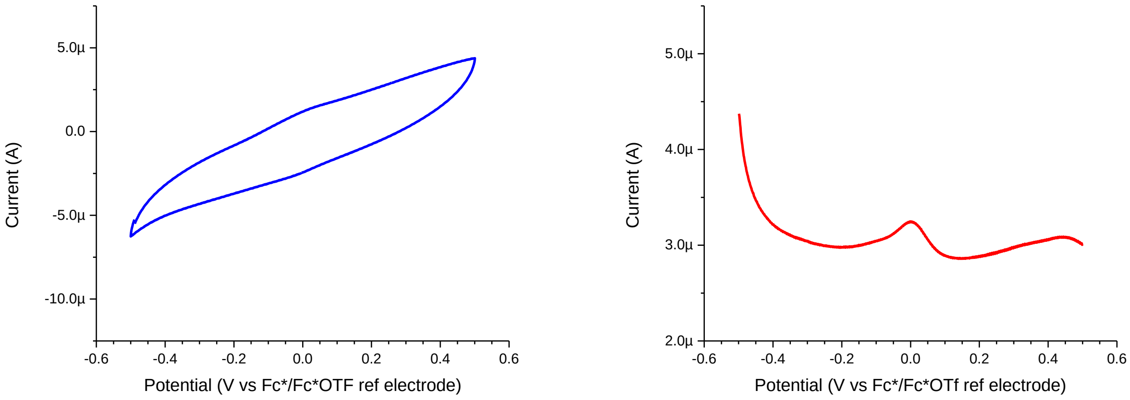

Figure 2.3 Left: CV of blank THF containing 1 M of NH_4OTf as supporting electrolyte. Right: corresponding SQW at same condition right after taking CV. Working electrode: GC; counter electrode: Pt disk; reference electrode: Pt wire immersed in THF containing 1 M NH_4OTf, 3 mM of Fc*, and 3 mM of Fc*OTf with CoralPor fused tip; scan rate: 100 mV/s

To test the stability of the reference electrode in the absence of NH_3, CV of 1 mM Fc* was taken which shows no drifting throughout 50 scans with the $E_{1/2}$ of 0 V (Figure 2.4).

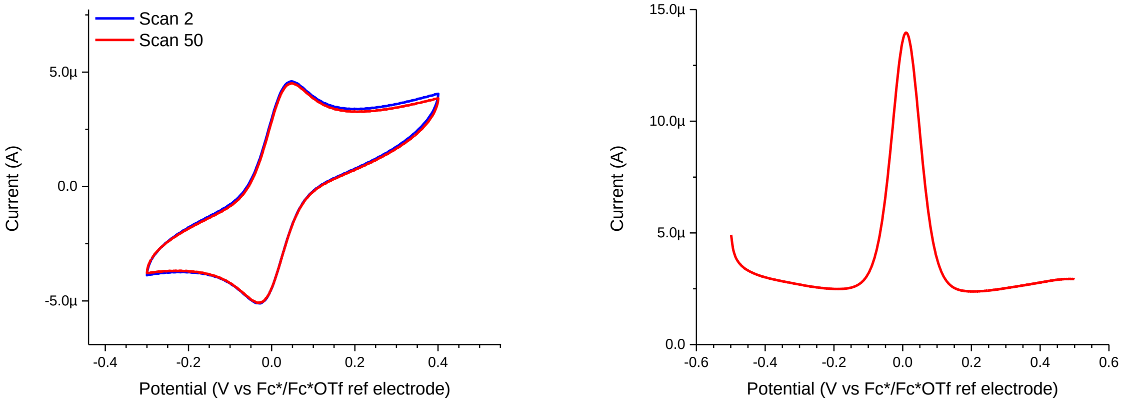

Figure 2.4 Left: CV of 1 mM Fc* in THF with 1 M NH_4OTf as supporting electrolyte. Right: corresponding SQW at same condition right after taking CV. Working electrode: GC; counter electrode: Pt disk; reference electrode: Pt wire immersed in THF containing 1 M NH_4OTf, 3 mM of Fc*, and 3 mM of Fc*OTf with CoralPor fused tip; scan rate: 100 mV/s

After bubbling NH_3 (2.8 M NH_3) into the 1 mM solution of Fc* in THF, 50 consecutive CVs were taken again. No potential drift was observed after saturating the solution with NH_3 and also after 50 consecutive scans (Figure 2.5). These data suggest that Fc*/Fc*$^+$ is the best reference electrode for CV measurements in solutions containing NH_3.

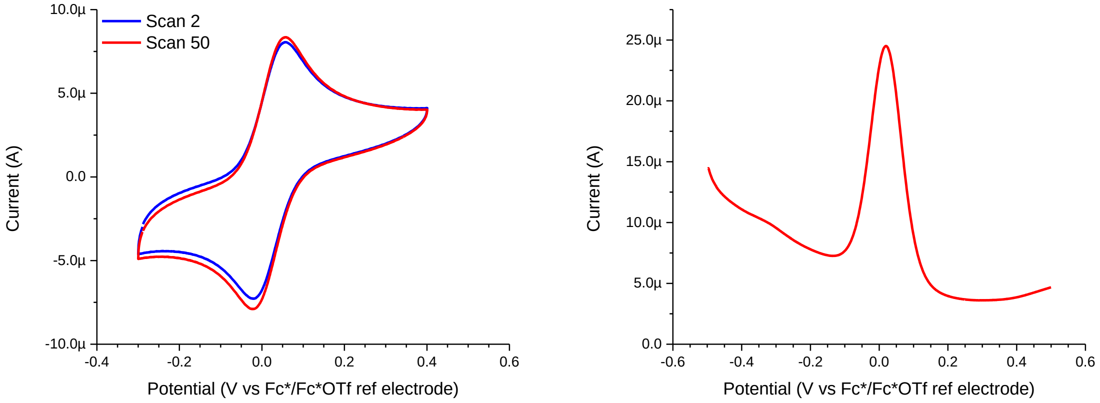

Figure 2.5 Left: CV of 1 mM Fc* in THF with 1 M NH_4OTf as supporting electrolyte after bubbling NH_3 (2.8 M NH_3). Right: corresponding SQW at same condition right after taking CV. Working electrode: GC; counter electrode: Pt disk; reference electrode: Pt wire immersed in THF containing 1 M NH_4OTf, 3 mM of Fc*, and 3 mM of Fc*OTf with CoralPor fused tip; scan rate: 100 mV/s

2.1.3. $E_{1/2}$ of Fc vs. Fc* in THF and MeCN with NH_4OTf and $TBAPF_6$ Electrolytes

In most of the literature,[32,33] the $E_{1/2}$ of complexes in non–aqueous media were reported vs Fc. For converting the $E_{1/2}$ of Fc to Fc* for making an accurate comparison between $E_{1/2}$ of complexes, CVs of Fc were taken in THF and MeCN in the presence of Fc*, and the results are summarized in Table 2.1.

Table 2.1 $E_{1/2}$ of Fc vs. Fc* in MeCN and THF

	THF	MeCN
2 M NH_4OTf	$E_{1/2}$ Fc = 449 mV (vs. Fc*)	–
0.1 M $TBAPF_6$	$E_{1/2}$ Fc = 459 mV (vs. Fc*)	$E_{1/2}$ Fc = 508 mV (vs. Fc*)

Different references report –810 V[32,34,35] and –0.826 V[31,33] for converting NHE to Fc/Fc$^+$ in THF at room temperature. Based on Table 2.1 it can be straightforward to convert the reported $E_{1/2}$ vs. Fc/Fc$^+$ or NHE in literature to Fc*/Fc*$^+$.

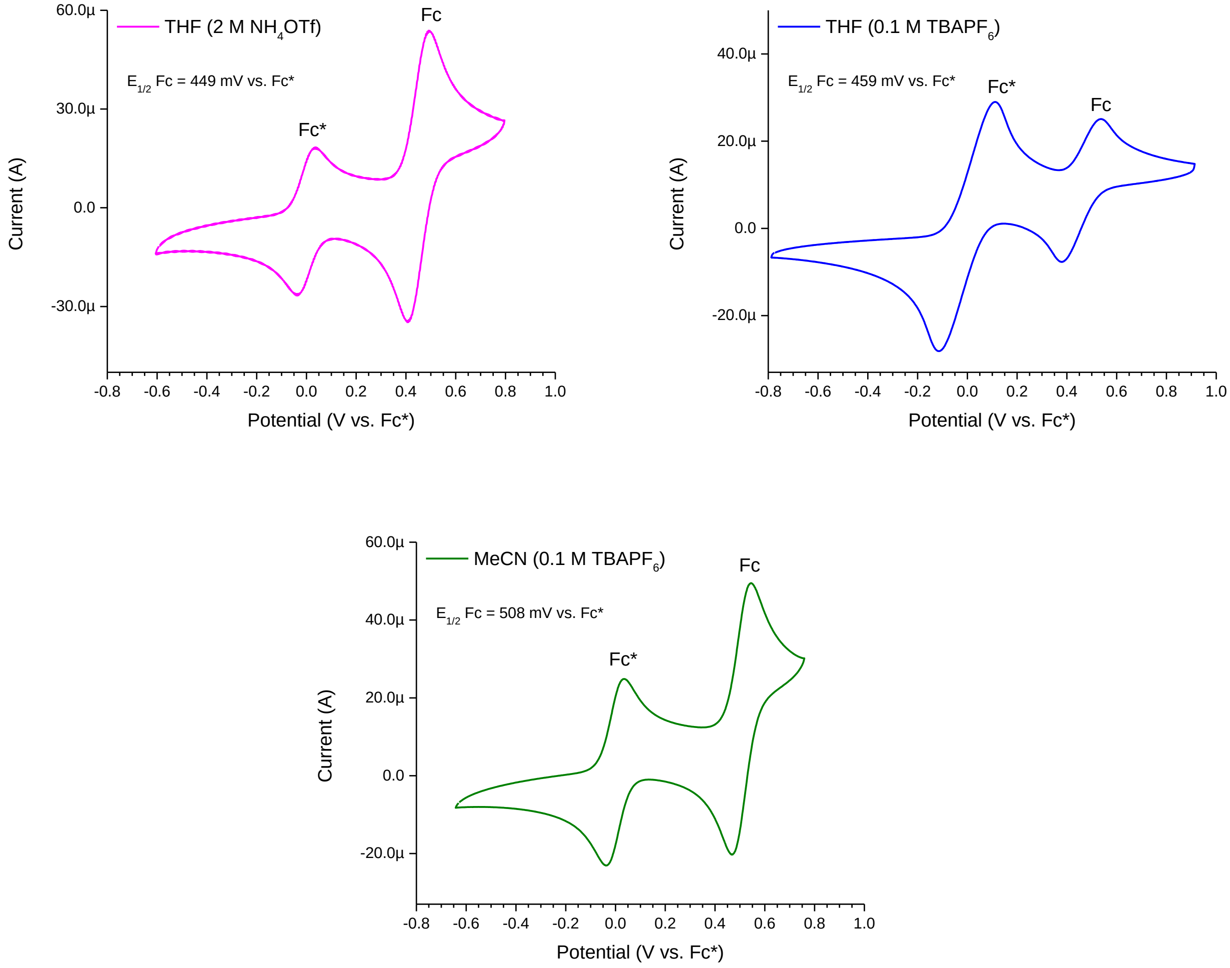

Figure 2.6 CV of Fc in the presence of Fc* in MeCN and THF

2.1.4. Bulk Electrolysis

Bulk electrolysis experiments have been conducted in a 60 mL–sized pear shape electrochemical cell with four fused 14/20 thermometer adapters cap and Viton O-ring. Regarding electrodes, a GC plate as the working electrode, Pt mesh as the counter electrode, and an Fc* reference electrode were used. GC plate is dangling from a Pt wire which is connected to a copper wire inside a 1/4-inch diameter glass tube with silver epoxy covered with Loctite EA 1C^{TM} (HYSOL$^{®}$) adhesive. Pt mesh was also connected to a copper wire in the same manner. The cell was filled with solvent in such a way that the Pt wire which the GC plate is hanging would not be in touch with the solution. The top and bottom parts of the glass tubes were sealed with a glue gun and Loctite EA 1C^{TM} (HYSOL$^{®}$) adhesive, respectively. A stir bar also was put in the cell for stirring the solution during bulk electrolysis.

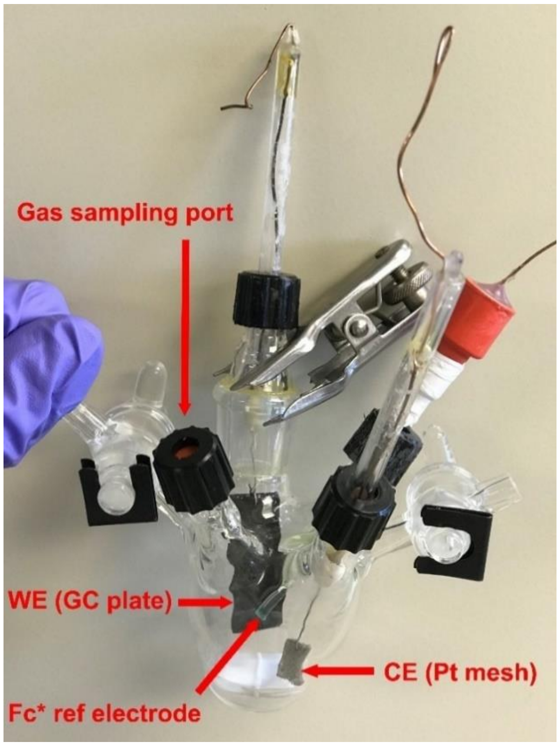

Figure 2.7 Designed electrochemical cell for bulk electrolysis experiments

For the gas sampling port, a 3-layer, 1/2-inch diameter HAMILTON 76006 septum was used. Gas analysis was performed by the HIDEN HPR-20 R&D benchtop gas analysis system.

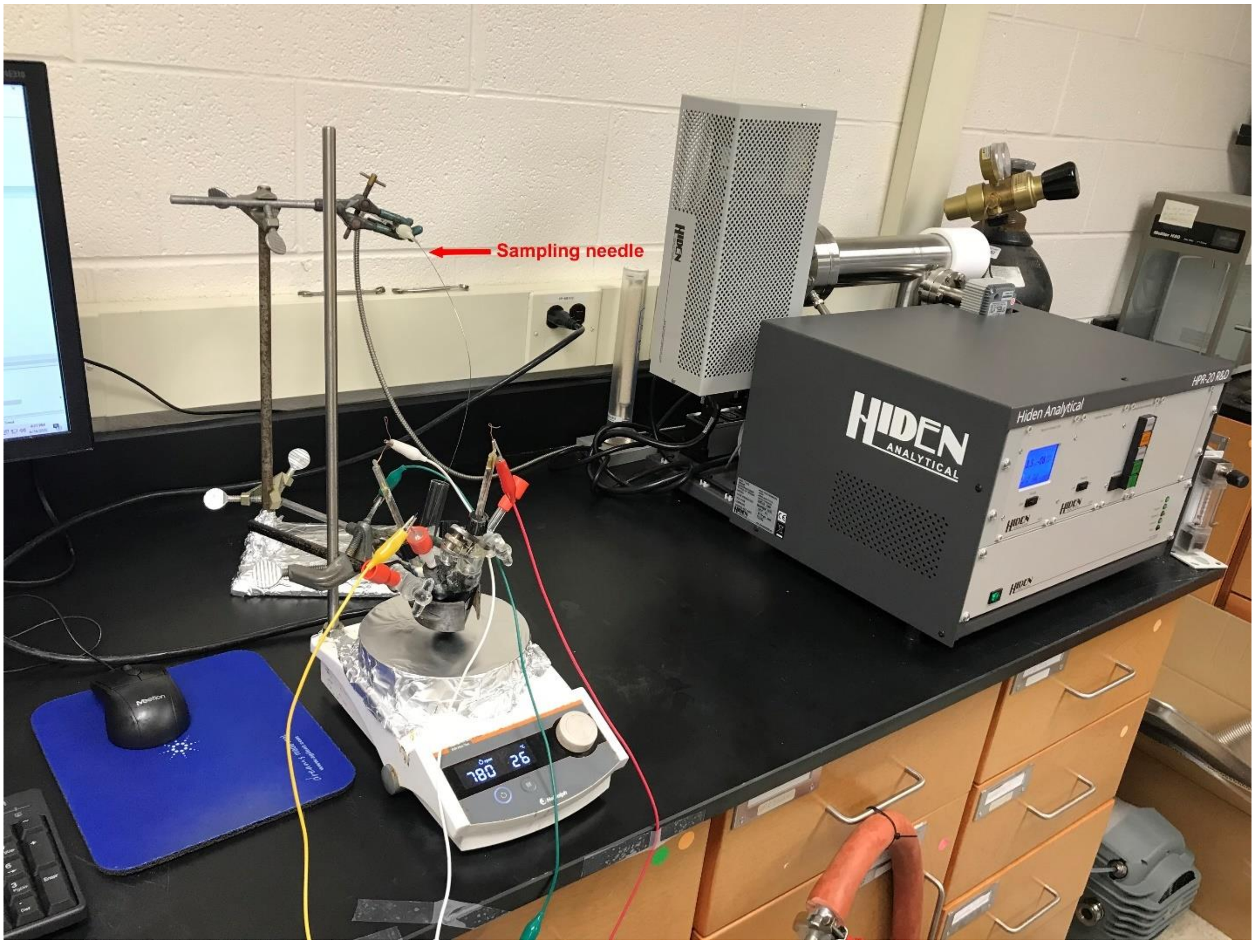

Figure 2.8 BE experiment accompanied by gas analysis

For gas analysis, because the instrument only reports the percentage of gases, a certain volume of ultra-pure helium was injected into the cell before the experiment, and moles of produced gases were calculated based on moles of injected helium.

2.2. Synthesis

2.2.1. Synthesis of Decamethylferrocenium triflate (Fc*OTf)

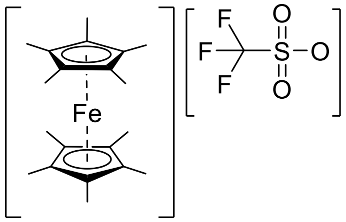

According to the previously described procedure,[32] decamethylferrocene first was sublimed at 140 °C at 0.01 torr as a yellow solid. In the air, 108 mg (0.996 mmol, 0.65 equiv) of *p*-benzoquinone was dissolved in 35 mL of THF and while stirring, 0.3 mL (3.524 mmol, 2.3 equiv) of triflic acid was added. The pale-yellow color of the *p*-benzoquinone turns orange. Then immediately decamethylferrocene (500 mg, 1.532 mmol, 1 equiv) was added as a solid. The color changed to green and Fc*OTf crashed out. After stirring for 5 min, the green solid was collected and washed with THF, and dried overnight under vacuum. Yield: 684 mg, 94%. ^{1}H NMR (500 MHz, MeCN-d_3) δ –37.42 (s, br). ^{19}F NMR (470 MHz, MeCN–d_3) δ –79.46 (s).

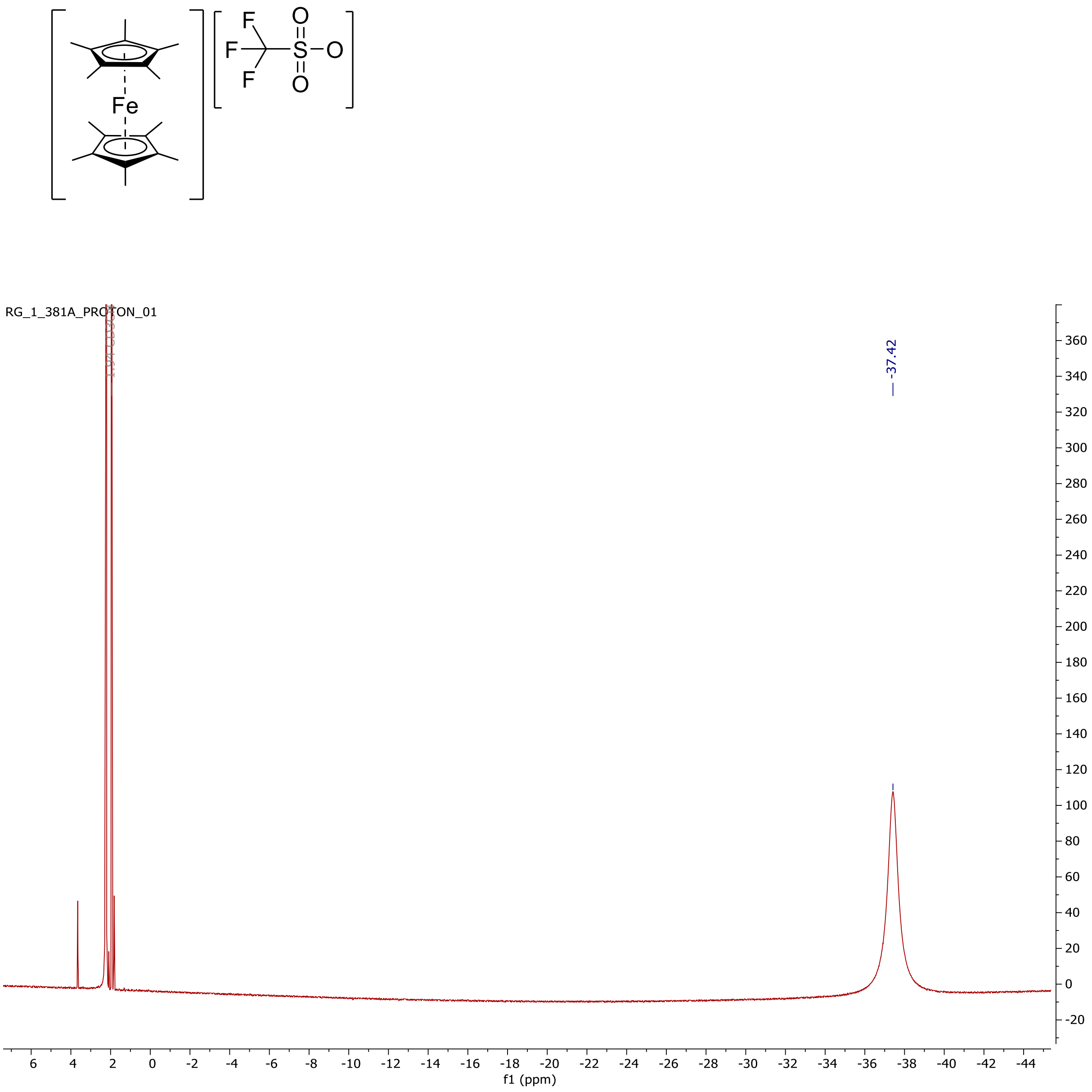

Figure 2.9 ^{1}H NMR of Fc*OTf in MeCN-d_6

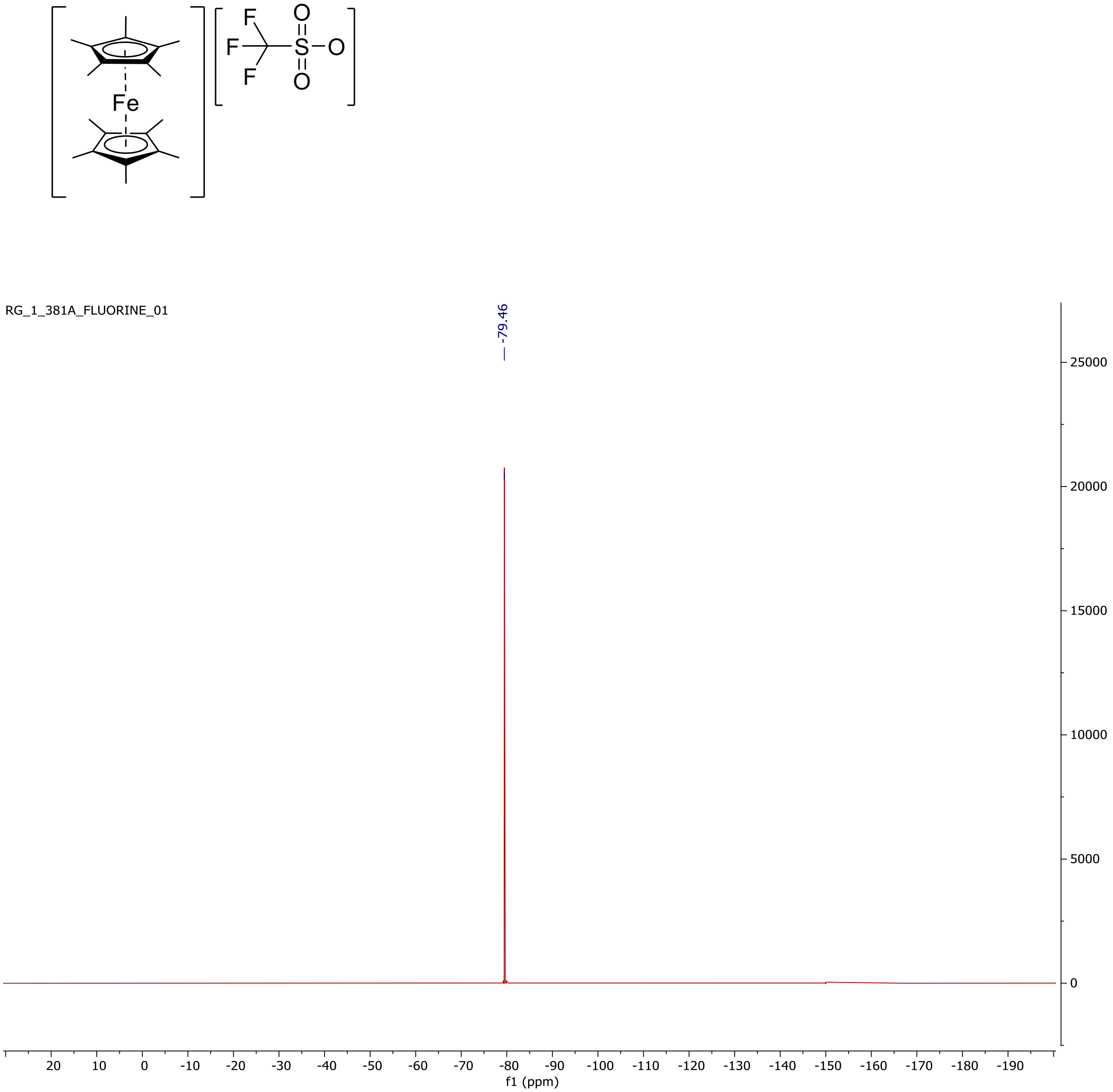

Figure 2.10 ^{19}F NMR of Fc*OTf in MeCN-d_6

2.2.2. Synthesis of tris(4-bromophenyl)amine radical cation

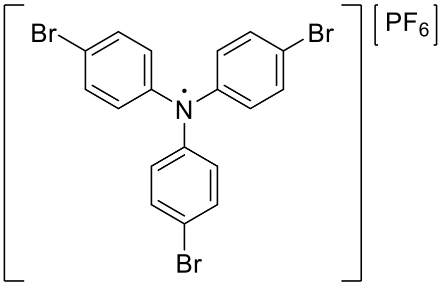

Following the previously reported procedure,[36,37] in the glovebox 6.361 g (13.19 mmol, 1 equiv) of tris(4–bromophenyl)amine was dissolved in 25 mL of degassed and dry DCM. While stirring, 2.54 g (14.51 mmol, 1.1 equiv) of $NOPF_6$ was added slowly as a solid. The color immediately changes from pale yellow to dark blue. Once the addition is complete, the solution was stirred for 10 minutes. Upon addition of 75 mL of Et_2O a brown–purple solid crashes out. Solids were filtered and washed with Et_2O until the washings were colorless. Solids were collected and dried under vacuum and stored in the freezer of the glovebox at –33 °C. Yield: 4.4 g, 53%. No ^1H or ^{13}C NMR signals were observed for the product.

2.3. DFT Calculations

All the free energies (ΔG) were calculated at 1 atm and 298.15 K by density functional theory (DFT) using Gaussian 16 software package,[38] and natural bond orbital (NBO) analysis with version 7.0.8.[39] All the geometries of complexes were fully optimized with the B3LYP functional[40] and def2-TZVP basis set.[41] The SMD solvation model[42] was applied to the gas-phase optimized structures to calculate the effect of solvation in THF on the free energies. The visualization of orbitals and optimized structures were done using GaussView software.[43]

Chapter 3. IRON AMMINE COMPLEXES CONTAINING A TRIPODAL PHOSPHINE LIGAND FOR ELECTROCATALYTIC AMMONIA OXIDATION

3.1. Introduction

Iron coordination complexes have been studied extensively for catalytic N_2 reduction to NH_3. The reverse reaction, where NH_3 is oxidized to N_2, protons, and electrons, has recently garnered renewed interest because it completes a cycle for storage and distribution of renewable hydrogen as NH_3, using the most abundant gas in Earth's atmosphere as the feedstock.

Chart 1.1 summarizes various Fe-based catalysts for NH_3 oxidation reported by 2022. In 2019, Peters and co-workers reported electrochemical NH_3 oxidation facilitated by a polypyridyl iron complex.[44] Due to the high onset potential of NH_3 oxidation relative to the thermodynamic limit in their iron system (0.7 V vs Fc/Fc^+ in MeCN with boron-doped diamond (BDD) as the working electrode), they reported another iron complex in 2021 that shifted the onset of AO to lower (~250 mV) potential compared to previous one at same conditions.[45] In 2022, Wang and co-workers reported a ferric ammine system that decreases the onset of AO to –0.04 V vs Fc/Fc^+ in THF with glassy carbon as the working electrode.[46]

While the AO mechanism for Peters' polypyridyl Fe systems is ambiguous, Wang and co-workers have proposed a mechanism that is shown in Scheme 3.1. According to this mechanism, Fe(III) first gets oxidized to Fe(IV) followed by deprotonation of ammine ligand by NH_3 to yield the corresponding Fe(IV) amido complex. One–electron oxidation of Fe(IV) amide to Fe(V) amide accompanied by nucleophilic attack of NH_3 to amide forms a hydrazido Fe(III) complex in which the NH group of ancillary ligand gets protonated to NH_2. Further oxidation of N_2H_4 to N_2, protons, and electrons completes the mechanism cycle.

Chart 1.1 Previously reported Fe catalysts for NH_3 oxidation

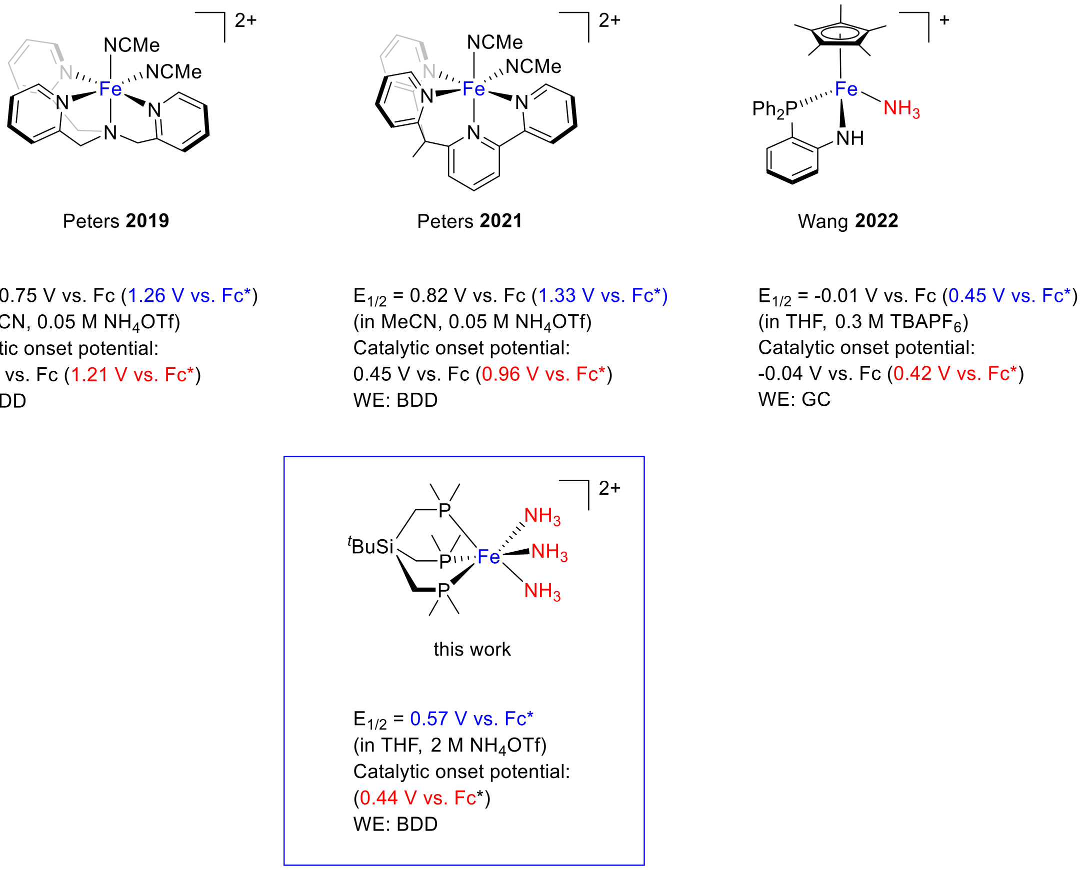

Peters **2019**

$E_{1/2}$ = 0.75 V vs. Fc (1.26 V vs. Fc*)
(in MeCN, 0.05 M NH_4OTf)
Catalytic onset potential:
0.70 V vs. Fc (1.21 V vs. Fc*)
WE: BDD

Peters **2021**

$E_{1/2}$ = 0.82 V vs. Fc (1.33 V vs. Fc*)
(in MeCN, 0.05 M NH_4OTf)
Catalytic onset potential:
0.45 V vs. Fc (0.96 V vs. Fc*)
WE: BDD

Wang **2022**

$E_{1/2}$ = -0.01 V vs. Fc (0.45 V vs. Fc*)
(in THF, 0.3 M $TBAPF_6$)
Catalytic onset potential:
-0.04 V vs. Fc (0.42 V vs. Fc*)
WE: GC

this work

$E_{1/2}$ = 0.57 V vs. Fc*
(in THF, 2 M NH_4OTf)
Catalytic onset potential:
(0.44 V vs. Fc*)
WE: BDD

The coordination chemistry of first–row transition metals containing tripodal phosphine ligands and their catalytic reactions are well established.[47,48] Phosphines have been utilized for synthesizing a large number of iron complexes due to their decent electron donor ability and production of diamagnetic complexes amenable for further NMR studies. Scheme 3.2 highlights some examples of iron ammine complexes with Fe–P bonds.[49–52] Four-coordinated complex **A** reported by Sellman in 1975 is one of the first examples of diamagnetic Fe(II) mono(ammine) complexes containing phosphine ligands. Complex **B**, however, is a low-spin, tris(ammine) phosphine complex of Fe(II) synthesized by Winfield and co-workers in 1988 in which the PMe_3 ligands have both *fac* and *mer* configurations.

Scheme 3.1 Proposed mechanism by Wang and co-workers[46]

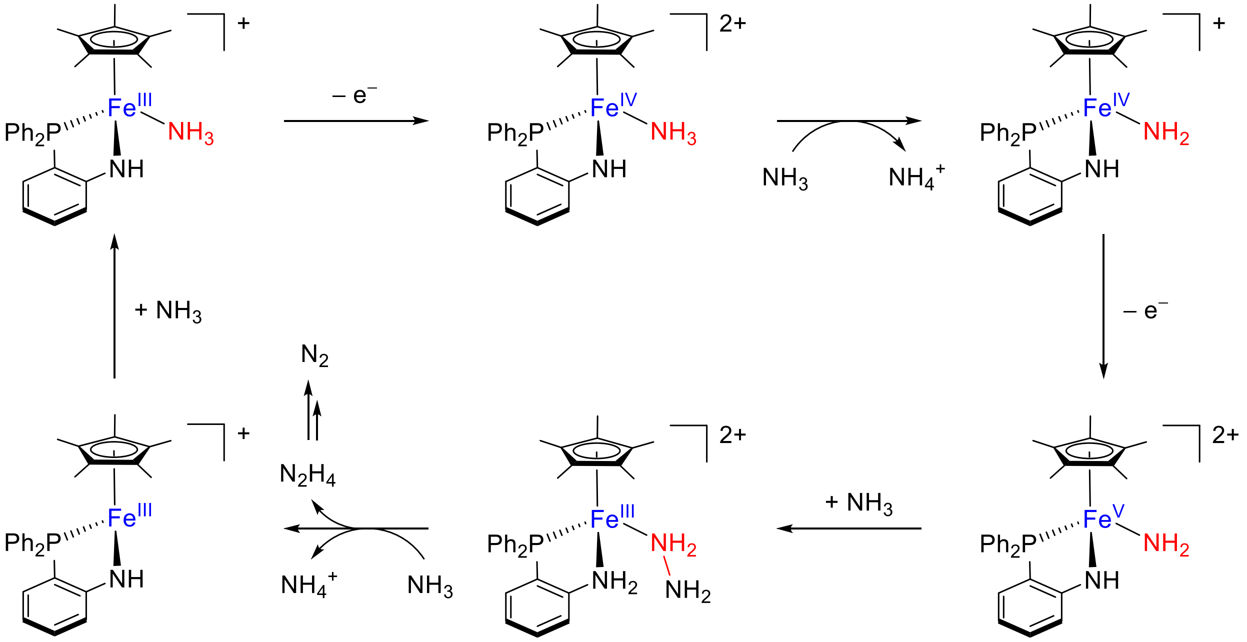

Complex **C** reported by Peters is an unusual paramagnetic five-coordinate Fe(I) mono(ammine) complex (S = 3/2) supported by a tris(phosphine)borane ligand with weak Fe–B bond that is yielded by decomposition of its N_2H_4 counterpart in benzene at room temperature. Another example of isolating Fe ammine complex containing phosphine ligands by N–N bond cleavage of N_2H_4 has been reported by Umehara et al.[51] (complex **D**), which bears a pyrazole-based ligand. Since hydrazine complexes can be regarded as possible intermediates in catalytic NH_3 oxidation reactions,[53,54] reproduction of Fe-NH_3 by cleaving the N–N bond of bound hydrazine can close the catalytic cycle.

In this chapter, we report a Fe(II) tris(ammine) AO catalyst supported by a tripodal phosphine ligand. The electrochemical behavior of this six–coordinated diamagnetic complex has been evaluated in the absence and presence of ammonia.

Scheme 3.2 Selected examples of Fe ammine complexes containing phosphine ligands

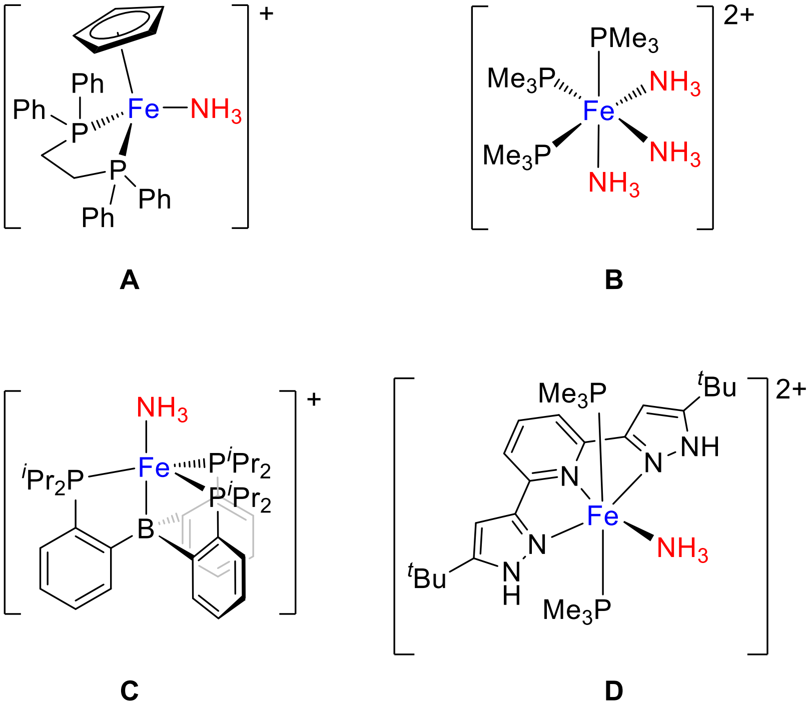

The effect of different electrolytes and electrodes on the catalysis and stability of the catalyst has been accessed as well. For investigating and isolation the possible intermediates of the catalytic ammonia oxidation mechanism, deprotonation, and chemical oxidation of the Fe(II) tris(ammine) complex have been evaluated. All the complexes have been isolated and characterized by various spectroscopic methods.

In the end, for evaluating the effect of ancillary ligands on the oxidation potential of the catalyst, two of the ammine ligands of Fe(II) tris(ammine) complex have been displaced by 1,2–bis(dimethylphosphino)ethane (dmpe) to yield a mono(ammine) complex. Cyclic voltammograms of mono and tris(ammine) complexes have been assessed and compared to each other. Moreover, Density Functional Theory (DFT) calculations have been employed for calculating the theoretical oxidation potentials.

3.2. Results and discussion

The first attempts for evaluating the electrocatalytic activity of Fe(II) ammine complexes supported by phosphine ligands started with synthesizing Fe phosphine complexes with labile ligands, such as MeCN, which are amenable to displacement with NH_3. Abstraction of the bridged chlorides of the previously reported Fe dimer **1**[55] by silver triflate in acetonitrile at room temperature yields tris(acetonitrile) complex **2** in which all chlorides are substituted by acetonitrile.

Scheme 3.3 Synthesis of Fe(II) ammine complex **3**

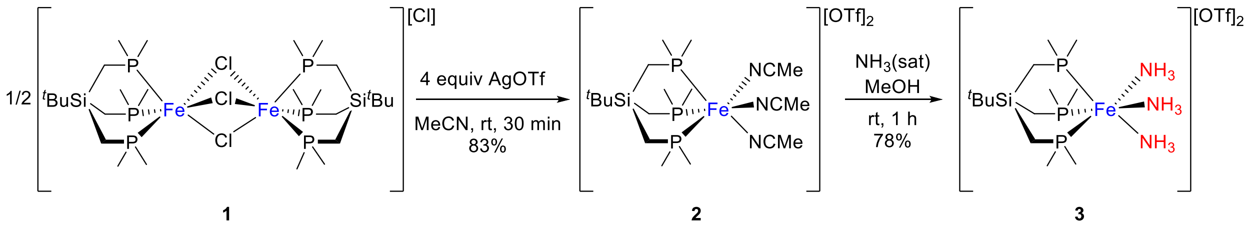

Substitution of the MeCN ligands of **2** with NH_3 in methanol saturated with ammonia in the course of 1 h and precipitation by Et_2O affords **3** in 78% yield. MeCN rapidly displaces the NH_3 ligands at ambient temperature in the absence of excess NH_3 therefore MeCN-d_6 was avoided as the NMR solvent. $^{31}P\{^1H\}$ NMR of **3** in $MeNO_2$-d_3 shows one singlet at 38.07 ppm, which compared to **2** shifted 4.17 ppm downfield. The $^{31}P\{^1H\}$ NMR spectrum of complex **3** in DMSO-d_6 shows a singlet resonance at 41.79 ppm, and the ^1H NMR spectrum has a resonance at 2.02 ppm for the NH_3 protons, which suggests that the NH_3 ligands are still bound to Fe. Even though the NH_3 ligands in **3** are displaced yielding tri-solvate compound **2** when it is dissolved in MeCN, the fact that **3** is stable in DMSO-d_6 suggests that the kinetics and thermodynamics of NH_3 binding in this system are nuanced. These features are discussed in more depth when we describe efforts to prepare dicationic mono(ammine) species ${}^{t}\mathrm{SiP_3Fe(L_2)(NH_3)}$ where **L_2** is a neutral bidentate chelating ligand. Even though the lability of N–donor ligands made it impossible to synthesize some target molecules, that lability is advantageous for an ammonia oxidation sequence.

Single crystals of **2** and **3** suitable for crystallography were obtained from slow diffusion of Et_2O into the acetonitrile and methanol, respectively, at ambient temperature (Figure 3.1).

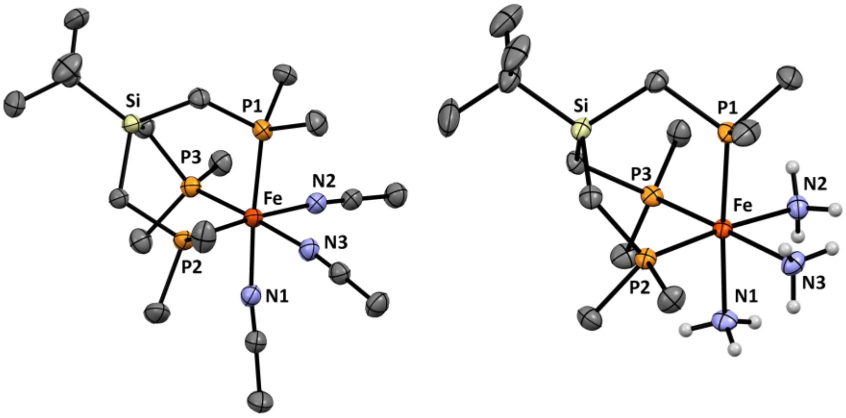

Figure 3.1 Molecular structures of complex **2** (left) and **3** (right) with thermal ellipsoids at the 50% probability level (Hydrogen atoms of carbons, triflate counter ions, and solvent molecules were omitted for clarity). Selected bond lengths (Å) and angles (deg) for complex 2 (left): Fe–P1 2.2298(10), Fe–P2 2.2374(10), Fe–P3 2.2468(10), Fe–N1 1.972(3), Fe–N2 1.976(3), Fe–N3 1.963(3); P1–Fe–P2 91.50(3), P1–Fe–P3 92.03(3), P2–Fe–P3 92.46(4), N1–Fe–P1 176.11(9), N1–Fe–P2 92.22(8), N1–Fe–P3 88.93(8). Complex 3 (right): Fe–P1 2.228(3), Fe–P2 2.225(3), Fe–P3 2.228(3), Fe–N1 2.09(1), Fe–N2 2.10(1), Fe–N3 2.07(1); P1–Fe–P2 91.6(1), P1–Fe–P3 91.9(1), P2–Fe–P3 91.6(1), N1–Fe–P1 175.2(3), N1–Fe–P2 91.2(3), N1–Fe–P3 91.9(3)

The electrochemical behavior of 0.5 mM of **2** was evaluated by cyclic voltammetry (CV) in THF containing 0.1 M of $TBAPF_6$ as the supporting electrolyte and GC as the working electrode (Figure 3.2). The CV of **2**, exhibits one quasi-reversible wave with anodic and cathodic peaks at 1.15 and 1.04 V, respectively, and a peak-to-peak separation of 0.11 V at $E_{1/2} = 1.09$ V vs Fc^{*}/Fc^{*+}. The theoretical $E_{1/2}$ value (1.44 V vs Fc^{*}/Fc^{*+}) was calculated by an SMD-THF solvent model relative to the following reaction **2** + $Fc^{*+} \rightarrow$ **2**$^{+}$ + Fc^{*} ($\Delta G^{\circ}_{298K} = 33.4143$ kcal/mol).

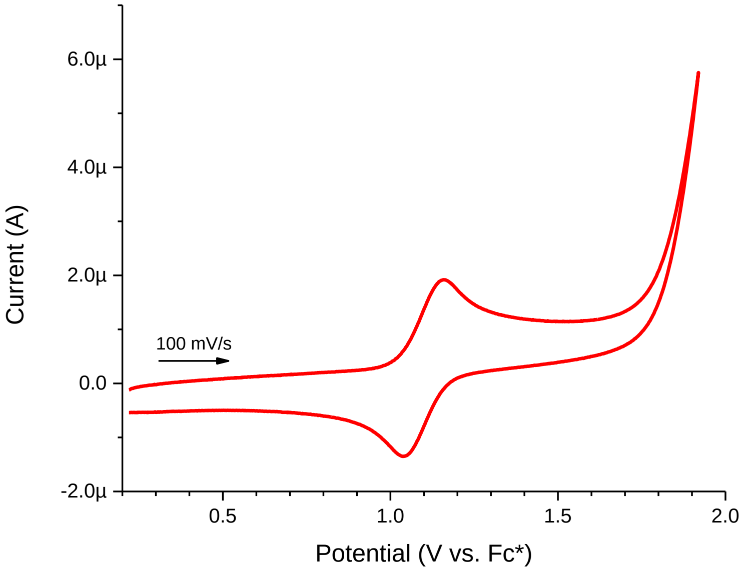

Figure 3.2 CV of 0.5 mM **2** in THF containing 0.1 M $TBAPF_6$ as supporting electrolyte. WE: GC, CE: Pt disk, scan rate: 100 mV/s

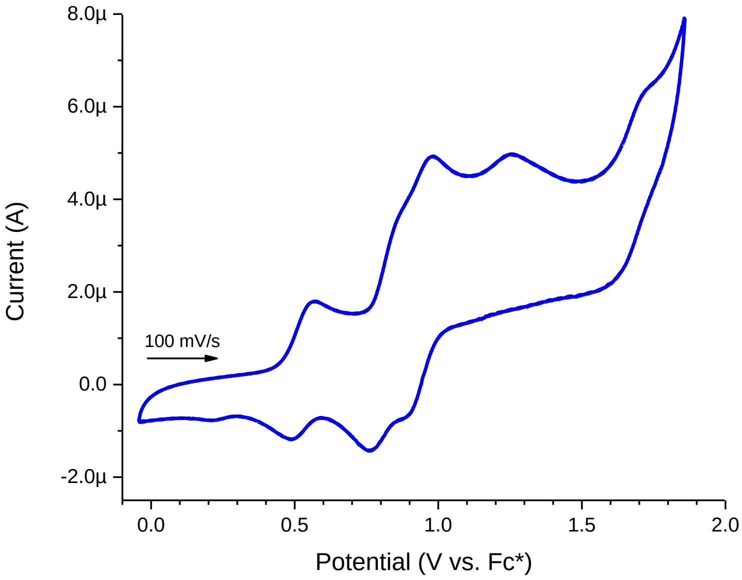

Figure 3.3 CV of 0.5 mM **3** in THF containing 0.1 M $TBAPF_6$ as supporting electrolyte. WE: GC, CE: Pt disk, scan rate: 100 mV/s

In contrast, the CV of **3** under the same conditions shows five anodic redox waves between 0.5 and 1.8 V and four peaks in the cathodic return (Figure 3.3). The first anodic wave appearing at 0.55 V vs Fc*/Fc*$^+$ can be compared to the theoretical $E_{1/2}$ = 1.17 V for oxidation of **3** obtained by electron transfer free energy from complex **3** to Fc*$^+$ (**3** + Fc*$^+$ → **3**$^+$ + Fc*, ΔG°_{298K} = 27.008 kcal/mol).

By changing the supporting electrolyte to 2 M NH_4OTf, the CV of **3** shows one anodic and one cathodic peak at 0.63 V and 0.50 V respectively with $E_{1/2}$ of 0.56 V vs Fc*/Fc*$^+$. To examine the effect of $[TBA]^+$ cation and $[PF_6]^-$ anion on the CV of **3**, 0.5 M of $TBAPF_6$ and 0.5 M of TBAOTf was added to the 1 mM solution of **3** in THF containing 2 M of NH_4OTf.

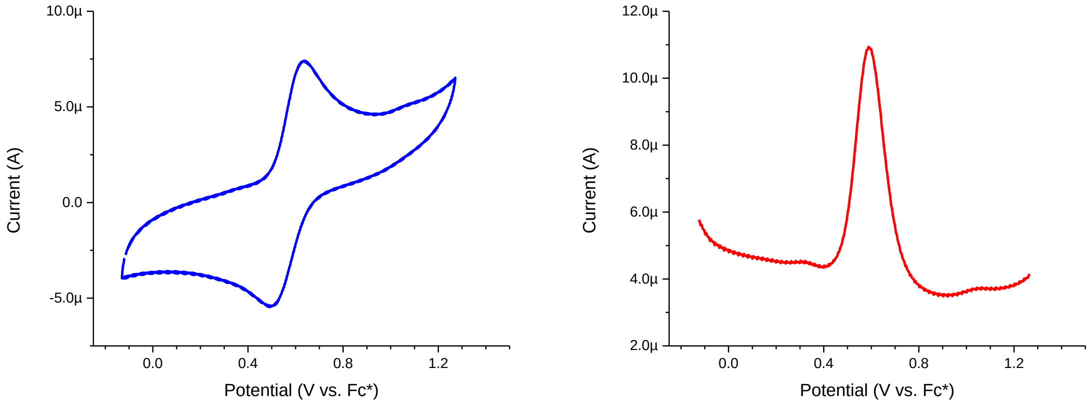

Figure 3.4 Left: CV of 1 mM **3** in THF containing 2 M NH_4OTf as supporting electrolyte. WE: GC, CE: Pt disk, scan rate: 100 mV/s. Right: SQW taken after CV

As shown in Figure 3.5, by adding $TBAPF_6$ and TBAOTf to 1 mM solutions of **3** in THF with 2 M NH_4OTf as the electrolyte, the shape of CV changes significantly. Both TBA salts show the same behavior. This suggests reaction of **3** with TBA upon oxidation on the surface of the electrode.

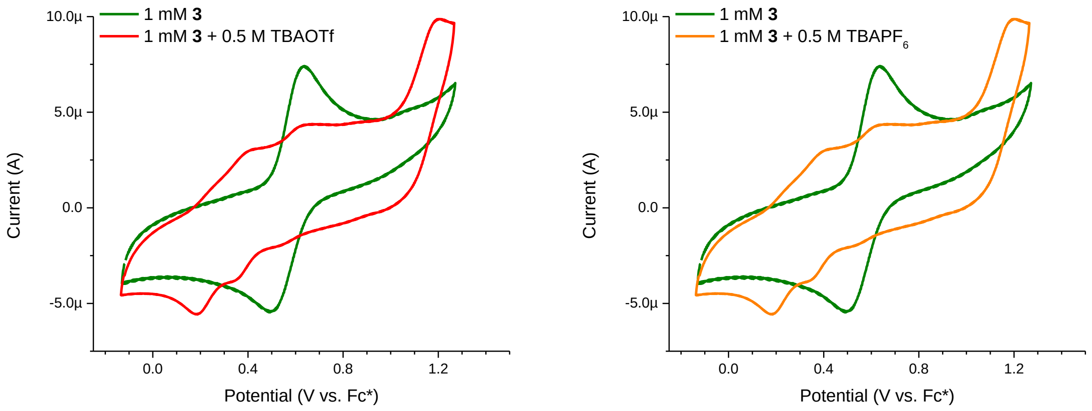

Figure 3.5 Left: CV of 1 mM **3** in THF containing 2 M NH_4OTf as supporting electrolyte (green); same CV after adding 0.5 M of TBAOTF (red). Right: CV of 1 mM **3** in THF containing 2 M NH_4OTf as supporting electrolyte (green); same CV after adding 0.5 M of $TBAPF_6$ (orange). WE: GC, CE: Pt disk, scan rate: 100 mV/s

In addition to the electrochemical oxidation of **3** on the surface of the electrode, an attempt was made to chemically oxidize it by tris(4-bromophenyl)amine radical cation (Scheme 3.4). In the glovebox, 1 equiv (349 mg, 0.163 mmol) of $BAr^F{}_{24}$ salt of **3** was dissolved in 15 mL THF. The oxidant was dissolved in THF (0.183 mmol, 115 mg) and added dropwise to the solution of **3**. Color changes from orange to purple. Pentane was added to further precipitation until the purple solids crashed out, and the THF became colorless. Solids were collected on a frit and washed with pentane (yield: 97%).

Scheme 3.4 Chemical oxidation of **3** by tris(4-bromophenyl)amine radical

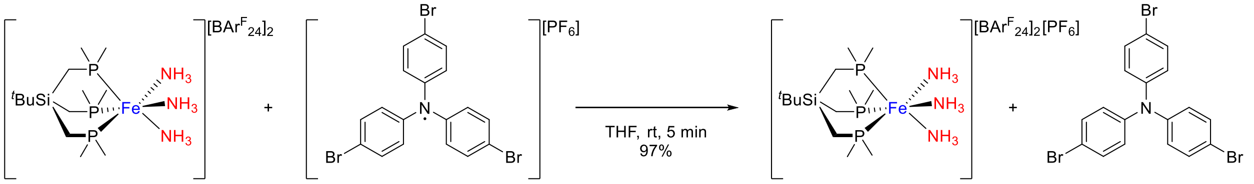

The EPR spectrum of one electron oxidized **3** in THF is shown in Figure 3.6 at two different temperatures. The spectrum features two resolved peaks suggestive of low and high spin Fe(III) complexes with axial symmetry.

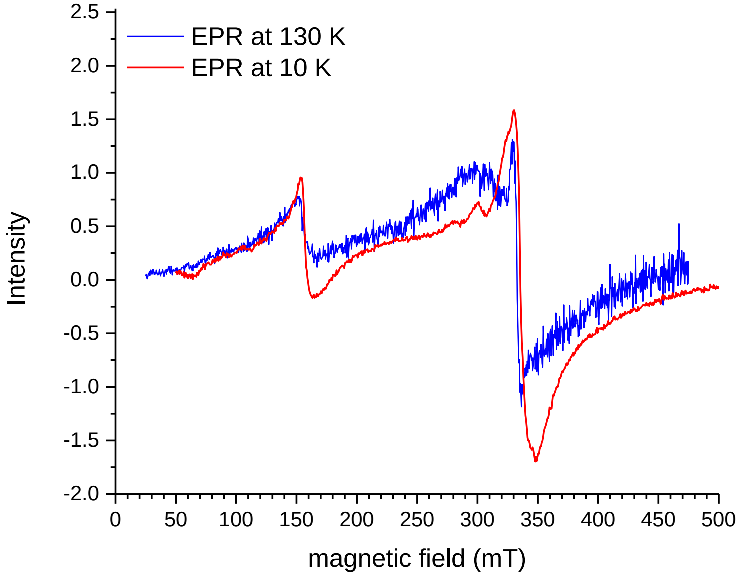

Figure 3.6 EPR spectrum of one electron oxidized **3** in THF at 130 and 10 K

Given that the pK_a values of NH_3 protons typically decrease upon coordination to metal cations,[56] we attempted to deprotonate **3** by a hindered base. To achieve this, complex **3** was treated with 1.6 equiv of $LiN(SiMe_3)_2$, which resulted in a new species being formed (Scheme 3.5). Single crystals of the product were grown by slow diffusion of diethyl ether into THF solution. The X-ray structure reveals a diferrrous cation with the formula $[(^tSiP_3Fe)_2(\mu\text{-}NH_2)_3][OTf]$ (**4**) (Figure 3.7). This is the first structurally characterized dinuclear iron complex with three NH_2 ligands in the bridging positions. Transition metal dinuclear complexes bridged by three μ-NH_2 ligands have been reported for Cr,[57] Co,[58,59] Mo,[60] and Pt.[61] Solid state structures have been determined for all but the Mo example.

Scheme 3.5 Deprotonation of complex **3** with $LiN(SiMe_3)_2$

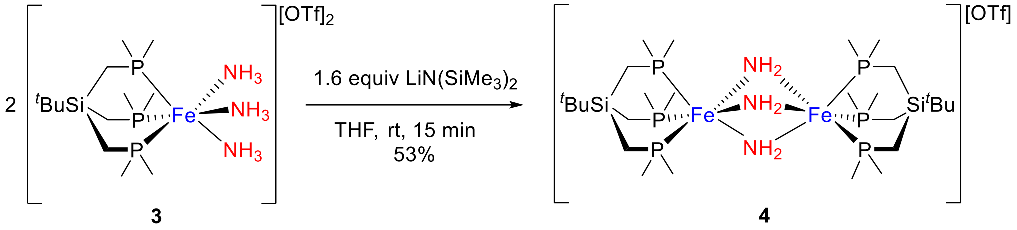

3

4

The average Fe–NH_2 bond length of 2.026(8) Å in complex **4** is longer than the average Co–N bond length of 1.939(5) Å for the bridging NH_2 ligands in $[\{(NH_3)_3Co\}_2(\mu\text{-}NH_2)_3][ClO_4]_3$ and identical to the Cr–NH_2 distance (2.027(2) Å) in $[\{(NH_3)_3Cr\}_2(\mu\text{-}NH_2)_3][I_3]$. The Fe–Fe distance of 2.840(1) Å is longer than the Co–Co (2.60 Å) and Cr–Cr (2.649(1) Å) distances in the aforementioned complexes.[57–59] The shorter distance for the Co is expected since both have d^6 low-spin configurations, and Co(III) has a higher effective nuclear charge. Cr(II) d^4 complexes typically adopt high-spin configurations, and the Cr–Cr distance is comparable to those in dinuclear Cr(III)Cr(III) compounds where Cr–Cr bonding has been invoked.[62,63] The most closely related Fe complex is the low-spin diiron(II) complex $\{[PhB(CH_2P(CH_2Cy)_2)_3]Fe\}_2(\mu\text{–}\eta^1\text{:}\eta^1\text{–}N_2H_2)(\mu\text{–}NH_2)_2$ synthesized by Peters and co-workers.[64] The average Fe–NH_2 (2.041 Å) and Fe–Fe (3.087 Å) distances for this complex are longer than those in **4**.

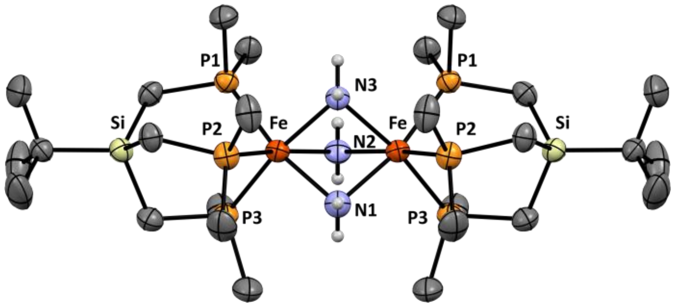

Figure 3.7 Molecular structures of complex **4** with thermal ellipsoids at the 50% probability level (Hydrogen atoms of carbons, triflate counter ion, and solvent molecules were omitted for clarity). Selected bond lengths (Å) and angles (deg) for complex **4**: Fe–P1 2.1900(15), Fe–P2 2.1895(16), Fe–P3 2.1938(16), Fe–N1 2.029(5), Fe–N2 2.029(5), Fe–N3 2.022(4); P1–Fe–P2 92.37(6), P1–Fe–P3 92.54(6), P2–Fe–P3 92.37(6), N1–Fe–P1 168.49(17), N1–Fe–P2 93.2(2), N1–Fe–P3 97.3(2), Fe–N2–Fe 45.60(14), Fe–N1–Fe 45.59(14), Fe–N3–Fe 45.41(11)

The $^{31}P\{^1H\}$ NMR spectrum of **4** in DMSO-d_6 shows one singlet peak at 43.75 ppm, which is shifted 1.96 ppm down-field compared to the ^{t}SiP$_3$ resonance in compound **3**. In addition to the characteristic resonances of ^{t}SiP$_3$ ligand, the protons of the bridging NH$_2$ ligands appear at –2.79 ppm in the ^{1}H NMR spectrum of the compound, which is 4.82 ppm up-field of the resonance for the NH$_3$ ligands in compound **3**.

Upon chemical oxidation of complex **4** with 2 equiv of AgOTf in CH$_2$Cl$_2$, a solid precipitated over the course of the reaction. Upon recrystallization, a pure compound formulated as [(^{t}SiP$_3$)$_2$Fe][OTf]$_2$ (**5**) was obtained in 35% yield (Scheme 3.6). Characterization was based on the observation of single resonances for CH$_2$ and PMe$_2$ ligand protons in the ^{1}H NMR spectrum, and one singlet in the $^{31}P\{^1H\}$ spectrum. The chemical shifts of these resonances are very similar to [L$_2$Fe][BF$_4$]$_2$, L = bis(1,1,1–tris(dimethylphosphinomethyl)ethane, which is closely related to **5**, where the CH$_2$PMe$_2$ arms of the ^{t}SiP$_3$ ligand are connected to CMe instead of ^{t}BuSi.[65] The Fe required for mass balance in the oxidation of **4** in Scheme 3.6 is presently unaccounted for.

Scheme 3.6 Ligand redistribution promoted by chemical oxidation of **4**

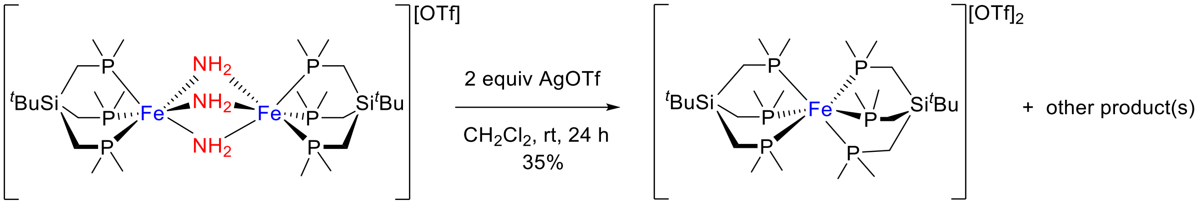

4 **5**

The four–coordinate Fe(II) imido complex ^{t}SiP$_3$Fe=NAryl (Aryl = 2,6–(^{i}Pr$_2$)$_2$C$_6$H$_3$), has been oxidized to a stable Fe(III) cation with AgSbF$_6$ by Odom and co-workers.[66] Thus, the ligand redistribution via comproportionation triggered by the oxidation of compound **4** was unexpected. We turned to theory to understand why attempted 2 e$^-$ oxidation of **4** triggered ligand redistribution.

Density Functional Theory (DFT) calculations of **4** gave Fe–Fe and average Fe–NH$_2$ bond lengths of 2.859 and 2.047 Å that are close to the respective experimental values of 2.840(1) and 2.026(8) Å. Natural Bond Orbital (NBO) theory predicts that the HOMO is comprised of 67.3% of Fe 3d$_{x2-y2}$ atomic orbitals (AOs) and 25.7% of 2p$_x$ N AOs of the μ-NH$_2$ ligands, which have 46% non–bonding and 54% anti–bonding character.[39,67] Shortening of the Fe–NH$_2$ bonds would be expected after a 2 e$^-$ oxidation of **4** to **4**$^{2+}$ since the anti–bonding character in HOMO of **4** would be lost. This is consistent with the theory where the Fe–NH$_2$ bonds in **4**$^{2+}$ contract ~0.10 Å relative to **4**.

The theoretical Fe–Fe distance decreases from 2.85 Å in **4** to 2.40 Å in **4**$^{2+}$. NBO theory indicates an Fe–Fe bond in **4**$^{2+}$—an expected consequence of 2 e$^-$ oxidation—comprised of Fe 3d$_{x2-y2}$ (72%) and 3d$_{z2}$ (24%) AOs, and a quantum theory of atoms in molecules (QTAIM) analysis reveals a bond critical point between the Fe centers,[68,69] with an electron density of ρ= 34 kcal/mol.

Along with a decrease in Fe–N and Fe–Fe distances, DFT predicts the lengthening of Fe–P bonds by ~0.13 Å upon 2 e$^-$ oxidation, which is consistent with $n_N \longrightarrow \sigma_{FeP}*$ 2nd–order interactions from NBO theory analysis. Populating an orbital with P–C anti-bonding character is consistent with Fe–P lengthening in Fe–NH_2 bonds in **4**$^{2+}$. Metal π-back bonding to P–C σ* orbitals also contributes to the stabilization of M–P bonds, which would diminish upon oxidation of Fe(II) to Fe(III). Indeed, NBO theory estimates that 18 kcal/mol stabilization in compound **4** arises from second-order interactions between Fe(II) lone pairs and anti-bonding P–C NBOs. In the 2 e$^-$ oxidized compound **4**$^{2+}$, no interactions of this type exceeded the 0.05 kcal/mol threshold. Hence, loss of Fe–P π-back bonding accompanies Fe–P elongation when **4** is oxidized.

Also, the Fe–Fe distance decreases from 2.85 Å in **4** to 2.40 Å in **4**$^{2+}$ due to the shortening of the Fe–NH_2 bond, which leads to the formation of the Fe–Fe bond. The Fe–Fe bond in **4**$^{2+}$ constitutes 83.35% of HOMO–6 with 91.6% bonding character (Figure 3.8). These calculations may explain the decomposition of **4** upon oxidation.

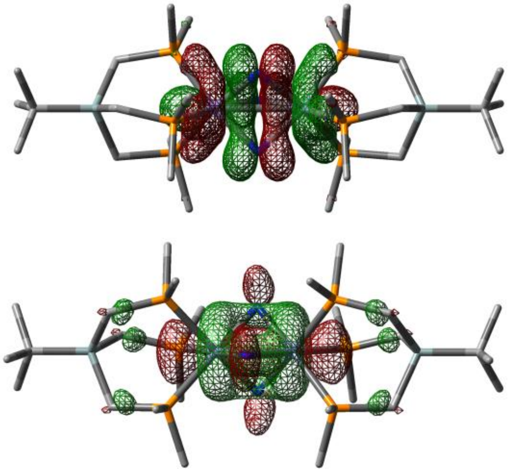

Figure 3.8 Top: visualized HOMO of complex **4**. Bottom: visualized HOMO–6 of 2 e$^-$ oxidized complex **4**

Wolczanski has used CO, and other ligands, as reporters for charge distribution between ligands and metals in transition metal complexes. We applied his Charge Distribution Via Reporters (CDVR) method for insight into the phosphine redistribution reaction that occurs when complex **4** reacts with AgOTf.[70]

The CDVR method relies on Equation 1, where C_{ML} is the total charge on the metal complex, C_{M} is the charge on the metal center, $x_{\mathrm{L}(i)}$ is the number of ligands L(i) bound to M, and $c_{\mathrm{L(i)}}$ is the charge on ligand L(i).

Equation 1 $$C_{\mathrm{ML}} = C_{\mathrm{M}} + x_{\mathrm{L1}}c_{\mathrm{L1}} + x_{\mathrm{L2}}c_{\mathrm{L2}} + \ldots + x_{\mathrm{L(i)}}c_{\mathrm{L(i)}}$$

Since the ^{59}Fe Mössbauer isomer shifts for $[Fe(CO)_6]^{2+}$, $Fe(CO)_5$, and $[Fe(CO)_4)]^{2-}$ span a narrow range of 0.17 mm/s, the charge on Fe in these complexes is assumed to be identical and C_{Fe} is set to 2.0. With this assumption, the c_{CO} values calculated from Equation 1 for $[Fe(CO)_6]^{2+}$, $Fe(CO)_5$, and $[Fe(CO)_4)]^{2-}$ are 0, –0.4, and –1, respectively. Plots of c_{CO} vs. ν_{CO} of these Fe complexes, and analogous plots for Ru and Os congeners, are linear, which makes it straightforward to calculate c_{CO} from ν_{CO} values according to Equation 2.

Equation 2 $$c_{\mathrm{CO}} = \{\nu_{\mathrm{CO}} - 2207\}\ \mathrm{cm}^{-1}/475\ \mathrm{cm}^{-1}$$

With a value for $c_{\mu\mathrm{NH2}}$, CDVR can be applied to calculate charges on P of the ^{t}SiP$_3$ ligand. The complex $Fe_2(CO)_6(\mu\text{-N}^{i}PrC(H)(CO_2Me)C(H)(CO_2Me)\text{-}\mu\text{-N}^{i}Pr)$ has μ–NR$_2$ and CO as the only ligands. From the average of the reported ν_{CO} values (ν_{CO} = 2006 cm^{-1}) for this complex and Equation 1, $c_{\mathrm{CO}} = -0.42$. Setting $c_{\mathrm{Fe}} = 2.0$, and making the recommended correction for an Fe–Fe bond, the application of Equation 1 gives $c_{\mu\mathrm{NR2}} = -0.43$ for the bridging amides.

Assuming that $c_{\mu NR2} \sim c_{\mu NH2}$ and $c_{Fe} = 2.0$, the application of Equation 1 gives $c_P = -0.28$ for the coordinated phosphorus atoms in complex **4**. For $[({}^tSiP_3Fe)_2(\mu\text{-}NH_2)_3]^{2+}$ (**4**$^+$) and $[({}^tSiP_3Fe)_2(\mu\text{-}NH_2)_3]^{3+}$ (**4**$^{2+}$), the calculated c_P values for **4**$^+$ and **4**$^{2+}$ are –0.12 and 0.05, respectively. Fe–P π-back bonding diminishes as c_P increases, which synergistically weakens Fe–P σ-bonding. With simple arithmetic and qualitative molecular orbital arguments, CDVR captures the essence of more rigorous quantum chemical analyses that rationalize the ligand redistribution triggered by oxidizing complex **4**.

Given that the pK_a values of NH_3 protons typically decrease upon coordination to metal cations,[56] we hypothesized that oxidation of compound **3** from Fe(II) to Fe(III) can trigger deprotonation, particularly if dissociation of bound NH_3 generates a proton acceptor. We examined this hypothesis by theoretically calculating the pK_a value of the bound NH_3 to Fe(III) center (pK_a = 8.36) by a THF protonated (THF—H$^+$—THF) model.[56] The ΔG_{rxn} for deprotonation of NH_3 on Fe(III) by THF (11.41 kcal/mol) is endergonic. Since weak bases (e.g. H_2O) catalyze the rapid exchange of coordinated NH_3 protons, the barriers for endoergic reactions are close to the thermodynamic limit. Thus, the intermediate $[({}^tSiP_3)Fe(NH_3)_2(NH_2)]^{2+}$ should be accessible in THF.

Based on NBO analysis, singly occupied molecular orbital (SOMO) in deprotonated form of **3a** (**3b**) resides ~ 40% on NH_2 (94% $2p_z$ of N) and 23% on Fe (67% $3d_{yz}$, 22% $3d_{xy}$). This arises the possibility of intermolecular N–N coupling between two **3b** intermediates to form a bridged N_2H_4 dinuclear complex which its further oxidation yields N_2 and H_2 (Scheme 3.7).

Scheme 3.7 Proposed mechanism of catalytic NH_3 oxidation by complex **3**

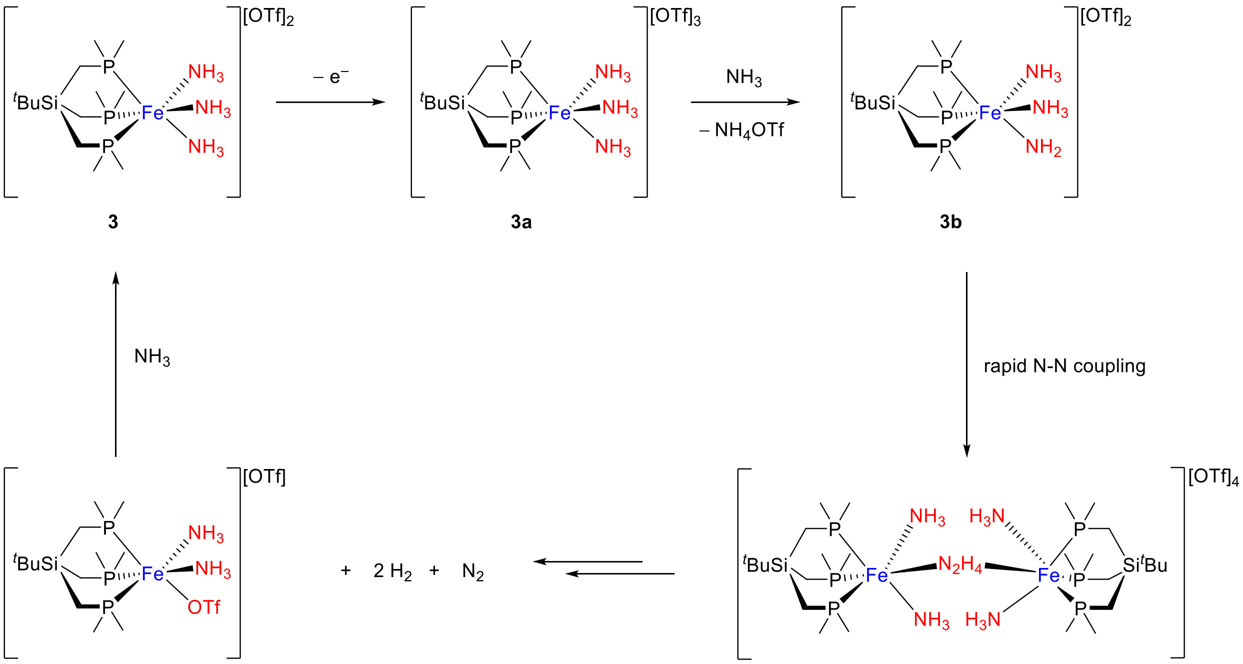

The electrocatalytic behavior of **3** was examined in THF in the presence of NH_3 containing 1 and 2 M concentrations of NH_4OTf on the surface of BDD and GC electrodes. Figure 3.9 shows the catalytic behavior of **3** in THF with 2 M of NH_4OTf as the supporting electrolyte, 3.24 M NH_4, and GC as the working electrode in the presence of 1 mM Fc* as the internal standard. For testing the stability of the catalyst on decomposition and passivation of the surface of the GC electrode, 51 consecutive scans were cycled to test any current drop during the catalysis (Figure 3.10). As shown in Figure 3.10 , no current drop or electrode poisoning was observed during 51 scans. It is worth noting that in the presence of $TBAPF_6$ and/or TBAOTf as supporting electrolytes, the catalytic current drops significantly due to the reaction of oxidized forms of **3** with TBA followed by electrode passivation.

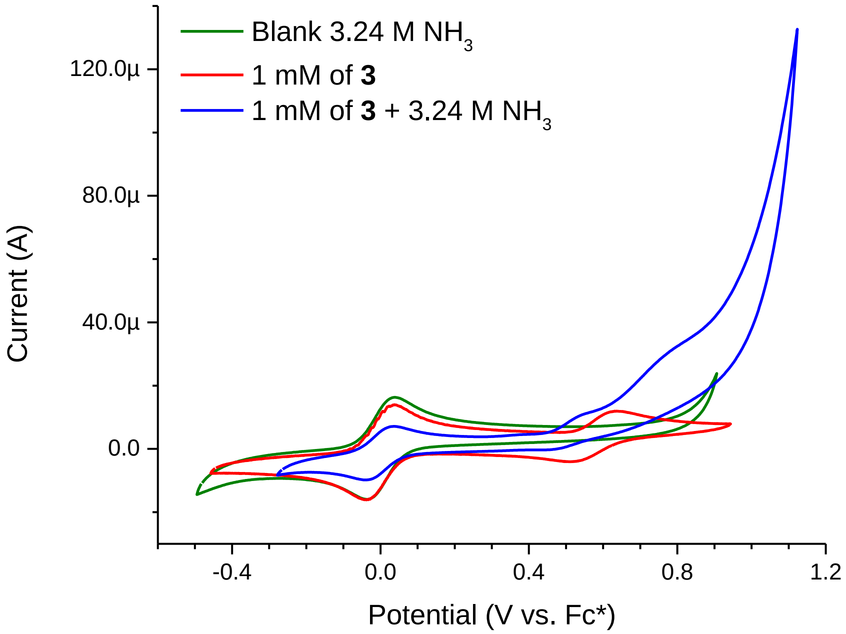

Figure 3.9 Green: CV of 1 mM of Fc* in THF with 3.24 M NH_3. Red: CV of 1 mM of **3** in THF in the presence of 1 mM Fc*. Blue: CV of 1 mM of **3** in THF in the presence of 1 mM Fc* with 3.24 M NH_4. Supporting electrolyte: 2 M NH_4OTf, WE: GC, CE: Pt disk, scan rate: 100 mV/s

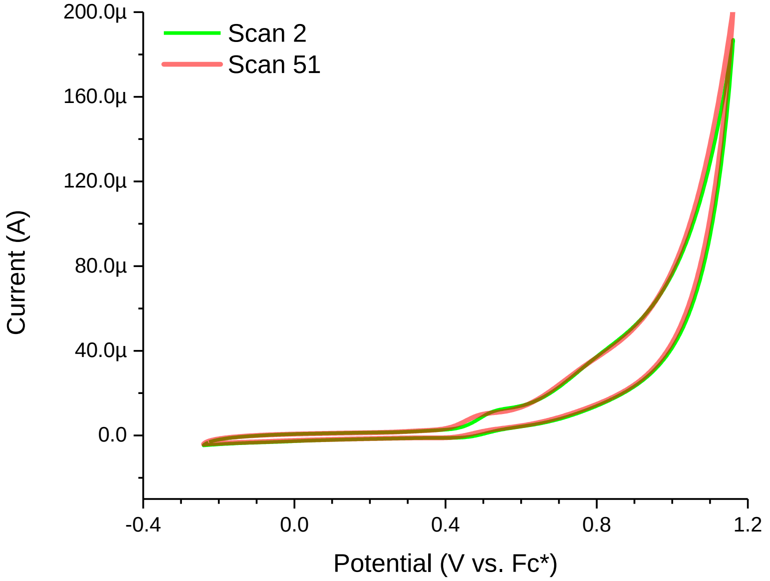

Figure 3.10 Cycling 1 mM of **3** in THF containing 2 M NH_4OTf, and 3.24 M NH_3 for 51 scans (CV was plotted starting form 2nd scan) with overlay of 2nd and 51st scans. WE: GC, CE: Pt disk, scan rate: 100 mV/s

In addition to the GC electrode, the electrocatalytic behavior of complex **3** was investigated with the BDD electrode. NH_3 gets oxidized on the surface of the BDD electrode in ~ 360 mV higher potential than GC (Figure 3.11); therefore, BDD is suitable for studying the electrocatalytic behavior of complexes with relatively high oxidation potential.

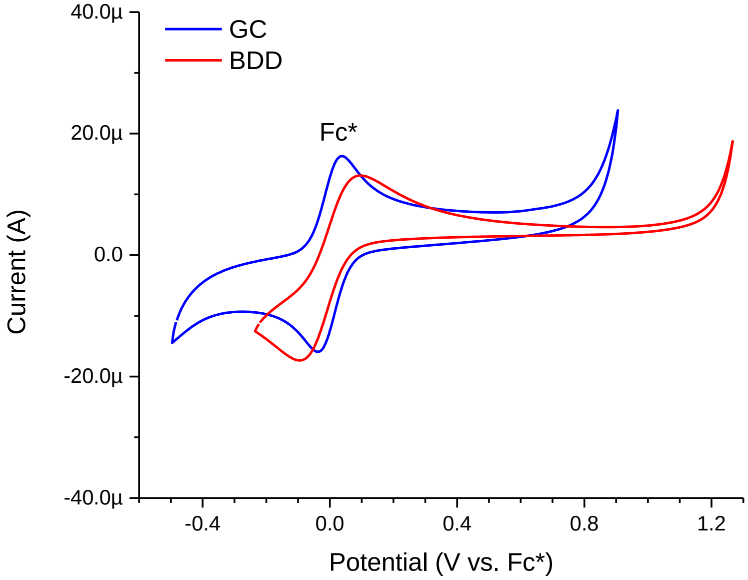

Figure 3.11 Comparison of the potential of NH_3 oxidation in THF in the presence of 3.24 M NH_3 and 1 mM Fc* on the surface of GC (blue) and BDD (red) electrodes. Note that the current obtained by the BDD electrode is normalized for overlay by multiplying by a factor of 6.5. Supporting electrolyte: 2 M NH_4OTf, WE: GC (blue) and BDD (red), CE: Pt disk, scan rate: 100 mV/s

Figure 3.12 shows the CV of complex **3** with and without the presence of NH_3 in the presence of 1 mM of Fc* as the internal standard. Also, 50 consecutive scans were cycled in the presence of NH_3 to evaluate the stability of the catalyst (Figure 3.13). No current passivation was observed in the course of these multiple scans.

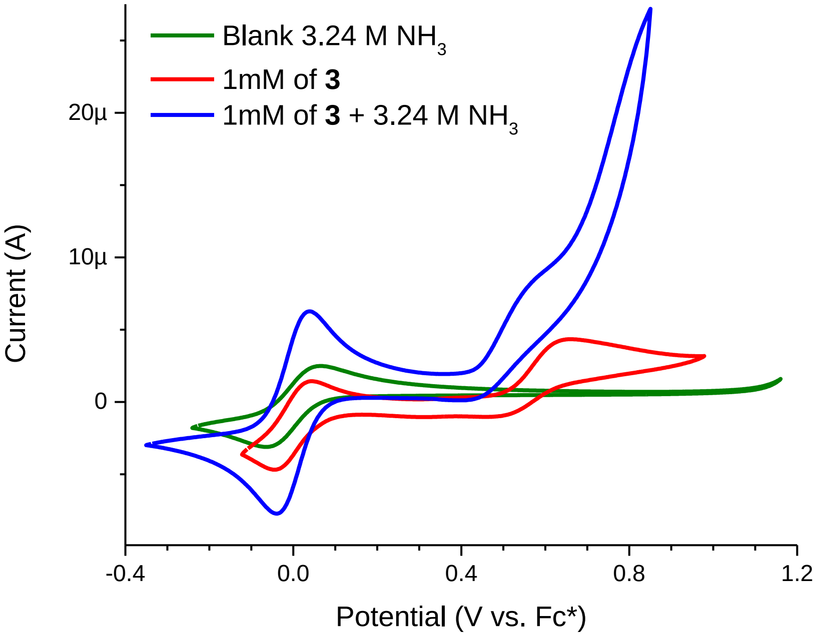

Figure 3.12 Green: CV of 1 mM of Fc* in THF with 3.24 M NH_3. Red: CV of 1 mM of **3** in THF in the presence of 1 mM Fc*. Blue: CV of 1 mM of **3** in THF in the presence of 1 mM Fc* with 3.24 M NH_4. Supporting electrolyte: 2 M NH_4OTf, WE: BDD, CE: Pt disk, scan rate: 100 mV/s

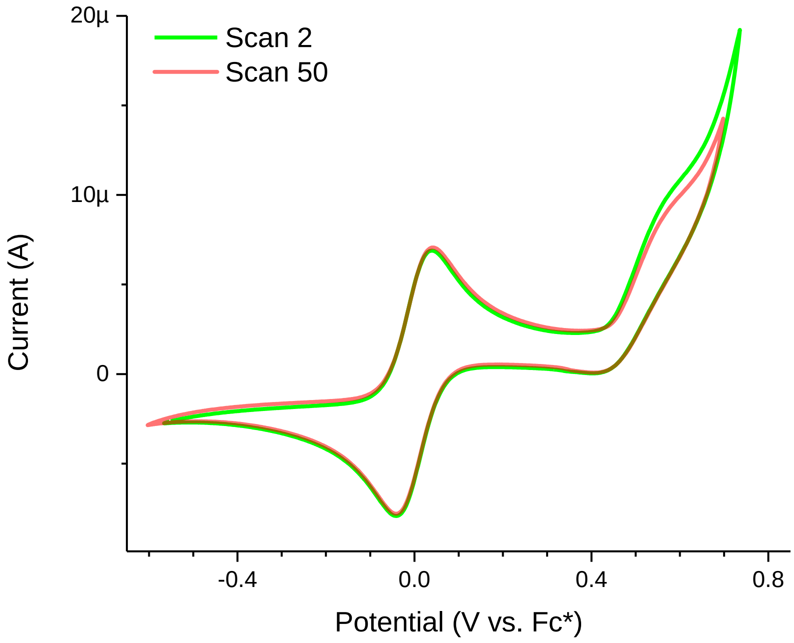

Figure 3.13 Cycling 1 mM of **3** in THF containing 2 M NH_4OTf, and 3.24 M NH_3 for 50 scans (CV was plotted starting from the 2nd scan) with an overlay of 2nd and 50th scans in the presence of 1 mM of Fc* as internal standard. WE: BDD, CE: Pt disk, scan rate: 100 mV/s

For identifying the amount of produced N_2(g) on the anode in the presence of the catalyst, controlled potential electrolysis (CPE), i.e., bulk electrolysis (BE) was conducted by applying a constant potential vs. Fc*/Fc*$^+$ reference electrode. For better mass transport during the BE, the solution was vigorously stirred. BE was performed in THF with 1 M of NH_4OTf as supporting electrolyte, 2.8 M NH_3, and 1 mM of complex **3**. A GC plate was used as the working electrode, and a Pt mesh was used as the counter electrode. A controlled BE experiment was carried out for 1 h without the presence of **3** at an applied potential of 0.8 V (vs. Fc*) (Figure 3.14).

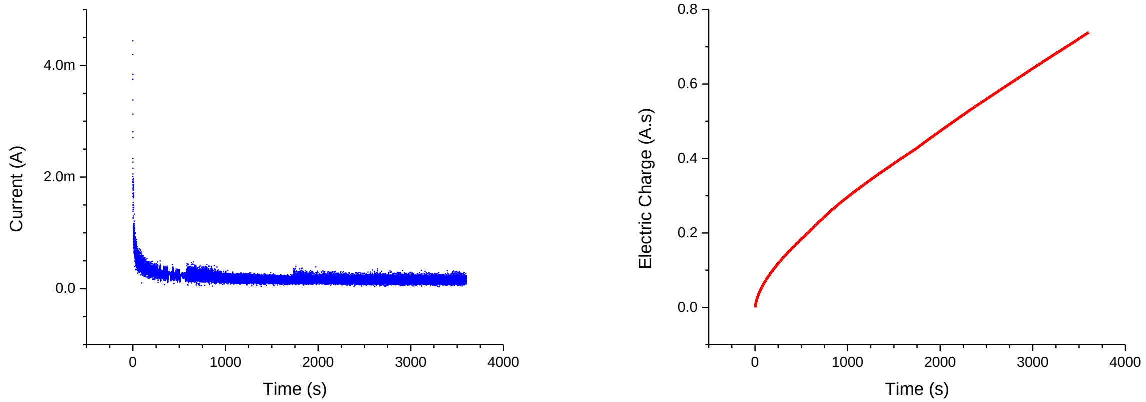

Figure 3.14 Left: control BE of THF solution with 2.8 M NH_3 in the absence of catalyst for 1 h by applying 0.8 V (vs. Fc*). Right: the amount of the charge passed (C) during 1 h of BE. Supporting electrolyte: 1 M NH_4OTf, WE: GC plate, CE: Pt mesh

During 1 h, 0.738417 C charge was passed. Analysis of the headspace of BE cell, reveals the formation of ~ 1.3 µM N_2(g). After BE of blank, 1 mM of complex **3** was added quickly to the same cell by an airtight syringe, and 0.8 V (vs. Fc*) was applied to the WE again for 1 h. At this time 2.88861 C charge was passed in the course of 1 h (Figure 3.15). Analysis of the BE's cell headspace shows the formation of ~ 4.56 µM N_2(g) with faradic efficiency of 91.4%.

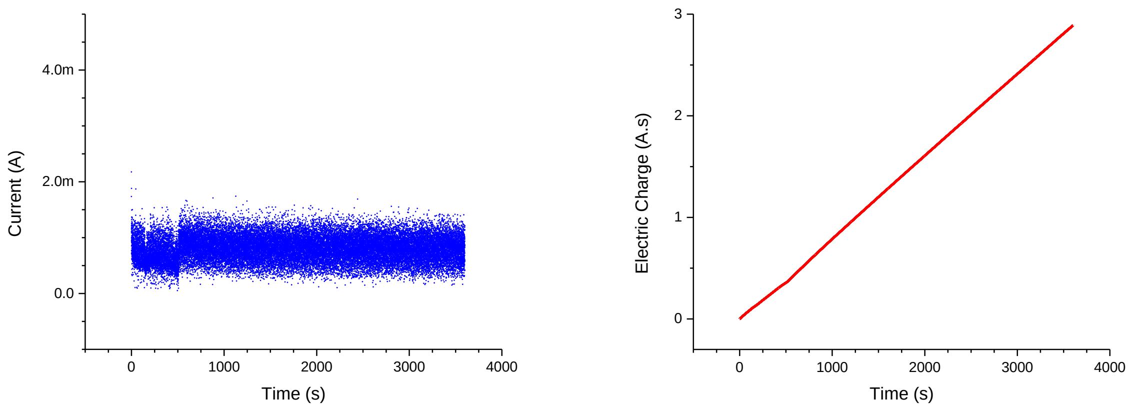

Figure 3.15 Left: BE of THF solution with 2.8 M NH_3 in the presence of 1 mM complex **3** for 1 h by applying 0.8 V (vs. Fc*). Right: the amount of the charge passed (C) during 1 h of BE. Supporting electrolyte: 1 M NH_4OTf, WE: GC plate, CE: Pt mesh

After the BE, the GC plate was rinsed with THF and then its surface was analyzed by XPS for detection of any iron species that can elevate the possibility of heterogeneous catalysis. Table 3.1 shows the results of the XPS surface analysis of the GC plate before and after the BE.

Table 3.1 XPS data of the surface of the GC plate before and after the BE

Element	Before BE	After BE
O 1s	7.68%	7.79%
C 1s	78.72%	66.28%
N 1s	12.78%	21.40%
F 1s	0.35%	1.57%
Fe 2p	–	0.26%
S 2p	–	0.96%
Si 2p	0.46%	0.59%
P 2p	–	1.16%

According to the XPS data, Fe was deposited on 0.26% of the surface of the electrode. To test the possible heterogeneous catalysis with this low percentage of Fe on the surface of the GC electrode, the following experiment was designed. The potential of 0.8 V (vs. Fc*) was applied to the GC electrode in THF containing 1 M NH_4OTf, 2.8 M NH_4 and 1 mM **3**. After 1 h, the GC electrode was taken out, and rinsed with THF, and inserted into a fresh solution of THF with 1 M NH_4OTf and 2.8 M NH_4. No catalytic current was observed after this rinse test.

Figure 3.16 shows the correlation between the measured current at potential 0.68 V (vs. Fc*) and the concentration of added complex **3** in THF solution with 2 M NH_4OTf, BDD as a working electrode, and 3.24 M of NH_3. As shown in Figure 3.16, the catalytic current has a linear dependence (1st order) on the concentration of complex **3**.

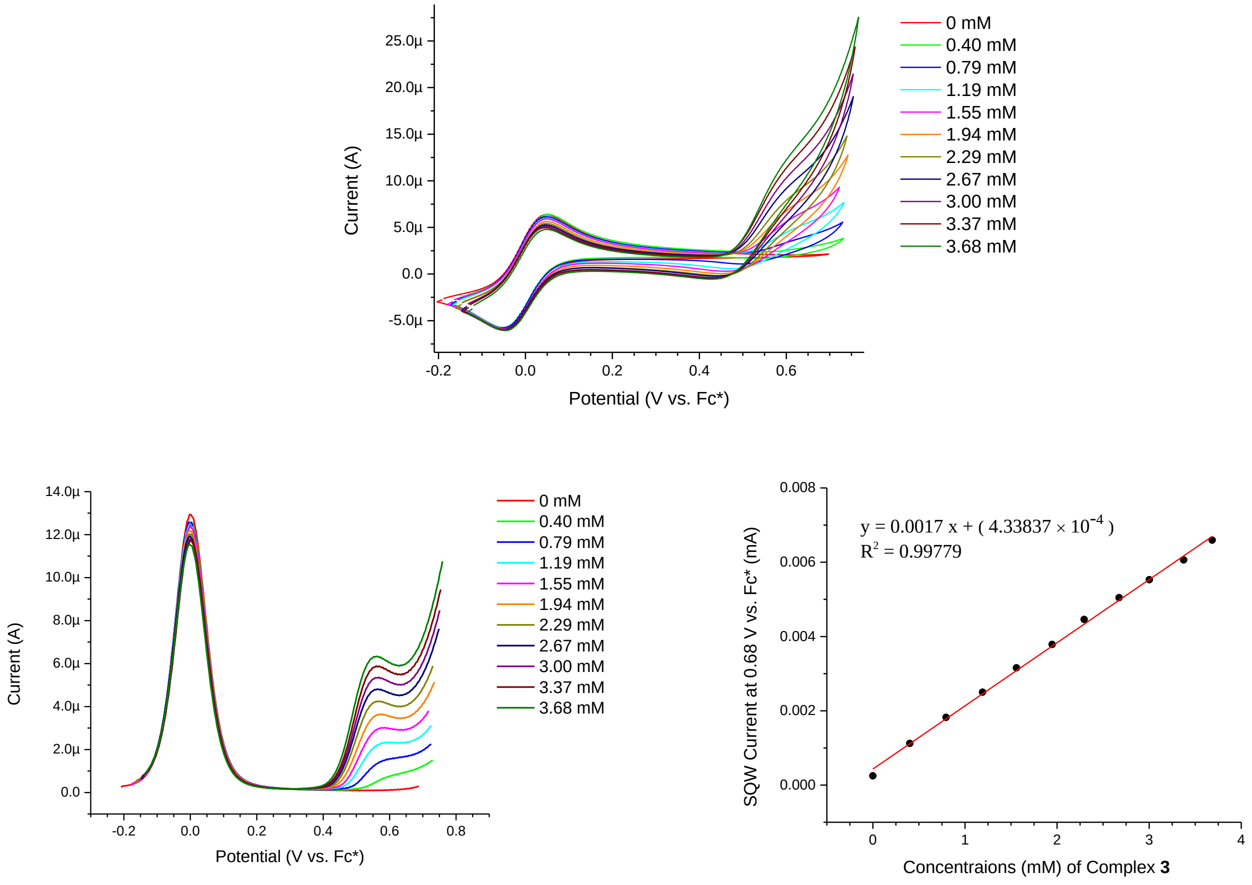

Figure 3.16 Top: CV of THF solution containing 2.4 M NH_3, and 1 mM Fc* as internal standard with different concentrations of complex **3**. Bottom left: corresponding SQW taken instantly after each CV. Bottom right: SQW current at 0.68 V (vs. Fc*) vs. different concentrations of complex **3**. WE: BDD, CE: Pt disk, scan rate: 100 mV/s

The dependence of catalytic current on NH_3 concentration, however, does not show any linear correlation. Upon the first addition of a low concentration of NH_3, the current slightly increases but by addition of other small consecutive NH_3 concentrations, no current increase is observed. Saturation of solution with NH_3 (2 – 3 M NH_3) results in a catalytic current.

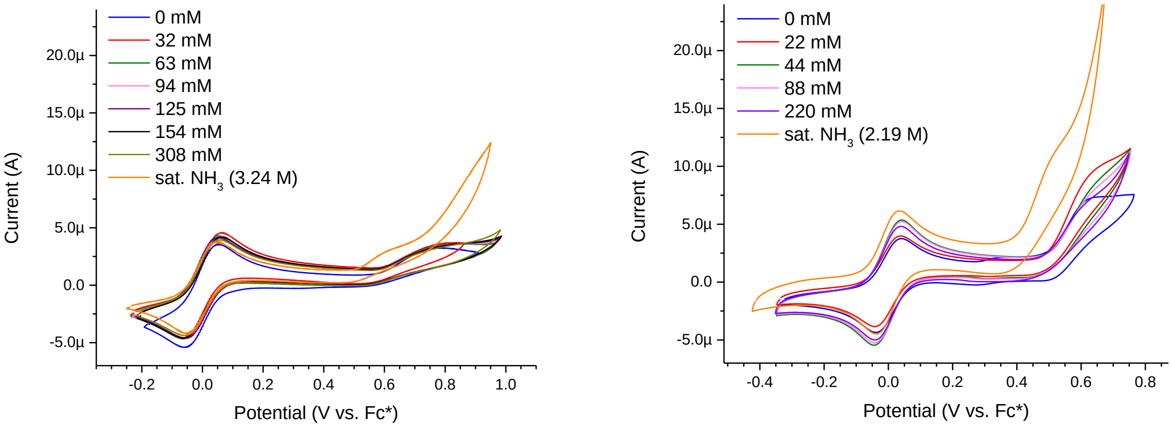

Figure 3.17 Left: CV of 1 mM complex **3** with varying concentrations of NH_3 in THF with 2 M of NH_4OTf, 1 mM Fc* as internal standard, and GC as working electrode. Right: CV of 1 mM complex **3** with varying concentrations of NH_3 in THF with 1 M of LiOTf, 1 mM Fc* as internal standard, and BDD as working electrode. In both cases, the scan rate is 100 mV/s and the Pt disk was used as CE.

Figure 3.17 shows the CVs of complex **3** with NH_4OTf (left) and LiOTf (right) as supporting electrolytes taken with GC and BDD as working electrodes respectively in the presence of different concentrations of NH_3.

Reactions of **2** and **3** with bidentate chelating ligands were next explored to prepare mono(ammine) complexes and investigate the effect of chelation on the oxidation potential of the iron ammine complexes. Our initial attempts to displace NH_3 and acetonitrile from complexes **2** and **3**, respectively, with bipyridine, gave recovered starting materials (Scheme 3.8).

Scheme 3.8 Attempted Syntheses of [(^{t}SiP$_3$)Fe(bpy)(L)][OTf]$_2$ Complexes

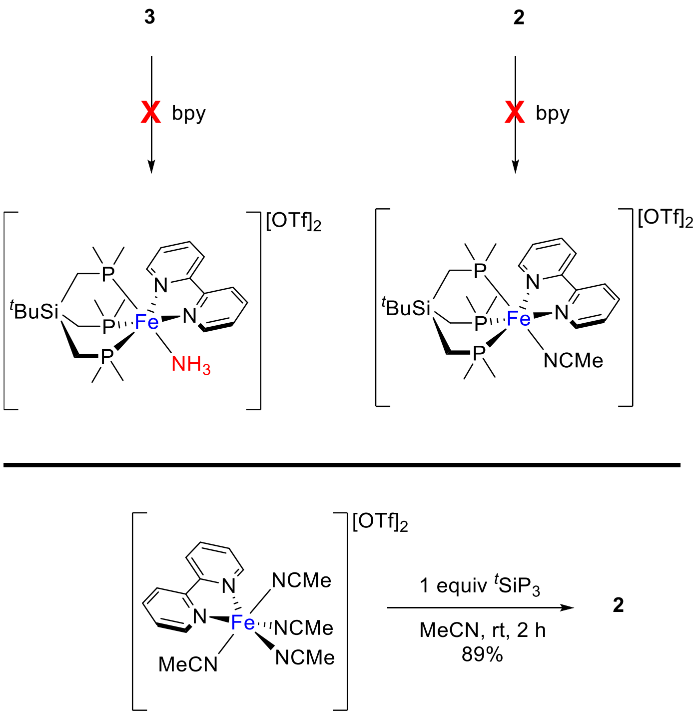

The latter case was surprising since compound **3** was synthesized by displacing acetonitrile ligands from **2** with NH_3. The reaction of ^{t}SiP$_3$ with [(bpy)Fe(NCMe)$_4$][OTf]$_2$ was tested as an alternate route to a monoacetonitrile compound. Instead, compound **2** and bipyridine were formed, (Scheme 3.8) which can be attributed to the strong trans-influence imparted by phosphine ligands that deter the bpy ligand from binding to the Fe center.[71] Indeed the only reported complex of this kind is zero-valent, five-coordinate Fe complex bearing bpy and PhP(CH$_2$CH$_2$PPh$_2$)$_2$ ligands reported by Mukhopadhyay et al.[72]

We performed an NBO analysis to test the feasibility of forming any bond between 2,2′–bipyridine (bpy) and Fe with the formula [^{t}SiP$_3$Fe(bpy)(NH$_3$)][OTf]$_2$. NBO analysis indicates a 3–center–4–electron hyper bond (3CHB) between phosphines trans to bpy, Fe, and nitrogens of bpy.

The resonance hybrid shows a higher P–Fe bonding character (63%) than Fe–N (37%). Also according to the other segments of NBO analysis, the high occupancy of σ_{FeP}* (0.25 *e*) and low occupancy of n_N (1.73 *e*), and large estimated $n_N \rightarrow \sigma_{FeP}$* 2nd–order interaction energy (62 kcal/mol) are all consistent with strong P–Fe–N hyberbond character. Similar results were obtained for [^{t}SiP$_3$Fe(bpy)(MeCN)][OTf]$_2$ as well.

Since the bpy complexes could not be prepared, we targeted [^{t}SiP$_3$Fe(dmpe)(L)][OTf]$_2$ (L = MeCN, NH$_3$, dmpe = 1,2–bis(dimethyl–phosphino)ethane) expecting that that dmpe would bind more strongly than bpy. Compound **2** reacted with dmpe provided [^{t}SiP$_3$Fe(dmpe)(MeCN)][OTf]$_2$ (**6**) in good yield.

Attempts to prepare [^{t}SiP$_3$Fe(dmpe)(NH$_3$)][OTf]$_2$ (**7**) by displacing MeCN from **6** with NH$_3$ gave low yields of **7**. Displacing two NH$_3$ ligands from compound **3** with dmpe required heating to 60 °C, generating a reaction mixture where **7** was a minor species.

We circumvented MeCN complexes by reacting the previously reported pentaphospine Fe(II) complex [^{t}SiP$_3$Fe(dmpe)(Cl)][Cl] (**8**)[55] with AgOTf in 1:1 ratio of THF:CH$_2$Cl$_2$ yielding the violet triflate complex [^{t}SiP$_3$Fe(dmpe)(OTf)][OTf] **9**. Preliminary data from 2 different X–ray crystallography data collections produce the triflate bond complex. However, data worthy of publication could not be obtained. The ^{31}P{^{1}H} NMR spectrum of **9** shows three moderately broad resonances at 39.82, 27.29, and 16.23 ppm in THF-d_8, and the ^{19}F NMR spectrum reveals a sharp singlet peak at –61.59 and a broad peak at –75.34 ppm. The latter ^{19}F chemical shift is similar to unbound triflate ions in the other complexes we have prepared, and the downfield shift upon coordination is typical for triflate binding to Fe(II).[73,74]

Scheme 3.9 Synthesis of Fe(II) mono(ammine) complex **7**

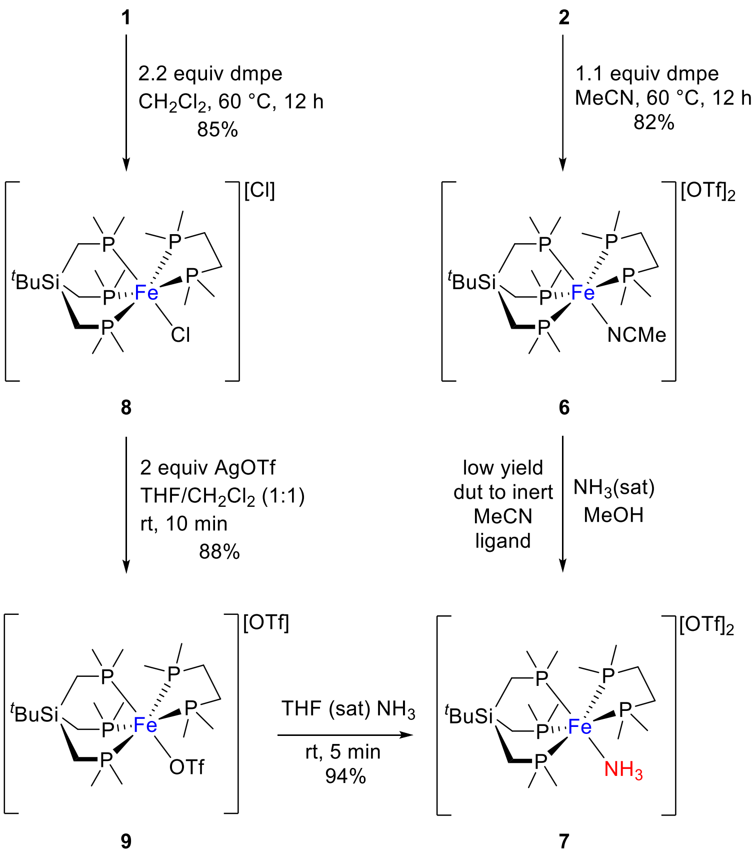

The spectroscopic data are consistent with our formulation for compound **9**, which reacts rapidly when NH_3 is added to a THF solution, accompanied by a color change from violet to orange.

[^{t}SiP$_3$Fe(dmpe)(NH_3)][OTf]$_2$ (**7**) was isolated by removing the THF solvent and washing the solid material with Et_2O to give an orange powder with 94% yield. The ^{31}P{^{1}H} NMR spectrum of **7** shows coupling typical for an AA´BB´C spin system where AA´ and BB´ refer to chemically equivalent P nuclei of respective dmpe and ^{t}SiP$_3$ ligands, and C is the ^{t}SiP$_3$ P that lies in the mirror plane containing Fe and the NH_3 ligand. The ^{1}H NMR spectrum of **7** (DMSO-d_6) has resonances for phosphine ligand protons at similar chemical shifts seen for compound **6** and an additional resonance integrating to three protons at 0.83 ppm for the NH_3 ligand.

Compounds **6** and **7** were also characterized by single-crystal X-ray diffraction experiments. The crystal structures and selected distances and angles are shown in Figure 3.18.

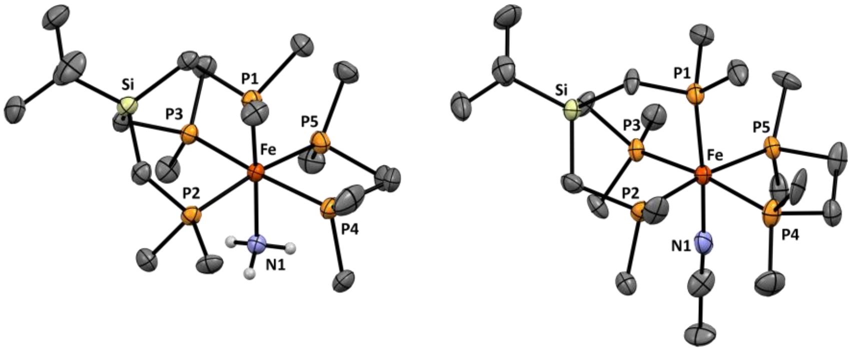

Figure 3.18 Molecular structures of complex **7** (left) and **6** (right) with thermal ellipsoids at the 50% probability level (Hydrogen atoms of carbons, triflate counter ions and solvent molecules were omitted for clarity). Selected bond lengths (Å) and angles (deg) for complex 6 (left): Fe–P1 2.2708(12), Fe–P2 2.2814(12), Fe–P3 2.2911(12), Fe–P4 2.3143(13), Fe–P5 2.3143(13), Fe–N1 2.113(3); P1–Fe1–P2 89.28(4), P1–Fe1–P3 90.16(4), P1–Fe1–P4 91.69(4), P1–Fe1–P5 101.10(5), P2–Fe1–P3 90.07(4), P2–Fe1–P4 96.59(5), P2–Fe1–P5 169.60(5), P3–Fe1–P4 173.11(5), P3–Fe1–P5 89.25(5), P4–Fe1–P5 83.88(5), N1–Fe1–P1 174.48(10), N1–Fe1–P2 85.66(10), N1–Fe1–P3 92.05(10), N1–Fe1–P4 86.70(10), N1–Fe1–P5 83.99(10). Complex **6** (right): Fe–P1 2.273(5), Fe–P2 2.286(4), Fe–P3 2.304(4), Fe–P4 2.305(4), Fe–P5 2.344(4), Fe–N1 1.944(16); P1–Fe1–P2 90.37(17), P1–Fe1–P3 89.76(16), P1–Fe1–P4 100.89(18), P1–Fe1–P5 95.13(16), P2–Fe1–P3 90.44(16), P2–Fe1–P4 91.24(17), P2–Fe1–P5 172.99(17), P3–Fe1–P4 169.20(18), P3–Fe1–P5 93.93(15), P4–Fe1–P5 83.46(16), N1–Fe1–P1 175.0(4), N1–Fe1–P2 88.4(5), N1–Fe1–P3 85.4(4), N1–Fe1–P4 84.0(4), N1–Fe1–P5 86.5(5)

The CV of complex **6** is shown in Figure 3.19. Complex **6** has anodic and cathodic peaks at 1.43 and 1.35 V (vs. Fc*), respectively, with a peak–to–peak separation of 0.08 V and $E_{1/2}$ = 1.39 V. The theoretical $E_{1/2}$ value for **6** was found to be 1.29 V vs Fc^*/Fc^{*+} according to the following reaction (**6** + Fc^{*+} → **6b** + Fc*, ΔG°_{298K} = 29.7340 kcal/mol) in which **6b** is the one-electron oxidized form of **6**.

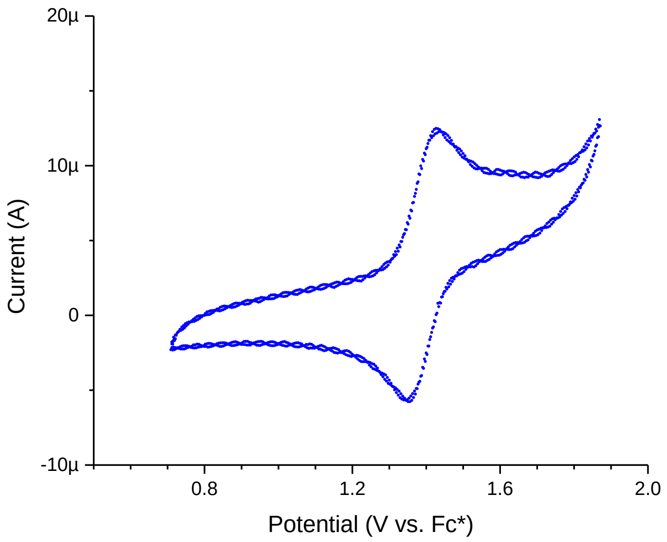

Figure 3.19 CV of 1 mM **6** in THF containing 2 M NH_4OTf as supporting electrolyte. WE: GC, CE: Pt disk, scan rate: 100 mV/s

The CV of compound **7** is shown in Figures 8a and 8b, respectively. Complex **7** has anodic and cathodic peaks at 1.20 and 1.10 V (vs. Fc*), respectively, with a peak–to–peak separation of 0.10 V and $E_{1/2}$ = 1.15 V. The theoretical $E_{1/2}$ value for **6** was found to be 1.09 V vs Fc*/Fc*$^{+}$ according to the following reaction (**7** + Fc*$^{+}$ → **7b** + Fc*, $\Delta G^{\circ}_{298\mathrm{K}}$ = 25.1345 kcal/mol) in which **7b** is the one-electron oxidized form of **7**.

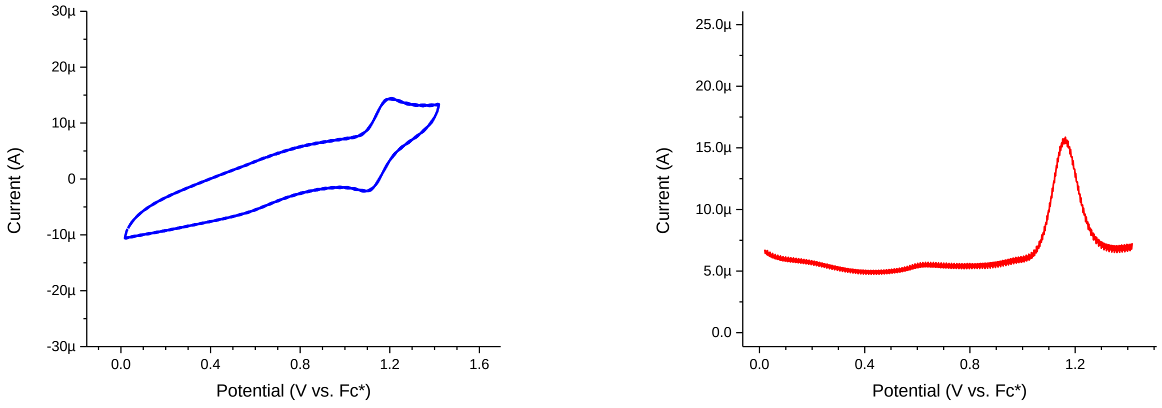

Figure 3.20 Left: CV of 1 mM **7** in THF containing 2 M NH_4OTf as supporting electrolyte. WE: GC, CE: Pt disk, scan rate: 100 mV/s. Right: SQW taken after CV

Table 3.2 summarizes the theoretical and experimental $E_{1/2}$ potentials of complexes **2**, **3**, **6**, and **7** vs. Fc*. Acetonitrile complexes show higher $E_{1/2}$ potentials compared to their ammine analogs both in theoretical and experimental values. The calculated $E_{1/2}$ potential of complex **3** shows a higher deviation from its experimental value. Also, theoretical calculations suggest that ligation of Fe by dmpe ligand should decrease the $E_{1/2}$ of the complex; however, experimental values do not match with the theoretical predictions. Indeed, $E_{1/2}$ of complex **6** is higher than the onset potential of NH_3 oxidation on the surface of the GC electrode and hence its electrocatalytic behavior cannot be accessed by GC as the working electrode.

Table 3.2 Comparison of the theoretical and experimental $E_{1/2}$ (V vs. Fc*) values of Complexes **2**, **3**, **6**, and **7**

Redox reaction	**Theoretical** ΔG°_{298K} **(kcal.mol^{-1})**	**Theoretical $E_{1/2}$ (V vs. Fc*)**	**Exp. $E_{1/2}$ (V vs. Fc*)**
2 + $Fc^{*+} \longrightarrow$ **2b** + Fc*	33.414	1.4489	1.09
3 + $Fc^{*+} \longrightarrow$ **3b** + Fc*	27.008	1.1711	0.56
6 + $Fc^{*+} \longrightarrow$ **6b** + Fc*	29.7340	1.2893	1.39
7 + $Fc^{*+} \longrightarrow$ **7b** + Fc*	25.1345	1.0899	1.15

Attempts to deprotonate **7** with hindered bases like $LiN(SiMe_3)_2$ and $LiN(^iPr)_2$ were unsuccessful. This can be explained by the steric effects of the methyl groups of phosphine ligand that protect bound NH_3 from hindered bases. A similar observation was reported for $[Fe(dppe)(cp)NH_3]^+$ complex (dppe = 1,2-bis(diphenylphosphino)ethane, cp = cyclopentadiene) in THF by Sellman *et al*. in which deprotonation with $NaN(SiMe_3)_2$ and BuLi did not yield the desired product. Utilizing $LiAlH_4$ by Sellman *et al*., however, provides the corresponding hydrido complex.[75]

There is precedent for the formation of $(dmpe)_5Fe_2$ and *trans*-$Fe(dmpe)_2Cl_2$ complexes as byproducts during the reduction of complex **8**.[55] Also structural interconversion of similar Fe(II) systems with reversible κ^2/κ^3-coordination modes of flexible tripodal phosphine ligand has been established.[76] These structural dynamics should also be taken into account during the evaluation of the electrocatalytic behavior of these types of complexes.

Since hydrazine complexes are plausible intermediates in Fe-catalyzed N_2 reductions and NH_3 oxidation,[53] syntheses of hydrazine complexes with a ${}^{t}SiP_3Fe$ platform were explored. Reactions of hydrazine with tris(ammine) complex **3** gave a mixture of products, including the tris(hydrazine) product (vide infra). When hydrazine was added to THF solutions of **6**, no reaction was observed. However, when **6** was heated to 60 °C in neat hydrazine, compound **10** was isolated in 57% yield (Scheme 3.10). In addition to a κ^1-N_2H_4 ligand, **10** has a bidentate κ^2–acetamidrazone ligand that results from the formal addition of hydrazine to acetonitrile. The ${}^{31}P\{{}^{1}H\}$ NMR spectrum of **10** in DMSO–d_6 shows one doublet at 42.13 ppm ($J = 49.9$ Hz), and one triplet at 36.22 ppm ($J = 49.4$ Hz) with a ratio of 2:1 indicative of breaking the C_{3v} symmetry of complex.

The crystal structure of **10** shows the formation of κ^2–acetamidrazone complex $[{}^{t}SiP_3Fe(N_2H_4)(MeC(NH)NH_2NH)][OTf]_2$ (**10**). Fe κ^2–acetamidrazone ligands have been prepared previously by reacting $L_4Fe(II)(\kappa^2–N_2H_4)(NCR)$ ($L = P(OR)_3$) complexes with excess hydrazine.[77] The κ^2–acetamidrazone ligand in **10** might arise from the intramolecular nucleophilic attack of η^1–N_2H_4 from the putative intermediate $[{}^{t}SiP_3Fe(NCMe)(N_2H_4)_2)][OTf]_2$. Alternatively, free hydrazine could first attack coordinated acetonitrile in complex **6**, since the nucleophilic attack at nitrile carbons is facile when nitrile coordinates to Lewis acids like BF_3.

Scheme 3.10 Reaction of hydrazine with complex **6** and **9**

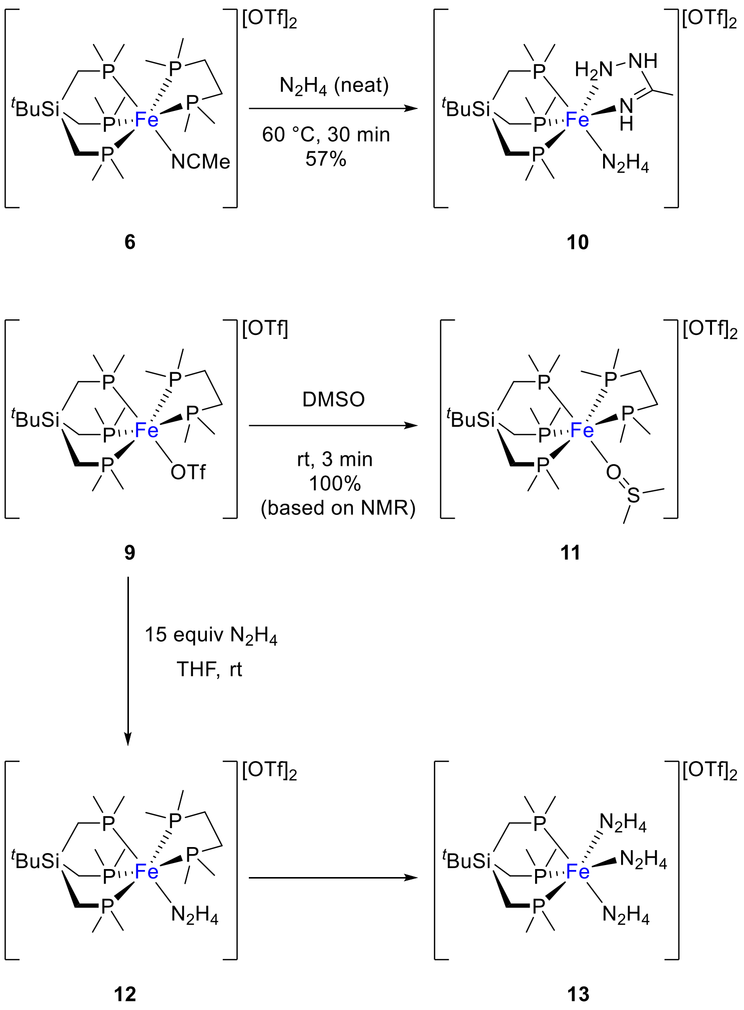

Compound **10** is not relevant to attempted electrocatalysis in THF solutions. We explored the reactivity of [^{t}SiP$_3$(dmpe)Fe(II)L)] complexes (L ≠ NCMe) with hydrazine. The reaction of **9** with hydrazine in THF, where bound triflate is labile and more prone to substitution, was explored. Triflate gets displaced by DMSO to yield **11** judged by a singlet peak in ^{19}F NMR spectrum at –77.79 ppm and the solid–state structure (Figure 3.22). The addition of 1 equiv of N_2H_4 to a solution of **9** in THF or DMSO did not form the corresponding mono(hydrazine) complex even with longer reaction times. By adding 15 equiv of N_2H_4 to the DMSO-d_6 solution of **9** in an NMR tube, the color changes instantly from blue-violet to orange. $^{31}P\{^1H\}$ NMR spectrum in DMSO-d_6 after 10 min shows three multiplets at 44.22, 18.81, and 17.05 ppm with the ratio of 2:1:2 which suggest the formation of the mono(hydrazine) complex **12**. Over time, a new singlet peak at 38.06 ppm in $^{31}P\{^1H\}$ NMR spectrum emerges accompanied by free dmpe at –46.23 ppm (Figure 3.21).

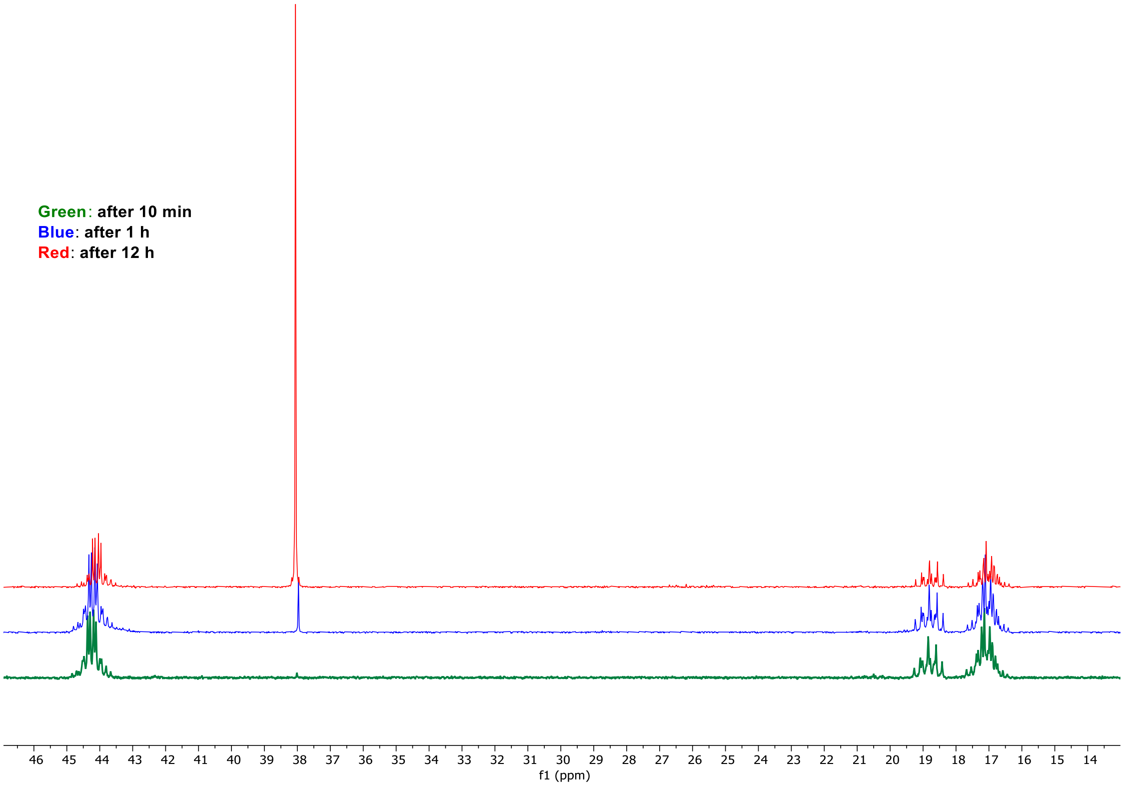

Figure 3.21 $^{31}P\{^1H\}$ NMR spectrum of reaction of complex **9** in DMSO–d_6 with 15 equiv of N_2H_4 in 10 min (green), 1 h (blue), and 12 h (red). Increasing the intensity of the peak at 38.06 ppm is indicative of the formation of the trishydrazine complex by displacing the dmpe ligand.

Addition of THF to this DMSO solution with a ratio of 2:1 and slow diffusion of Et_2O in 3 days, yields orange crystals suitable for X-ray crystallography. The X-ray structure shows the formation of tris(hydrazine) **10** (Figure 3.22). To the best of our knowledge, this is the first reported tris(hydrazine) Fe complex. It is surprising that dmpe gets displaced by N_2H_4 in the presence of excess hydrazine but not excess ammonia; even though NH_3 is a stronger base than N_2H_4.

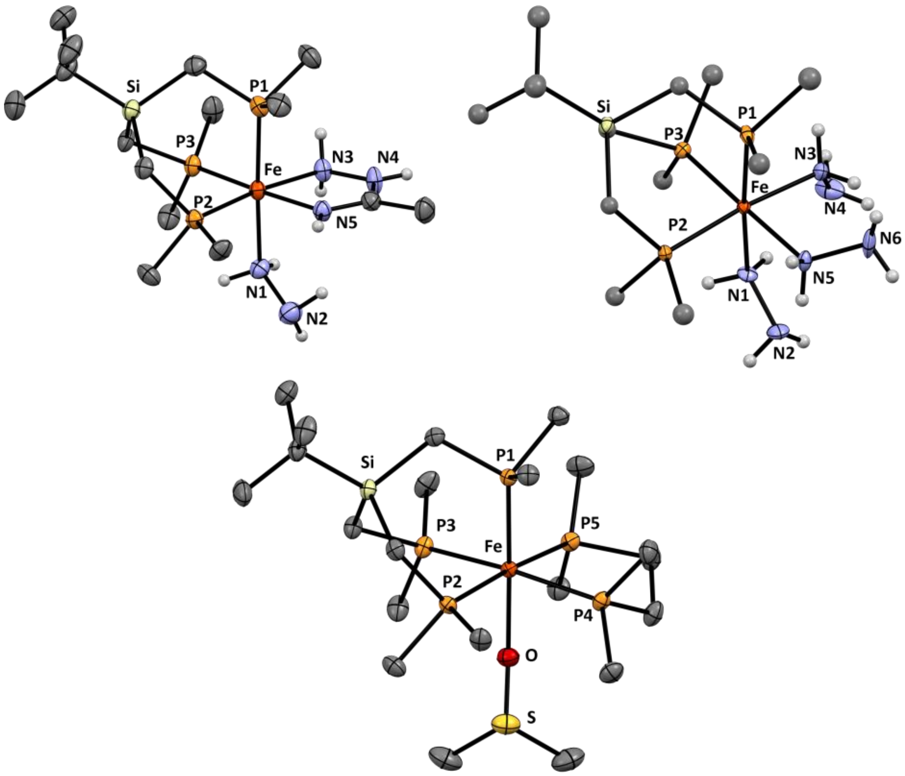

Figure 3.22 Molecular structures of complex **10** (top left) with thermal ellipsoids at the 50% probability level (Hydrogen atoms of carbons, counter ions and solvent molecules were omitted for clarity). Selected bond lengths (Å) and angles (deg) for complex **10** (top left): Fe–P1 2.225(1), Fe–P2 2.219(1), Fe–P3 2.231(1), Fe–N1 2.092(3), Fe–N3 2.071(4), Fe–N5 1.994(4), N1–N2 1.451(5), N3–N4 1.433(5); P1–Fe–P3 92.85(4), P1–Fe–P2 91.30(4), P1–Fe–N1 177.4(1), P1–Fe–N3 91.7(1), P1–Fe–N5 88.5(1), P3–Fe–P2 92.38(4), P3–Fe–N1 88.7(1), P3–Fe–N3 93.8(1), P3–Fe–N5 172.9(1), P2–Fe–N1 90.7(1), P2–Fe–N3 173.0(1), P2–Fe–N5 94.6(1), N1–Fe–N3 86.1(1), N1–Fe–N5 89.6(1), N3–Fe–N5 79.2(1), Fe–N3–N4 109.5(3). Complex **13** (top right): Fe–P1 2.219(2), Fe–P2 2.224(2), Fe–P3 2.224(2), Fe–N1 2.072(6), Fe–N3 2.082(6), Fe–N5 2.075(6); P1–Fe–P2 92.04(7), P1–Fe–P3 92.09(7), P1–Fe–N1 175.7(2), P1–Fe–N3 92.4(2), P1–Fe–N5 91.1(2), P2–Fe–P3 92.54(7), P2–Fe–N1 90.9(2), P2–Fe–N3 174.5(2), P2–Fe–N5 90.5(2), P3–Fe–N1 90.9(2), P3–Fe–N3 90.5(2), P3–Fe–N5 175.5(2), N1–Fe–N3 84.5(2), N1–Fe–N5 85.7(2), N3–Fe–N5 86.2(2). Complex **11** (bottom): Fe–P1 2.2497(6), Fe–P2 2.3096(5), Fe–P3 2.2953(6), Fe–P4 2.3126(6), Fe–P5 2.3331(5), Fe–O 2.149(2), S–O 1.519(2); P2–Fe–P3 89.99(2), P2–Fe–P1 88.21(2), P2–Fe–P5 175.07(2), P2–Fe–P4 96.87(2), P2–Fe–O1 91.10(4), P3–Fe–P1 92.45(2), P3–Fe–P5 89.58(2), P3–Fe–P4 169.26(2), P3–Fe–O1 86.79(4), P1–Fe–P5 96.71(2), P1–Fe–P4 96.01(2), P1–Fe–O1 178.97(5), P4–Fe–P5 82.88(2), P5–Fe–O1 83.98(4), P4–Fe–O1 84.83(4), Fe–O–S 138.8(1)

3.3. Conclusion

An Fe(II) tris(ammine) complex supported by a tridentate phosphine ligand, $[{}^{t}SiP_3Fe(NH_3)_3][OTf]_2$ (**3**), was synthesized, and its electrochemical behavior in the absence of NH_3 was investigated. The CV of **3** in THF containing 0.1 M of $TBAPF_6$ as supporting electrolyte shows multiple redox features. The same pattern was observed by changing the electrolyte to 0.1 M of TBAOTf as well. While electrocatalytic current decreases during AO in the presence of TBA-based electrolytes, no electrode passivation was observed by changing the supporting electrolyte to NH_4OTf, which suggests the reaction of TBA with possible Fe intermediates during the catalysis. Analysis of headspace gases of BE of solutions containing 1 mM of **3** in the presence of NH_3 and NH_4OTf as supporting electrolyte reveals the generation of N_2 as the anodic product. Rinse test and XPS analysis of the working electrode's surface, obviate the possibility of heterogeneous AO catalysis.

Chemical oxidation of **3** yields a paramagnetic complex, which upon addition of NH_3 regenerates **3**. Moreover, upon deprotonation of **3** with a hindered base, a diferrrous cation with the formula $[({}^{t}SiP_3Fe)_2(\mu\text{-}NH_2)_3][OTf]$ (**4**) was isolated, which is the first structurally characterized dinuclear iron complex with three NH_2 ligands on the bridging position. To investigate the effect of ancillary ligands on the oxidation potential of **3**, a mono(ammine) Fe(II) complex $[{}^{t}SiP_3Fe(dmpe)(NH_3)][OTf]_2$ (**7**) was synthesized and its electrochemical properties were compared to **3**. Displacing two NH_3 ligands in **3** with dmpe shifts the oxidation potential of the complex to higher potentials.

3.4. Synthesis

3.4.1. Synthesis of (dimethylphosphino)methyllithium

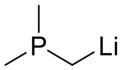

The previously reported procedure was employed for the synthesis.[78,79] Inside the glovebox, 12.2 g (16.27 ml, 160 mmol, 0.84 equiv) of PMe_3 was added to a 100 mL one-neck flask charged with a stir bar and sealed with a rubber septum quickly. 100 mL of ^{t}BuLi (1.9 M in pentane, 190 mmol, 1 equiv) was added by syringe at room temperature, and the rubber septum was displaced by a glass stopper with a Teflon sleeve and sealed with a Teflon tape. During stirring, a white precipitate slowly forms. After 6 days, stirring was turned off, and the flask was allowed to stand overnight in the box, waiting for the solid to settle at the bottom of flask. The yellowish supernatant on top was removed by a pipette. The white solids were dried under reduced pressure. (11.28 g, 86%).

Caution: *(Dimethylphosphino)methyllithium is an extremely pyrophoric solid. It will catch fire upon exposure to air. In addition to solids, supernatant contains unreacted ^{t}BuLi and PMe_3, which are highly flammable upon air exposure. Proper quenching procedures should be considered. Moreover, filtration of (dimethylphosphino)methyllithium inside the glove box should be avoided due to high static of solids, which will fly around the box's atmosphere and will result in serious contamination. Also, the mass of solids should be calculated based on the weight difference of empty flask to avoid taking the solids out of flask. All of the synthesized (dimethylphosphino)methyllithium was used for the next reaction step due to its high reactivity. Using a rubber septum should be avoided for sealing due to its reaction with the compound.*

3.4.2. Synthesis of ((*tert*-butylsilane)tris(methylene))tris(dimethylphosphane)

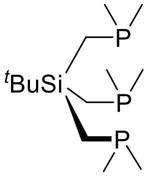

The previously reported procedure was employed for the synthesis.[55,78,79] In the glovebox, to a suspension of 11.27 g (137.42 mmol, 3.1 equiv) (dimethylphosphino)methyllithium in 250 mL Et_2O was added a solution of 8.49 g (44.33 mmol, 1 equiv) ^{t}BuSiCl$_3$ in Et_2O dropwise with vigorous stirring over 20 min. After stirring for 15 more min, the solution was filtered over dry and activated neutral alumina to remove LiCl. The solvent was evaporated to yield a slightly yellow-tinted oil. (9.157 g, 66%). ^{1}H NMR (500 MHz, C_6D_6) δ 1.16 (br s, 9H), 1.01 (br s, 18H), 0.81 (s, 6H). ^{31}P{^{1}H} NMR (202 MHz, C_6D_6) δ –54.88.

3.4.3. Synthesis of [(^{t}SiP$_3$Fe)$_2$(μ–Cl)$_3$][Cl] (1)

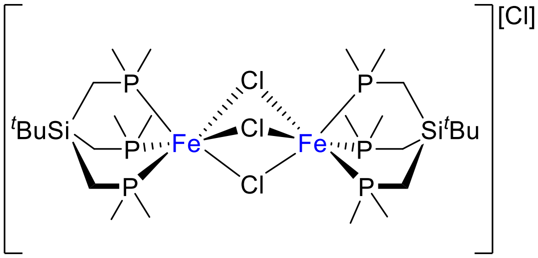

The procedure described by Boncella[80] and McNeil[55] was employed to synthesize [(^{t}SiP$_3$Fe)$_2$(μ–Cl)$_3$][Cl]. In the glove box, at room temperature, 4.445 g (35.076 mmol, 1.2 equiv) of $FeCl_2$ was suspended in CH_2Cl_2 and, while stirring, 9.157 g (29.23 mmol, 1 equiv) of ((*tert*-butylsilane)tris(methylene))tris(dimethylphosphane) was added dropwise. Upon addition, the color changed to deep purple. After stirring for 1 h, the solution was passed through activated neutral alumina to remove excess $FeCl_2$. After removing the solvent, the purple solid was washed first with 10 mL Et_2O and then 10 mL pentane and dried under reduced pressure (11.83 g, 92%). $^{31}P\{^1H\}$ NMR (202 MHz, MeCN-d_3) δ 43.58. ^1H NMR (500 MHz, MeCN–d_3) δ 1.53 (m, 36H), 0.8 (s, 18H), 0.62 (m, 12H).

3.4.4. Synthesis of [^{t}SiP$_3$Fe(NCMe)$_3$][OTf]$_2$ (2)

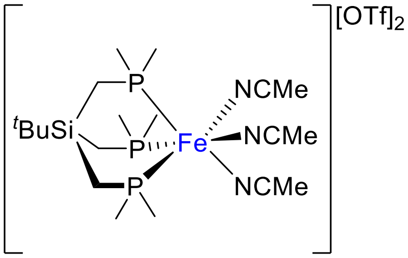

In the glove box, at room temperature, **1** (5.00 g, 5.718 mmol, 1 equiv) was dissolved in MeCN (200 mL) and a solution of AgOTf (6.024 g, 23.446 mmol) in MeCN was added dropwise. After 5 h of stirring at room temperature, the solution was filtered through activated neutral alumina using a fine glass frit to remove precipitated AgCl which yields a clear yellow solution. The MeCN solution was reduced in volume in vacuo and ether was added to precipitate a yellow fine powder. The yellow powder was collected on a frit and washed with ether, and was dried under vacuum (7.509 g, 83%). ^{1}H NMR (500 MHz, MeCN-d_3) δ 1.96 (s, 9H), 1.48 (m, 18H), 0.90 (s, 9H), 0.90–0.87 (m, 6H). ^{1}H NMR (500 MHz, MeNO$_2$-d_3) δ 2.49 (s, 9H), 1.59 (m, 18H), 0.98 (m, 6H), 0.92 (s, 9H). ^{13}C{^{1}H} NMR (126 MHz, MeCN-d_3) δ 130.80 (s), 26.03 (s), 18.77 (m), 17.32 (q, J = 5.7 Hz), 6.30 (dd, J = 7.2, 3.8 Hz), 4.57 (s). ^{31}P{^{1}H} NMR (202 MHz, MeCN-d_3) δ 34.24. ^{31}P{^{1}H} NMR (202 MHz, MeNO$_2$–d_3) δ 33.90. ^{19}F NMR (470 MHz, MeCN-d_3) δ –79.09 (s). Anal. Calcd for $C_{21}H_{42}F_6FeN_3O_6P_3S_2Si.Et_2O$: C, 34.85; H, 6.08; N, 4.88. Found: C, 35.03; H, 5.58; N, 4.94.

3.4.5. Synthesis of [^{t}SiP$_3$Fe(NH$_3$)$_3$][OTf]$_2$ (3)

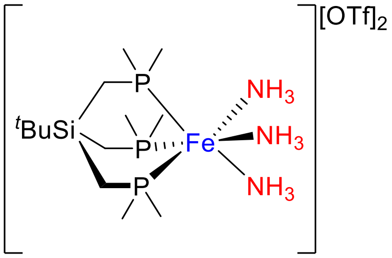

A 250 mL Schenck flask was charged with a stir bar and **2** in the glovebox and was sealed by a rubber septum. Then, the flask was taken out of the box and put under an N_2 atmosphere. 40 mL of degassed and dry methanol was added by syringe. After dissolving all the **2** in methanol, under stirring NH_3 was bubbled into the solution. The solution became hot, and the color changed from yellow to deep orange. After stirring for 15 min under continuous NH_3 bubbling, the NH_3 needle was taken out of flask. The N_2 pressure was increased, and the septum of the flask was removed. 200 mL of Et_2O was added at once under vigorous stirring. Orange microcrystalline powder precipitated, and the septum was replaced. The stirring was turned off, and the flask was put in dry ice/acetone bath to precipitate additional product, then the solvent was removed by cannula filtration. Orange solids were dried under vacuum and transferred to the glovebox (2.15 g, 78%). ^{1}H NMR (500 MHz, DMSO-*d*$_6$) δ 2.03 (s, 9H), 1.38 (m, 18H), 0.82 (s, 9H), 0.76 (m, 6H). ^{1}H NMR (500 MHz, MeNO$_2$-*d*$_3$) δ 1.95 (s, 9H), 1.56 (m, 18H), 0.97 (m, 6H), 0.92 (s, 9H). ^{13}C{^{1}H} NMR (126 MHz, DMSO-*d*$_6$) δ 25.60 (s), 17.96 (dd, *J* = 12.1, 6.4 Hz), 16.16 (q, *J* = 5.6 Hz), 7.53 (s). ^{31}P{^{1}H} NMR (202 MHz, MeNO$_2$-*d*$_3$) δ 38.07. ^{31}P{^{1}H} NMR (202 MHz, DMSO-*d*$_6$) δ 41.79. ^{19}F NMR (470 MHz, DMSO-*d*$_6$) δ –77.73 (s). Anal. Calcd for $C_{15}H_{42}F_6FeN_3O_6P_3S_2Si$: C, 25.18; H, 5.92; N, 5.87. Found: C, 25.31; H, 5.89; N, 5.43.

3.4.6. Synthesis of [(^{t}SiP$_3$)$_2$Fe$_2$(μ–NH$_2$)$_3$][OTf] (4)

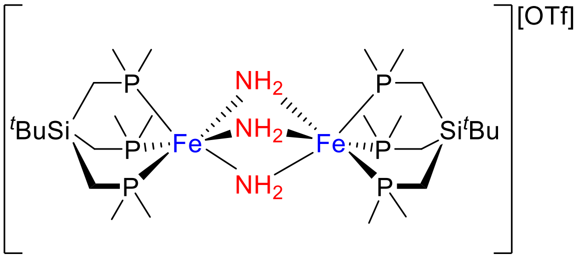

3 (219 mg, 0.306 mmol, 1 equiv) was suspended in 4 mL THF at room temperature, and 1 M solution of LiN(SiMe$_3$)$_2$ in THF (0.5 mL, 0.490 mmol, 1.6 equiv) was added slowly to yield a brown solution. After stirring for 10 min, the mixture was filtered, and the filtrate was layered with pentane and kept in the glove box's freezer at –32 °C. After 3 d, the orange precipitate was collected and washed with ether until the washings were colorless. Then, the powder was dried under reduced pressure (76 mg, 53%). ^{1}H NMR (500 MHz, THF-*d*$_6$) *δ* 1.42 (s, 36H), 0.80 (s, 18H), 0.64 (s, 12H), –2.63 (s, 6H). ^{1}H NMR (500 MHz, DMSO-*d*$_6$) *δ* 1.34 (s, 36H), 0.74 (s, 18H), 0.56 (s, 12H), –2.79 (s, 6H). ^{13}C{^{1}H} NMR (126 MHz, THF-*d*$_8$) δ 26.38 (s), 19.68 (s), 17.29 (s), 10.51 (s). ^{31}P{^{1}H} NMR (202 MHz, DMSO–*d*$_6$) *δ* 43.75 (s). ^{31}P{^{1}H} NMR (202 MHz, THF-*d*$_8$) *δ* 44.48 (s). ^{19}F NMR (470 MHz, DMSO-*d*$_6$) *δ* –77.79 (s). Anal. Calcd for $C_{27}H_{72}F_3Fe_2N_3O_3P_6SSi_2$**.**$LiCF_3SO_3$: C, 30.98; H, 6.69; N, 3.87. Found: C, 31.10; H, 6.69; N 3.40.

3.4.7. Synthesis of [^{t}SiP$_3$Fe(dmpe)(NCMe)][OTf]$_2$ (6)

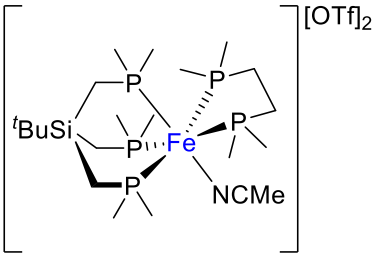

In a glove box, **2** (0.53 g, 0.677 mmol), dmpe (0.10 g, 0.677 mmol) and 10 mL of CH_2Cl_2 were placed in a pressure tube containing a magnetic stir bar and taken out of the box. The mixture was stirred at 60 °C for 12 h. Removing the solvent under reduced pressure afforded a yellow powder that was washed with Et_2O (2 × 3 mL) and dried under vacuum (0.475 g, 82%). ^{1}H NMR (500 MHz, MeCN-d_3) δ 2.02–1.95 (m, 4H), 1.75 (d, J = 6.3 Hz, 6H), 1.72 (d, J = 7.9 Hz, 6H), 1.57 (d, J = 7.1 Hz, 6H), 1.46 (d, J = 7.3 Hz, 6H), 1.39 (d, J = 8.1 Hz, 6H), 1.21 (m, 4H), 0.96 (s, 9H), 0.87 (d, J = 12.8 Hz, 2H). ^{31}P{^{1}H} NMR (202 MHz, MeCN-d_3) δ 45.89 (m, 2P), 19.07 (m, 1P), 15.92 (m, 2P). ^{13}C{^{1}H} NMR (126 MHz, MeCN-d_3) δ 136.37(s), 30.57 (dd, J = 23.4, 18.3 Hz), 26.57 (d, J = 24.1 Hz), 25.83 (s), 24.79 (m), 19.97 (m), 17.08 (q, J = 5.1 Hz), 15.96 (m), 12.63 (d, J = 7.6 Hz), 10.10 (s), 5.65 (s). ^{19}F NMR (470 MHz, MeCN-d_3) δ –78.98 (s). Anal. Calcd for $C_{23}H_{52}F_6FeNO_6P_5S_2Si$: C, 32.29; H, 6.13; N, 1.64. Found: C, 32.42; H, 6.13; N, 1.72.

3.4.8. [^{t}SiP$_3$Fe(dmpe)(Cl)][Cl] (8)

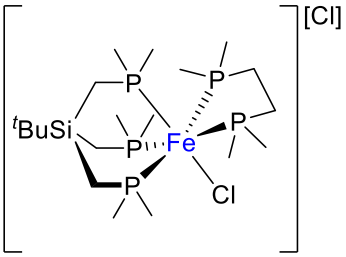

Following the previously reported procedure,[55] in a glove box, **1** (0.85 g, 0.965 mmol), dmpe (0.14 g, 0.965 mmol) and 25 mL of CH_2Cl_2 were placed in a pressure tube containing a magnetic stir bar and taken out of the box. The mixture was stirred at 60 °C for 12 h. Removing the solvent under reduced pressure afforded a crimson powder that was washed with Et_2O (2 × 3 mL) and dried under vacuum. (0.481 g, 85%). Spectroscopic data were consistent with the literature.

3.4.9. Synthesis of [^{t}SiP$_3$Fe(dmpe)(OTf)][OTf] (9)

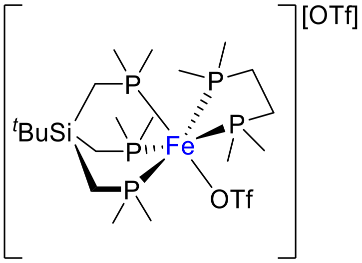

8 (204 mg, 0.347 mmol, 1 equiv) was dissolved in 8 mL of 1:1 THF:DCM, and AgOTf (179 mg, 0.694 mmol, 2 equiv) was added to the solution. After 10 min of vigorous stirring at room temperature in which color changes from crimson to blue-purple, the solution was filtered over Celite to yield a deep violet solution. Removing solvent in vacuo yields **9** (249 mg, 88%). ^{31}P{^{1}H} NMR (202 MHz, THF-d_8) δ 39.82 (br, 2P), 27.29 (br, 1P), 16.23 (br, 2P). ^{19}F NMR (470 MHz, THF-d_8) δ –61.59 (s), –75.34 (br). Anal. Calcd for $C_{21}H_{49}F_6FeO_6P_5S_2Si$: C, 30.97; H, 6.06. Found: C, 31.81; H, 5.90. Due to peak broadness (presumably because of solvent exchange with bound OTf) no satisfactory ^{1}H and ^{13}C NMR spectra were taken.

3.4.10. Synthesis of [^{t}SiP$_3$Fe(dmpe)(NH$_3$)][OTf] (7)

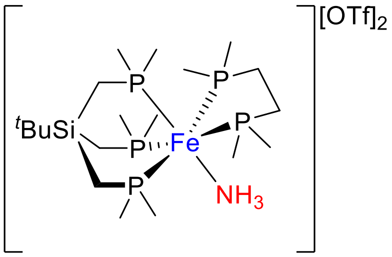

To a solution of **9** in THF, NH_3 was bubbled. The Color changed from blue-purple to orange. The solvent was removed in vacuo, and orange solids were washed with Et_2O and dried under reduced pressure (0.251 g, 94%). ^{1}H NMR (500 MHz, DMSO-*d*$_6$) *δ* 2.01 (m, 2H), 1.88 (m, 2H), 1.72 (d, *J* = 5.6 Hz, 6H), 1.67 (d, *J* = 7.8 Hz, 6H), 1.53 (m, 6H), 1.36 (m, 6H), 1.29 (d, *J* = 7.6 Hz, 6H), 1.24 – 1.17 (m, 2H), 1.17 – 1.10 (m, 2H), 0.91 (s, 9H), 0.82 (t, *J* = 3.8 Hz, 3H), 0.77 (d, *J* = 12.0 Hz, 2H). ^{31}P NMR (202 MHz, DMSO-*d*$_6$) *δ* 48.78 (m, 2P), 20.92 (m, 1P), 19.49 (m, 2P). ^{13}C{^{1}H} NMR (126 MHz, DMSO-*d*$_6$) δ 29.02 (m), 26.76 (d, *J* = 22.1 Hz), 25.40 (s), 23.88 (dd, *J* = 15.9, 9.8 Hz), 20.10 (m), 18.03 (m), 16.19 (q, *J* = 5.0 Hz), 14.45 (m), 12.45 (d, *J* = 5.4 Hz), 9.53 (s). Anal. Calcd for $C_{21}H_{52}F_6FeNO_6P_5S_2Si$: C, 30.33; H, 6.30; N, 1.68. Found: C, 29.49; H, 5.92; N 1.33.

Chapter 4. CATALYTIC AMMONIA OXIDATION BY A MONONUCLEAR RUTHENIUM COMPLEX SUPPORTED BY AN ISOINDOLE-BASED LIGAND

4.1. Introduction

Homogeneous electrocatalytic ammonia oxidation (AO) by mononuclear mono(ammine) Ru complexes has been reported previously.[81,82] Scheme 4.1 summarizes some of the selected Ru-based AO electrocatalysts.[81,82]

Among the various proposed mechanisms for catalytic AO, hydrazine/hydrazido and nitride pathways have attracted the most attention. As shown in (Scheme 4.2), in the hydrazine/hydrazido cycle, nucleophilic attack of NH_3 on the imido complex (which is an en route intermediate of Ru(III) ammine disproportionation to Ru(II)–NH_3 and Ru(IV)–NH) results in N-N bond formation to yield a Ru(II)–N_2H_4 complex. Hydrazine complexes can be oxidized to their diazene counterparts, while further oxidation can generate dinitrogen.

In the nitride pathway, consecutive 3 e^- oxidation and proton transfer from Ru(II)–NH_3 yields a Ru(IV) nitride intermediate. Intermolecular coupling of two Ru(IV) nitride complexes forms a dinitrogen bridge intermediate. Further displacement of N_2 by NH_3 completes the catalytic cycle.

Scheme 4.1 Ru mononuclear AO electrocatalysts

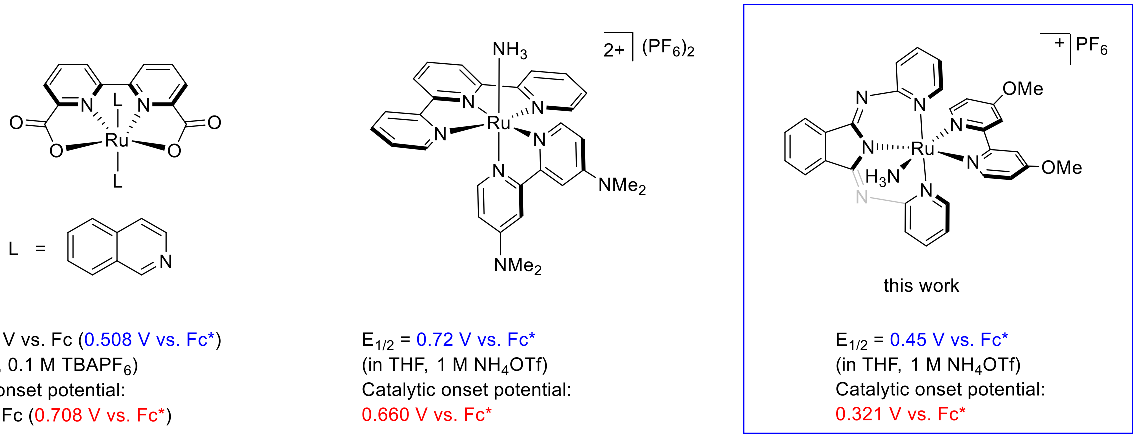

$E_{1/2}$ = 0.0 V vs. Fc (0.508 V vs. Fc*)
(in MeCN, 0.1 M $TBAPF_6$)
Catalytic onset potential:
0.20 V vs Fc (0.708 V vs. Fc*)

$E_{1/2}$ = 0.72 V vs. Fc*
(in THF, 1 M NH_4OTf)
Catalytic onset potential:
0.660 V vs. Fc*

$E_{1/2}$ = 0.45 V vs. Fc*
(in THF, 1 M NH_4OTf)
Catalytic onset potential:
0.321 V vs. Fc*

Scheme 4.2 Proposed electrocatalytic AO by hydrzine/hydrazido mechanism

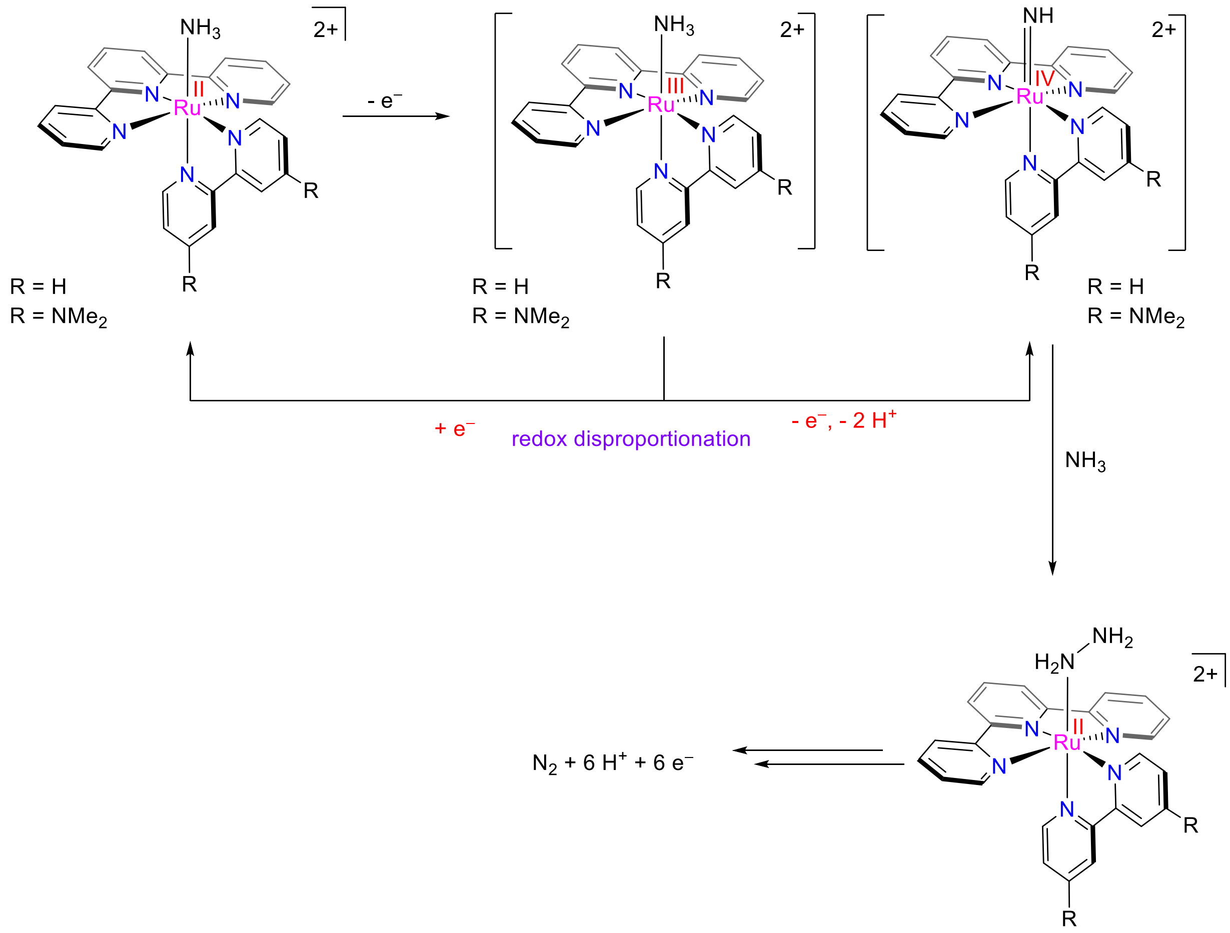

Smith and co-workers proposed a hydrazine/hydrazido mechanism based on the previous works of Meyer[83–86] for a Ru(II)–NH_3 complex supported by polypyridyl ligands (Scheme 4.2). Indeed, in 1981, Meyer and co-workers published a paper on the oxidation of coordinated NH_3 in $[Ru(trpy)(bpy)NH_3]^{2+}$ to nitrate by nucleophilic attack of H_2O on the Ru(IV) imido complex in aqueous media. So far, the Ru(IV) imido intermediate in these Ru ammine polypyridyl systems has not been isolated; however, a related $[Os^{IV}(trpy)(bpy)(NNR)]^{2+}$ intermediate has been trapped in the presence of a secondary amine in place of NH_3.[87]

In 2019, Nishibayashi and co-workers proposed the nitride pathway for a Ru AO catalyst supported by a 2,2′-bipyridyl-6,6′-dicarboxylate ligand (Scheme 4.3).[81] The N_2–bridged bimetallic Ru complex was synthesized and characterized independently by oxidizing the Ru ammine complex with tris(4-bromophenyl)amine radical cation in the presence of NH_4PF_6 and 2,4,6–collidine (as the base) in MeCN at –40 °C. In addition to the coupling of two Ru nitride complexes, there are some reported examples of the formation of the N–N bond via nucleophilic attack on Ru nitride, which are shown in Scheme 4.4.[88–90] For stabilizing the high oxidation states of Ru in its nitride complexes, the supporting ligands should be good electron donors. Salen ligands (Scheme 4.4), for example, are good candidates, which have been used widely in oxidation chemistry of transition metals.[89–92]

Scheme 4.3 Proposed electrocatalytic AO by Nishibayashi and co-workers[81]

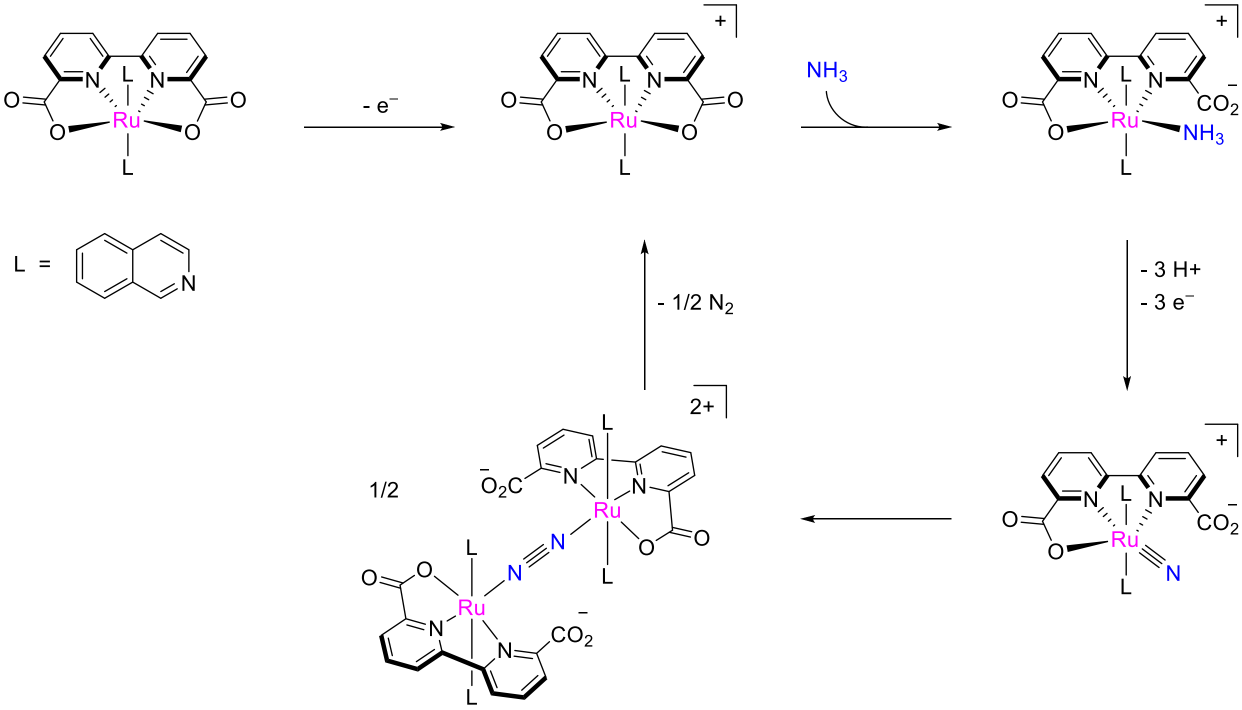

Scheme 4.4 Examples of the formation of an N–N bond via nucleophilic attack on Ru nitride

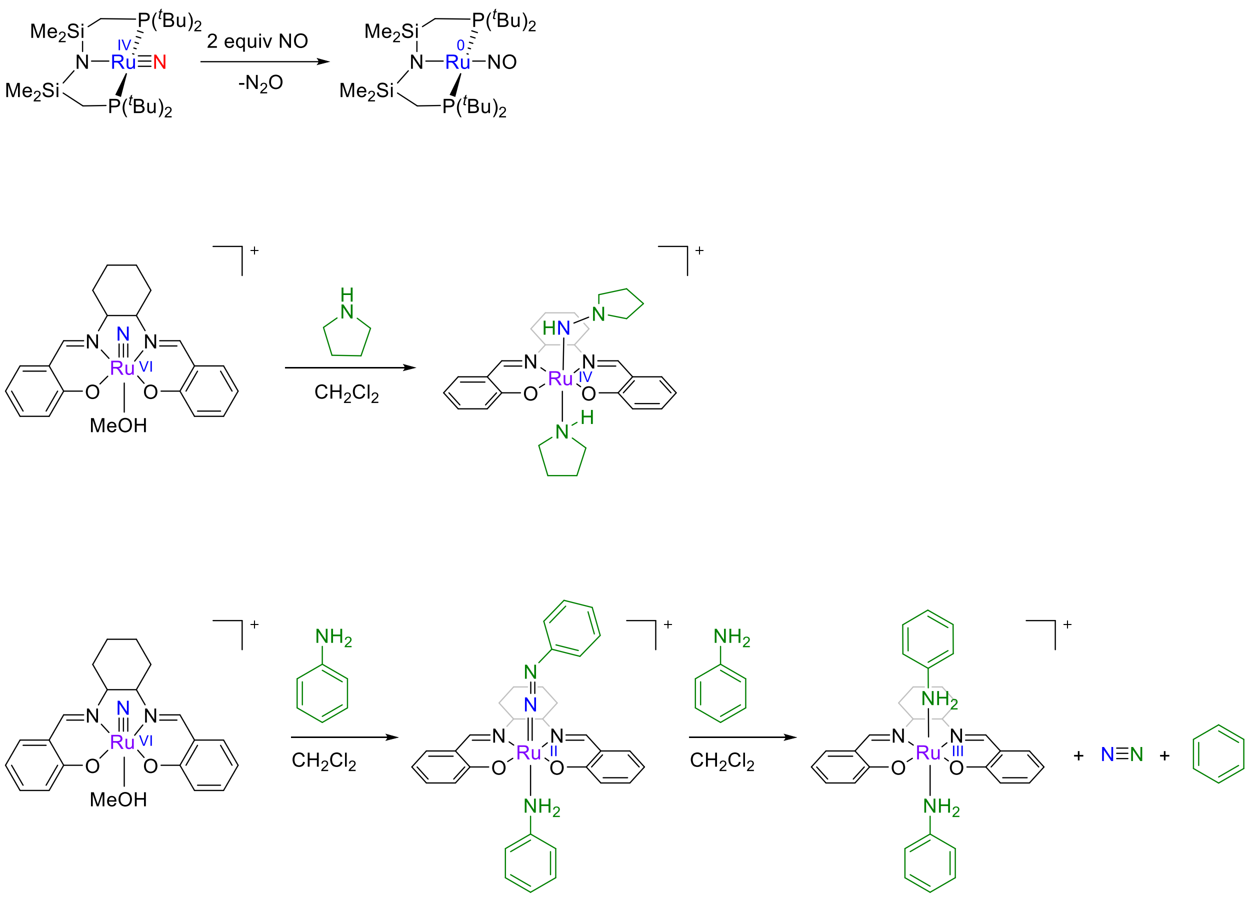

In this chapter, the synthesis, characterization, and electrocatalytic activity of a Ru ammine complex supported by an isoindole-based ligand will be discussed. The catalytic onset potential of the complex toward NH_3 oxidation in different organic solvents has been accessed and compared to other reported AO Ru electrocatalysts. Chemical oxidation of the Ru(II) ammine complex has also been investigated. For characterizing the products of NH_3 oxidation in the presence of the catalyst, bulk electrolysis has been conducted, and the release of dinitrogen gas as the anodic product of AO has been monitored by gas analysis of the electrochemical cell's headspace.

4.2. Results and Discussion

One strategy to lower the overpotential of electrocatalytic NH_3 oxidation is the synthesis of complexes with a reduced net charge. Despite 2,2':6',2"-terpyridine (trpy) which is a rigid and neutral tridentate ligand, (1-Z,3-Z)-N^1,N^3-bis(pyridin-2-yl)isoindolin-1,3-diimine (Hbid) bears a negative charge once deprotonated and also has a larger chelate bite angle compare to trpy. Also, the formation of $Ru(bid)_2^{n+}$ is less likely than $Ru(trpy)_2^{n+}$ during catalysis due to trans-influence effects. The Hbid ligand was prepared by the previously reported reaction by Siegl (Scheme 4.5).[93,94]

Scheme 4.5 One-pot Synthesis of Hbid ligand

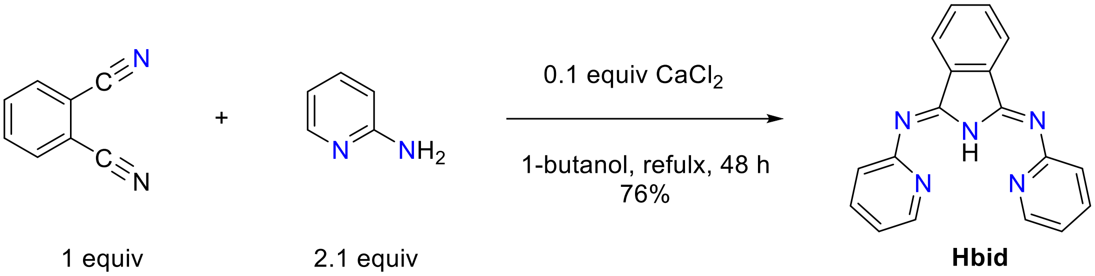

The reaction of Hbid with $RuCl_3{\cdot}3H_2O$ in ethanol yields $[Ru(bid)Cl_3]H^+$ as a brown color powder which has been used as the precursor for the synthesis of Ru catalysts.[95,96] Ru(bid)(bpy')Cl (**1**) was prepared by previously reported procedure by llobet and co-workers via the reaction of $[Ru(bid)Cl_3]H^+$ with 1 equiv of 4,4'-dimethoxy-2,2'-bipyridine (bpy').[97]

Displacement of Cl^- with NH_3 in **1** followed by anion exchange to PF_6 gives blue-purple $[Ru(bid)(bpy')NH_3][PF_6]$ (**2**) in 83% isolated yield (Scheme 4.6).

Scheme 4.6 Preparation of [Ru(bid)(bpy')NH_3][PF_6] (**2**)

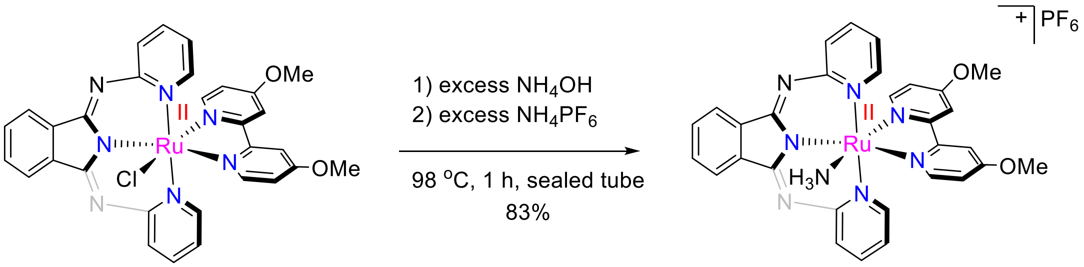

1 2

Single crystals of **2** suitable for X-ray crystallography were prepared by slow vapor diffusion of diethyl ether into the dichloromethane solution of **2**. Figure 4.1 exhibits the solid-state structure of **2**, and its caption summarizes its selected bond lengths and bond angles.

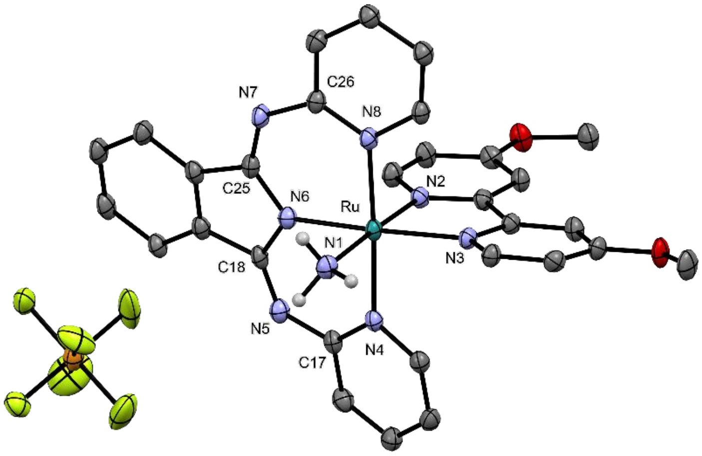

Figure 4.1 Crystal structure of complex **2** with thermal ellipsoids at the 50% probability level. Solvent molecules and hydrogens on carbon atoms have been removed for clarity. Selected bond lengths (Å) and angles (deg) for complex **2**: Ru–N1 2.156(3), Ru–N2 2.048(2), Ru–N3 2.098(2), Ru–N4 2.087(3), Ru–N6 2.013(2), Ru–N8 2.093(2), N5–C17 1.381(3), N5–C18 1.298(3), N6–C18 1.380(3), N6–C25 1.367(3), N7–C25 1.301(4), N7–C26 1.377(3). Bond angles: N1–Ru–N2 178.00(9), N1–Ru–N3 100.65(9), N2–Ru–N6 94.44(9), N4–Ru–N8 177.26(9), N3–Ru–N4 91.35(9), N6–Ru–N8 89.05(9)

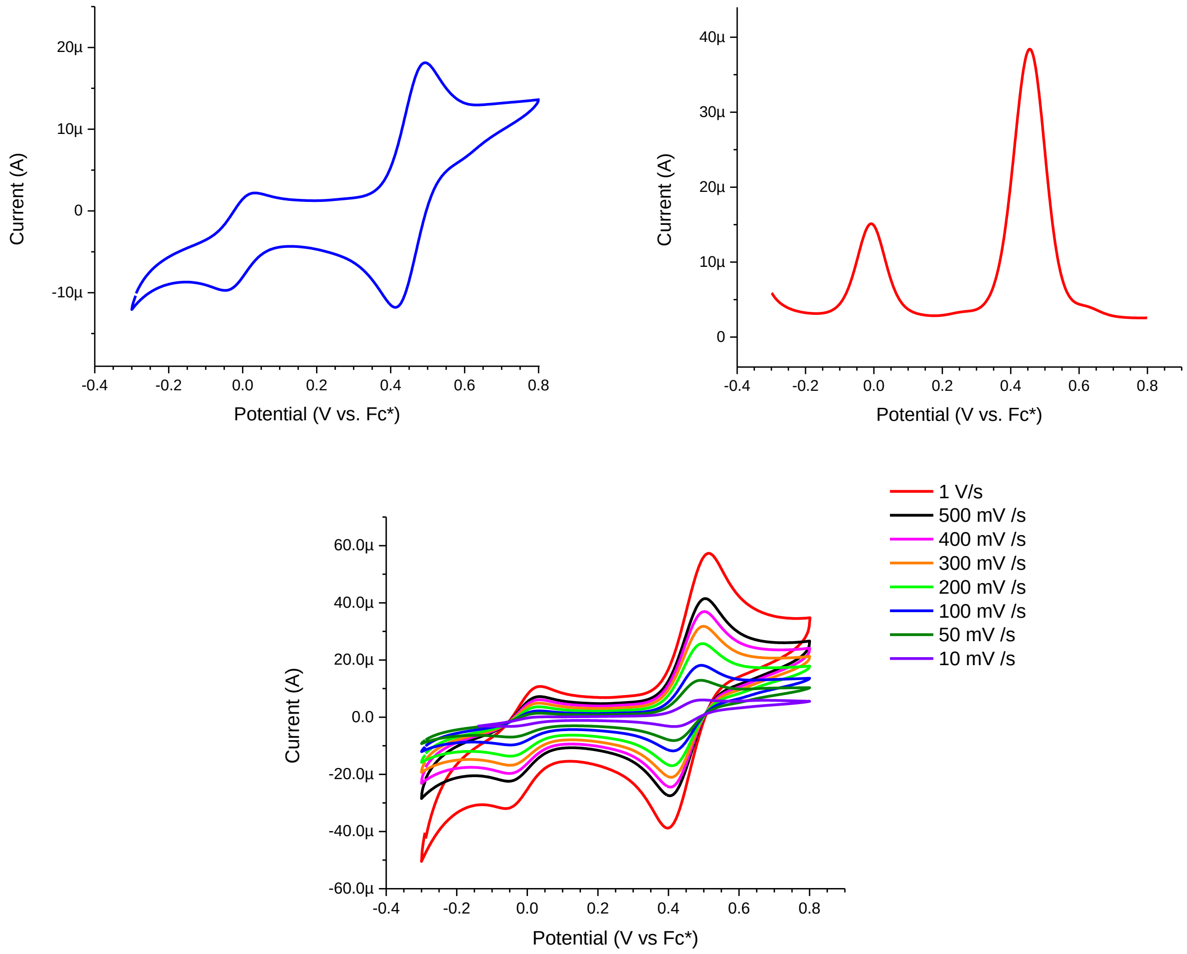

Figure 4.2 Left: CV of 1 mM of Complex **2** in the presence of 0.2 mM of Fc* as the internal standard in THF containing 1 M of NH_4OTF as supporting electrolyte. Right: correspondent SQW has taken instantly after CV. WE: GC, CE: Pt disk, scan rate: 100 mV/s

The cyclic voltammogram of complex **2** is shown in Figure 4.2. One anodic peak at the potential of E_{pa} = 0.49 V (vs. Fc*) and one reverse cathodic peak at the potential of E_{pc} = 0.41 V (vs. Fc*) with the $E_{1/2}$ = 0.45 V (vs. Fc*) were observed. The diffusion coefficient ($D_\circ$) of **2** in THF containing 1 M of NH_4OTf, was calculated by Randles–Sevcik equation:

$$i_p = 0.446nFA\left(\frac{nF\nu D_\circ}{RT}\right)^{\frac{1}{2}} \qquad D_\circ = \left(\frac{slope}{0.4463nFAC^\circ}\right)^2 \frac{RT}{nF}$$

which n is the number of electrons transferred in the redox event (n = 1), F is the Faradic constant (F = 96485.3321 C.mol^{-1}), ν is the scan rate (V.s^{-1}), A is the electrode's geometrical surface area (A = 0.07068 cm^{2}), C° is the bulk concentration of analyte (1 mol.cm^{-3}), R is the gas constant (R = 8.3144621 J.K^{-1}.mol^{-1}), and T is the temperature (T = 295.37 K). By measuring the CV of **2** with different scan rates (Figure 4.3), $D_\circ$ was calculated to be 9.19×10^{-6} cm^{2}s^{-1} for oxidation of **2** and 4.08×10^{-6} cm^{2}s^{-1} for reduction of [Ru(bid)(bpy')NH_3][PF_6][OTf].

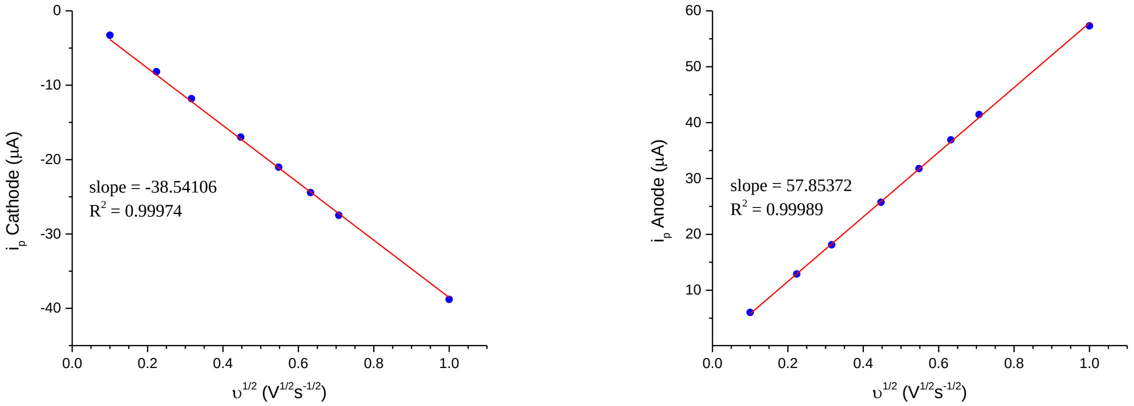

Figure 4.3 Plotting cathodic (left) and anodic (right) peak currents (i_p) versus square root of scan rate ($\nu^{1/2}$) for complex **2** in THF containing 1 M of NH_4OTf result in a linear line that from their slops diffusion coefficients were calculated to be 9.19×10^{-6} cm^{2}s^{-1} for oxidation of **2** and 4.08×10^{-6} cm^{2}s^{-1} for reduction of [Ru(bid)(bpy')NH_3][PF_6][OTf]. WE: GC, CE: Pt disk

By bubbling NH_3 through the solution ([NH_3] = 2.8 M) after taking the CV of **2** in THF with 1 M NH_4OTf as the supporting electrolyte and glassy carbon (GC) as the working electrode, a catalytic current was obtained with an onset of 0.32 V (vs. Fc*) (Figure 4.4). To confirm that the catalysis is homogeneous and not related to the formation of Ru species on the surface of the GC electrode, a rinse test was performed by rinsing the GC electrode with THF and inserting it back into the solution of THF with 2.8 M NH_3 and 1 M NH_4OTf with no catalyst present. No catalytic current was observed after rinsing, which suggests that the catalysis is homogeneous. The peak shape of the catalytic current resembles the KT-type electrocatalysis operating by an EC' mechanism.[98,99] Due to the fast kinetics of electrocatalysis in KT, the oxidized form of electrocatalyst consumes all available substrate, in this case NH_3, within the reaction diffusion layer. Because all substrate is consumed and there is no available substrate left for the electrocatalyst to react with, the oxidized electrocatalyst is regenerated at potentials anodic to the catalysis-initiating redox event.[98] This may explain the nature of the second wave in Figure 4.4, which occurs at a potential of 0.6 V (vs. Fc*).

The mechanism of electrocatalytic NH_3 oxidation, however, may be more complicated than the simplified KT mechanism as it is a 6 e^-, and 6-proton multistep reaction.

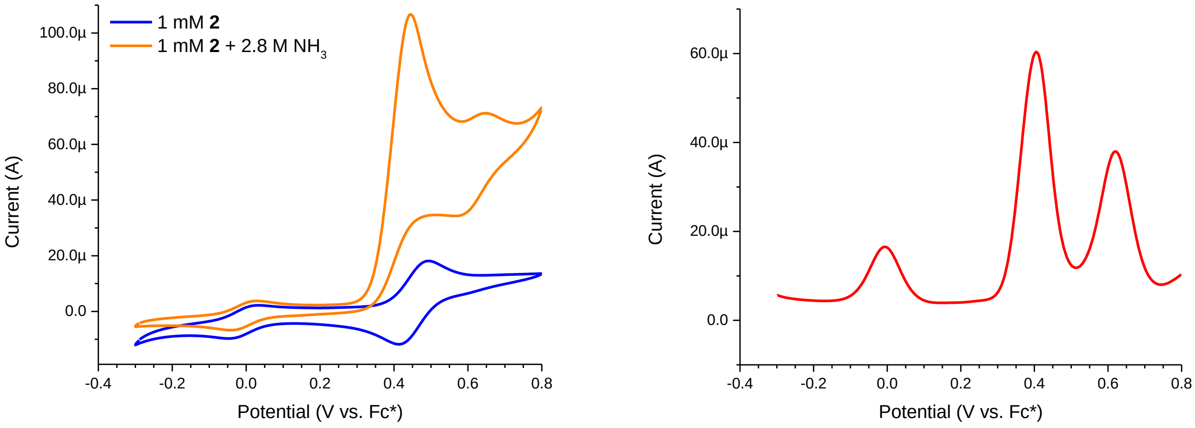

Figure 4.4 Left: CV (blue line) of 1 mM solution of complex **2** in THF with 1 M of NH_4OTf as supporting electrolyte and 0.2 M of Fc* as internal standard; CV (orange line) after bubbling NH_3 ($[NH_3]$ = 2.8 M) through a 1 mM solution of complex **2** in THF with 1 M NH_4OTf as supporting electrolyte and 0.2 M Fc*. Right: SQW of 1 mM solution of complex **2** in THF with 1 M NH_4OTf as supporting electrolyte and 0.2 M Fc* in the presence of 2.8 M NH_3. WE: GC, CE: Pt disk, scan rate: 100 mV/s

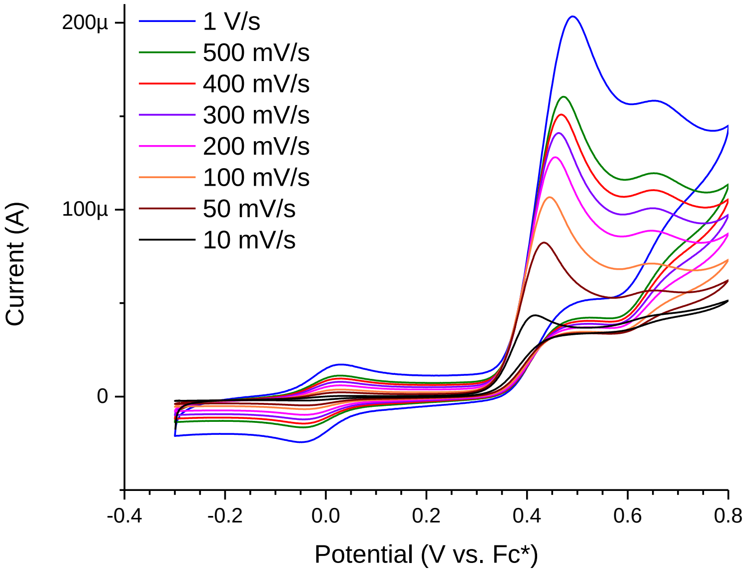

Figure 4.5 CV of 1 mM solution of complex **2** with different scan rates in THF with 1 M NH_4OTf as supporting electrolyte and 0.2 M Fc* in the presence of 2.8 M NH_3. WE: GC, CE: Pt disk

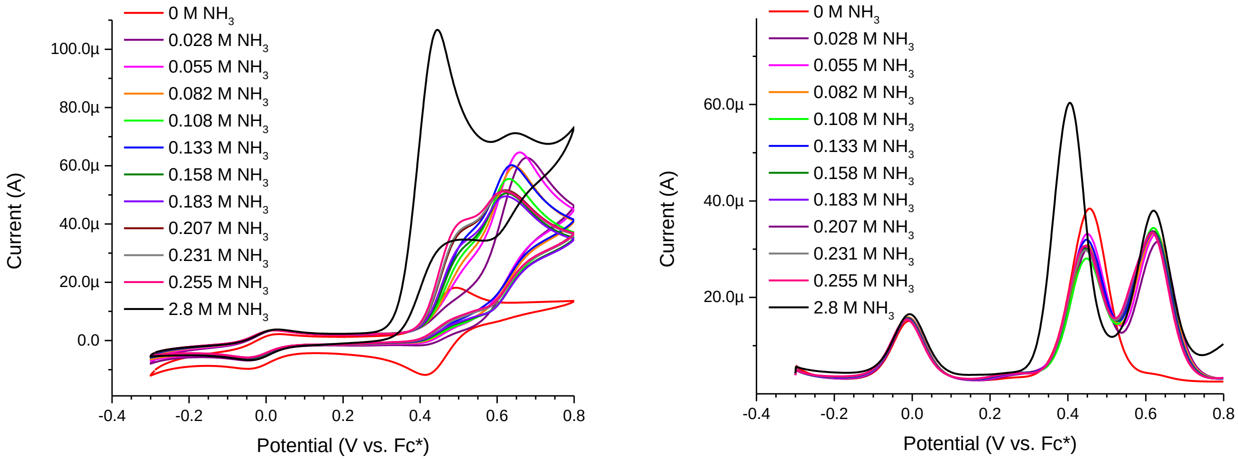

Figure 4.6 Left: CV of complex **2** in THF with 1 M NH_4OTf and different concentrations of NH_3in the presence of 0.2 mM Fc* as internal standard. Right: corresponding SQW has taken instantly after each CV. WE: GC, CE: Pt disk, scan rate: 100 mV/s

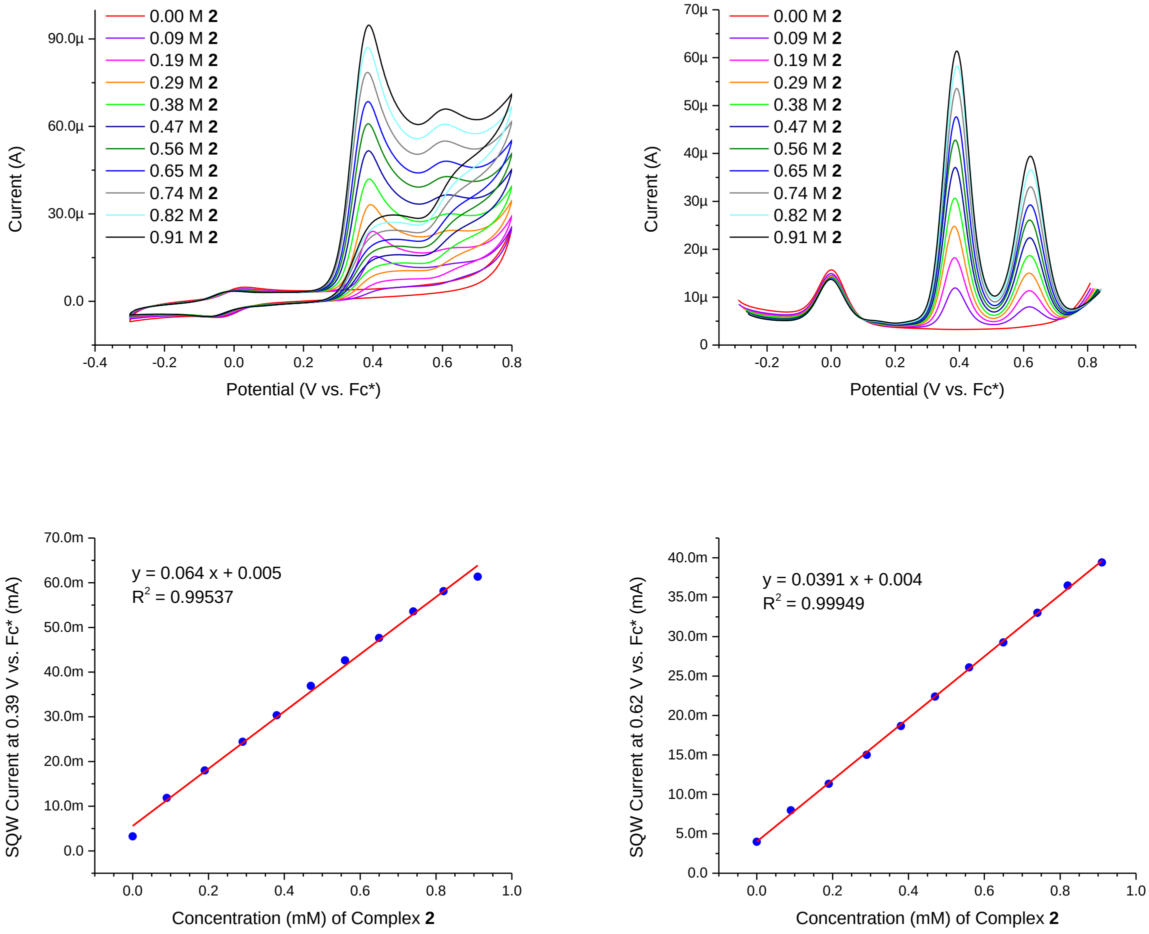

Figure 4.7 Top left: CV of various concentrations of complex **2** in THF containing 2.8 M NH_3, 1 M NH_4OTf, and 0.2 mM Fc* as internal standard. Top right: corresponding SQW taken after each CV. Bottom left: SQW current of the first peak at 0.39 V (vs. Fc*) plotted vs. concentration of complex **2**. Bottom right: SQW current of the second peak at 0.62 V (vs. Fc*) plotted vs. concentration of complex **2**. WE: GC, CE: Pt disk, scan rate: 100 mV/s

Figure 4.5 depicts the CV with different scan rates of 1 mM **2** in THF in the presence of 2.8 M NH_3 and 1 M NH_4OTf as supporting electrolyte. The second peak was observed at all scan rates starting from 1 V/s to 10 mV/s. The CV of **2** was also taken in THF with different concentrations of NH_3 (Figure 4.6). By adding a small concentration of NH_3 to the solution of 1 mM **2** in THF, two anodic peaks were observed.

The CV of **2** at different concentrations was also examined in THF with 2.8 M NH_3 and 1 M NH_4OTf. As shown in Figure 4.7, both peaks at 0.39 V (vs. Fc*) and 0.62 V (vs. Fc*) have a linear dependence on the concentration of **2**.

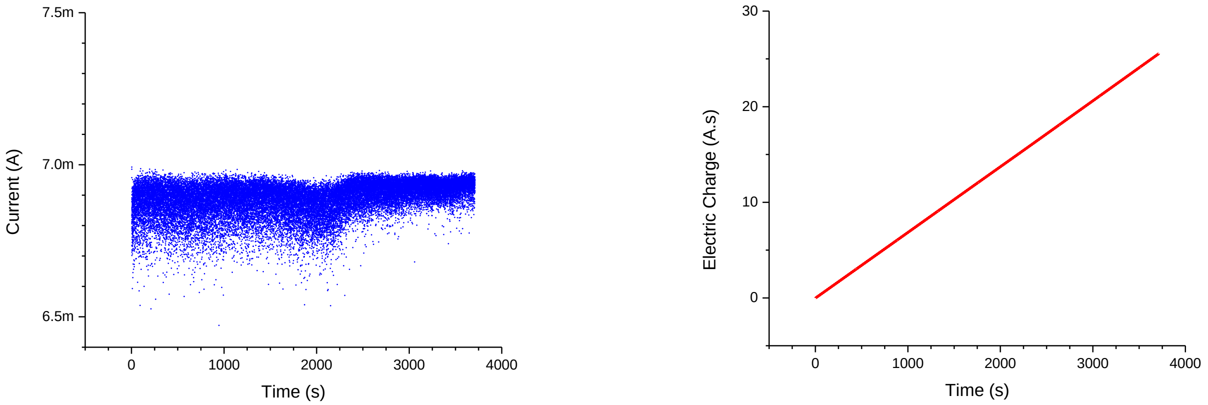

Figure 4.8 Left: BE of THF solution with 2.8 M NH_3 in the presence of 1 mM complex **2** for 1 h by applying 0.8 V (vs. Fc*). Right: the amount of the charge passed (C) during 1 h of BE. Supporting electrolyte: 1 M NH_4OTf, WE: GC plate, CE: Pt mesh

For quantifying the amount of produced N_2 on the anode, controlled potential electrolysis (bulk electrolysis–BE) was conducted in THF with 2.8 M NH_3, 1 M NH_4OTf, and 1 mM **2** (Figure 4.8). The potential was fixed at 0.8 V (vs. Fc*), and a GC plate and Pt mesh were used as working and counter electrodes, respectively. During 1 h of BE, 25.5374 Columb of charge was passed. Analyzing the headspace gas reveals the formation of 41 µmol of N_2 with 94% faradic efficiency.

BE of **2** was also done in MeCN under the same conditions. In the first minutes of BE, the color of the solution changed from blue-purple to red-violet. For characterization of the formed species during BE, water was added to the BE solution for precipitation of solid and removal of dissolved NH_4OTf. After filtering the red-violet solids and taking ^1H NMR in MeCN-d_3, the product was characterized as [Ru(bid)(bpy')(MeCN)][X], (X = OTf^- or PF_6^-). This was confirmed by comparing the ^{1}H NMR of independently synthesized [Ru(bid)(bpy')(MeCN)][PF$_6$] (Figure 4.9).

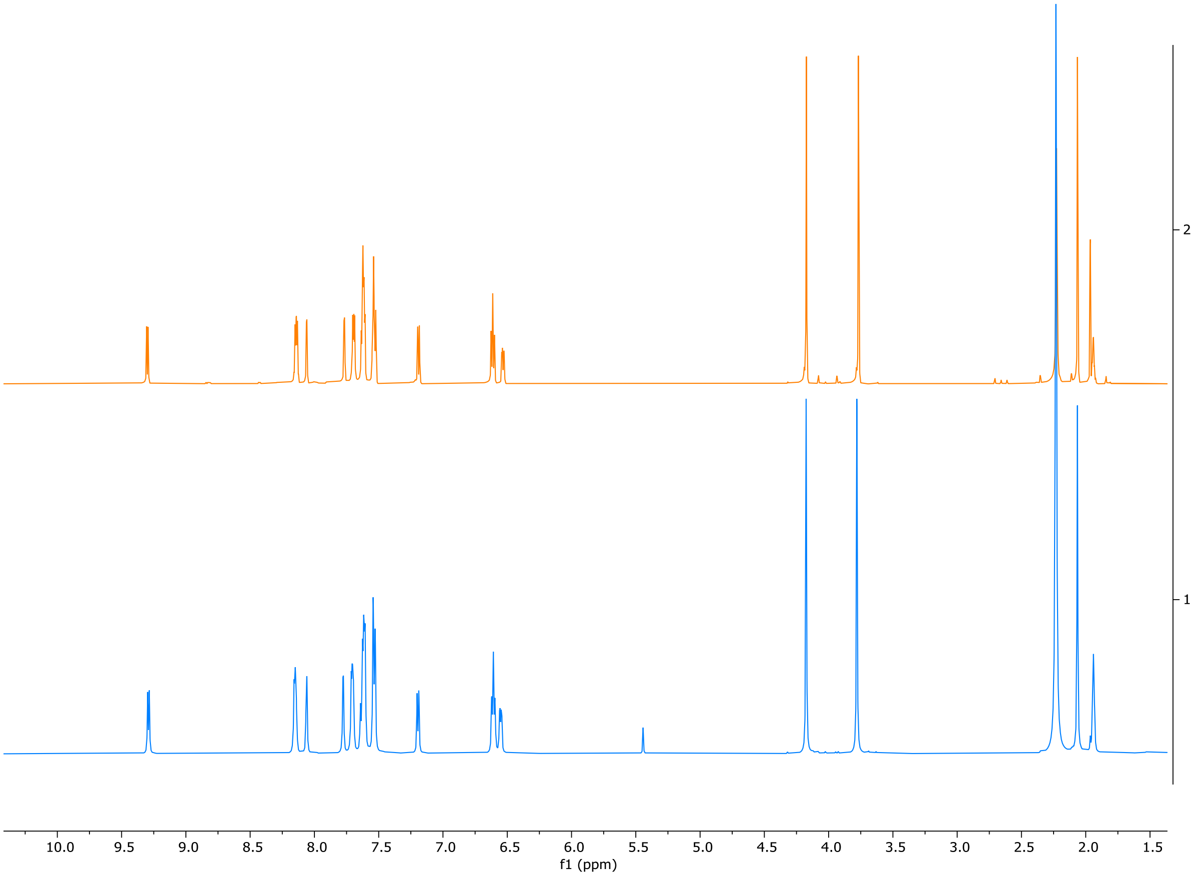

Figure 4.9 Orange: ^{1}H NMR of independently synthesized [Ru(bid)(bpy')(MeCN)][PF$_6$]; Blue: ^{1}H NMR of product form in the first minutes of BE of complex **2** in acetonitrile

Complex **2** was chemically oxidized by tris(4-bromophenyl)amine radical cation (Scheme 4.7). Upon addition of the oxidant to the blue-purple solution of **2** in THF, the color changes to brown. The oxidized form of **2** (complex **3**) was isolated as a brown powder with 91% yield.

Scheme 4.7 Chemical oxidation of **2** with tris(4-bromophenyl)amine radical cation

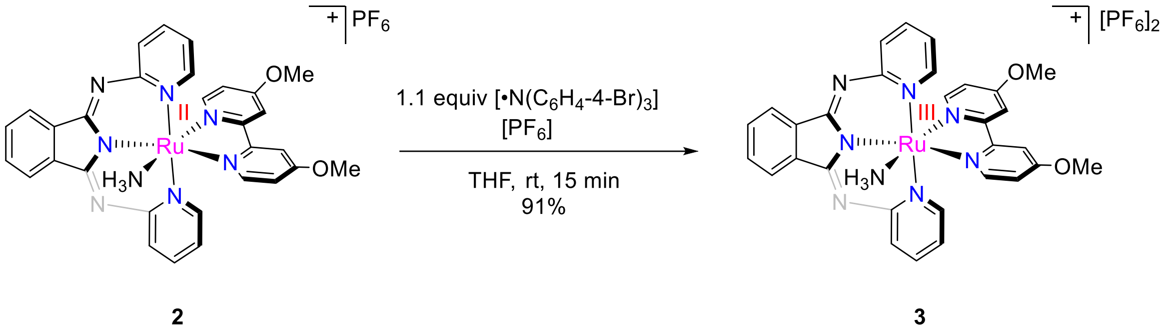

Upon addition of NH_3 to the brown solution of **3** in THF, the color changed instantly to blue-purple to regenerate **2**. Figure 4.10 shows the UV-vis spectra of **2** and **3** before and after addition of NH_3. After the addition of excess NH_3 to THF solution of **3**, the UV–vis spectrum of product matches with the spectrum of **2**. Interestingly, the brown color of the solution of **3** in THF slowly changes to green in hours. Slow evaporation of THF yields some green crystals suitable for X-ray crystallography. The structure of complex reveals the protonation of the imine nitrogen of the bid ligand to give ($[Ru(Hbid)(bpy')NH_3][PF_6]_2$) (**4**) (Figure 4.11). Because the ammine ligand coordinated to a Ru(III) center is acidic[56], its deprotonation by a basic imine nitrogen of bid ligand is not surprising.

The UV–vis spectrum of **4** is shown in Figure 4.10. Upon addition of excess NH_3 to the THF solution, the color changes from green to blue-purple. The UV-vis spectrum of the blue–purple solution matches well with the spectrum of **2**. The other products of self-deprotonation of **3** can be characterized by ^{15}N NMR of its correspondent $^{15}NH_3$ labeled complex. Scheme 4.8 summarizes the overall oxidation, reduction, protonation, and deprotonation of the Ru complexes.

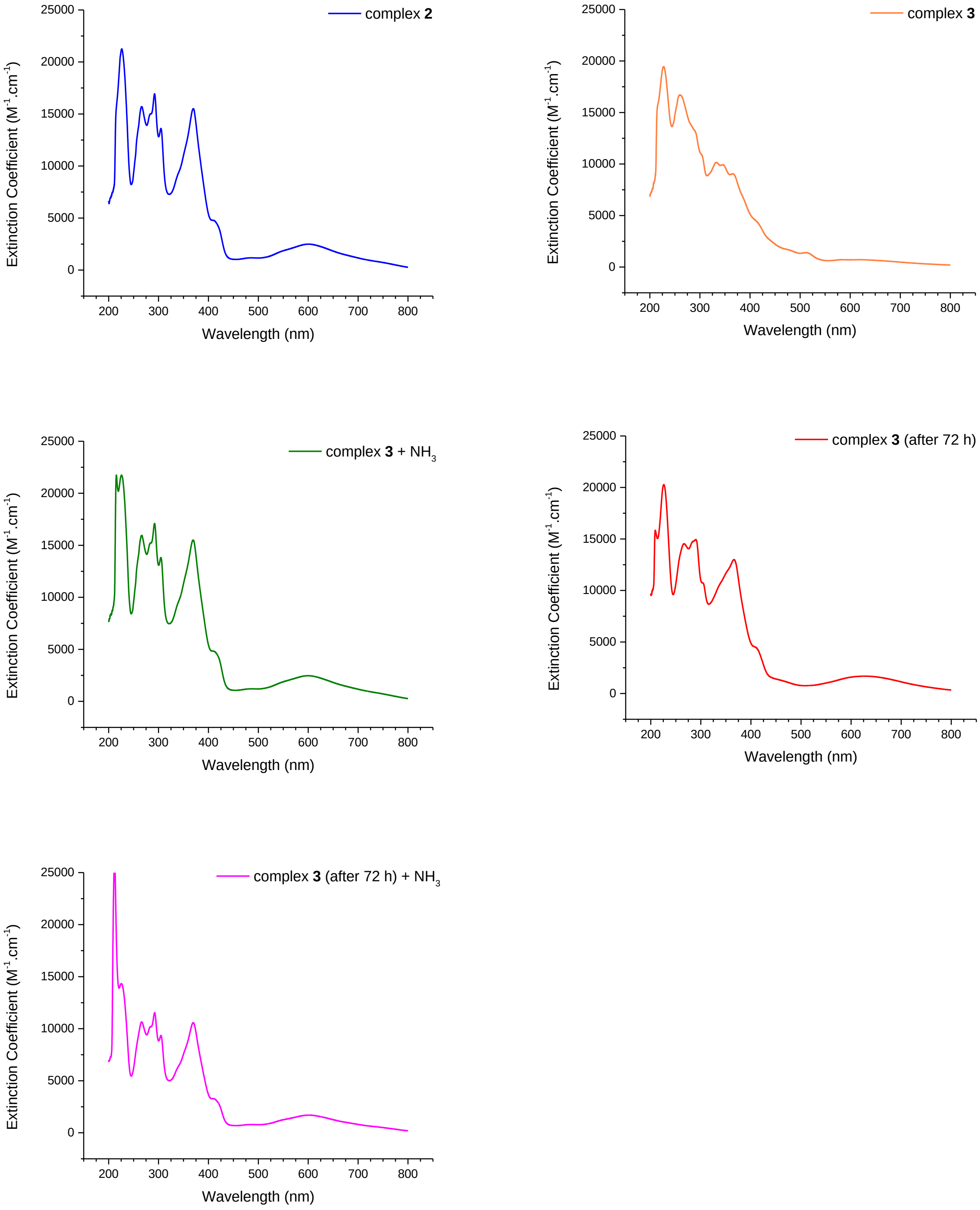

Figure 4.10 Top left: UV-vis spectrum of complex **2**. Top right: UV-vis spectrum of complex **3**. Middle left: UV-vis spectrum of complex **3** after addition of excess amount of NH_3. Middle right: UV-vis spectrum of complex **3** in THF taken after 72 h. Bottom left: UV-vis spectrum after addition of NH_3 to complex **3** which has been in THF for 72 h

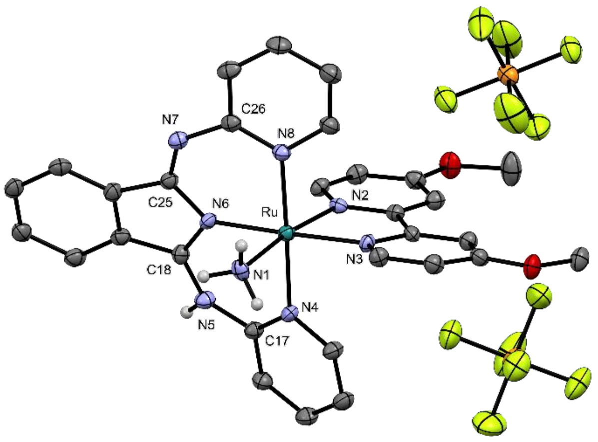

Figure 4.11 Crystal structure of complex **4** with thermal ellipsoids at the 50% probability level. Solvent molecules and hydrogens on carbon atoms have been removed for clarity. Selected bond lengths (Å) and angles (deg) for complex **4**: Ru–N1 2.147(5), Ru–N2 2.066(5), Ru–N3 2.063(4), Ru–N4 2.100(4), Ru–N6 2.020(4), Ru–N8 2.078(4), N5–C17 1.390(7), N5–C18 1.343(7), N6–C18 1.323(6), N6–C25 1.406(6), N7–C25 1.279(7), N7–C26 1.384(7). Bond angles: N1–Ru–N2 172.9(2), N1–Ru–N3 96.4(2), N2–Ru–N6 100.8(2), N4–Ru–N8 177.5(2), N3–Ru–N4 92.5 (2), N6–Ru–N8 89.1(2)

Scheme 4.8 Overall oxidation, reduction, protonation, and deprotonation of Ru Bid complex

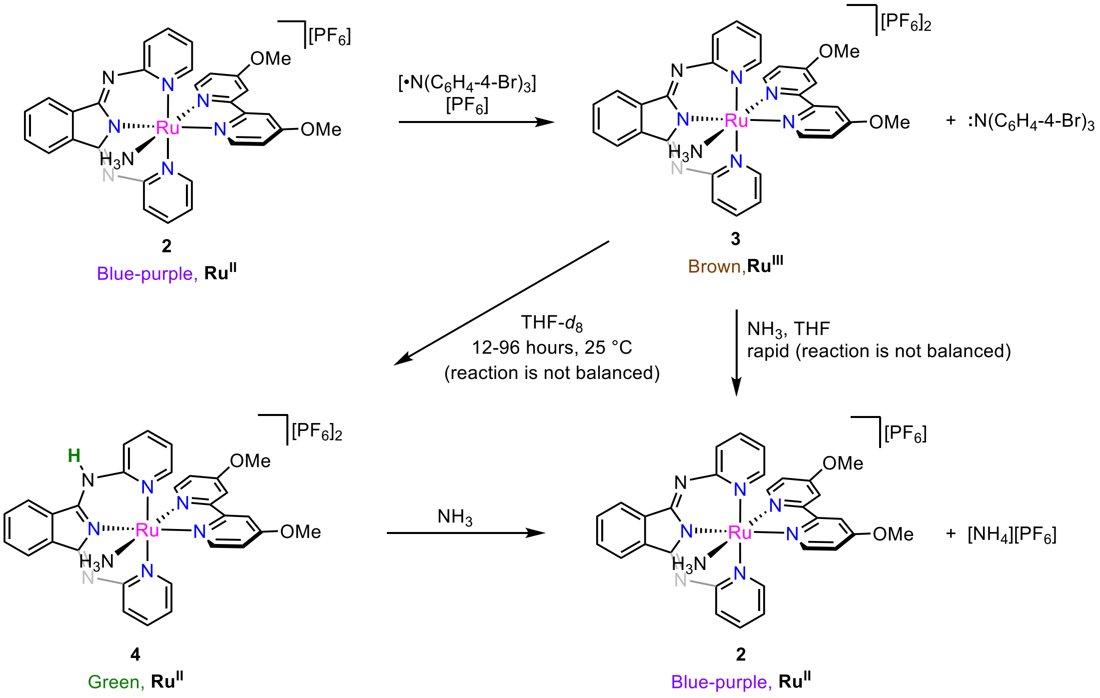

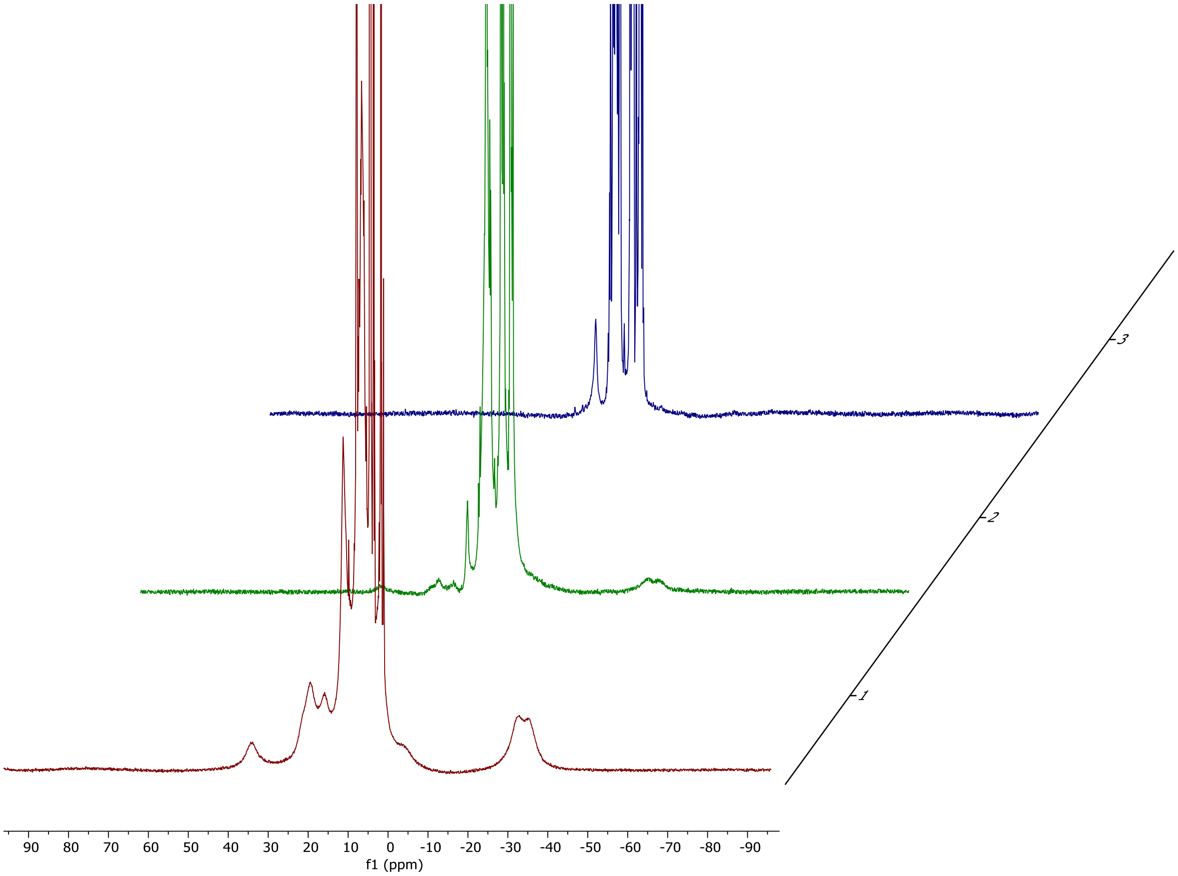

Figure 4.12 ^{1}H NMR of complex **3** in THF-*d*$_6$ in different time intervals at room temperature. Crimson: t = 0 h; green: t = 20 h; blue: t = 96 h.

In Figure 4.12, room temperature ^{1}H NMR of **3** in THF-*d*$_6$ at t = 0 h shows broad peaks in the chemical shift range of –40 to 40 ppm, which is the characteristic of a paramagnetic Ru(III) complexe. Over hours, the intensity of the broad peaks decreases while new peaks emerge in the diamagnetic range of 0 to 14 ppm. After 96 h, no broad peaks corresponding to paramagnetic species were observed. The growth of a peak at 12.8 ppm can be assigned to the protons of the protonated imine of the bid ligand in **4**.

4.3. Conclusion

An isoindole-based Ru ammine complex, [Ru(bid)(bpy')NH_3][PF_6] (**2**), was prepared and its electrocatalytic activity was evaluated in the presence of NH_3 in THF. The cyclic voltammogram of **2** in THF containing 1 M of NH_4OTf as the supporting electrolyte shows one peak with the $E_{1/2}$ = 0.45 V (vs. Fc*). The addition of **2** to the NH_3-saturated THF solution shifted the anodic current of NH_3 oxidation to 0.32 V vs. Fc*. Chemical oxidation of **2** by tris(4-bromophenyl)amine radical cation yielded a paramagnetic Ru(III) complex (**3**), which upon addition of NH_3 regenerated the Ru(II) ammine complex (**2**). Analysis of the headspace gases of the electrochemical cell after bulk electrolysis of the NH_3-saturated THF solutions showed the release of N_2 gas as the anodic product.

In the absence of NH_3, the Ru(III) ammine complex (**3**) undergoes self–deprotonation, suggested by X-ray crystallography, NMR, and UV spectroscopy. Conducting bulk electrolysis experiments of 1 mM solutions of **2** in MeCN saturated with NH_3 resulted in the displacement of MeCN after one cycle of the electrocatalysis and confirmed by NMR spectroscopy.

4.4. Synthesis

4.4.1. General Synthesis

Hbid,[93,94] [Ru(bid)Cl$_3$][H$^+$],[95,96] and Ru(bid)(bpy')Cl[97] (**1**) were synthesized according to previously reported procedures.

4.4.2. Synthesis of [Ru(bid)(bpy')NH$_3$]PF$_6$, (complex 2)

A pressure tube was charged with **1** (1.015 g, 1.5589 mmol), a stir bar, and 50 mL of NH$_4$OH. The pressure tube was sealed and heated to 98 °C for 1 h under stirring. The tube was cooled to room temperature and opened to air. An H$_2$O-saturated solution of NH$_4$PF$_6$ was added to the solution to precipitate the PF$_6$ salt of **2**. Solids were collected and washed with ether to give blue-purple powder (970 mg, 83%).

^{1}H NMR (500 MHz, MeCN-d_3) δ 9.04 (d, 1H), 8.19 (dd, 2H), 8.05 (d, 1H), 7.76 (d, 1H), 7.74 – 7.67 (m, 4H), 7.63 – 7.57 (m, 2H), 7.55 (d, 1H), 7.54 – 7.50 (m, 2H), 7.03 (d, 1H), 6.56 (td, 2H), 6.48 (dd, 1H), 4.17 (s, 3H), 3.77 (s, 3H), 1.83 (s, 3H). Anal. Calcd for $C_{30}H_{27}F_6N_8O_2PRu.(Et_2O)_{1/2}$: C, 47.18; H, 3.96; N, 13.75. Found: C, 47.59; H, 3.68; N, 13.48.

4.4.3. Synthesis of [Ru(bid)(bpy')MeCN]PF$_6$

A solution of TlPF$_6$ (48 mg, 0.1381 mmol, 1.1 equiv) in 5 mL of MeCN was added to a solution of **1** (100 mg, 0.1256 mmol, 1 equiv) in 10 mL of MeCN under stirring. The mixture was heated to 50 °C for 1 h. During the reaction, the color changed from green-blue to red-purple. The solution was filtered over Celite to remove TlCl. MeCN was removed in vacuo and the solids were washed with water to remove any excess TlPF$_6$. The solids were dried under reduced pressure (97 mg, 96%). ^{1}H NMR (500 MHz, MeCN-d_3) δ 9.30 (d, 1H), 8.17 – 8.10 (m, 2H), 8.06 (d, 1H), 7.76 (d, 1H), 7.73 – 7.66 (m, 2H), 7.65 – 7.57 (m, 4H), 7.56 – 7.48 (m, 3H), 7.19 (d, 1H), 6.61 (m, 2H), 6.53 (dd, 1H), 4.17 (s, 3H), 3.77 (s, 3H), 2.06 (s, 3H).

Chapter 5. DINUCLEAR RUTHENIUM BIS(AMMINE) COMPLEXES FOR INTRAMOLECULAR N–N COUPLING

5.1. Introduction

Intramolecular N-N coupling of coordinated NH_3 ligands in a dimeric Ru complex containing a Ru-O-Ru motif has been reported by Meyer and co-workers.[84,85] Electrochemical oxidation of a 1:1 mixture of ^{15}N labeled and unlabeled *cis*,*cis*-$[(bpy)_2(H_3N)Ru^{III}ORu^{III}(NH_3)(bpy)_2]^{4+}$ in aqueous solution resulted in the formation of $^{15}N_2$ and $^{14}N_2$ in equimolar ratios; this result establishes that intramolecular dinitrogen formation is the sole pathway for this system.[85]

Scheme 5.1 Intramolecular N–N coupling by *cis*,*cis*-$[(bpy)_2(H_3N)Ru^{III}ORu^{III}(NH_3)(bpy)_2]^{4+}$

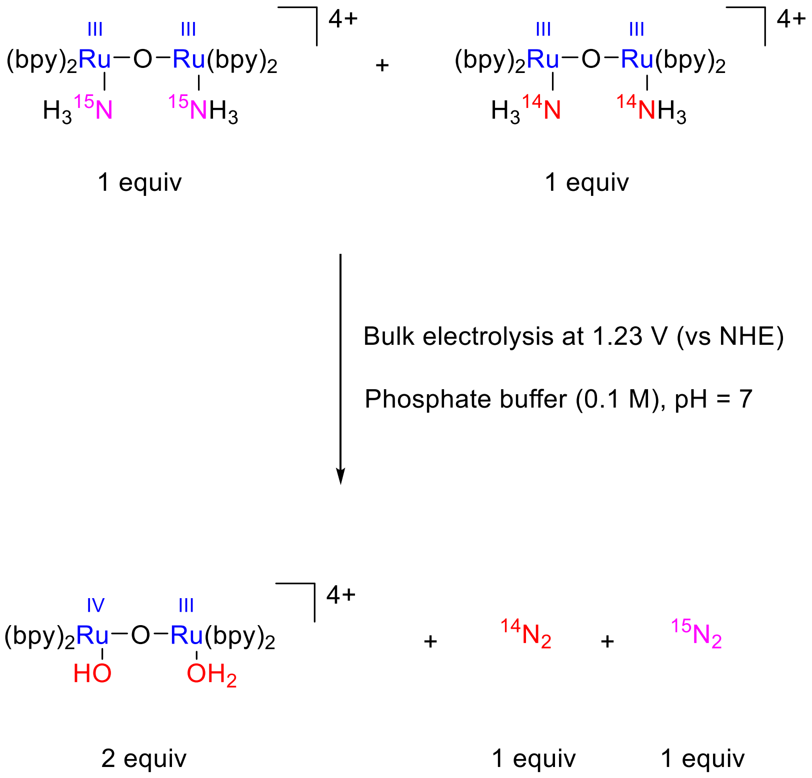

Although this experiment suggests the intramolecular N–N coupling of NH_3 ligand, it should be noted that there was no free NH_3 in the solution to assess the possibility of N–N coupling of free NH_3 and bound ammine.

We have begun investigating the possible electrocatalytic behavior of *cis*,*cis*-$[(bpy)_2(H_3N)Ru^{III}ORu^{III}(NH_3)(bpy)_2]^{4+}$ toward NH_3 oxidation in nonaqueous solvents saturated with NH_3. Preliminary results indicate that *cis*,*cis*-$[(bpy)_2(H_3N)Ru^{III}ORu^{III}(NH_3)(bpy)_2]^{4+}$ does not show any catalytic behavior, which we attribute to the presence of a fragile μ-oxo bridge prone to fragmentation. Instability of the reduced *cis*,*cis*-$[(bpy)_2(H_3N)Ru^{III}ORu^{III}(NH_3)(bpy)_2]^{4+}$ toward loss of the μ-oxo bridge is already established.[100] Taking these challenges into account, we focused on the synthesis of dimeric Ru systems bearing more rigid bridging ligands with high stability toward oxidation and reduction. Thus, starting from previously reported μ-chloro dinuclear ruthenium complex $[Ru_2^{II}(\mu\text{-Cl})(bpp)(trpy)_2]^{2+}$,[101] bpp: bis(2-pyridyl)-3,5-pyrazolate, we synthesized $[Ru_2^{II}(NH_3)_2(bpp)(trpy)_2]^{3+}$ in which the chloride bridge is displaced by NH_3 ligands.

In $[Ru_2^{II}(NH_3)_2(bpp)(trpy)_2]^{3+}$, the Ru centers are held in close proximity by the bpp bridging ligand, which in turn orients the ammine ligands toward each other to allow a facile intramolecular coupling. Also, the oxidation state of the Ru centers is +2 which in Meyer's complex is +3.

Scheme 5.2 Structure of $[Ru_2^{II}(NH_3)_2(bpp)(trpy)_2][PF_6]_3$ (**3**)

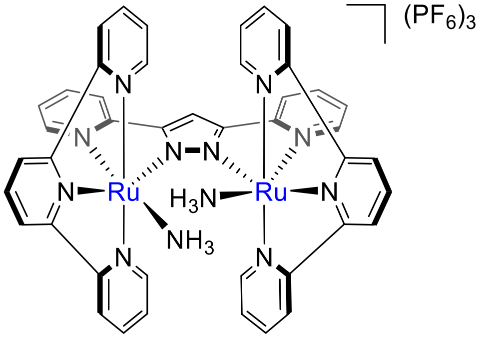

5.2. Results and Discussion

Heating a solution of μ-chloro dinuclear ruthenium complex $[Ru_2^{II}(\mu\text{-}Cl)(bpp)(trpy)_2]^{2+}$ (**1**),[101] bpp: bis(2-pyridyl)-3,5-pyrazolate, in methanol saturated with NH_3 in pressure tube at 70 °C for 30 min yields mono(ammine) complex $[Ru^{II}NH_3Ru^{II}Cl(bpp)(trpy)_2]^{2+}$ (**2**). Abstraction of chloride by $AgNO_3$ in water with 0.1 M Na_3PO_4 buffer and excess $(NH_4)_2SO_4$ yields $[Ru_2^{II}(NH_3)_2(bpp)(trpy)_2]^{3+}$ (**3**) in 36% isolated yield. The Ru centers are held in close proximity by the bpp bridging ligand, which in turn orients the ammine ligands toward each other to allow a facile intramolecular coupling. CV of **3** in MeCN shows two major anodic peaks at 0.28 and 0.59 V vs. $Ag/AgNO_3$, which can tentatively be assigned to the Ru^{II}/Ru^{III} couples of the two Ru centers, and one small peak at 0.76 vs. $Ag/AgNO_3$, which was not observed in 1,2–difluorobenzene (DFB) solvent.

Scheme 5.3 Synthesis of Ru dinuclear mono and bis(ammine) complexes

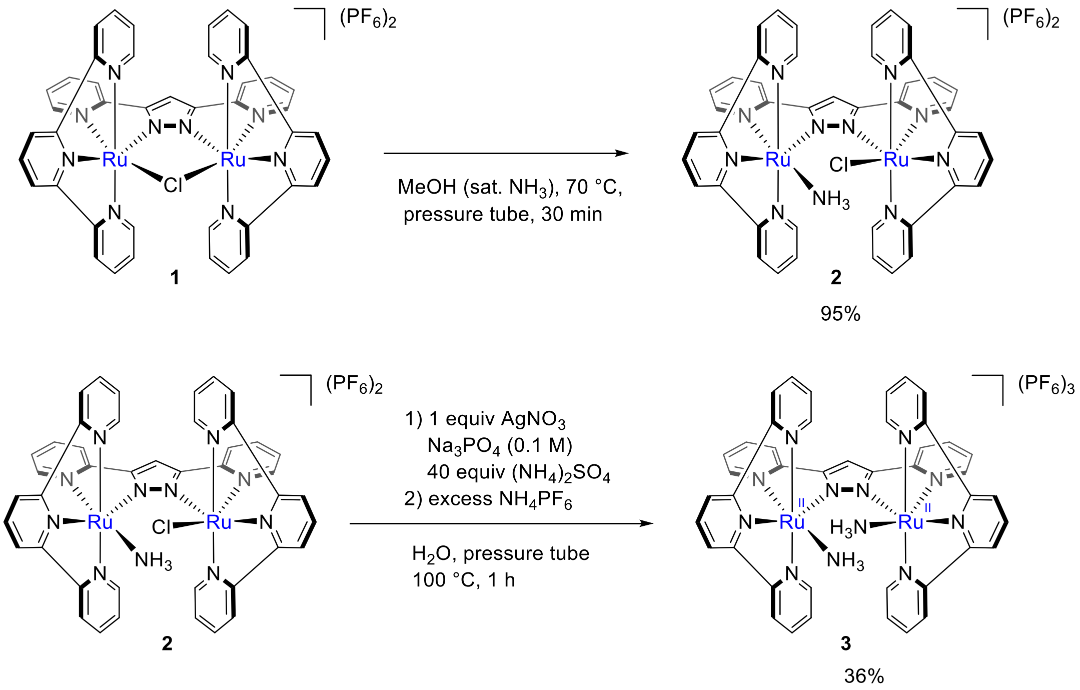

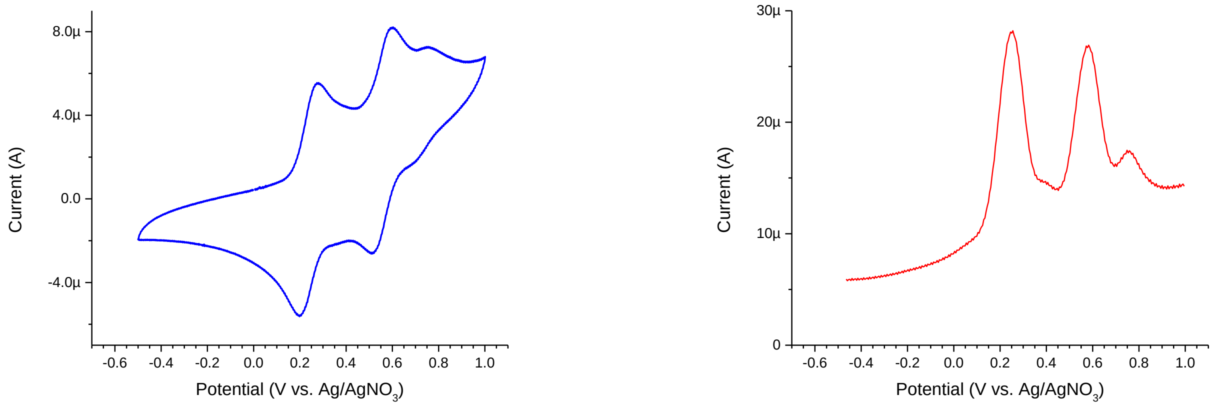

Figure 5.1 Left: CV of **3** in MeCN containing 0.1 M TBAPF$_6$ as supporting electrolyte Right: corresponding SQW taken instantly after CV. WE: GC, CE: Pt mesh, RE: Ag/AgNO$_3$, scan rate: 10 mV/s

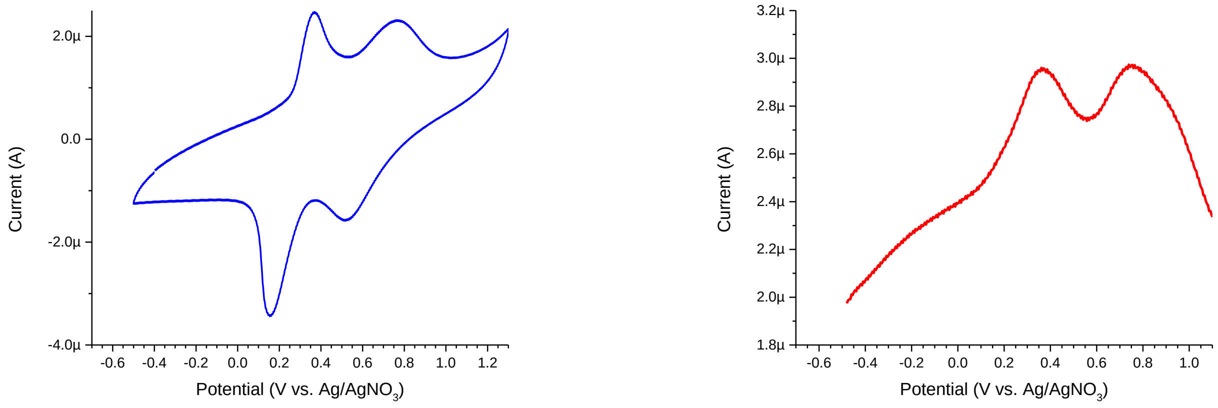

Figure 5.2 Left: CV of **3** in 1,2–difluorobenzene containing 0.1 M TBAPF$_6$ as supporting electrolyte Right: corresponding SQW taken instantly after CV. WE: GC, CE: Pt mesh, RE: Ag/AgNO$_3$, scan rate: 10 mV/s

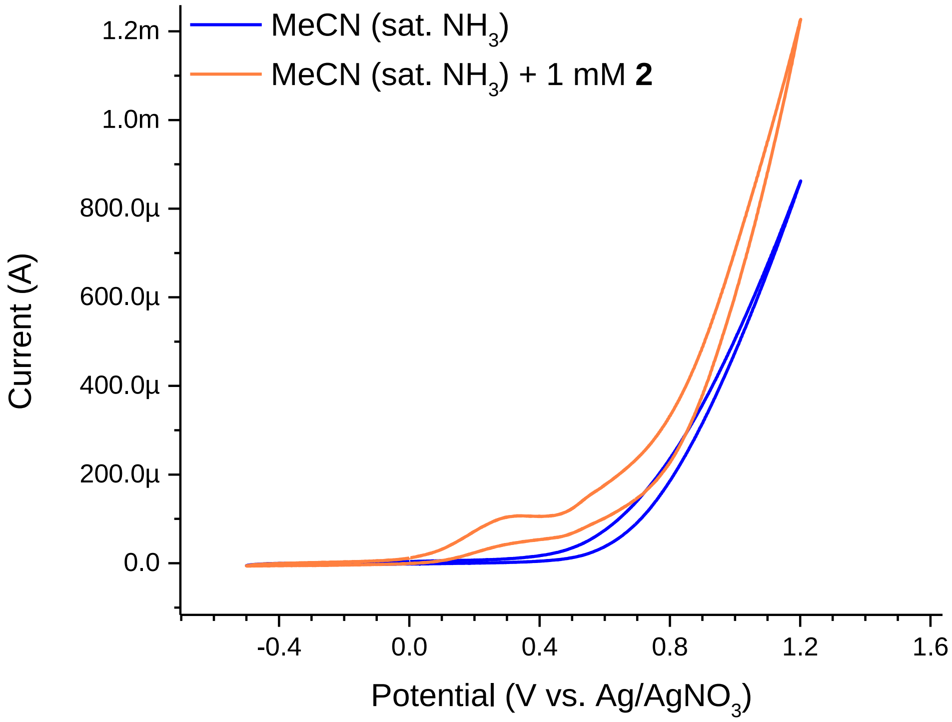

Figure 5.3 Blue: CV of MeCN saturated with NH_3. Orange: CV of MeCN saturated with NH_3 after the addition of 1 mM of **3**. WE: GC, CE: Pt mesh, RE: $Ag/AgNO_3$, scan rate: 100 mV/s, 0.1 M $TBAPF_6$ as supporting electrolyte

Figure 5.3 shows the CV of MeCN saturated with NH_3 (blue trace). 1 mM **3** was added right after taking the CV of the blank. A catalytic current was observed at the potential of 0.07 V vs. $Ag/AgNO_3$ and the onset of NH_3 oxidation was shifted by 440 mV to less anodic potentials. The onset potential of the catalytic plateau suggests that catalysis starts with the oxidation of the first Ru center. Presumably, upon oxidation of Ru(II) to Ru(III), excess NH_3 deprotonates the ammine ligand. One possible mechanism might be the disproportionation of Ru(III) amido to Ru(II) ammine and Ru(IV) imido followed by either intramolecular or intermolecular N–N coupling.

Scheme 5.4 Intermolecular vs. intramolecular N–N coupling

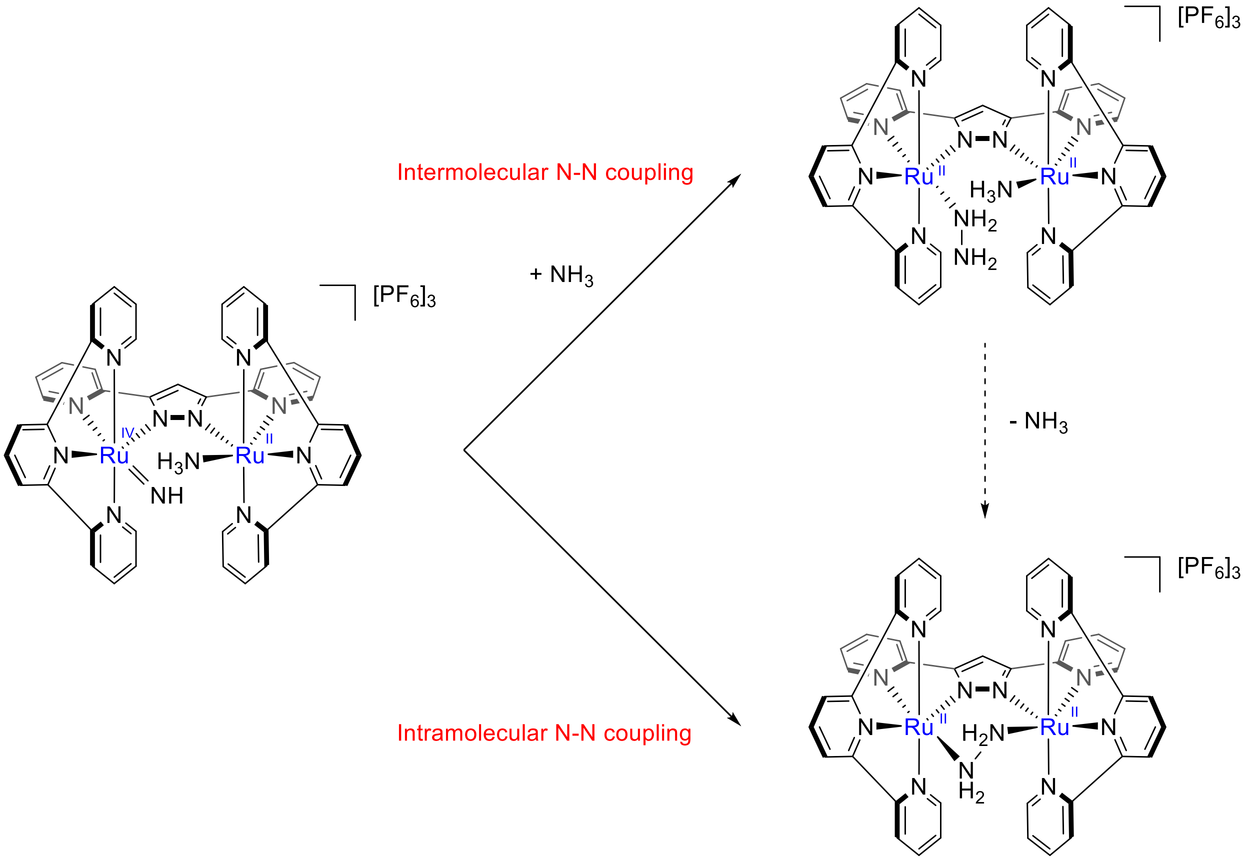

In the case of intramolecular N–N coupling, **3** can be envisioned as one of the intermediates en route to N_2 formation. The possibility of the formation of the hydrogen-bridged dinuclear Ru complex was examined by attempting to synthesize it independently. In fact $[Ru_2^{II}(\mu\text{-}N_2H_4)(bpp)(trpy)_2]^{3+}$ (**4**) was synthesized by stirring **1** in 98% hydrazine at room temperature, followed by addition of a hydrazine solution to a saturated aqueous solution of NH_4PF_6 to precipitate the product (Scheme 5.5).

The ^1H NMR spectrum of **4** shows a singlet resonance for protons of bridged hydrazine at 5.74 ppm in $(CD_3)_2CO$ and 4.37 ppm in MeCN-d_3

Scheme 5.5 Synthesis of dinuclear Ru hydrazine complex

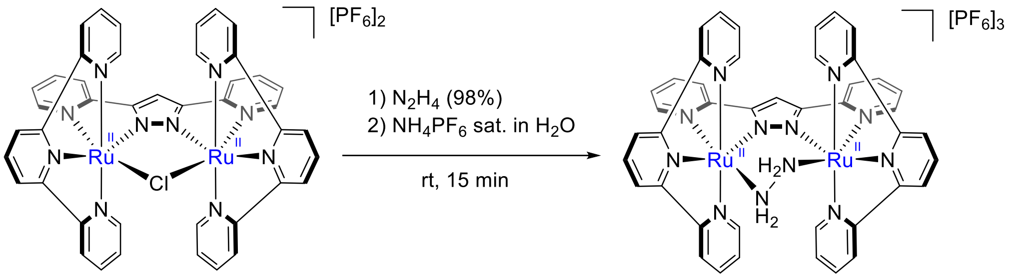

75%

1

4

Hydrazine-bridged dinuclear Ru complexes have been reported previously. In 1992, Collman and co-workers reported the NH_3 oxidation by a bis(ammine) cofacial dinuclear Ru diporphyrin complex.[102] Oxidation of this complex yielded intramolecular N–N bond formation and ultimately a bridged dinitrogen complex through bridged hydrazine and diazene intermediates.

Complex **3** was chemically oxidized by tris(4-bromophenyl)amine radical cation to yield complex **3b** (Scheme 5.6). Relatively sharp peaks in the ^1H NMR spectrum of **3b** in a wide chemical shift range (–60 to 40 ppm) are indicative of the electronic coupling of two Ru(III) centers through the bpp bridging ligand. This ^1H NMR spectrum pattern has also been observed on previously reported *cis,cis*–$[(bpy)_2(NH_3)Ru^{III}ORu^{III}(NH_3)(bpy)_2]^{4+}$ complex.[103]

The addition of NH_3 or a hindered base like 2,6–dimethylpyridine to the acetonitrile solution of **3b** regenerates complex **3** (Scheme 5.6) along with the disappearance of all paramagnetic peaks. A new set of peaks in the diamagnetic region also appears in the ^1H NMR spectrum, which can be correlated to the other product(s) of the reaction. More experiments including $^{15}NH_3$ isotope labeling can be envisioned for the characterization of the possible intermediates en route to intramolecular N–N coupling of catalytic NH_3 oxidation.

Scheme 5.6 Chemical oxidation of Ru dimer bis(ammine) **3**

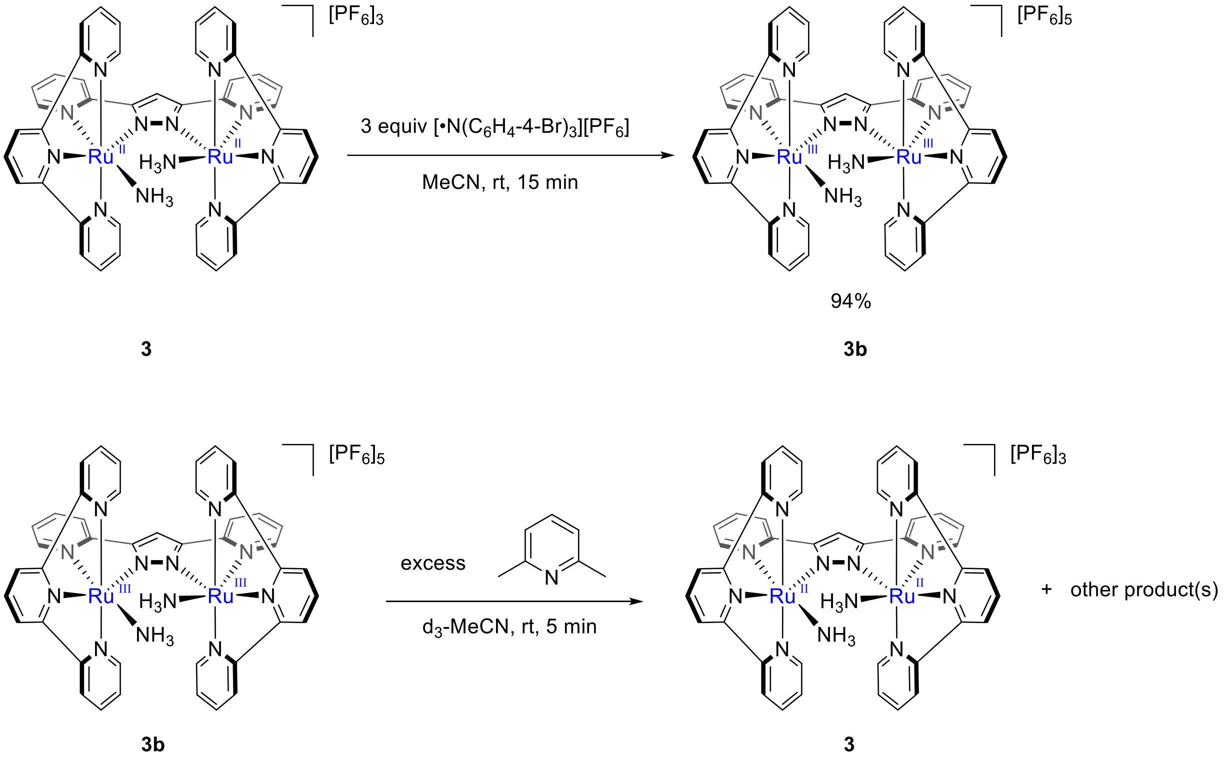

Finally, introducing electron-donating groups on the polypyridyl ligands can shift the oxidation potential of the Ru(II) centers to more cathodic potentials, reducing the overpotential of the NH_3 oxidation. In addition, the possibility of the AO by heteronuclear bis(ammine) complexes can be examined with this system. For example, displacing one of the Ru centers with Fe may provide versatile information about the effect of Fe on the potential and mechanism of N–N formation in the case of catalysis.

5.3. Conclusion

For investigating the intramolecular N–N coupling for catalytic AO, a dinuclear Ru bis(ammine) complex (**3**) was synthesized in which two NH_3 ligands are in close proximity. CV of the **3** in MeCN in the absence of NH_3 shows two major peaks assigned to the oxidation of Ru(II) centers to Ru(III). A catalytic current was observed when 1 mM of **3** was added to the MeCN solution saturated with NH_3. Hydrazine–bridged analogous complex **4** which may be considered as one of the possible intermediates in AO was also prepared and characterized. The bis(ammine) complex **3** was chemically oxidized as well. The addition of NH_3 or a hindered base to the oxidized species (**3b**) regenerated the diamagnetic dinuclear Ru(II) bis(ammine) **3**.

5.4. Synthesis

5.4.1. General Synthesis

Hbpp, and $[Ru_2^{II}(\mu\text{-Cl})(bpp)(trpy)_2]^{2+}$ (**1**) were synthesized according to previously reported procedures.[101]

5.4.2. Synthesis of $[Ru_2^{II}(NH_3)Cl(bpp)(trpy)_2][PF_6]_2$ (2)

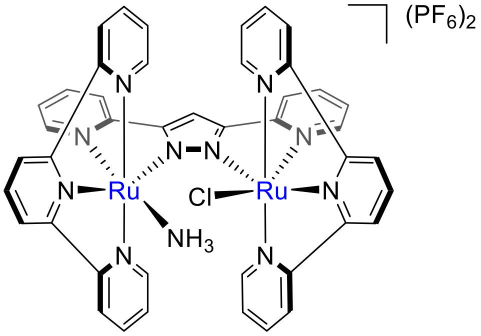

Inside a glove bag filled with N_2, a pressure tube was charged with **1** (450 mg, 0.370 mmol), 50 mL dry and degassed MeOH saturated with NH_3, and a stir bar. After sealing, the pressure tube was taken out and heated for 30 min at 70 °C with stirring. After cooling to room temperature, the pressure tube was opened to air, and N_2 was bubbled into the solution to remove the dissolved NH_3. MeOH was removed on the rotovap to yield brown-purple solids. The solids were washed with Et_2O and dried under vacuum (433 mg, 95%). ^1H NMR (500 MHz, acetone-d_6) δ 8.68 (dd, J = 8.1, 7.4 Hz, 4H), 8.58 (ddt, J = 14.8, 8.1, 1.1 Hz, 4H), 8.45 (s, 1H), 8.40 (ddd, J = 5.5, 1.6, 0.7 Hz, 2H), 8.29 (ddd, J = 5.4, 1.5, 0.7 Hz, 2H), 8.20 – 8.09 (m, 4H), 7.99 (tdd, J = 7.9, 2.7, 1.5 Hz, 4H), 7.76 (dtd, J = 12.8, 7.7, 1.4 Hz, 2H), 7.43 (ddd, J = 7.6, 5.5, 1.3 Hz, 2H), 7.37 (ddd, J = 7.6, 5.5, 1.3 Hz, 2H), 7.34 (dt, J = 5.7, 1.2 Hz, 1H), 7.26 (dt, J = 5.6, 1.2 Hz, 1H), 6.94 (ddd, J = 7.3, 5.7, 1.4 Hz, 1H), 6.90 (ddd, J = 7.4, 5.8, 1.4 Hz, 1H), 3.06 (s, 3H).

5.4.3. Synthesis of $[Ru_2^{II}(NH_3)_2(bpp)(trpy)_2][PF_6]_3$ (3)

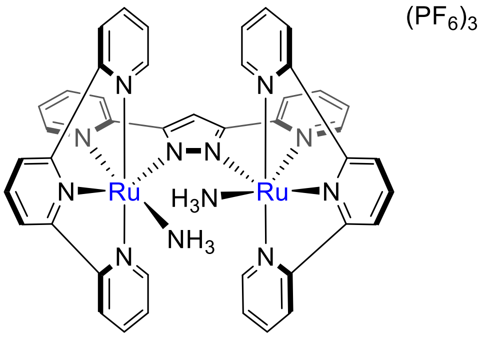

Inside a glove bag filled with N_2, a pressure tube was charged with **2** (1 equiv, 400 mg, 0.324 mmol), 50 mL degassed 0.1 M Na_3PO_4, $AgNO_3$ (1 equiv, 55 mg, 0.324 mmol), $(NH_4)_2SO_4$ (40 equiv, 1.71 g, 12.98 mmol), and a stir bar. After sealing, the pressure tube was taken out, and the suspension was stirred at 100 °C for 1 h. After cooling to room temperature, the pressure tube was opened to air, and the solution was filtered through Celite to remove AgCl. Excess NH_4PF_6 was added to precipitate the solids to yield a mixture of **3** and $[Ru(trpy)_2][PF_6]_2$ as by-product, which can be separated based on the insolubility of **3** and solubility of $[Ru(trpy)_2][PF_6]_2$ in CH_2Cl_2. **3** can be further purified by crystallization with slow diffusion of Et_2O into acetone solution (158 mg, 36%). ^{1}H NMR (500 MHz, acetone-d_6) δ 8.75 (d, J = 8.1 Hz, 4H), 8.64 (d, J = 8.1 Hz, 4H), 8.53 (s, 1H), 8.33 (d, J = 5.1 Hz, 4H), 8.26 (t, J = 8.1 Hz, 2H), 8.19 (d, J = 8.0 Hz, 2H), 8.06 (td, J = 7.9, 1.5 Hz, 4H), 7.84 (td, J = 7.8, 1.5 Hz, 2H), 7.48 (ddd, J = 7.4, 5.7, 1.3 Hz, 4H), 7.38 (d, J = 5.7 Hz, 2H), 6.97 (ddd, J = 7.3, 5.7, 1.4 Hz, 2H), 2.84 (s, 6H). ^{13}C NMR (126 MHz, acetone-d_6) δ 160.83, 160.54, 156.17, 156.14, 154.33, 151.05, 138.74, 137.59, 135.79, 129.43, 125.21, 124.00, 123.91, 121.09, 105.59.

5.4.4. Synthesis of $[Ru_2^{II}(\mu\text{-}N_2H_4)(bpp)(trpy)_2][PF_6]_3$ (4)

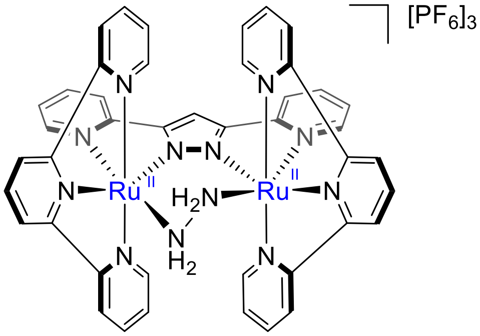

1 (350 mg, 0.288 mmol) was stirred in 15 mL of 98% hydrazine at room temperature for 15 min. The solution was poured into the 40 mL of water saturated with NH_4PF_6 to precipitate the product as brown solids, which were collected, washed with Et_2O, and dried under reduced pressure (293 mg, 75%) ^1H NMR (500 MHz, acetone-*d*$_6$) δ 8.69 (d, J = 8.1 Hz, 4H), 8.59 (s, 1H), 8.58–8.53 (m, 8H), 8.30 (d, J = 8.0 Hz, 2H), 8.21 (t, J = 8.1 Hz, 2H), 8.05 (t, J = 7.9 Hz, 4H), 7.85 (t, J = 7.8 Hz, 2H), 7.64 (t, J = 6.6 Hz, 4H), 7.32 (d, J = 5.7 Hz, 2H), 6.90 (t, J = 6.7 Hz, 2H), 5.74 (s, 4H).

Chapter 6. SUMMARY AND FUTURE DIRECTIONS

The initial work in ammonia oxidation by molecular systems began with synthesizing Fe ammine coordination complexes, examining their electrochemistry, and evaluating them as electrocatalysts for NH_3 oxidation. We began with the preparation of a low-spin Fe tris(ammine) complex, supported by a tripodal phosphine ligand. Cyclic voltammograms (CVs) for anodic scans of NH_3-saturated THF solutions when the Fe complex is present and absent were taken. When the Fe complex was present, a catalytic current was observed, and further bulk electrolysis experiments revealed the production of N_2 at the anode electrode. Moving toward the more accessible and stable iron complexes, Fe phthalocyanine complexes may be considered good candidates for this purpose. The preliminary results of CVs in THF saturated with NH_3 (3.24 M) utilizing a boron-doped diamond (BDD) as the working electrode showed a catalytic onset in the presence of 1 mM of Fe phthalocyanine (Figure 6.1).

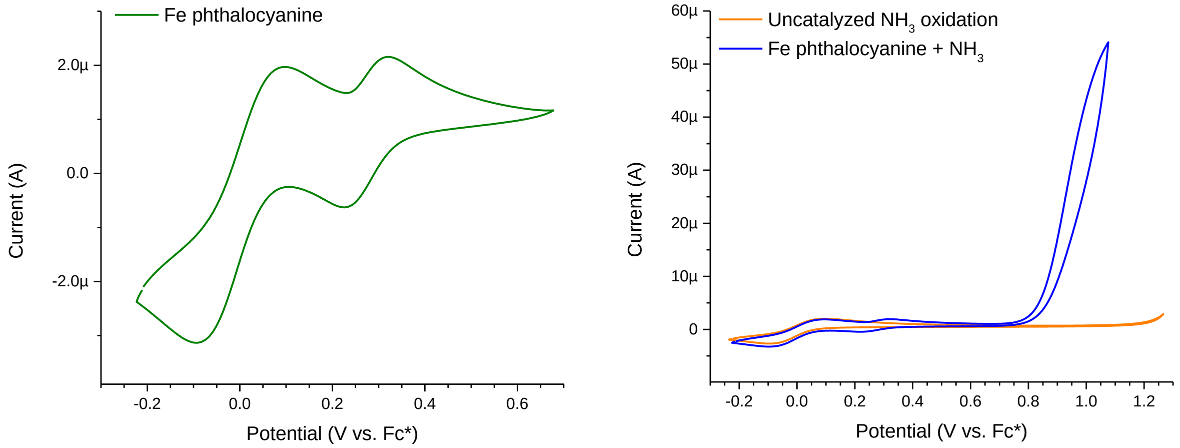

Figure 6.1 Left: CV of 1mM of Fe phthalocyanine in THF in the presence of Fc* as internal standard shows a peak with $E_{1/2}$ of 0.27 V (vs. Fc*). Right: CV of 1mM of Fe phthalocyanine in THF saturated with NH_3 (3.24 M) in the presence of Fc* as internal standard shows a catalytic current with the onset of 0.79 V (vs. Fc*). WE: BDD, CE: Pt disk, 2 M NH_4OTf as supporting electrode, scan rate: 100 mV/s

Iron(II) phthalocyanine bis(ammine) complexes have already been synthesized and their oxidation chemistry has been reported in the literature.[104–108] By introducing an axial ligand the oxidation potential of catalysis can be tuned; also, by anchoring groups the complex can be immobilized on the surface of the electrode for heterogeneous electrochemical NH_3 oxidation (Scheme 6.1).[109] Furthermore, the synthesis of phthalocyanines through the cyclotetramerization of various phthalic acid derivatives are well established and thus can be utilized to prepare various ligands with different binding affinities and specificities.[110]

Scheme 6.1 Fe phthalocyanines as candidates for the electrochemical NH_3 oxidation

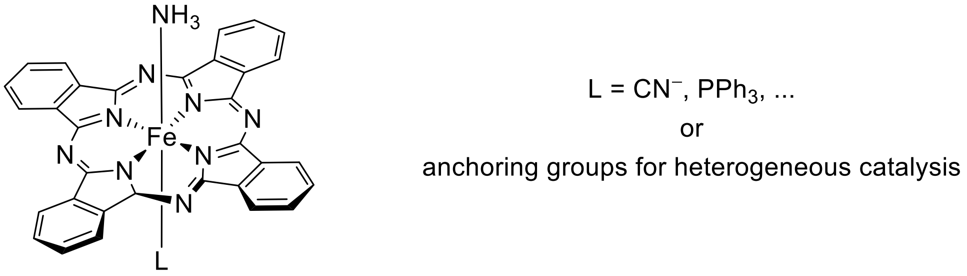

In chapter 4, an isoindole-based Ru ammine complex was prepared. Its electrocatalytic activity was evaluated in the presence of NH_3 in THF which shifted the anodic current of NH_3 oxidation to 0.32 V vs. Fc*. For shifting the potential to more cathodic values, more electron donor substituent groups e.g., NMe_2, can be put on both bpy and bid ligands (Scheme 6.2).

Also, variant temperature NMR studies with ^{15}N labeled Ru ammine complexes may reveal more details on the mechanism of the catalysis by characterizing the possible intermediates.

Scheme 6.2 More electron donor substituent groups on ligands

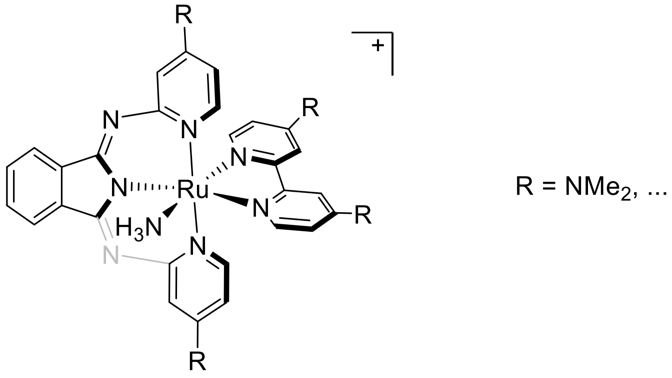

In chapter 5, the synthesis of a dinuclear Ru bis(ammine) complex was described. Non-catalytic intramolecular N–N coupling by an oxo-bridged dinuclear Ru bis(ammine) complex has been reported by Meyer and co-workers.[84,85] Unlike the oxo-bridged Ru dimers, the rigid pyrazole-based bridging ligand is not prone to fragmentation.[100] The cyclic voltammogram of an acetonitrile solution of this complex shows two quasi-reversible peaks which can be attributed to sequential oxidations of the Ru(II) centers to Ru(III). CVs of an NH_3-saturated, 1 mM solution of the complex in acetonitrile exhibit an electrocatalytic current at a potential that is ~300 mV lower than the onset of oxidation of an NH_3-saturated acetonitrile solution at the glassy carbon anode. This is the first example of a dinuclear Ru bis(ammine) complex capable of catalytic NH_3 oxidation.

To make Ru centers more electron efficient and therefore shift the oxidation potential of the catalyst to less anodic potentials, both trpy and Hbpp ligands were functionalized by NMe_2 groups. Scheme 6.3 summarizes the multistep synthesis of the NMe_2 functionalized Hbpp ligand. In addition to the substitution of pyridyls by NMe_2 groups, the 1,3-diketone can also be functionalized by anchoring groups for heterogeneous catalysis before the last step of the reaction. Figure 6.2 compares the ^{1}H NMR of Hbpp and NMe_2-substituted Hbpp bridging ligands in DMSO-d_6.

Scheme 6.3 Synthesis of the bridging ligand with more electron donor groups

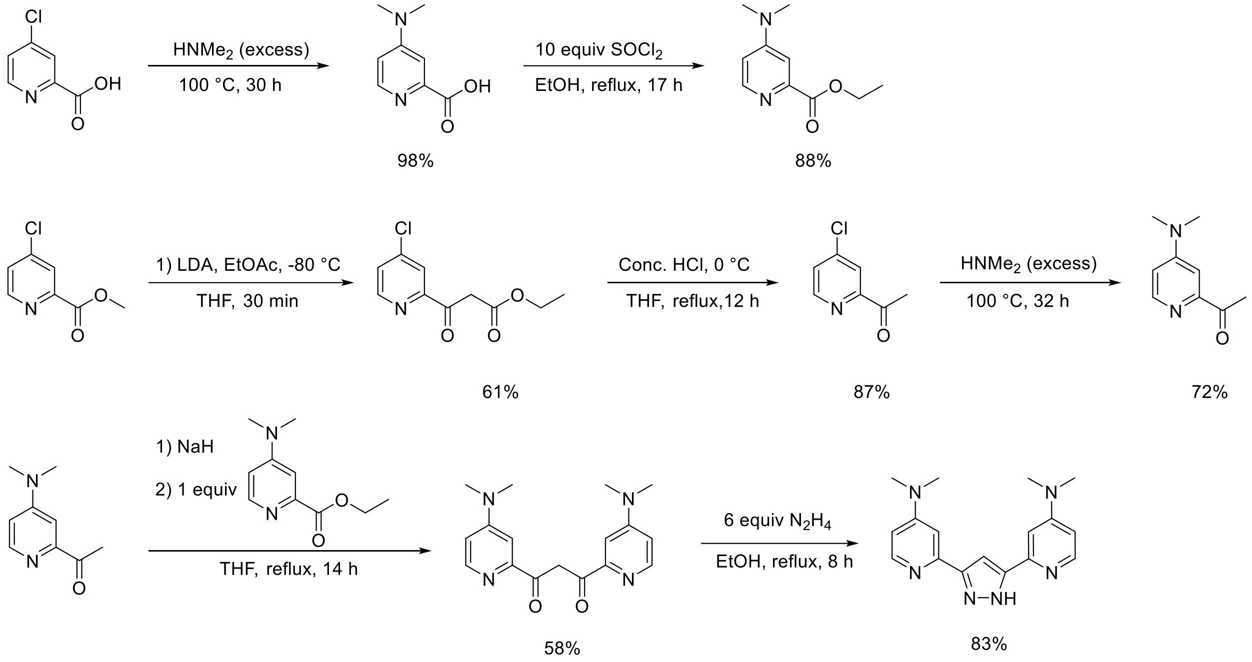

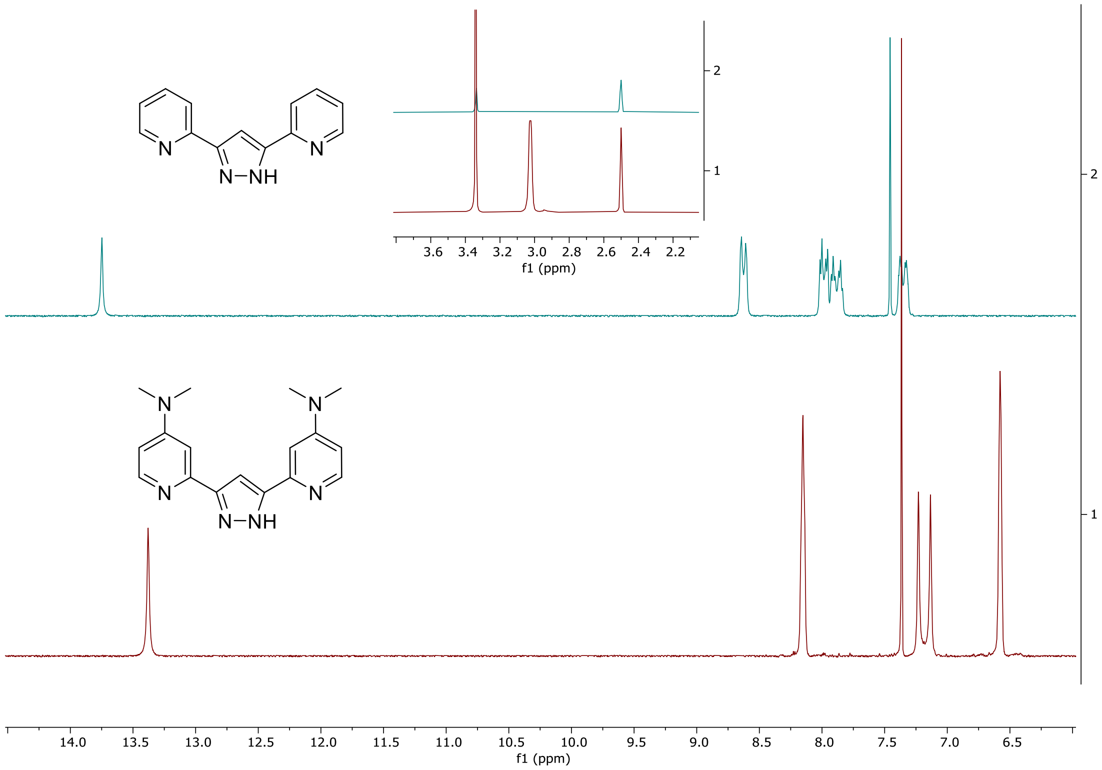

Figure 6.2 ^{1}H NMR of Hbpp (green) and NMe$_2$-substituted Hbpp (red) in DMSO-d_6

The NMe_2-Hbpp bridging ligand was used to synthesize the corresponding Cl-bridged dinuclear Ru complex (Scheme 6.4). The solubility of this complex compared to its unsubstituted counterpart is much lower in most of the organic solvents.

Scheme 6.4 Synthesis of the Cl-bridged dinuclear Ru complex supported by NMe_2-bpp

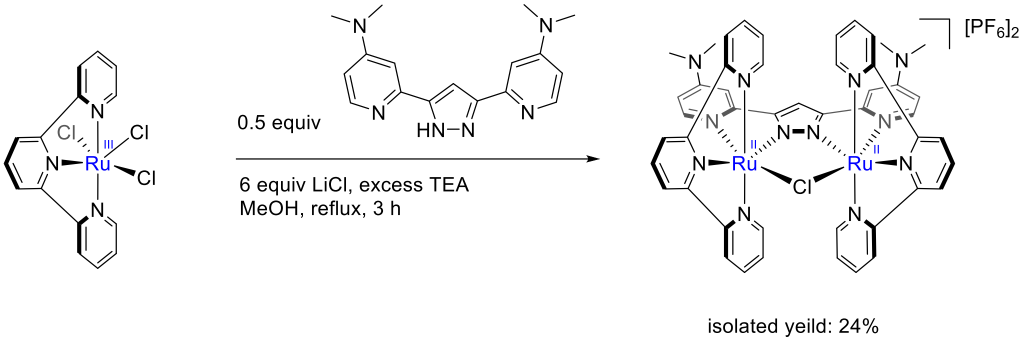

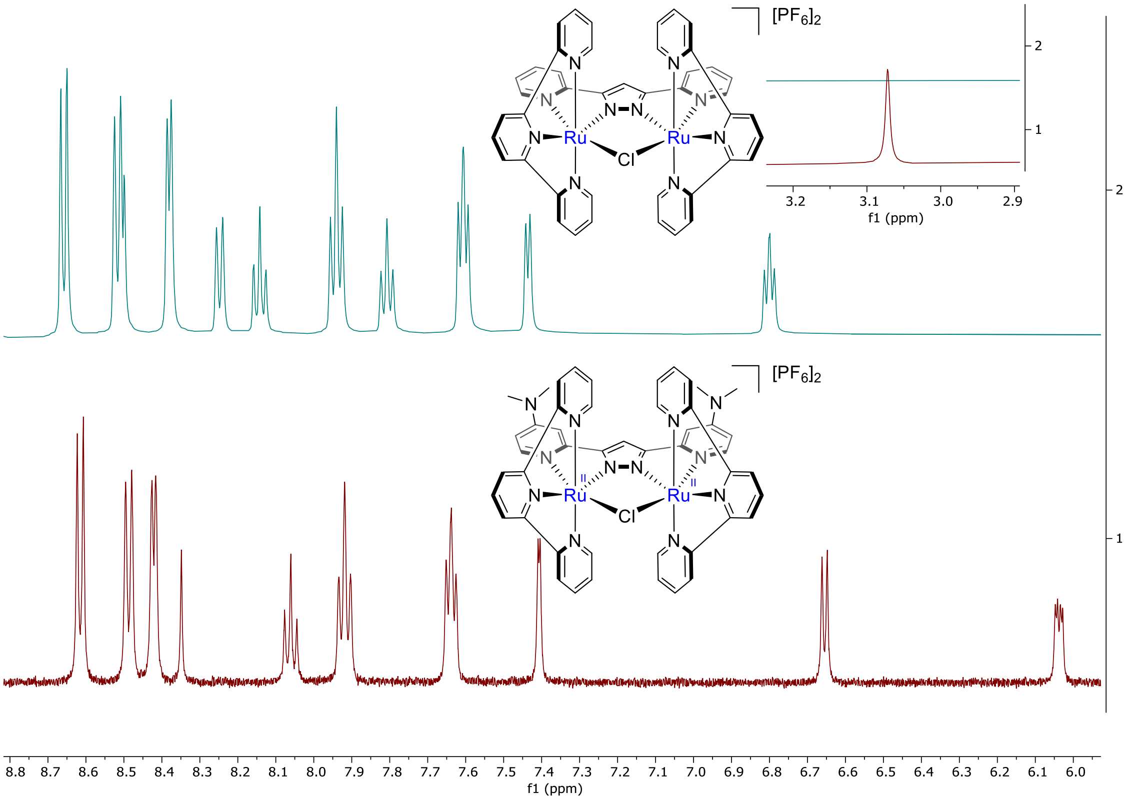

Figure 6.3 Comparison of ^{1}H NMR of bpp and NMe_2-bpp bridged Ru dimers in acetone-d_6

NMe_2-substituted terpyridine tridentate ligand was also synthesized according to Scheme 6.5.

Scheme 6.5 Synthesis of NMe_2-substituted trpy ligand

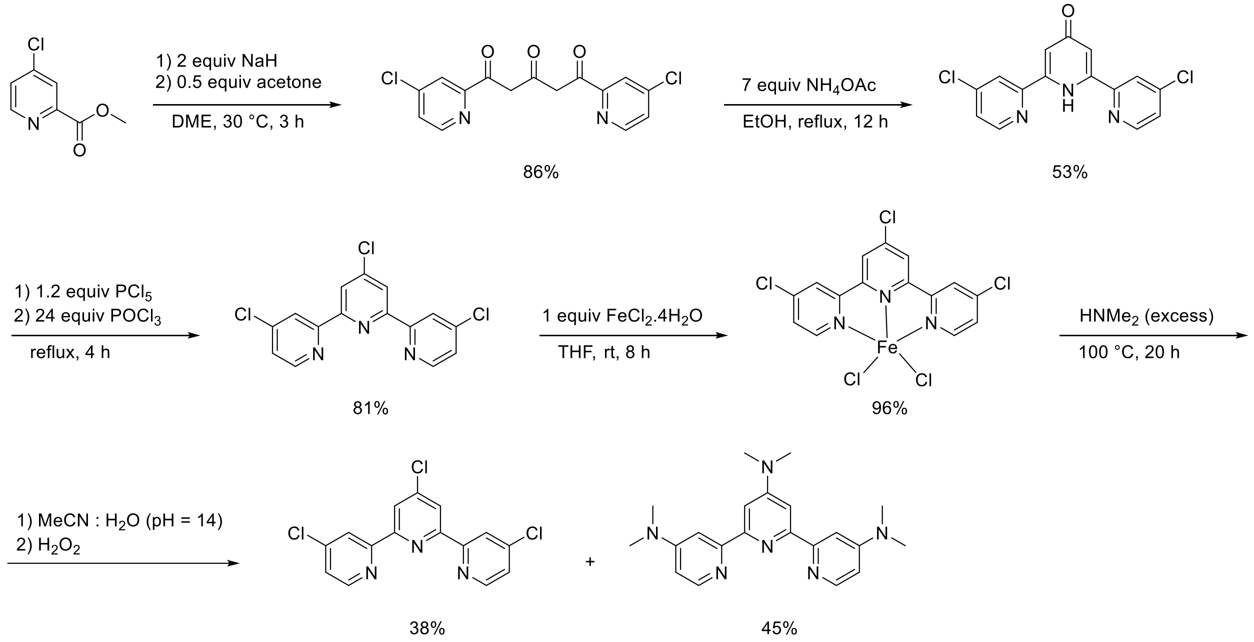

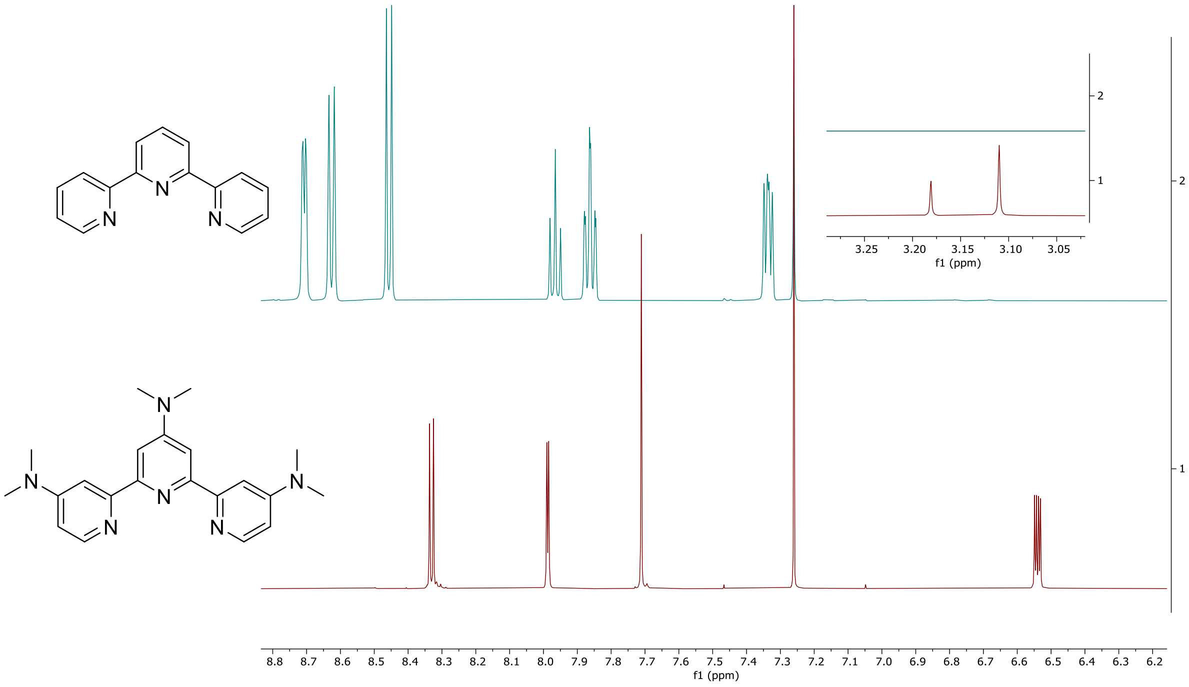

Figure 6.4 ^1H NMR of trpy and NMe_2-substituted trpy in $CDCl_3$

Synthesis of the dinuclear Ru bis(ammine) complexes with bid ligand can also be envisioned. The two bid ligands will reduce the overall charge of the complex by 2 and thus can lower the oxidation potential of the complex to much lower potentials (Scheme 6.6).

Scheme 6.6 Dinuclear Ru bis(ammine) complexes supported by bid ligands

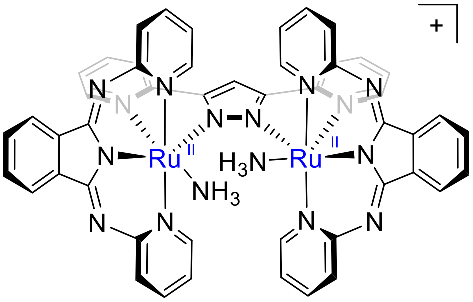

Last but not least, a wide range of heterodinuclear bis(ammine) complexes can be prepared via these systems to investigate the synergistic effects of various metals on catalytic NH_3 oxidation.

REFERENCES

(1) Diffenbaugh, N. S.; Field, C. B. Changes in Ecologically Critical Terrestrial Climate Conditions. *Science* **2013**, *341*, 486–492.

(2) BP Statistical Review of World Energy_70th Edition https://www.bp.com/content/dam/bp/business-sites/en/global/corporate/pdfs/energy-economics/statistical-review/bp-stats-review-2021-full-report.pdf (accessed May 25, 2022).

(3) Carbon Dioxide Information Analysis Center (CDIAC) Database https://cdiac.ess-dive.lbl.gov/trends/emis/meth_reg.html (accessed May 25, 2022).

(4) Fawcett, A. A.; Iyer, G. C.; Clarke, L. E.; Edmonds, J. A.; Hultman, N. E.; McJeon, H. C.; Rogelj, J.; Schuler, R.; Alsalam, J.; Asrar, G. R.; Creason, J.; Jeong, M.; McFarland, J.; Mundra, A.; Shi, W. CLIMATE POLICY. Can Paris Pledges Avert Severe Climate Change? *Science* **2015**, *350*, 1168–1169.

(5) Jacobson, M. Z.; Colella, W. G.; Golden, D. M. Cleaning the Air and Improving Health with Hydrogen Fuel-Cell Vehicles. *Science* **2005**, *308*, 1901–1905.

(6) Turner, J. A. Sustainable Hydrogen Production. *Science* **2004**, *305*, 972–974.

(7) Sherif, S. A.; Barbir, F.; Veziroglu, T. N. Principles of Hydrogen Energy Production, Storage and Utilization. *Journal of Scientific & Industrial Research* **2003**, *62*, 46–63.

(8) Satyapal, S.; Petrovic, J.; Read, C.; Thomas, G.; Ordaz, G. The U.S. Department of Energy's National Hydrogen Storage Project: Progress towards Meeting Hydrogen-Powered Vehicle Requirements. *Catal. Today* **2007**, *120*, 246–256.

(9) Wang, L.; Xia, M.; Wang, H.; Huang, K.; Qian, C.; Maravelias, C. T.; Ozin, G. A. Greening Ammonia toward the Solar Ammonia Refinery. *Joule* **2018**, *2*, 1055–1074.

(10) Li, J.; Lai, S.; Chen, D.; Wu, R.; Kobayashi, N.; Deng, L.; Huang, H. A Review on Combustion Characteristics of Ammonia as a Carbon-Free Fuel. *Frontiers in Energy Research* **2021**, *9*.

(11) Boretti, A.; Castelletto, S. NH_3 Prospects in Combustion Engines and Fuel Cells for Commercial Aviation by 2030. *ACS Energy Lett.* **2022**, *7*, 2557–2564.

(12) Kobayashi, H.; Hayakawa, A.; Somarathne, K. D. K. A.; Okafor, E. C. Science and Technology of Ammonia Combustion. *Proc. Combust. Inst.* **2019**, *37*, 109–133.

(13) Woo, Y.; Jang, J. Y.; Lee, Y. J.; Kim, J.-N. Recent Progress on the Ammonia-Gasoline and the Ammonia-Diesel Dual Fueled Internal Combustion Engines in Korea. *11th NH_3 FUEL CONFERENCE* **2014**.

(14) Lan, R.; Tao, S. Ammonia as a Suitable Fuel for Fuel Cells. *Front. Energy Res.* **2014**, *2*, 1–4.

(15) Afif, A.; Radenahmad, N.; Cheok, Q.; Shams, S.; Kim, J. H.; Azad, A. K. Ammonia-Fed Fuel Cells: A Comprehensive Review. *Renewable Sustainable Energy Rev.* **2016**, *60*, 822–835.

(16) Boggs, B. K.; Botte, G. G. On-Board Hydrogen Storage and Production: An Application of Ammonia Electrolysis. *J. Power Sources* **2009**, *192*, 573–581.

(17) Li, G.; Kanezashi, M.; Tsuru, T. Catalytic Ammonia Decomposition over High-Performance Ru/Graphene Nanocomposites for Efficient CO_x-Free Hydrogen Production. *Catalysts* **2017**, *7*, 23.

(18) Li, L.; Wang, Y.; Xu, Z. P.; Zhu, Z. Catalytic Ammonia Decomposition for CO-Free Hydrogen Generation over Ru/Cr_2O_3 Catalysts. *Appl. Catal. A* **2013**, *467*, 246–252.

(19) Chung, D. B.; Kim, H. Y.; Jeon, M.; Lee, D. H.; Park, H. S.; Choi, S. H.; Nam, S. W.; Jang, S. C.; Park, J.-H.; Lee, K.-Y.; Yoon, C. W. Enhanced Ammonia Dehydrogenation over $Ru/La_{(x)}–Al_2O_3$ (x = 0–50 Mol%): Structural and Electronic Effects of La Doping. *Int. J. Hydrogen Energy* **2017**, *42*, 1639–1647.

(20) David, W. I. F.; Makepeace, J. W.; Callear, S. K.; Hunter, H. M. A.; Taylor, J. D.; Wood, T. J.; Jones, M. O. Hydrogen Production from Ammonia Using Sodium Amide. *J. Am. Chem. Soc.* **2014**, *136*, 13082–13085.

(21) Vitse, F.; Cooper, M.; Botte, G. G. On the Use of Ammonia Electrolysis for Hydrogen Production. *J. Power Sources* **2005**, *142*, 18–26.

(22) Palaniappan, R.; Ingram, D. C.; Botte, G. G. Hydrogen Evolution Reaction Kinetics on Electrodeposited Pt–M (M = Ir, Ru, Rh, and Ni) Cathodes for Ammonia Electrolysis. *J. Electrochem. Soc.* **2014**, *161*, E12–E22.

(23) Bunce, N. J.; Bejan, D. Mechanism of Electrochemical Oxidation of Ammonia. *Electrochim. Acta* **2011**, *56*, 8085–8093.

(24) Zhong, C.; Hu, W. B.; Cheng, Y. F. Recent Advances in Electrocatalysts for Electro-Oxidation of Ammonia. *J. Mater. Chem. A Mater. Energy Sustain.* **2013**, *1*, 3216–3238.

(25) Nagakura, S.; Iguchi, H.; Ezawa, H.; Iwamura, H.; Sato, F.; Kubo, R. Physics and Chemistry Dictionary. *Iwanami Shoten* **1988**, 1234.

(26) Hanada, N.; Hino, S.; Ichikawa, T.; Suzuki, H.; Takai, K.; Kojima, Y. Hydrogen Generation by Electrolysis of Liquid Ammonia. *Chem. Commun.* **2010**, *46*, 7775–7777.

(27) Little, D. J.; Smith, M. R., III; Hamann, T. W. Electrolysis of Liquid Ammonia for Hydrogen Generation. *Energy Environ. Sci.* **2015**, *8*, 2775–2781.

(28) *Handbook of Reference Electrodes*; Inzelt, G., Lewenstam, A., Scholz, F., Eds.; Springer, Berlin, Heidelberg, 2013.

(29) Bashkin, J. K.; Kinlen, P. J. Oxygen-Stable Ferrocene Reference Electrodes. *Inorg. Chem.* **1990**, *29*, 4507–4509.

(30) Su, B.; Hatay, I.; Ge, P. Y.; Mendez, M.; Corminboeuf, C.; Samec, Z.; Ersoz, M.; Girault, H. H. Oxygen and Proton Reduction by Decamethylferrocene in Non-Aqueous Acidic Media. *Chem. Commun.* **2010**, *46*, 2918–2919.

(31) Noviandri, I.; Brown, K. N.; Fleming, D. S.; Gulyas, P. T.; Lay, P. A.; Masters, A. F.; Phillips, L. The Decamethylferrocenium/Decamethylferrocene Redox Couple: A Superior Redox Standard to the Ferrocenium/Ferrocene Redox Couple for Studying Solvent Effects on the Thermodynamics of Electron Transfer. *J. Phys. Chem. B* **1999**, *103*, 6713–6722.

(32) Connelly, N. G.; Geiger, W. E. Chemical Redox Agents for Organometallic Chemistry. *Chem. Rev.* **1996**, *96*, 877–910.

(33) Bard, A. J.; Faulkner, L. R. *Electrochemical Methods: Fundamentals and Applications, 2nd Edition*; Wiley Global Education, 2000.

(34) Pavlishchuk, V. V.; Addison, A. W. Conversion Constants for Redox Potentials Measured versus Different Reference Electrodes in Acetonitrile Solutions at 25°C. *Inorganica Chim. Acta* **2000**, *298*, 97–102.

(35) Sawyer, D. T.; Sobkowiak, A.; Roberts, J. L. *Electrochemistry for Chemists, 2nd Edition*; John Wiley & Sons, Inc., 1995.

(36) Jahn, U.; Aussieker, S. Triarylaminium Salt Induced Oxidative Cyclizations of Tertiary Amines. Convenient Access to 2-Substituted Pyrrolidinium Salts. *Org. Lett.* **1999**, *1*, 849–852.

(37) Barham, J. P.; John, M. P.; Murphy, J. A. Contra-Thermodynamic Hydrogen Atom Abstraction in the Selective C–H Functionalization of Trialkylamine N-CH3 Groups. *J. Am. Chem. Soc.* **2016**, *138*, 15482–15487.

(38) M. J. Frisch, G. W. Trucks, H. B. Schlegel, G. E. Scuseria, M. A. Robb, J. R. Cheeseman, G. Scalmani, V. Barone, G. A. Petersson, H. Nakatsuji, X. Li, M. Caricato, A. V. Marenich, J. Bloino, B. G. Janesko, R. Gomperts, B. Mennucci, H. P. Hratchian, J. V. Ortiz, A. F. Izmaylov, J. L. Sonnenberg, D. Williams-Young, F. Ding, F. Lipparini, F. Egidi, J. Goings, B. Peng, A. Petrone, T. Henderson, D. Ranasinghe, V. G. Zakrzewski, J. Gao, N. Rega, G. Zheng, W. Liang, M. Hada, M. Ehara, K. Toyota, R. Fukuda, J. Hasegawa, M. Ishida, T. Nakajima, Y. Honda, O. Kitao, H. Nakai, T. Vreven, K. Throssell, J. A. Montgomery, Jr., J. E. Peralta, F. Ogliaro, M. J. Bearpark, J. J. Heyd, E. N. Brothers, K. N. Kudin, V. N. Staroverov, T. A. Keith, R. Kobayashi, J. Normand, K. Raghavachari, A. P. Rendell, J. C. Burant, S. S. Iyengar, J. Tomasi, M. Cossi, J. M. Millam, M. Klene, C. Adamo, R. Cammi, J. W. Ochterski, R. L. Martin, K. Morokuma, O. Farkas, J. B. Foresman, and D. J. Fox. *Gaussian 16, Revision A.03*; Gaussian, Inc., Wallingford CT, 2016.

(39) E. D. Glendening, J. K. Badenhoop, A. E. Reed, J. E. Carpenter, J. A. Bohmann, C. M. Morales, P. Karafiloglou, C. R. Landis, and F. Weinhold. *NBO 7.0*; University of Wisconsin, Madison, WI, 2018.

(40) Becke, A. D. Density-functional Thermochemistry. III. The Role of Exact Exchange. *J. Chem. Phys.* **1993**, *98*, 5648–5652.

(41) Weigend, F.; Ahlrichs, R. Balanced Basis Sets of Split Valence, Triple Zeta Valence and Quadruple Zeta Valence Quality for H to Rn: Design and Assessment of Accuracy. *Phys. Chem. Chem. Phys.* **2005**, *7*, 3297–3305.

(42) Marenich, A. V.; Cramer, C. J.; Truhlar, D. G. Universal Solvation Model Based on Solute Electron Density and on a Continuum Model of the Solvent Defined by the Bulk Dielectric Constant and Atomic Surface Tensions. *J. Phys. Chem. B* **2009**, *113*, 6378–6396.

(43) Dennington, R.; Keith, T. A.; Millam, J. M. *GaussView, Version 6*; Semichem Inc. Shawnee Mission KS, 2019.

(44) Zott, M. D.; Garrido-Barros, P.; Peters, J. C. Electrocatalytic Ammonia Oxidation Mediated by a Polypyridyl Iron Catalyst. *ACS Catal.* **2019**, *9*, 10101–10108.

(45) Zott, M. D.; Peters, J. C. Enhanced Ammonia Oxidation Catalysis by a Low-Spin Iron Complex Featuring Cis Coordination Sites. *J. Am. Chem. Soc.* **2021**, *143*, 7612–7616.

(46) Li, Y.; Chen, J.-Y.; Miao, Q.; Yu, X.; Feng, L.; Liao, R.-Z.; Ye, S.; Tung, C.-H.; Wang, W. A Parent Iron Amido Complex in Catalysis of Ammonia Oxidation. *J. Am. Chem. Soc.* **2022**, *144*, 4365–4375.

(47) Neumeyer, F.; Lipschutz, M. I.; Tilley, T. D. Group 8 Transition Metal Complexes of the Tripodal Triphosphino Ligands $PhSi(CH_2PR_2)_3$ (R = Ph, IPr). *Eur. J. Inorg. Chem.* **2013**, *2013*, 6075–6078.

(48) Aloisi, A.; Berthet, J.-C.; Genre, C.; Thuéry, P.; Cantat, T. Complexes of the Tripodal Phosphine Ligands $PhSi(XPPh_2)_3$ (X = CH_2, O): Synthesis, Structure and Catalytic Activity in the Hydroboration of CO_2. *Dalton Trans.* **2016**, *45*, 14774–14788.

(49) Sellmann, D.; Kleinschmidt, E. Einfache Synthese von $[C_5H_5Fe(CO)dppe]^+$ und photochemische Überführung in den Distickstoff-Komplex $[C_5H_5Fe(dppe)_2N_2]^{2+}$. *Angew. Chem. Weinheim Bergstr. Ger.* **1975**, *87*, 595–596.

(50) McGhee, L.; Siddique, R. M.; Winfield, J. M. Reactions of Hexakis(Acetonitrile)Iron(II) Hexafluorophosphate in Acetonitrile. Ligation of Ammonia, Pyridine, and Trimethylamine to Iron(II) and the Behaviour of Trimethyl Phosphite and Trimethylphosphine towards Iron(II), Nitrogen Donor Ligand Complex Cations. *J. Chem. Soc. Dalton Trans.* **1988**, No. 5, 1309–1314.

(51) Umehara, K.; Kuwata, S.; Ikariya, T. N–N Bond Cleavage of Hydrazines with a Multiproton-Responsive Pincer-Type Iron Complex. *J. Am. Chem. Soc.* **2013**, *135*, 6754–6757.

(52) Anderson, J. S.; Moret, M.-E.; Peters, J. C. Conversion of Fe–NH_2 to Fe–N_2 with Release of NH_3. *J. Am. Chem. Soc.* **2013**, *135*, 534–537.

(53) Chalkley, M. J.; Drover, M. W.; Peters, J. C. Catalytic N_2-to-NH_3 (or -N_2H_4) Conversion by Well-Defined Molecular Coordination Complexes. *Chem. Rev.* **2020**, *120*, 5582–5636.

(54) Gu, N. X.; Oyala, P. H.; Peters, J. C. Hydrazine Formation via Coupling of a Nickel(III)–NH 2 Radical. *Angew. Chem. Weinheim Bergstr. Ger.* **2021**, *133*, 4055–4059.

(55) Thoreson, K. A.; Follett, A. D.; McNeill, K. Synthesis and Characterization of Pentaphosphino Zero-Valent Iron Complexes and Their Corresponding Iron(II)-Chloride and -Hydride Complexes. *Inorg. Chem.* **2010**, *49*, 3942–3949.

(56) Najafian, A.; Cundari, T. R. Computational Mechanistic Study of Electro-Oxidation of Ammonia to N_2 by Homogenous Ruthenium and Iron Complexes. *J. Phys. Chem. A* **2019**, *123*, 7973–7982.

(57) Zachwieja, U.; Jacobs, H. Tri-µ-Amido-Bis-[Triamminchrom(III)]-Iodid, $[Cr_2(NH_2)_3(NH_3)_6]I_3$, Ein Neuer „hexagonaler Perowskit“. *Zeitschrift für Kristallographie - Crystalline Materials* **1993**, *206*, 247–254.

(58) Frank, W.; Hoffmann, K.; Heck, L. The Tri-µ-Amidobis[Triamminecobalt(III)] Cation: The First Triply Amido-Bridged Complex. *Angew. Chem. Int. Ed Engl.* **1990**, *29*, 1158–1159.

(59) Andersen, P.; Glerup, J.; Gumm, A.; Hansen, S. K.; Magnussen, M. Dinuclear 1,4,7-Triazacyclononane (Tacn) Complexes of Cobalt(Iii) with Amido and Tacn Bridges. Synthesis, Characterization and Reversible Acid-Accelerated Bridge Cleavage. *Dalton Transactions* **2004**, No. 18, 2929.

(60) Dell, W.; Ziegler, M. L. Darstellung Und Charakterisierung von Dreifach NR2-Verbrückten Molybdänkomplexen Des Typs η^3-$C_7H_7(CO)_2Mo(\mu–NR_2)_3Mo$-$\eta^7$-$C_7H_7$ / Synthesis and Characterization of Triply NR2-Bridged Molybdenum Complexes of the Type η^3-$C_7H_7(CO)_2Mo(\mu\text{-}NR_2)_3Mo$-$\eta^7$-$C_7H_7$. *Zeitschrift für Naturforschung B* **1982**, *37*, 7–12.

(61) Frank, W.; Heck, L.; Müller-Becker, S.; Raber, T. The Tri-µ-Amido-Bis[Triammineplatinum(IV)] Cation; Preparation, Structure and Acidity. *Inorganica Chimica Acta* **1997**, *265*, 17–22.

(62) Noh, S. K.; Sendlinger, S. C.; Janiak, C.; Theopold, K. H. $[Cp^*(Me)Cr(\mu\text{-}Me)]_2$, an Electron-Deficient Chromium(III) Alkyl with Bridging Methyl Groups and a Chromium-Chromium Bond. *Journal of the American Chemical Society* **1989**, *111*, 9127–9129.

(63) Ganesan, M.; Gabbaï, F. P. $[Cp^*Cr(C_6F_5)(Me)(Py)]$ as a Living Chromium(III) Catalyst for the “Aufbaureaktion.” *Organometallics* **2004**, *23*, 4608–4613.

(64) Saouma, C. T.; Müller, P.; Peters, J. C. Characterization of Structurally Unusual Diiron N(x)H(y) Complexes. *J. Am. Chem. Soc.* **2009**, *131*, 10358–10359.

(65) Kashiwabara, K.; Ozeki, Y.; Kita, M.; Fujita, J.; Nakajima, K. Synthesis and Crystal Structure of Bis(1,1,1-Tris(Dimethylphosphinomethyl)Ethane)Iron(II) Tetrafluoroborate Dihydrate. *Bull. Chem. Soc. Jpn.* **1995**, *68*, 3453–3457.

(66) Aldrich, K. E.; Fales, B. S.; Singh, A. K.; Staples, R. J.; Levine, B. G.; McCracken, J.; Smith, M. R., III; Odom, A. L. Electronic and Structural Comparisons between Iron (II/III) and Ruthenium (II/III) Imide Analogs. *Inorg. Chem.* **2019**, *58*, 11699–11715.

(67) Chaquin, P.; Canac, Y.; Lepetit, C.; Zargarian, D.; Chauvin, R. Estimating Local Bonding/Antibonding Character of Canonical Molecular Orbitals from Their Energy Derivatives. The Case of Coordinating Lone Pair Orbitals. *Int. J. Quantum Chem.* **2016**, *116*, 1285–1295.

(68) Bader, R. F. W. A Quantum Theory of Molecular Structure and Its Applications. *Chemical Reviews*. 1991, pp 893–928.

(69) Cortesguzman, F.; Bader, R. Complementarity of QTAIM and MO Theory in the Study of Bonding in Donor?Acceptor Complexes. *Coord. Chem. Rev.* **2005**, *249*, 633–662.

(70) Wolczanski, P. T. Flipping the Oxidation State Formalism: Charge Distribution in Organometallic Complexes As Reported by Carbon Monoxide. *Organometallics* **2017**, *36*, 622–631.

(71) Pinter, B.; Van Speybroeck, V.; Waroquier, M.; Geerlings, P.; De Proft, F. Trans Effect and Trans Influence: Importance of Metal Mediated Ligand-Ligand Repulsion. *Phys. Chem. Chem. Phys.* **2013**, *15*, 17354–17365.

(72) Mukhopadhyay, T. K.; Feller, R. K.; Rein, F. N.; Henson, N. J.; Smythe, N. C.; Trovitch, R. J.; Gordon, J. C. Investigation of Formally Zerovalent Triphos Iron Complexes. *Chem. Commun.* **2012**, *48*, 8670–8672.

(73) Britovsek, G. J. P.; England, J.; White, A. J. P. Iron(II), Manganese(II) and Cobalt(II) Complexes Containing Tetradentate Biphenyl-Bridged Ligands and Their Application in Alkane Oxidation Catalysis. *Dalton Trans.* **2006**, No. 11, 1399–1408.

(74) Britovsek, G. J. P.; England, J.; White, A. J. P. Non-Heme Iron(II) Complexes Containing Tripodal Tetradentate Nitrogen Ligands and Their Application in Alkane Oxidation Catalysis. *Inorg. Chem.* **2005**, *44*, 8125–8134.

(75) Sellmann, D.; Weber, W. Reaktionen an Komplexgebundenen Liganden: XXXVIII. [CpFe(Dppe)L]- Und [CpFe(Cdpe)L]-Komplexe Mit L = CO-, N_2-, NH_3-, Sowie N_3^--Liganden (Dppe = 1,2-Bis(Diphenylphosphino)Ethan, Cdpe = Cis-1,2-Bis(Diphenylphosphino)Ethen). *J. Organomet. Chem.* **1986**, *304*, 195–205.

(76) Petuker, A.; Merz, K.; Merten, C.; Apfel, U.-P. Controlled Flexible Coordination in Tripodal Iron(II) Phosphane Complexes: Effects on Reactivity. *Inorg. Chem.* **2016**, *55*, 1183–1191.

(77) Albertin, G.; Antoniutti, S.; Bordignon, E.; Pattaro, S. Synthesis, Characterisation and Reactivity of Hydrazine Complexes of Iron(II). *J. Chem. Soc. Dalton Trans.* **1997**, No. 22, 4445–4454.

(78) Gardner, T. G. Low-Valent Early Transition Metal Complexes Stabilized by the Chelating Tripod Phosphine Ligand (t-Butyl)Tris[(Dimethylphosphino)Methyl]Silane ("Trimpsi"). Ph.D. Thesis. University of Illinois, Urbana-Champaign, 1989.

(79) Karsch, H. H.; Appelt, A. Funktionelle Trimethylphosphanderivate, XVIII [1]. Methyl(Phosphinomethyl)Silane Und -Stannane / Functional Trimethylphosphane Derivatives, XVIII [1]. Methyl(Phosphinomethyl)Silanes and -Stannanes. *Zeitschrift für Naturforschung B* **1983**, *38B*, 1399–1405.

(80) Boncella, J. M.; Green, M. L. H. The Chemistry of Iron-Tris(Dimethylphosphinomethyl)Methylsilane Complexes: Crystal Structure of the Compound [Fe((Me$_2$PCH$_2$)$_3$SiMe)$_2$(Mu-H)$_2$(Mu-C=CH$_2$)] with a Vinylidene Group Which Is Derived from Ethylene. *J. Organomet. Chem.* **1987**, *325*, 217–231.

(81) Nakajima, K.; Toda, H.; Sakata, K.; Nishibayashi, Y. Ruthenium-Catalysed Oxidative Conversion of Ammonia into Dinitrogen. *Nat. Chem.* **2019**, *11*, 702–709.

(82) Habibzadeh, F.; Miller, S. L.; Hamann, T. W.; Smith, M. R., III. Homogeneous Electrocatalytic Oxidation of Ammonia to N$_2$ under Mild Conditions. *Proc. Natl. Acad. Sci. U. S. A.* **2019**, *116*, 2849–2853.

(83) Coia, G. M.; Demadis, K. D.; Meyer, T. J. Oxidation of Ammonia in Osmium Polypyridyl Complexes. *Inorg. Chem.* **2000**, *39*, 2212–2223.

(84) Ishitani, O.; White, P. S.; Meyer, T. J. Formation of Dinitrogen by Oxidation of [(Bpy)$_2$(NH$_3$)RuORu(NH$_3$)(Bpy)$_2$]$^{4+}$. *Inorg. Chem.* **1996**, *35*, 2167–2168.

(85) Ishitani, O.; Ando, E.; Meyer, T. J. Dinitrogen Formation by Oxidative Intramolecular N---N Coupling in Cis,Cis-[(Bpy)$_2$(NH$_3$)RuORu(NH$_3$)(Bpy)$_2$]$^{4+}$. *Inorg. Chem.* **2003**, *42*, 1707–1710.

(86) Thompson, M. S.; Meyer, T. J. Oxidation of Coordinated Ammonia to Nitrate. *J. Am. Chem. Soc.* **1981**, *103*, 5577–5579.

(87) Coia, G. M.; White, P. S.; Meyer, T. J.; Wink, D. A.; Keefer, L. K.; Davis, W. M. Preparation of Osmium Hydrazido Complexes by Interception of an Osmium(IV) Imido Intermediate. *J. Am. Chem. Soc.* **1994**, *116*, 3649–3650.

(88) Walstrom, A.; Pink, M.; Fan, H.; Tomaszewski, J.; Caulton, K. G. Radical (NO) and Nonradical (N_2O) Reagents Convert a Ruthenium(IV) Nitride to the Same Nitrosyl Complex. *Inorganic Chemistry*. 2007, pp 7704–7706.

(89) Man, W.-L.; Tang, T.-M.; Wong, T.-W.; Lau, T.-C.; Peng, S.-M.; Wong, W.-T. Highly Electrophilic (Salen)Ruthenium(VI) Nitrido Complexes. *Journal of the American Chemical Society*. 2004, pp 478–479.

(90) Man, W.-L.; Xie, J.; Pan, Y.; Lam, W. W. Y.; Kwong, H.-K.; Ip, K.-W.; Yiu, S.-M.; Lau, K.-C.; Lau, T.-C. C–N Bond Cleavage of Anilines by a (Salen)Ruthenium(VI) Nitrido Complex. *J. Am. Chem. Soc.* **2013**, *135*, 5533–5536.

(91) Keener, M.; Peterson, M.; Hernández Sánchez, R.; Oswald, V. F.; Wu, G.; Menard, G. Towards Catalytic Ammonia Oxidation to Dinitrogen: A Synthetic Cycle Using a Simple Manganese Complex. *Chemistry-A European Journal* **2017**.

(92) Clarke, R. M.; Storr, T. Tuning Electronic Structure To Control Manganese Nitride Activation. *J. Am. Chem. Soc.* **2016**, *138*, 15299–15302.

(93) Siegl, W. O. Metal Ion Activation of Nitriles. Syntheses of 1,3-Bis(Arylimino)Isoindolines. *J. Org. Chem.* **1977**, *42*, 1872–1878.

(94) Siegl, W. O. Metal-Chelating 1, 3-Bis (2′-Pyridylimino) Isoindolines. *J. Heterocycl. Chem.* **1981**, *18*, 1613–1618.

(95) Gagne, R. R.; Marritt, W. A.; Marks, D. N.; Siegl, W. O. Mononuclear and Binuclear Metal Complexes of 1,3-Bis(2-Pyridylimino)Isoindolines. *Inorg. Chem.* **1981**, *20*, 3260–3267.

(96) Marks, D. N.; Siegl, W. O.; Gagne, R. R. Synthesis and Characterization of Mononuclear and Binuclear Ruthenium Complexes of 1,3-Bis(2-Pyridylimino)Isoindolines. *Inorg. Chem.* **1982**, *21*, 3140–3147.

(97) Planas, N.; Ono, T.; Vaquer, L.; Miró, P.; Benet-Buchholz, J.; Gagliardi, L.; Cramer, C. J.; Llobet, A. Carbon Dioxide Reduction by Mononuclear Ruthenium Polypyridyl Complexes. *Phys. Chem. Chem. Phys.* **2011**, *13*, 19480.

(98) Savéant, J.-M. *Elements of Molecular and Biomolecular Electrochemistry: An Electrochemical Approach to Electron Transfer Chemistry*; John Wiley & Sons, 2006.

(99) Lee, K. J.; Elgrishi, N.; Kandemir, B.; Dempsey, J. L. Electrochemical and Spectroscopic Methods for Evaluating Molecular Electrocatalysts. *Nature Reviews Chemistry* **2017**, *1*, 0039.

(100) Jurss, J. W.; Concepcion, J. J.; Butler, J. M.; Omberg, K. M.; Baraldo, L. M.; Thompson, D. G.; Lebeau, E. L.; Hornstein, B.; Schoonover, J. R.; Jude, H.; Thompson, J. D.; Dattelbaum, D. M.; Rocha, R. C.; Templeton, J. L.; Meyer, T. J. Electronic Structure of the Water Oxidation Catalyst Cis,Cis-$[(Bpy)_2(H_2O)Ru(III)ORu(III)(OH_2)(Bpy)_2]^{4+}$, the Blue Dimer. *Inorg. Chem.* **2012**, *51*, 1345–1358.

(101) Sens, C.; Romero, I.; Rodríguez, M.; Llobet, A.; Parella, T.; Benet-Buchholz, J. A New Ru Complex Capable of Catalytically Oxidizing Water to Molecular Dioxygen. *J. Am. Chem. Soc.* **2004**, *126*, 7798–7799.

(102) Collman, J. P.; Hutchison, J. E.; Ennis, M. S.; Lopez, M. A.; Guilard, R. Reduced Nitrogen Hydride Complexes of a Cofacial Metallodiporphyrin and Their Oxidative Interconversion. An Analysis of Ammonia Oxidation and Prospects for a Dinitrogen Electroreduction Catalyst Based on Cofacial Metallodiporphyrins. *J. Am. Chem. Soc.* **1992**, *114*, 8074–8080.

(103) Arakawa, R.; Kubota, N.; Fukuo, T.; Ishitani, O.; Ando, E. Study of the Ligand Substitution Reactions of Cis,Cis-$[(Bpy)_2(L)RuORu(L')(Bpy)_2]N^+$ (L, L' = H_2O, OH^-, NH_3) Using Electrospray Ionization Mass Spectrometry and 1H NMR. *Inorg. Chem.* **2002**, *41*, 3749–3754.

(104) Ough, E. A.; Stillman, M. J. Analysis of the Absorption and Magnetic Circular Dichroism Spectra of Iron(II) Phthalocyanine. *Inorg. Chem.* **1994**, *33*, 573–583.

(105) Oña-Burgos, P.; Casimiro, M.; Fernández, I.; Navarro, A. V.; Fernández Sánchez, J. F.; Carretero, A. S.; Gutiérrez, A. F. Octahedral Iron(II) Phthalocyanine Complexes: Multinuclear NMR and Relevance as NO(2) Chemical Sensors. *Dalton Trans.* **2010**, *39*, 6231–6238.

(106) Huang, J.-S.; Yu, G.-A.; Xie, J.; Wong, K.-M.; Zhu, N.; Che, C.-M. Primary and Secondary Phosphine Complexes of Iron Porphyrins and Ruthenium Phthalocyanine: Synthesis, Structure, and P-H Bond Functionalization. *Inorg. Chem.* **2008**, *47*, 9166–9181.

(107) Fernández, I.; Pregosin, P. S.; Albinati, A.; Rizzato, S.; Spichiger-Keller, U. E.; Nezel, T.; Fernández-Sánchez, J. F. Solution NMR and X-Ray Structural Studies on Phthalocyaninatoiron Complexes. *Helv. Chim. Acta* **2006**, *89*, 1485–1496.

(108) Damos, F. S.; de Cássia Silva Luz, R.; Tanaka, A. A. Electroanalysis of Hydrazine and Related Compounds by Oxidation Promoted with MN4 Macrocyclics. In *Electrochemistry of N4 Macrocyclic Metal Complexes: Volume 2: Biomimesis, Electroanalysis and Electrosynthesis of MN4 Metal Complexes*; Zagal, J. H., Bedioui, F., Eds.; Springer International Publishing: Cham, 2016; pp 201–223.

(109) Beiler, A. M.; Denisiuk, A.; Holub, J.; Sánchez-Baygual, F.-J.; Gil-Sepulcre, M.; Ertem, M. Z.; Moonshiram, D.; Piccioni, A.; Llobet, A. Heterogeneous Electrochemical Ammonia Oxidation with a Ru-Bda Oligomer Anchored on Graphitic Electrodes via CH−π Interactions. *ACS Energy Lett.* **2022**, 172–178.

(110) Sorokin, A. B. Phthalocyanine Metal Complexes in Catalysis. *Chem. Rev.* **2013**, *113*, 8152–8191.

SUPPORTING INFORMATION (A) FOR CHAPTER 3

SA.1 NMR Spectra

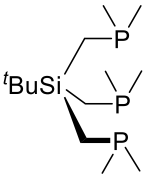

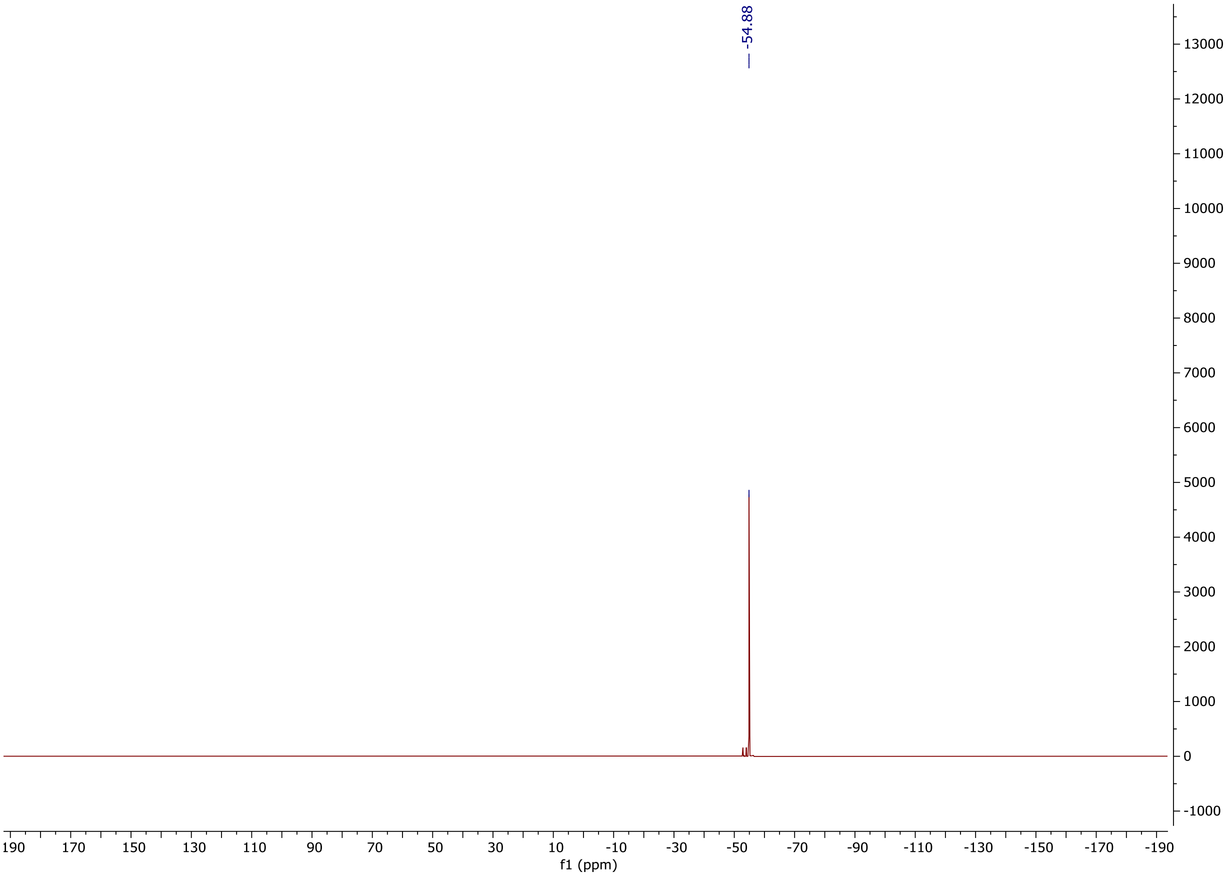

Figure SA.1 $^{31}P\{^1H\}$ NMR of ^{t}SiP$_3$ in C_6D_6

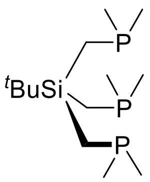

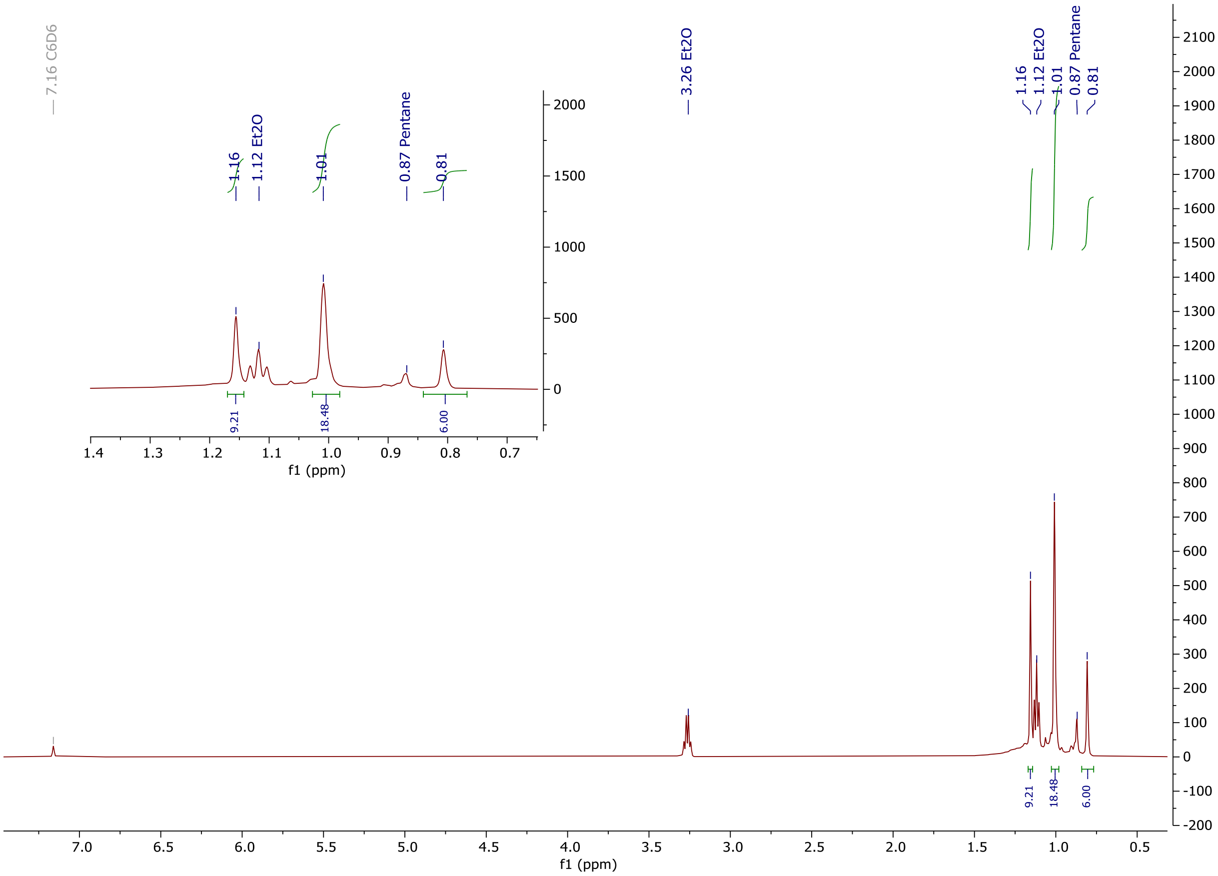

Figure SA.2 ^{1}H NMR of ^{t}SiP$_3$ in C$_6$D$_6$

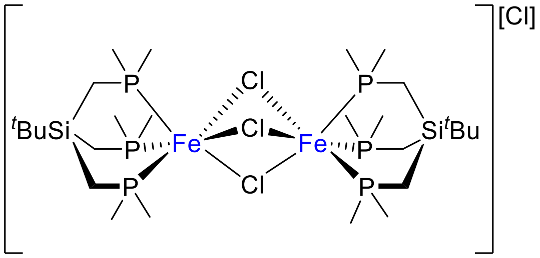

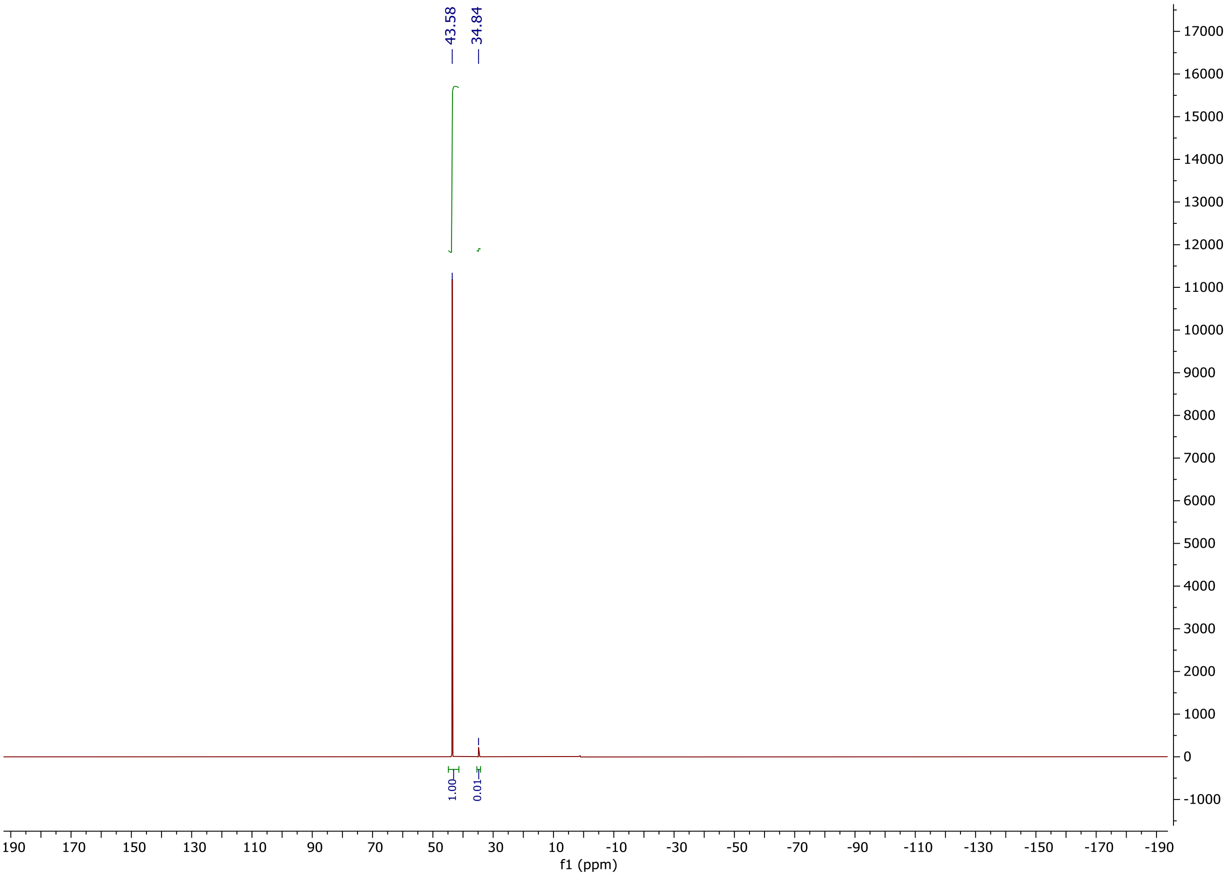

Figure SA.3 ^{31}P{^{1}H} NMR of [(^{t}SiP$_3$Fe)$_2$(μ–Cl)$_3$][Cl] (**1**) in MeCN-d_3. The peak at δ 34 ppm is assigned to displacement of bridged Cl with MeCN-d_3 to yield [^{t}SiP$_3$Fe(NCMe)$_3$][Cl]$_2$

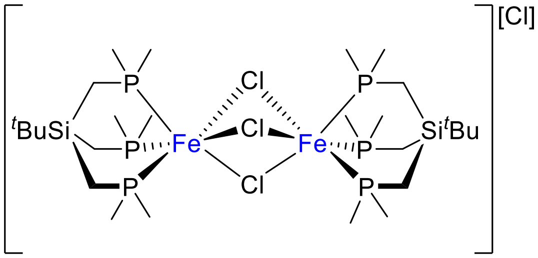

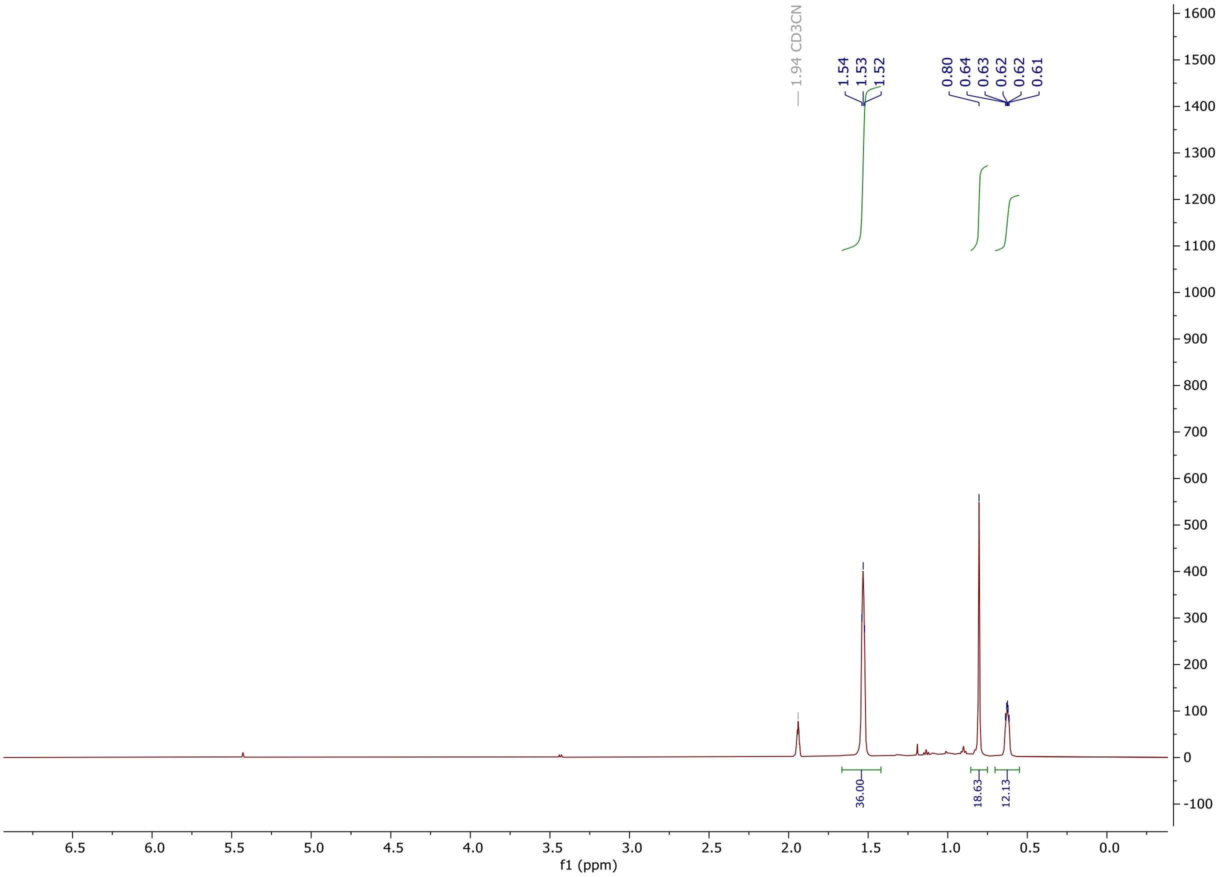

Figure SA.4 ^{1}H NMR of [(^{t}SiP$_3$Fe)$_2$(μ–Cl)$_3$][Cl] (**1**) in MeCN-d_3

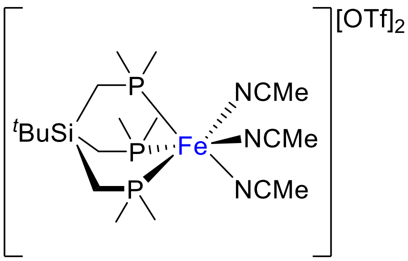

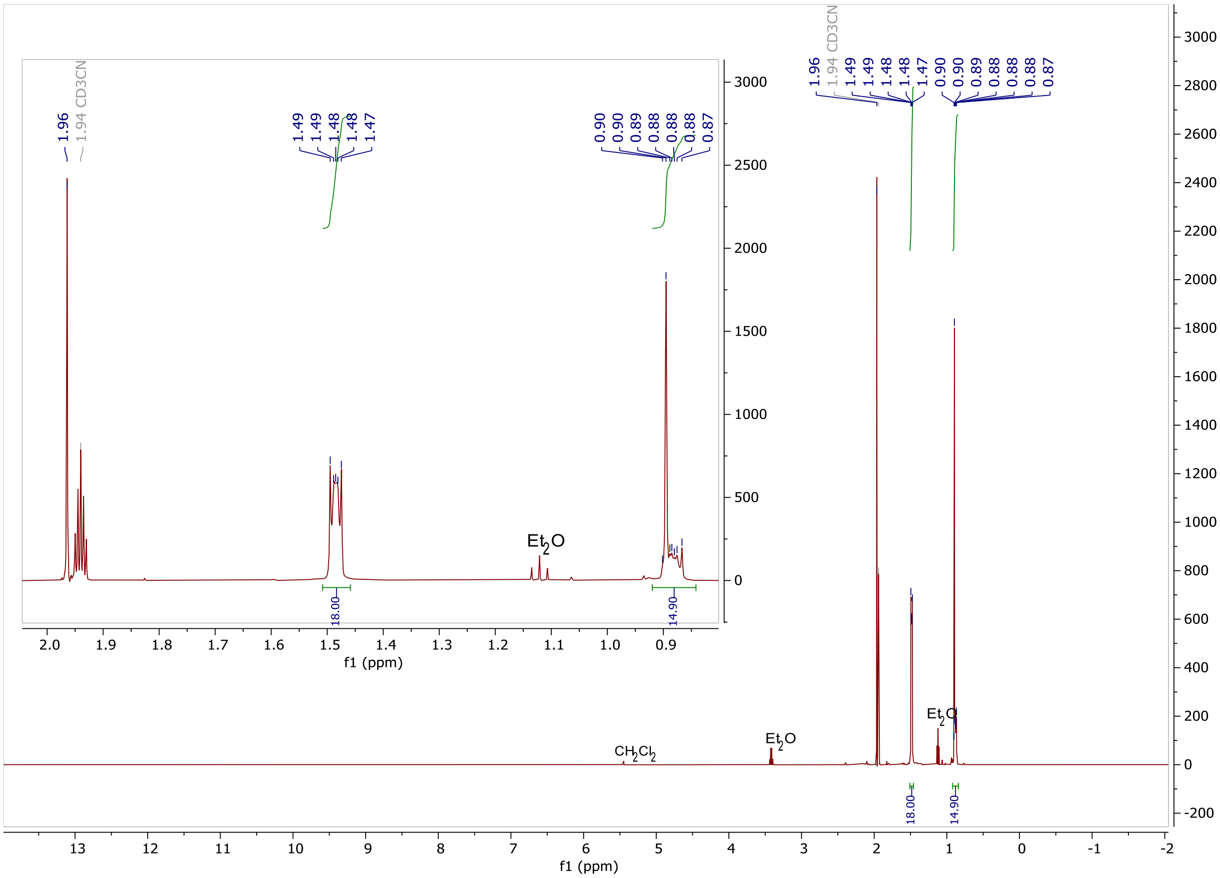

Figure SA.5 ^{1}H NMR of [^{t}SiP$_3$Fe(NCMe)$_3$][OTf]$_2$ (**2**) in MeCN-d_3

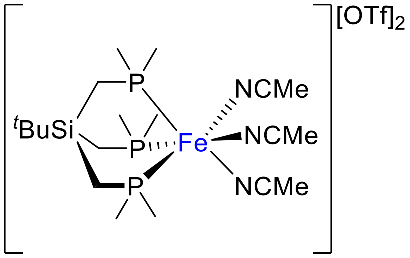

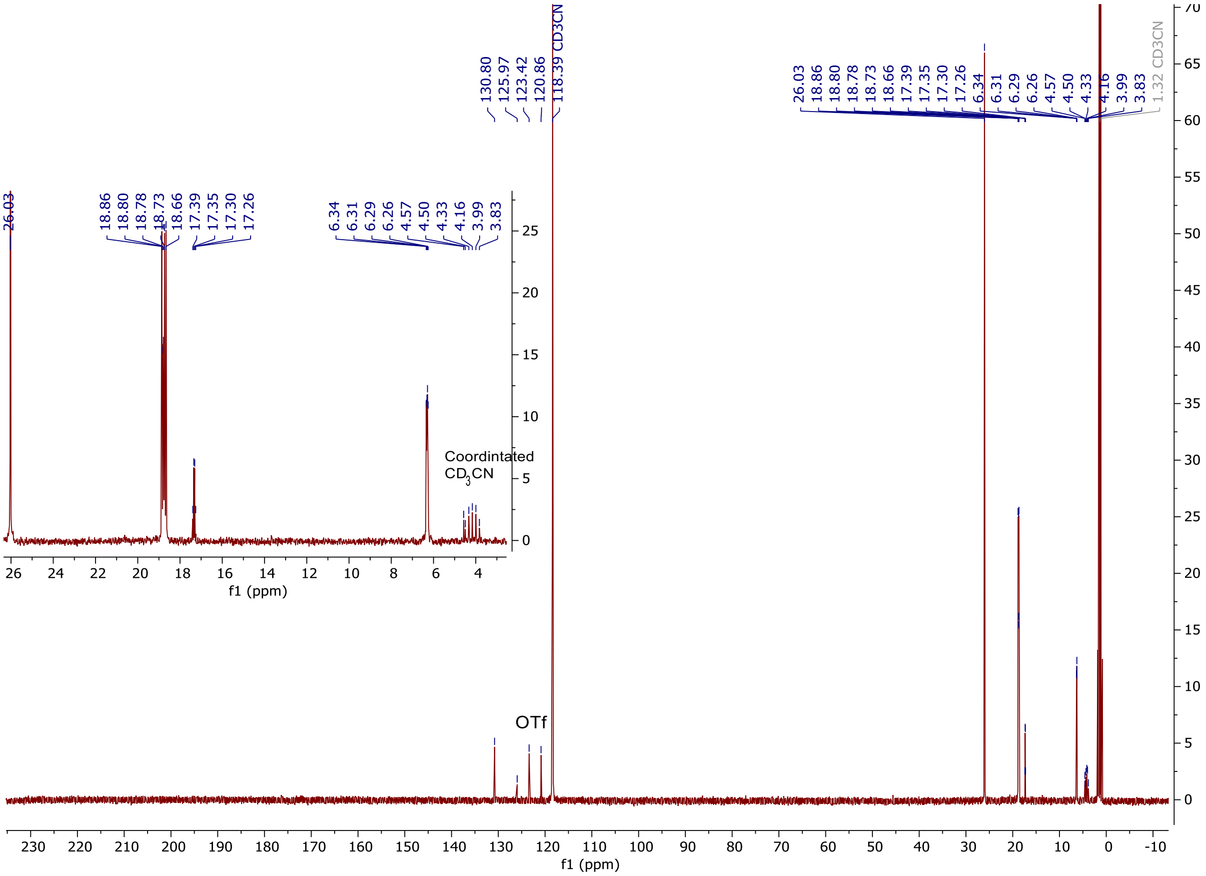

Figure SA.6 ^{13}C NMR of [^{t}SiP$_3$Fe(NCMe)$_3$][OTf]$_2$ (**2**) in MeCN-d_3

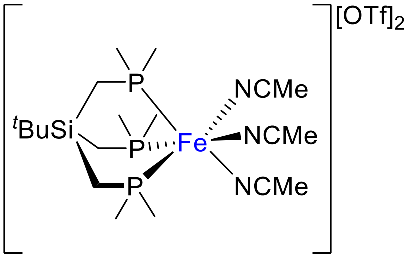

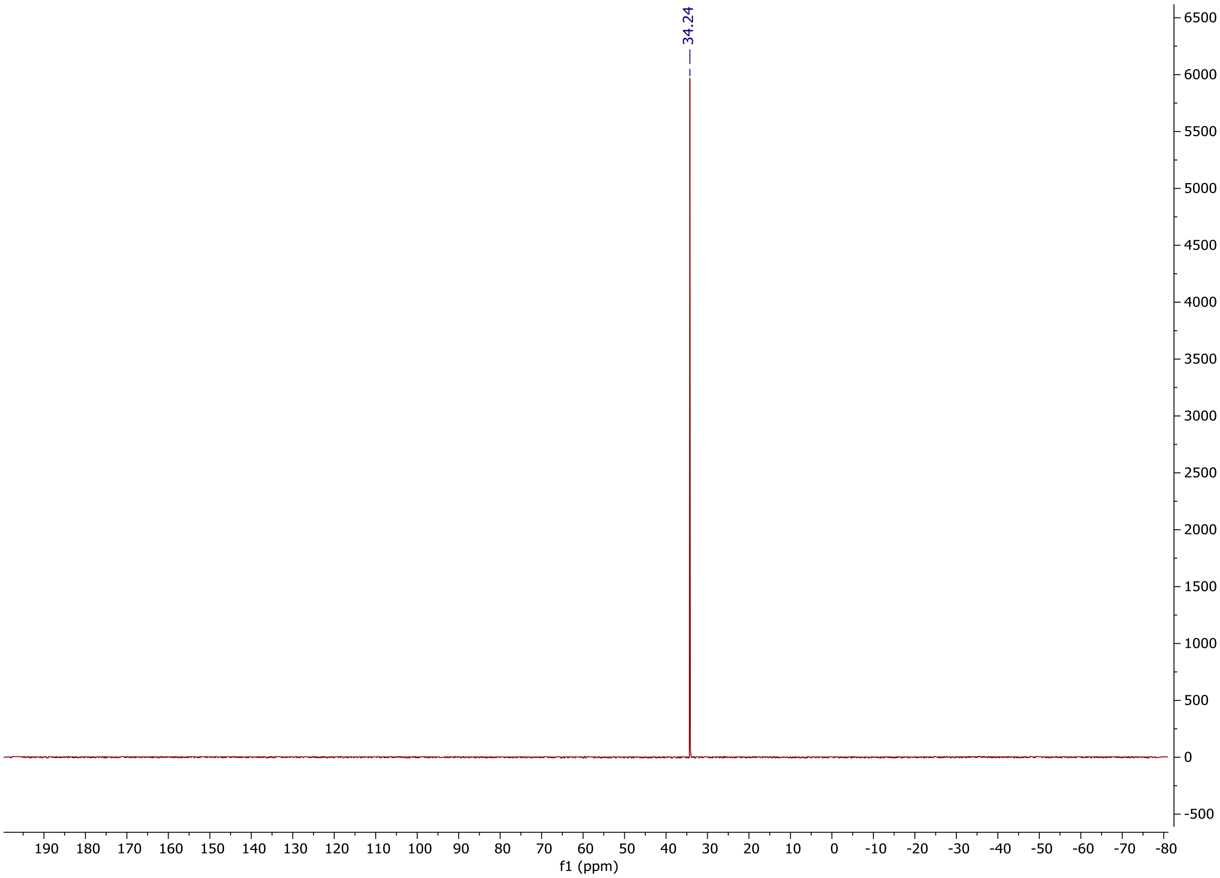

Figure SA.7 ^{31}P{^{1}H} NMR of [^{t}SiP$_3$Fe(NCMe)$_3$][OTf]$_2$ (**2**) in MeCN-d_3

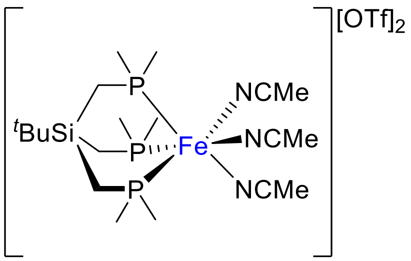

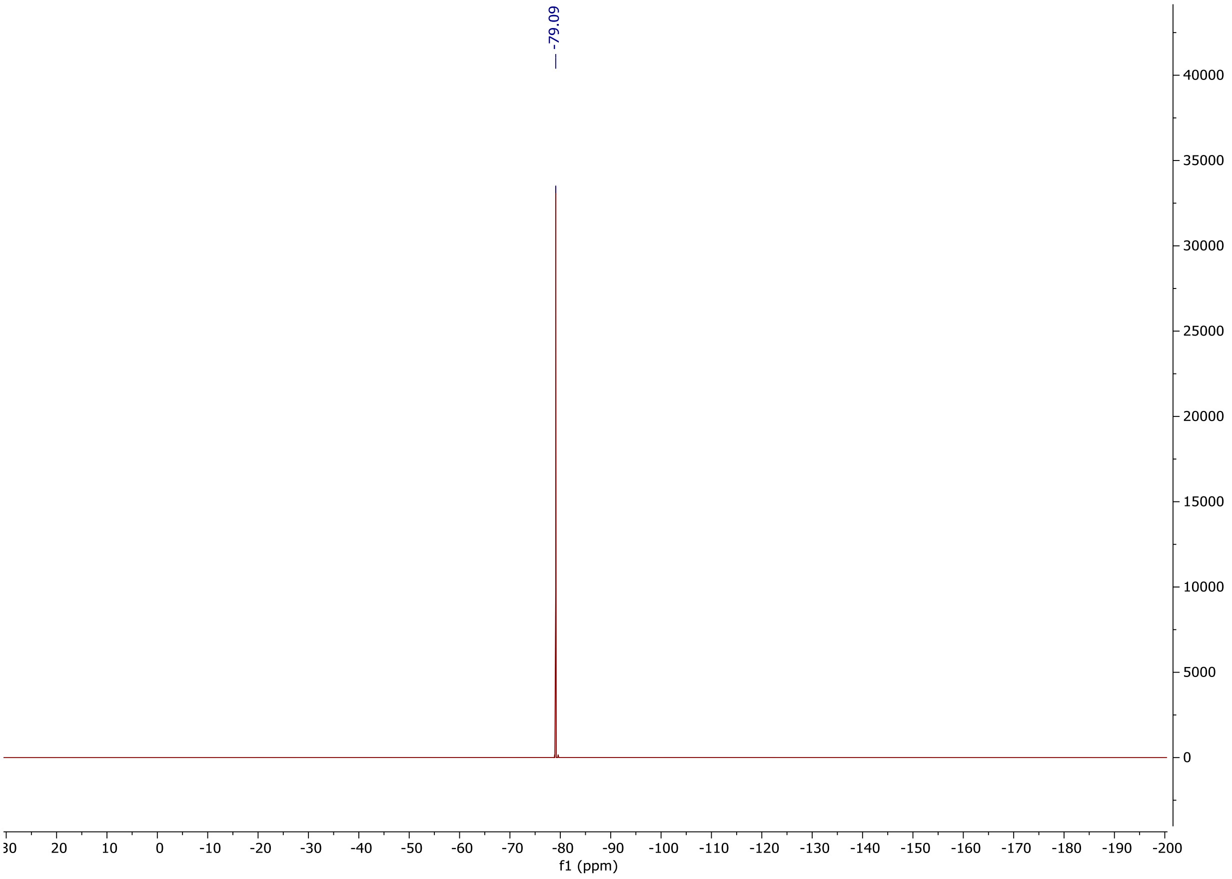

Figure SA.8 ^{19}F NMR of [^{t}SiP$_3$Fe(NCMe)$_3$][OTf]$_2$ (**2**) in MeCN-d_3

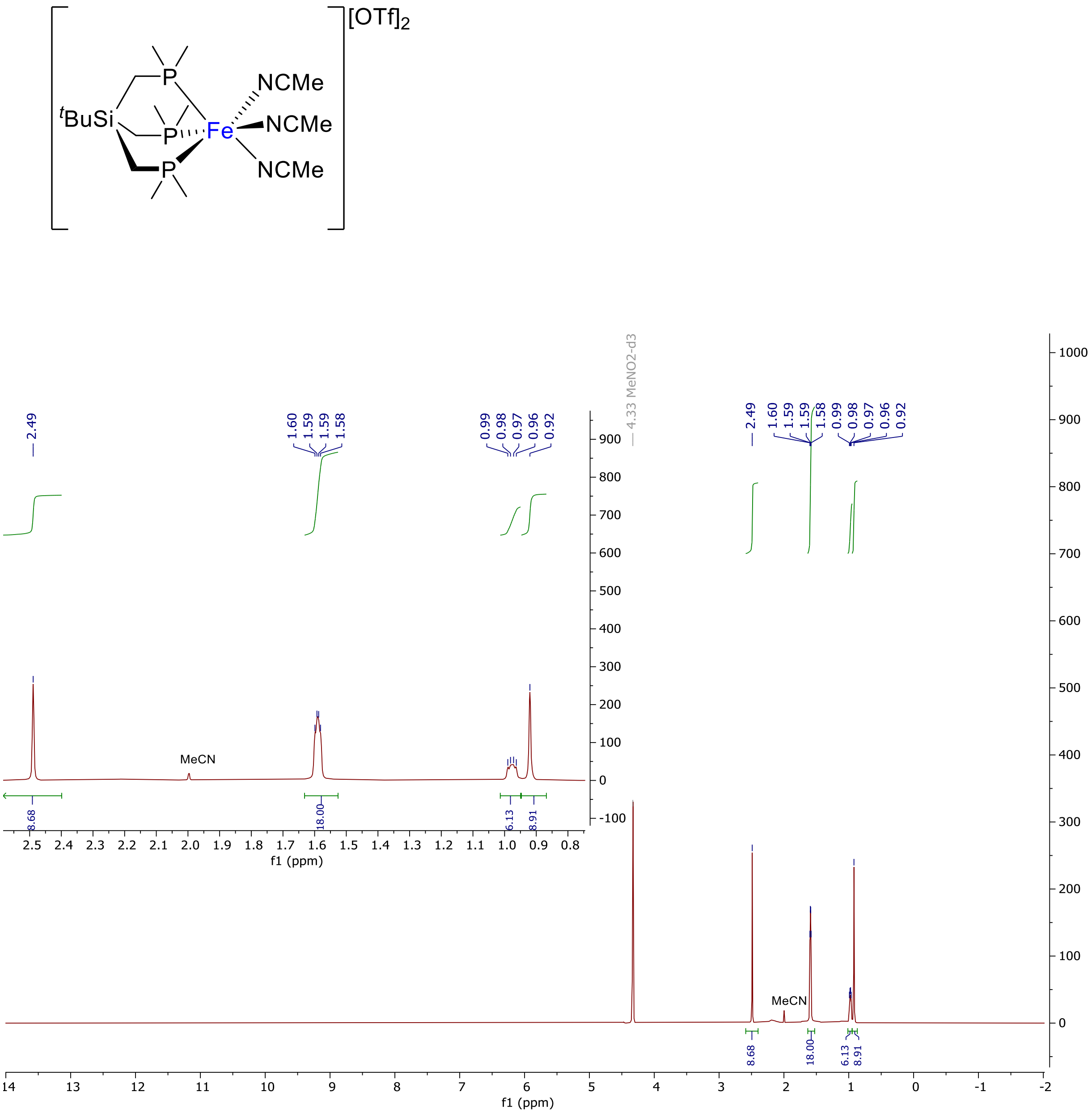

Figure SA.9 ^{1}H NMR of [^{t}SiP$_3$Fe(NCMe)$_3$][OTf]$_2$ (**2**) in MeNO$_2$-*d*$_3$

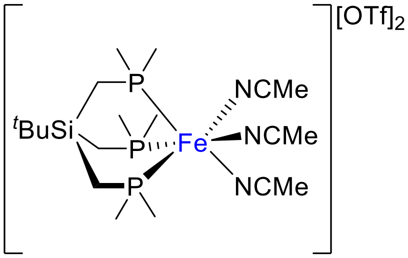

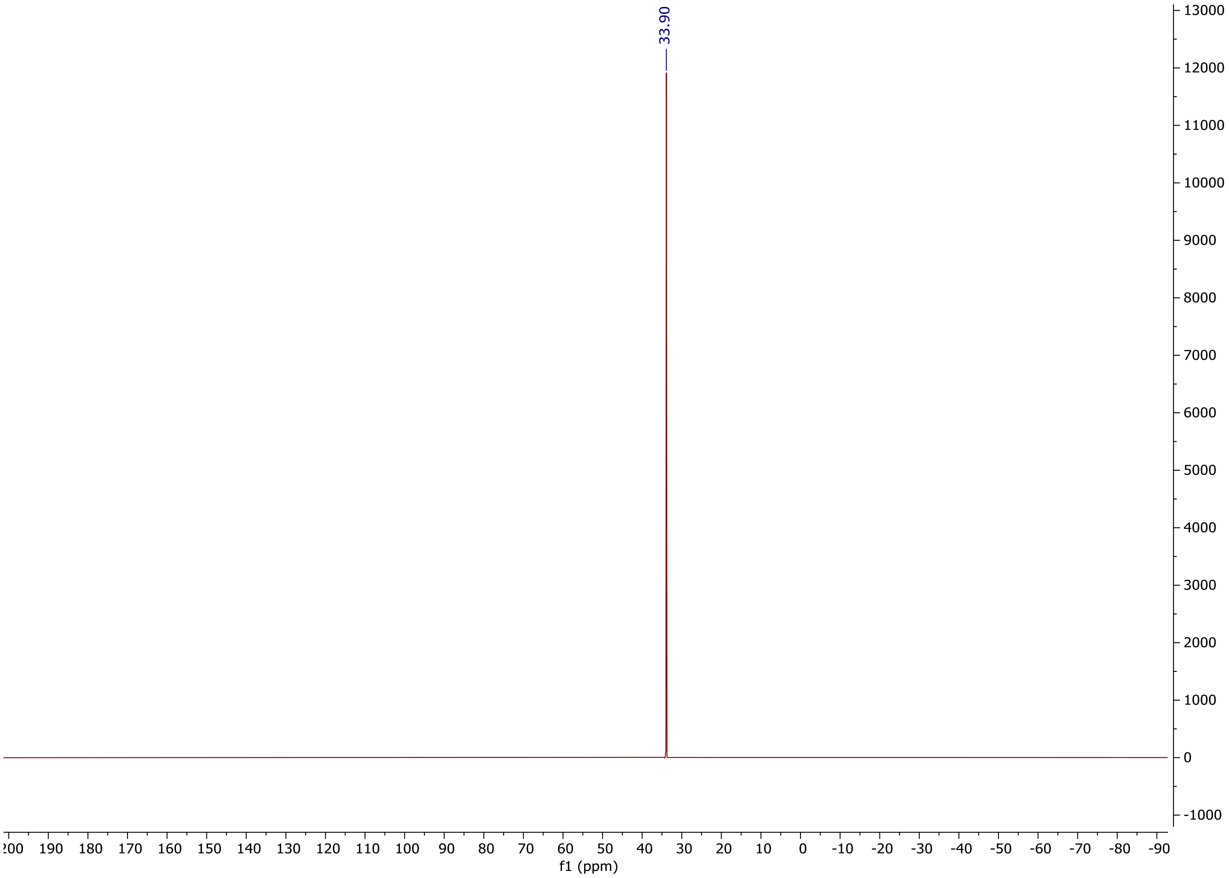

Figure SA.10 $^{31}P\{^{1}H\}$ NMR of $[^{t}SiP_3Fe(NCMe)_3][OTf]_2$ (**2**) in $MeNO_2$-d_3

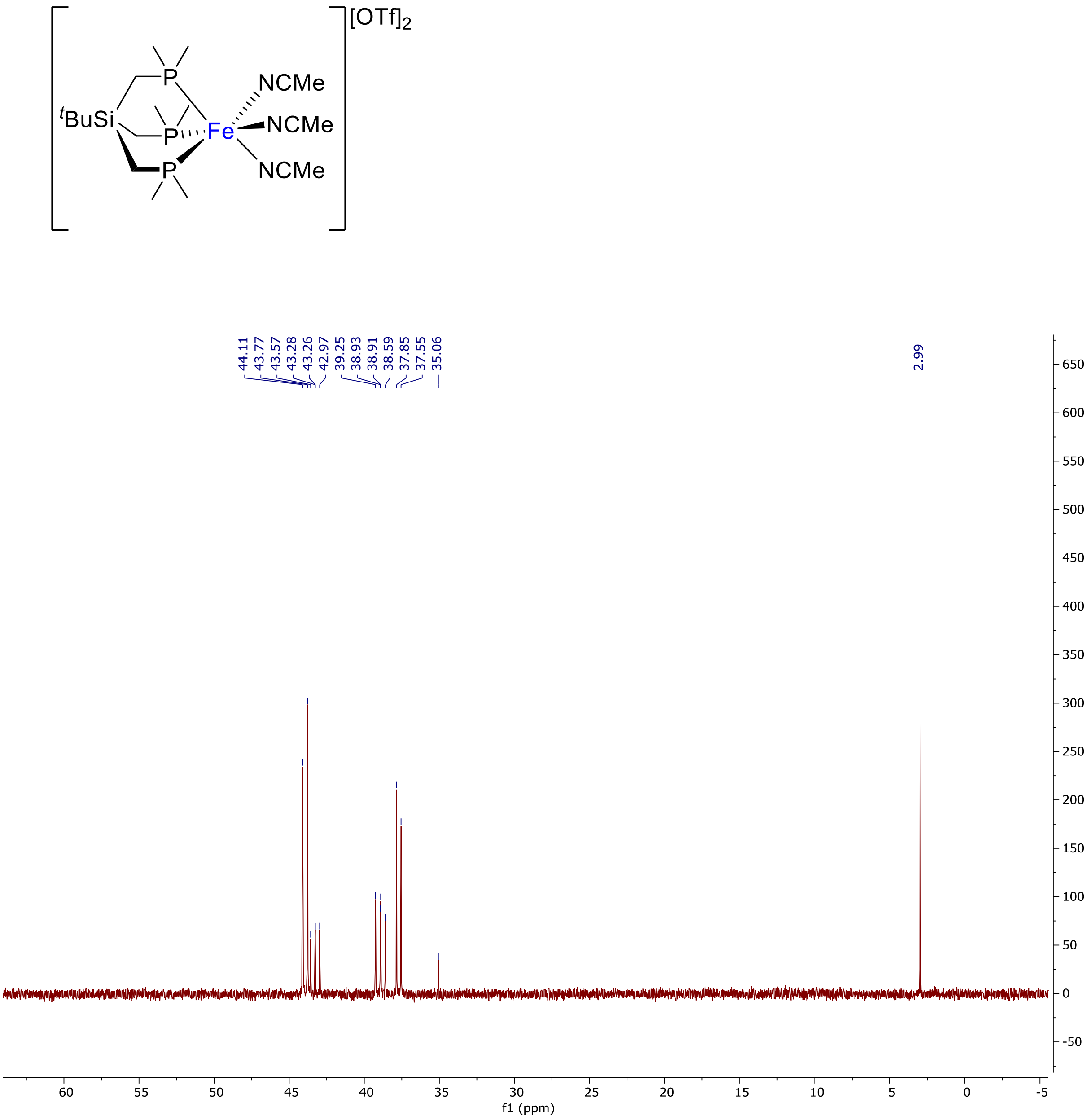

Figure SA.11 $^{31}P\{^1H\}$ NMR of [^{t}SiP$_3$Fe(NCMe)$_3$][OTf]$_2$ (**2**) in DMSO-d_6

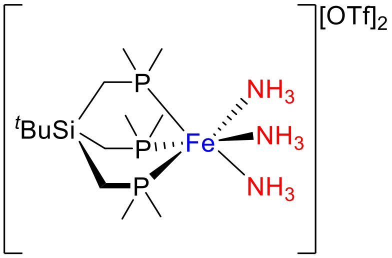

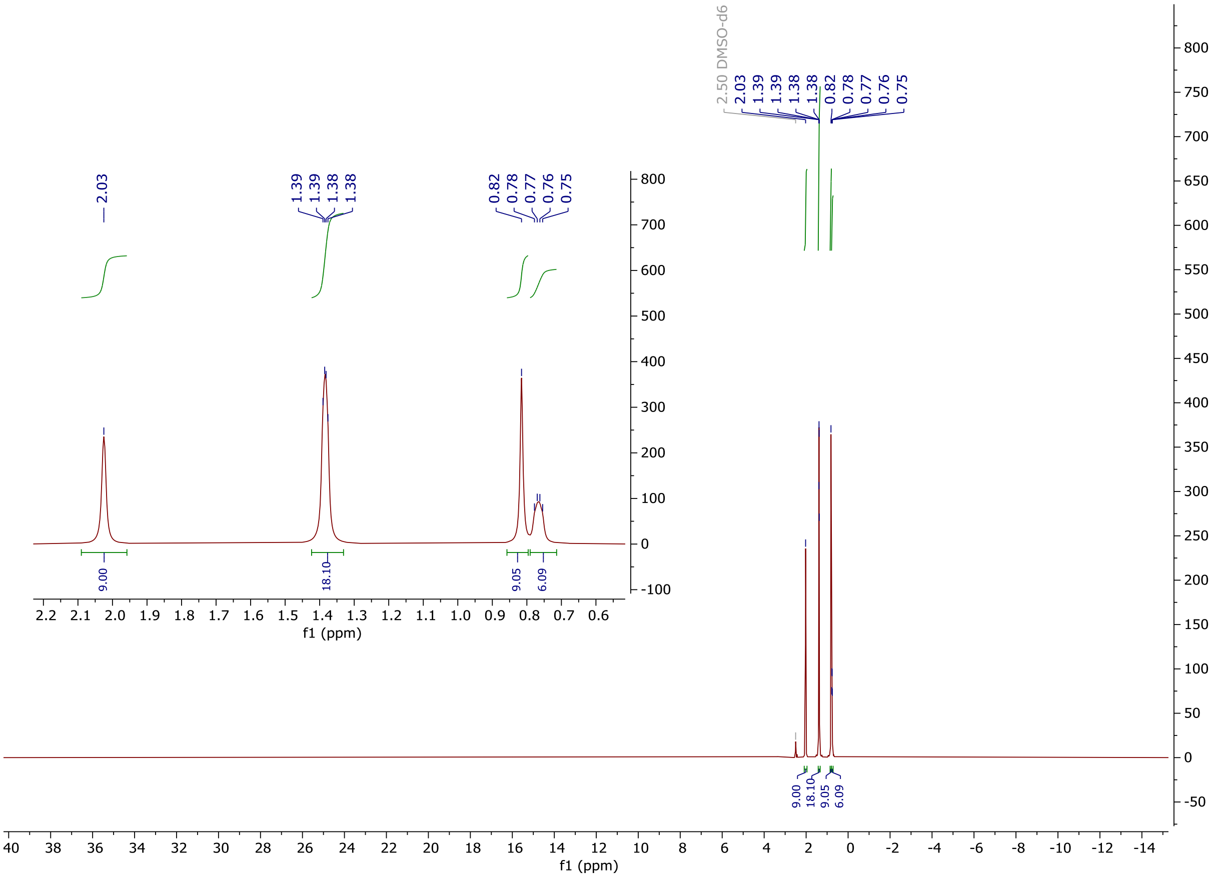

Figure SA.12 ^{1}H NMR of [^{t}SiP$_3$Fe(NH$_3$)$_3$][OTf]$_2$ (**3**) in DMSO-d_6

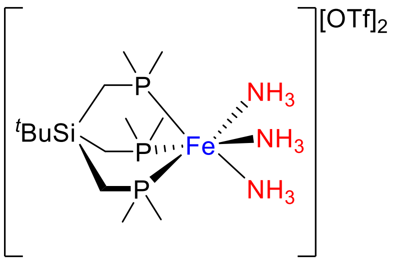

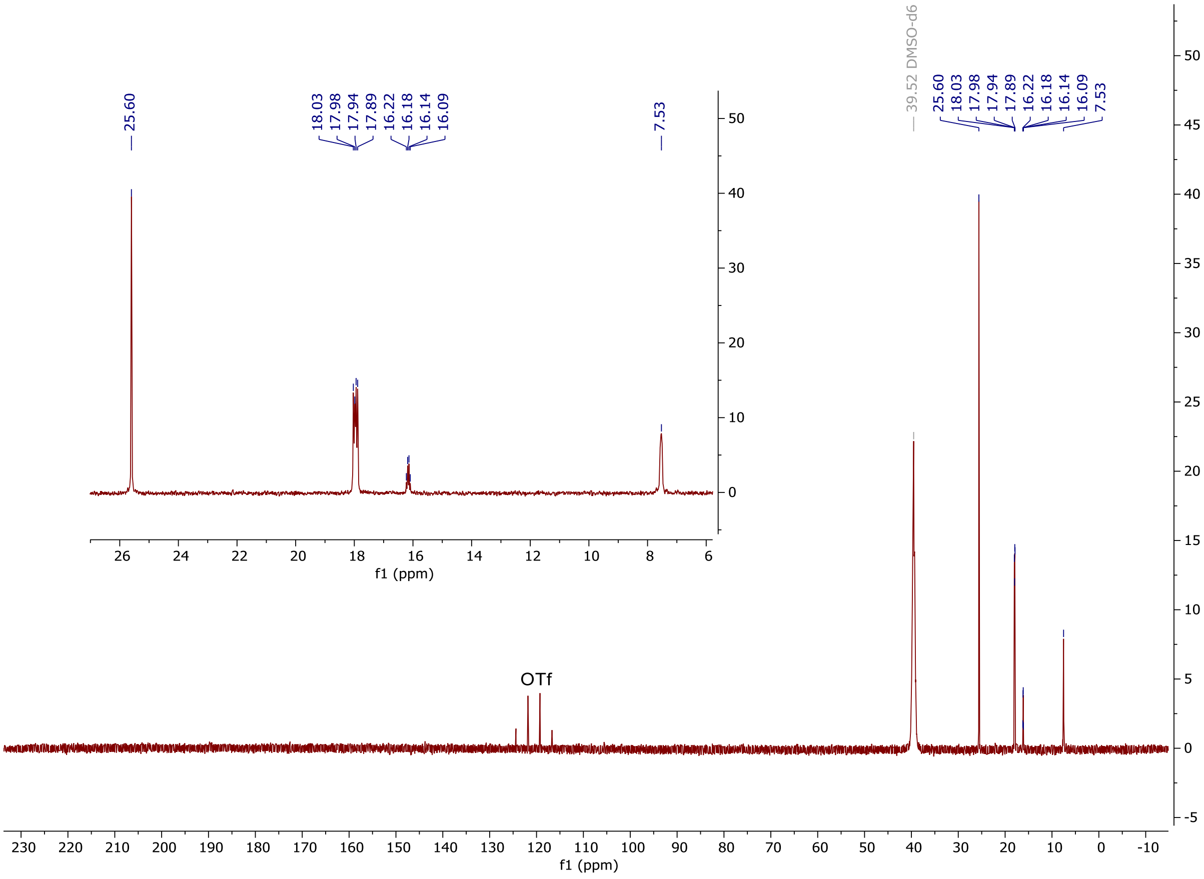

Figure SA.13 ^{13}C NMR of [^{t}SiP$_3$Fe(NH$_3$)$_3$][OTf]$_2$ (**3**) in DMSO-*d*$_6$

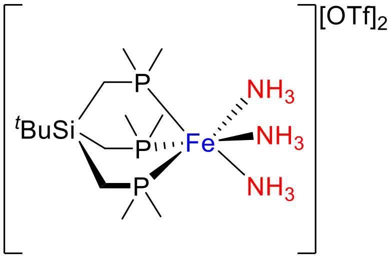

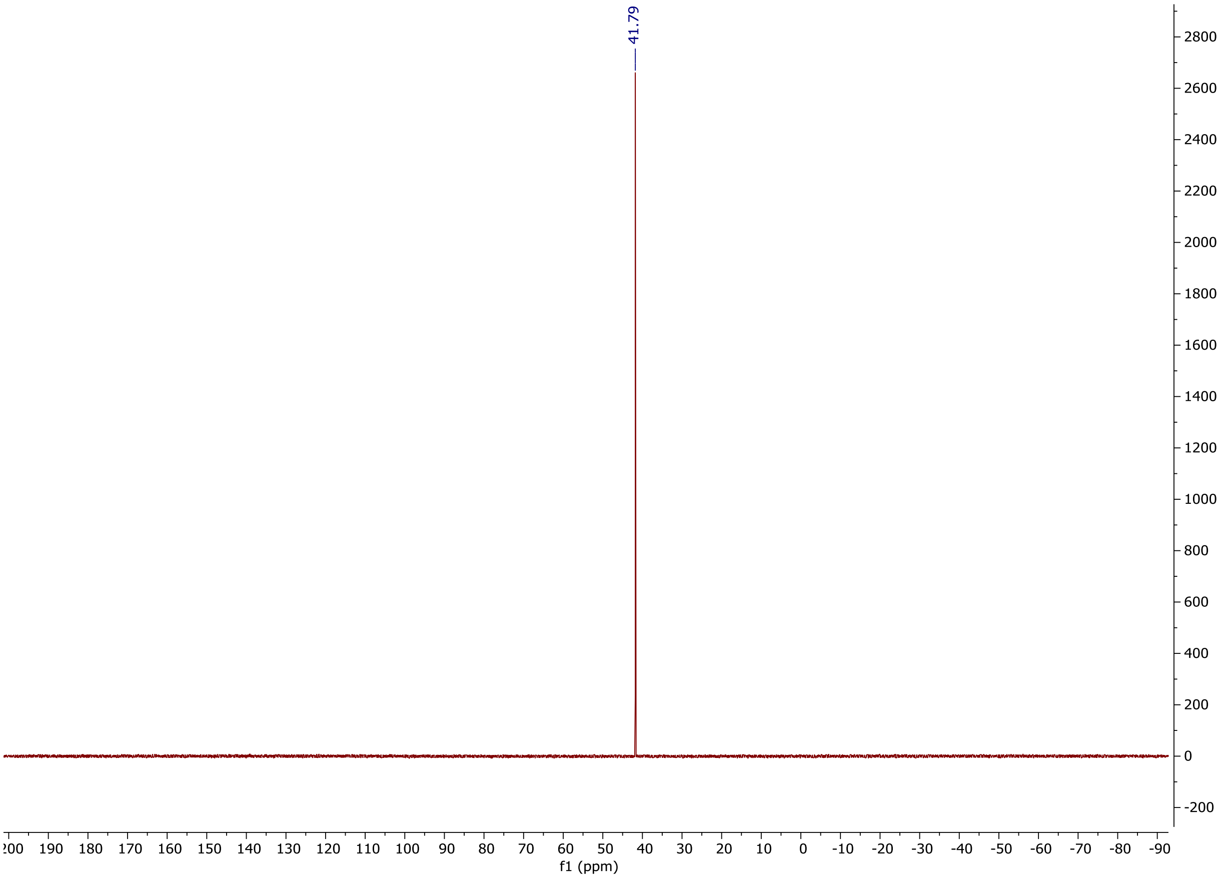

Figure SA.14 $^{31}P\{^{1}H\}$ NMR of [$^{t}SiP_3Fe(NH_3)_3$][OTf]$_2$ (**3**) in DMSO-d_6

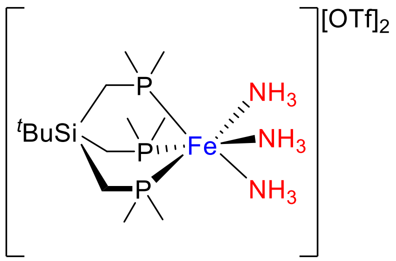

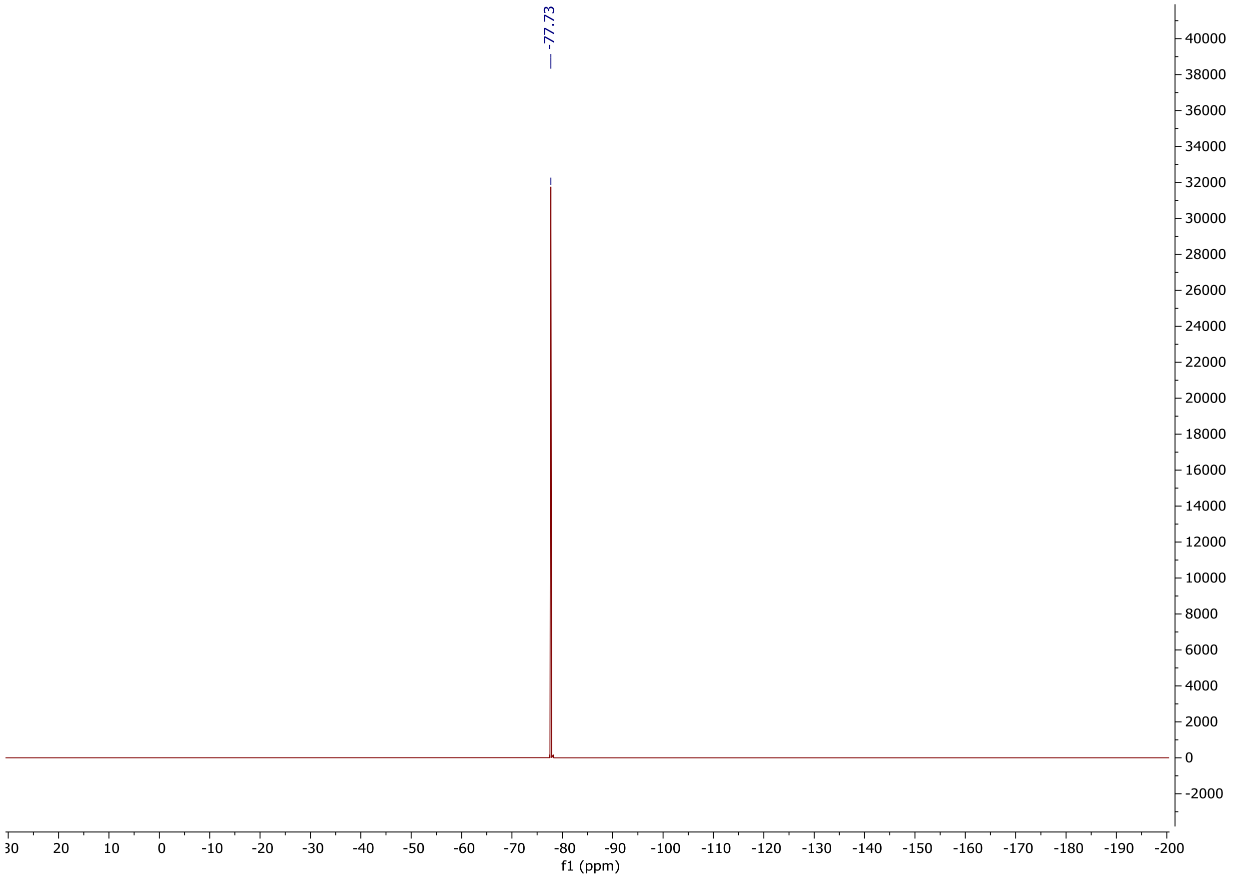

Figure SA.15 ^{19}F NMR of [^{t}SiP$_3$Fe(NH$_3$)$_3$][OTf]$_2$ (**3**) in DMSO-d_6

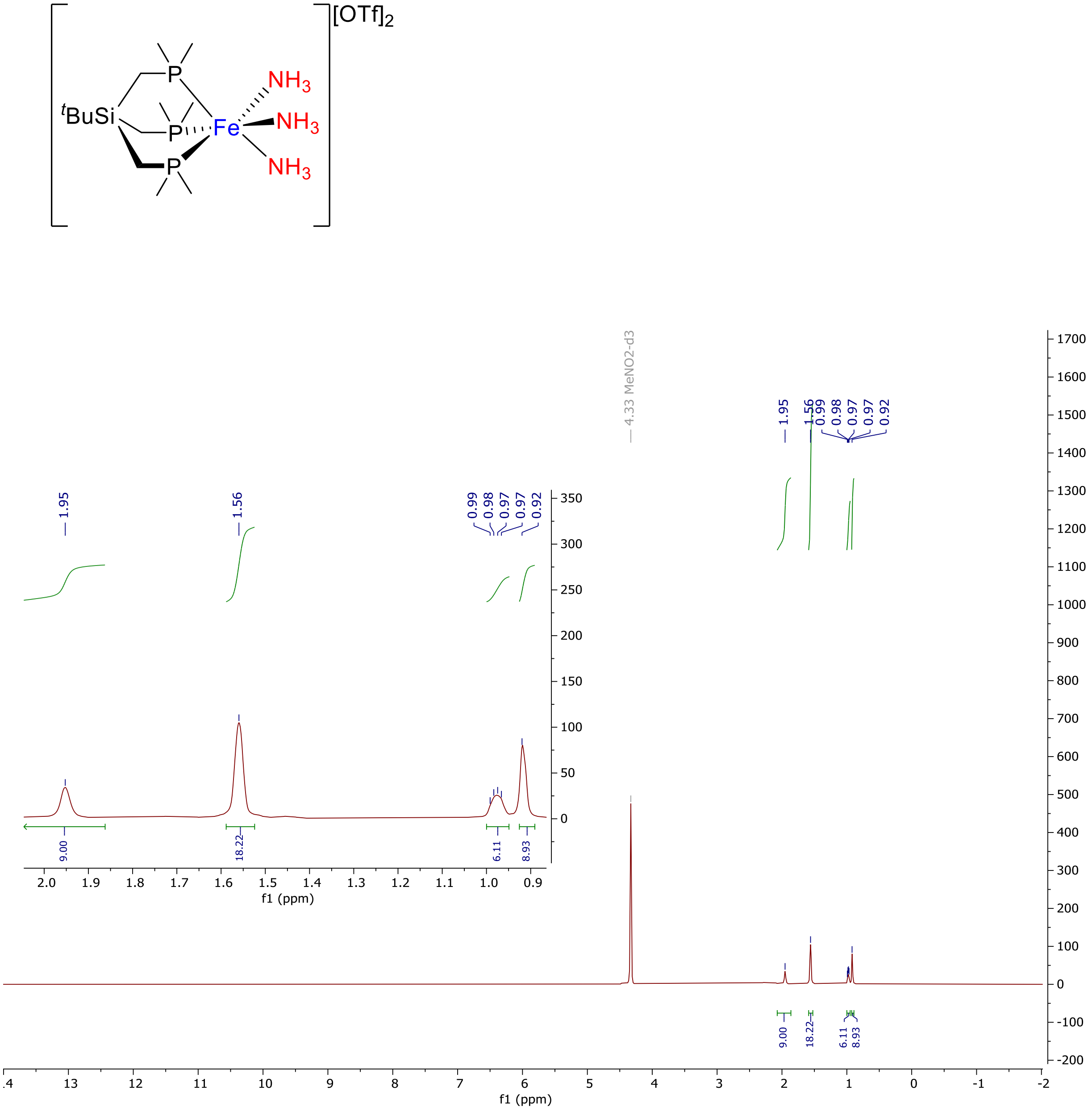

Figure SA.16 ^{1}H NMR of [^{t}SiP$_3$Fe(NH$_3$)$_3$][OTf]$_2$ (**3**) in MeNO$_2$-d_3

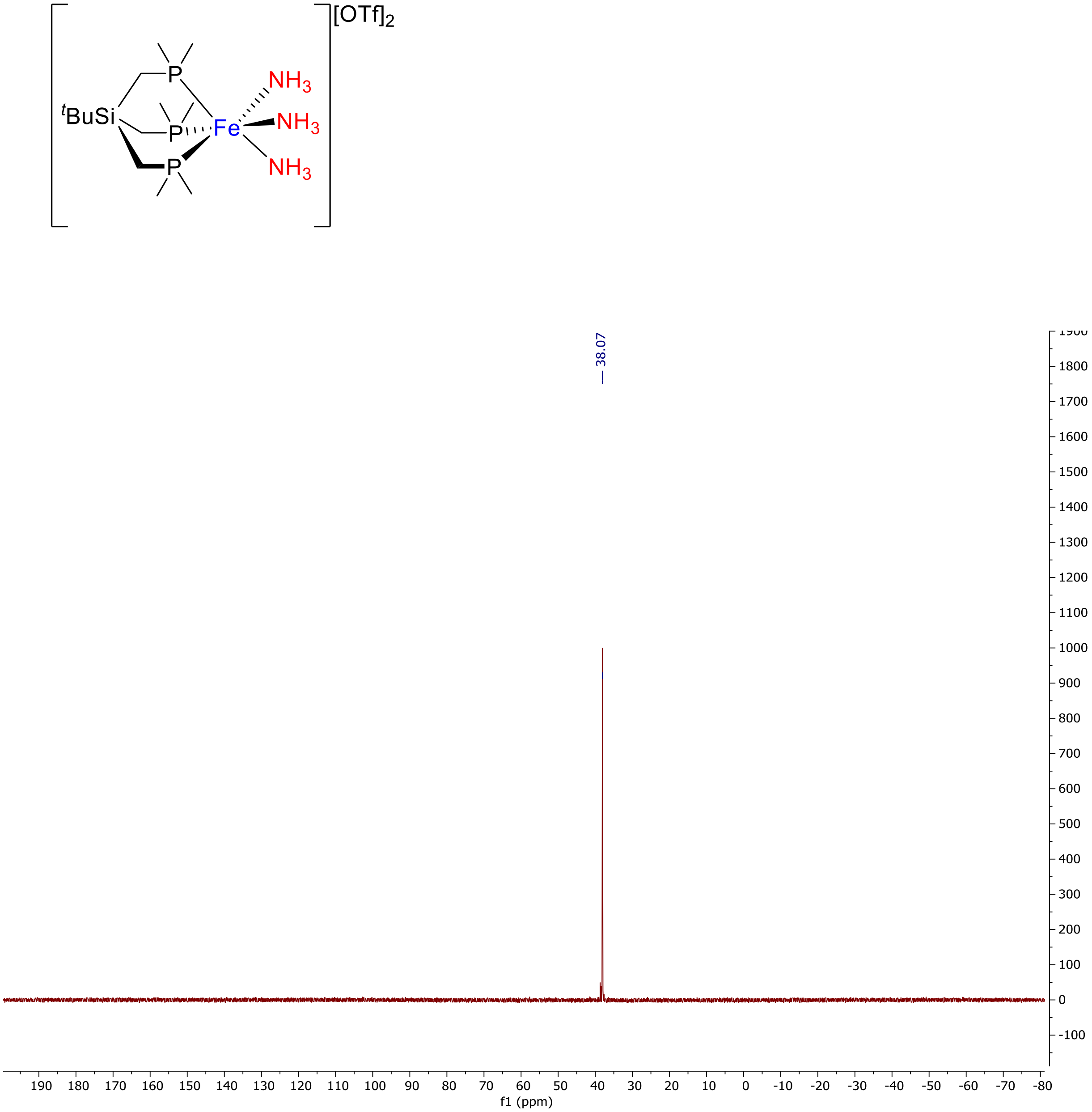

Figure SA.17 $^{31}P\{^{1}H\}$ NMR of [$^{t}SiP_3Fe(NH_3)_3$][OTf]$_2$ (**3**) in MeNO$_2$-d_3

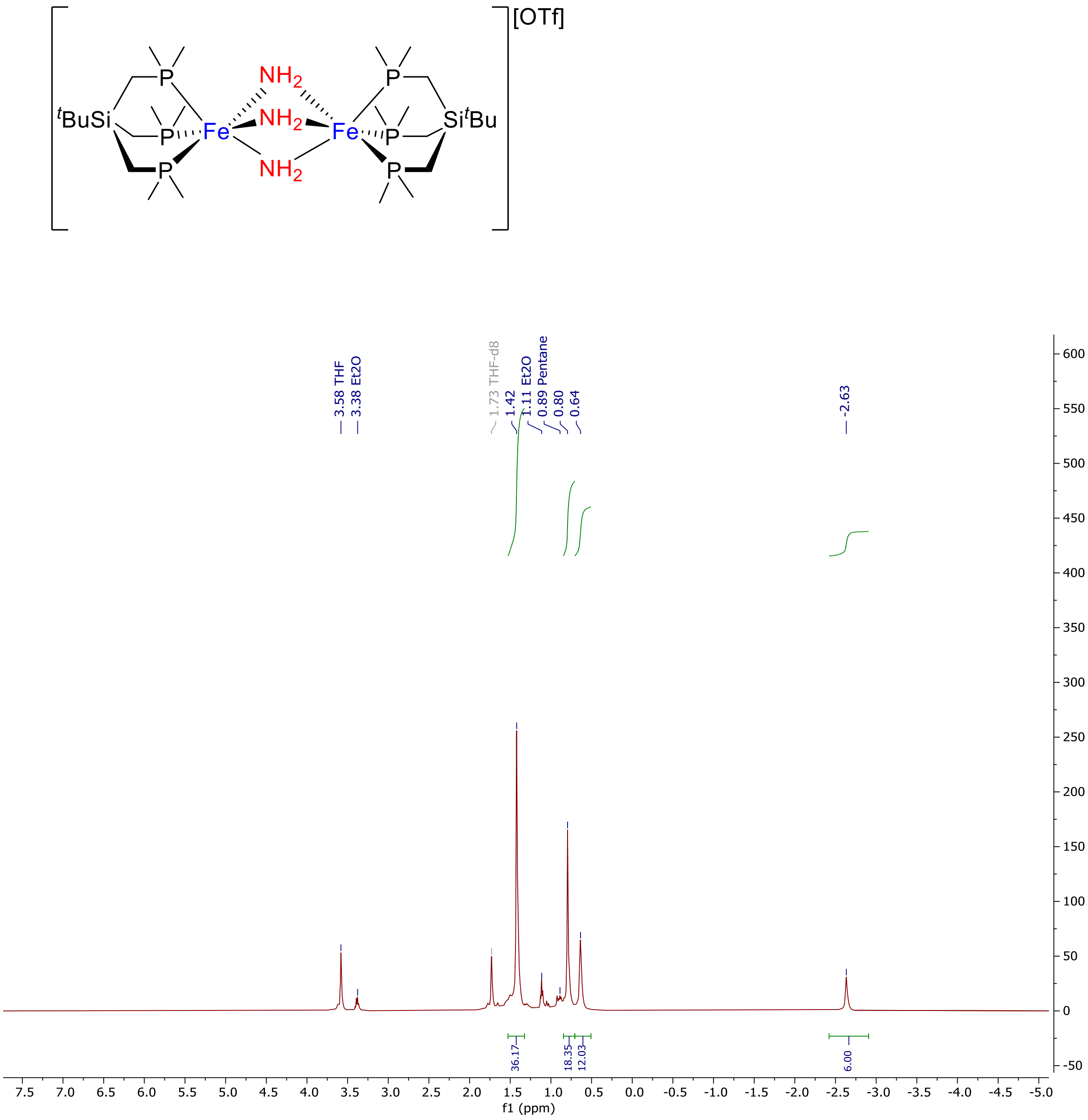

Figure SA.18 ^{1}H NMR of $[(^t\text{SiP}_3)_2\text{Fe}_2(\mu\text{–NH}_2)_3][\text{OTf}]$ (**4**) in THF-d_6

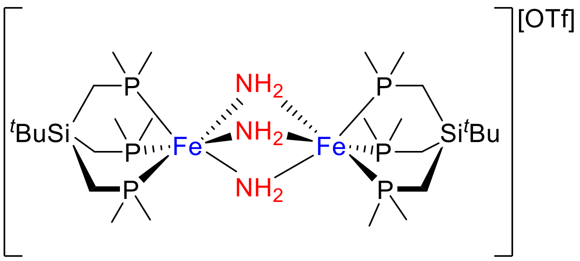

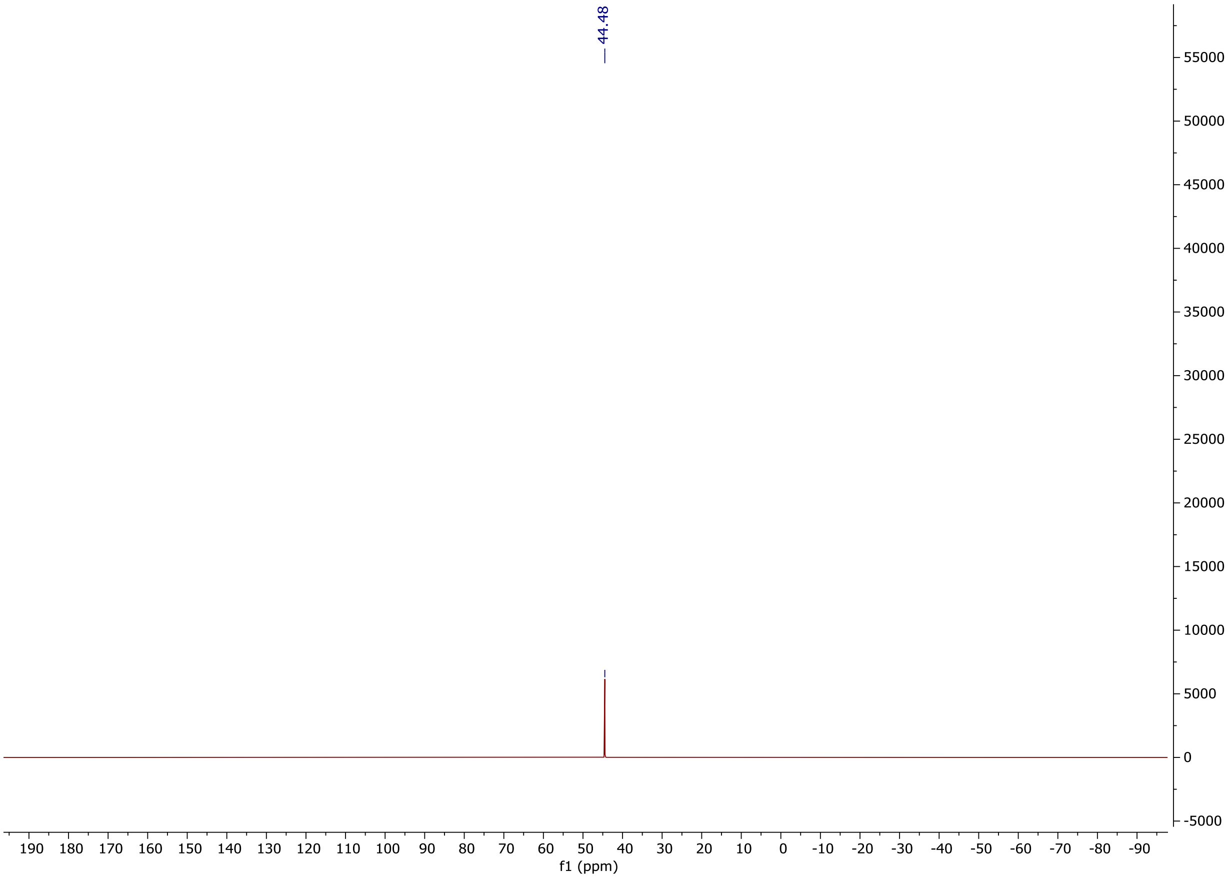

Figure SA.19 $^{31}P\{^{1}H\}$ NMR of $[(^{t}SiP_3)_2Fe_2(\mu\text{–}NH_2)_3][OTf]$ (**4**) in THF-d_6

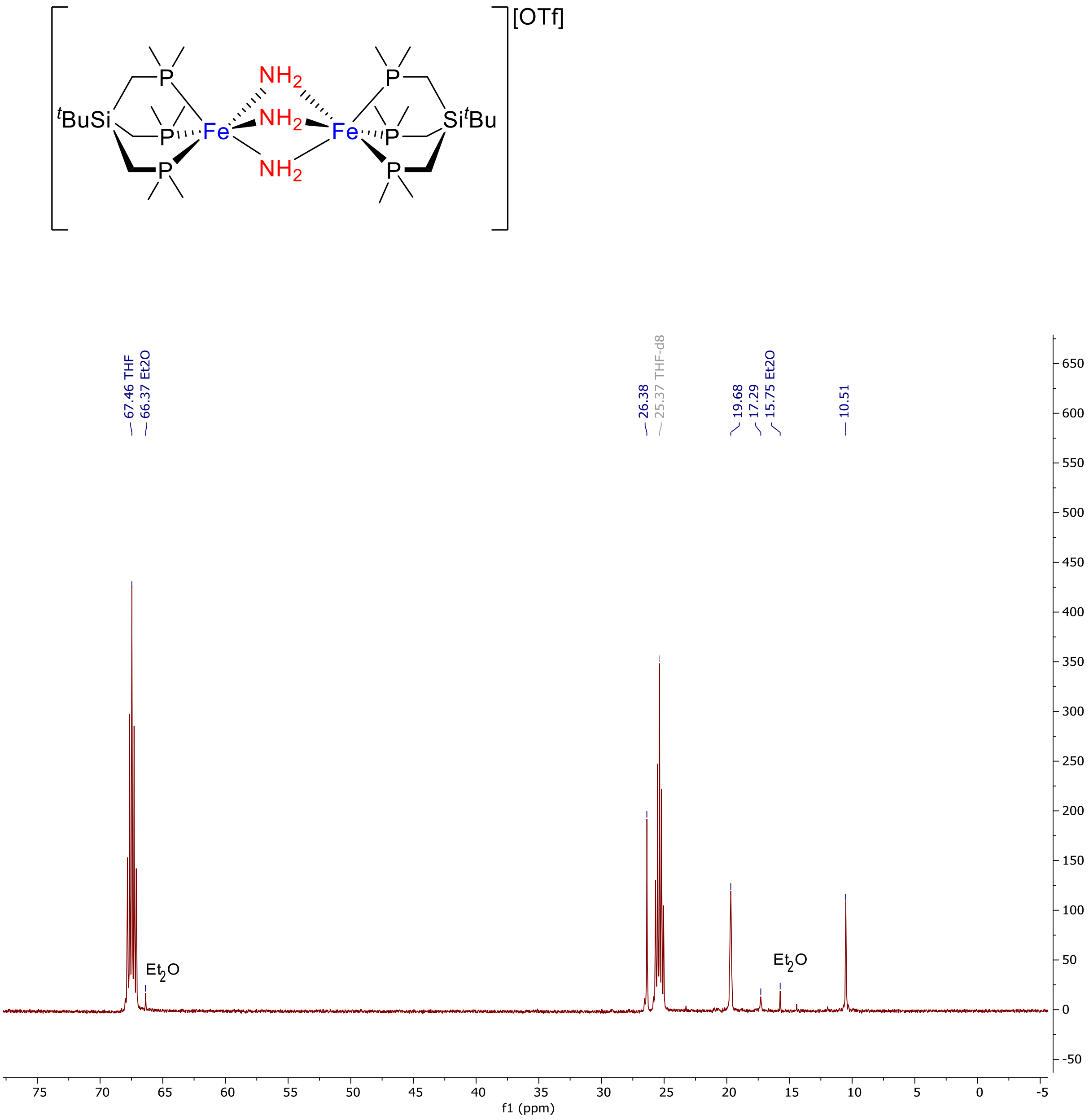

Figure SA.20 ^{13}C NMR of [(^{t}SiP$_3$)$_2$Fe$_2$(μ–NH$_2$)$_3$][OTf] (**4**) in THF-*d*$_6$

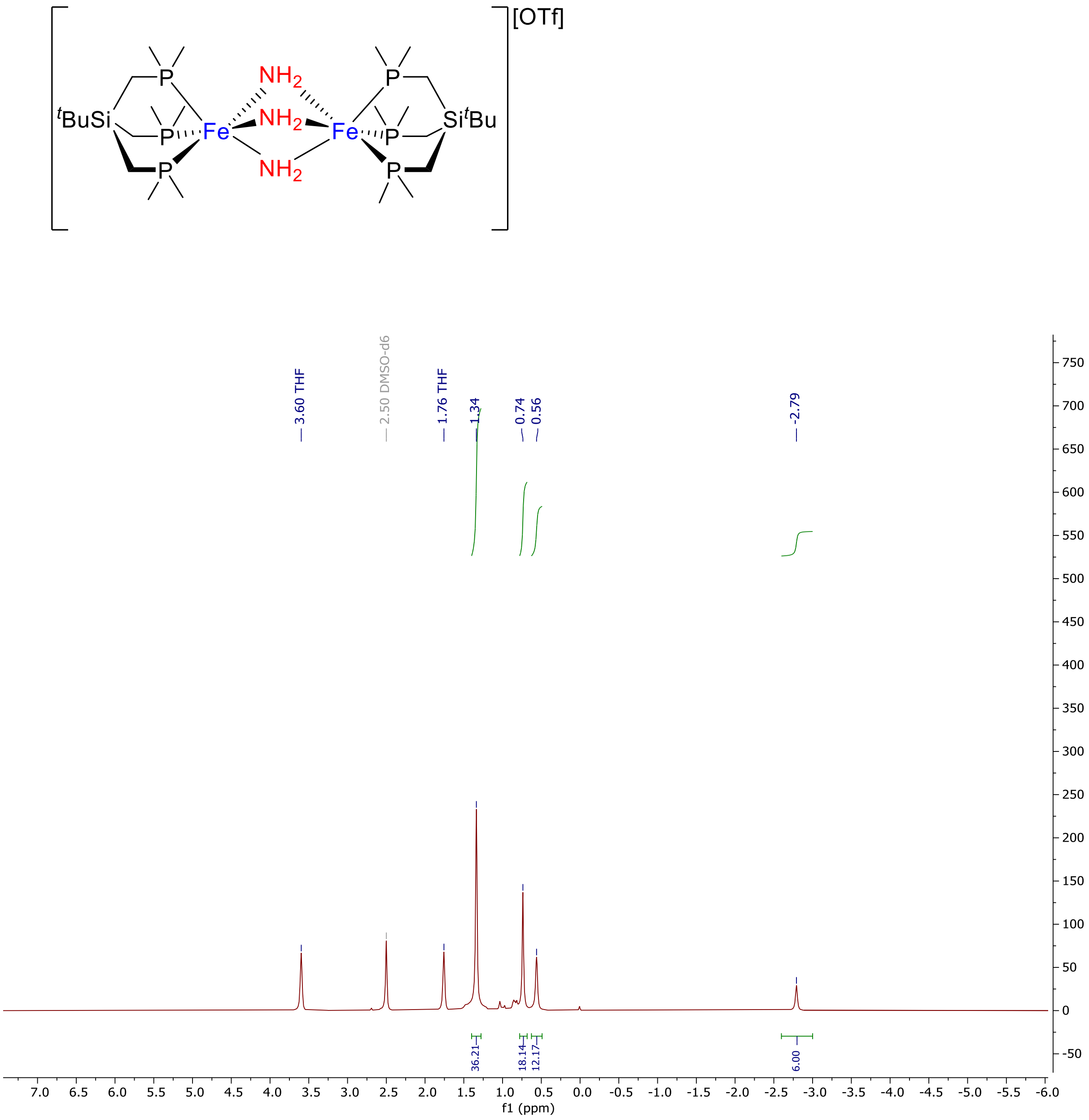

Figure SA.21 ^{1}H NMR of [(^{t}SiP$_3$)$_2$Fe$_2$(μ–NH$_2$)$_3$][OTf] (**4**) in DMSO-d_6

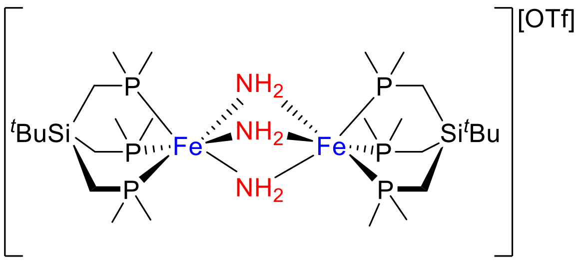

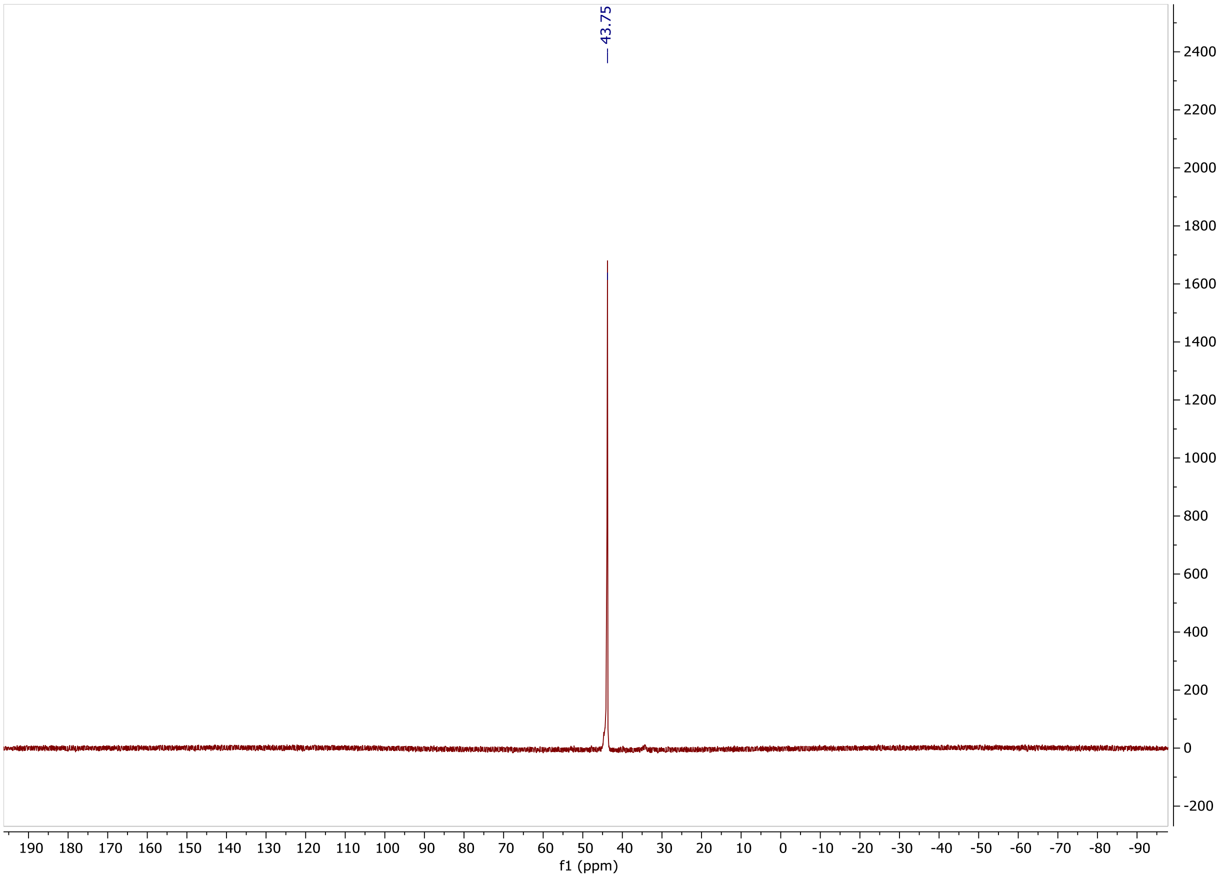

Figure SA.22 $^{31}P\{^{1}H\}$ NMR of [($^{t}SiP_3$)$_2$Fe$_2$(μ–NH$_2$)$_3$][OTf] (**4**) in DMSO-d_6

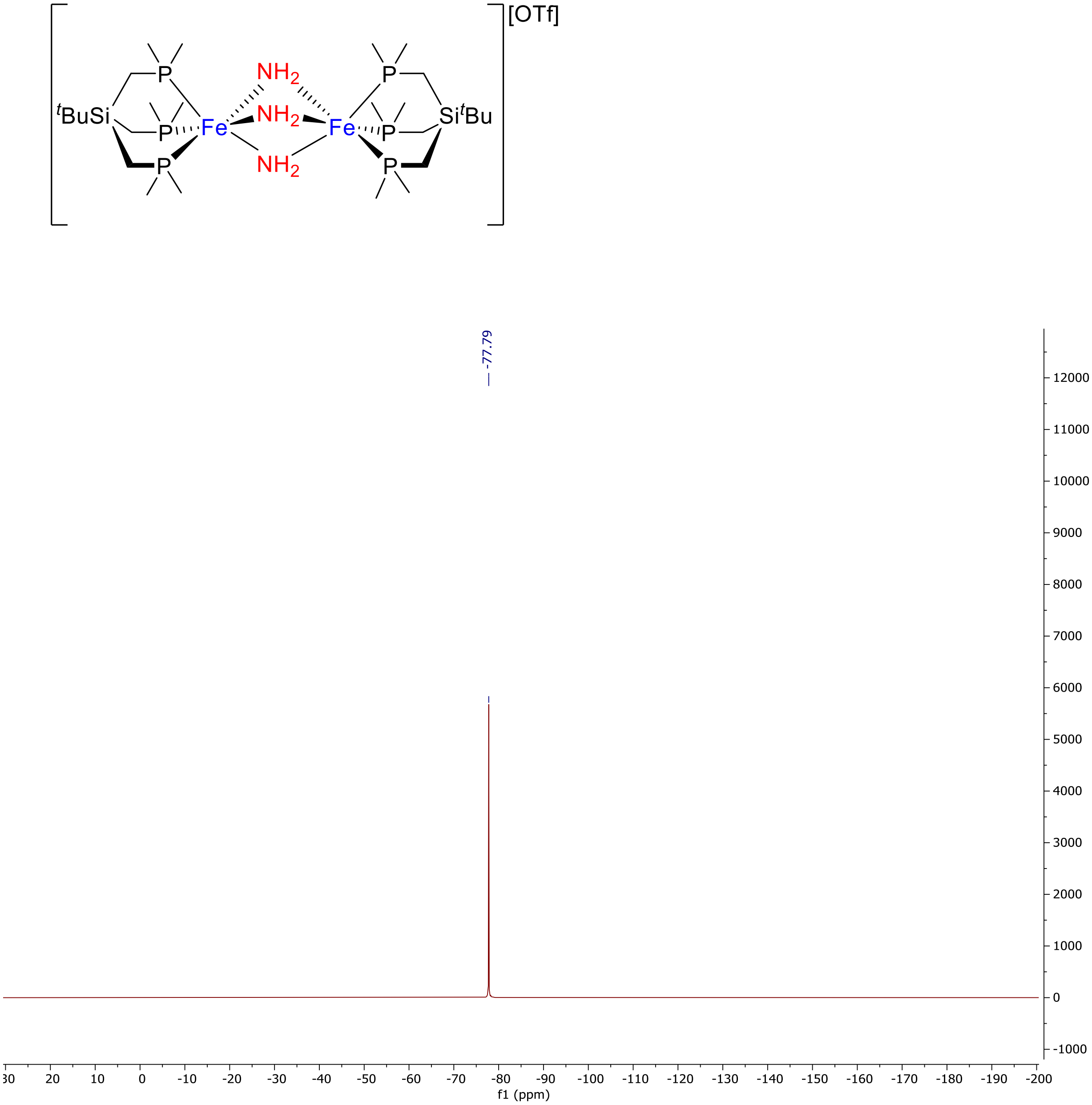

Figure SA.23 ^{19}F NMR of $[(^tSiP_3)_2Fe_2(\mu\text{–}NH_2)_3][OTf]$ (**4**) in DMSO-d_6

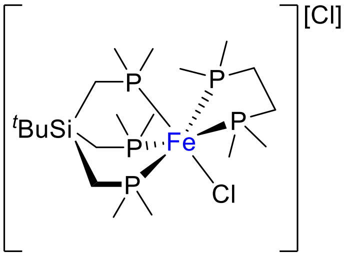

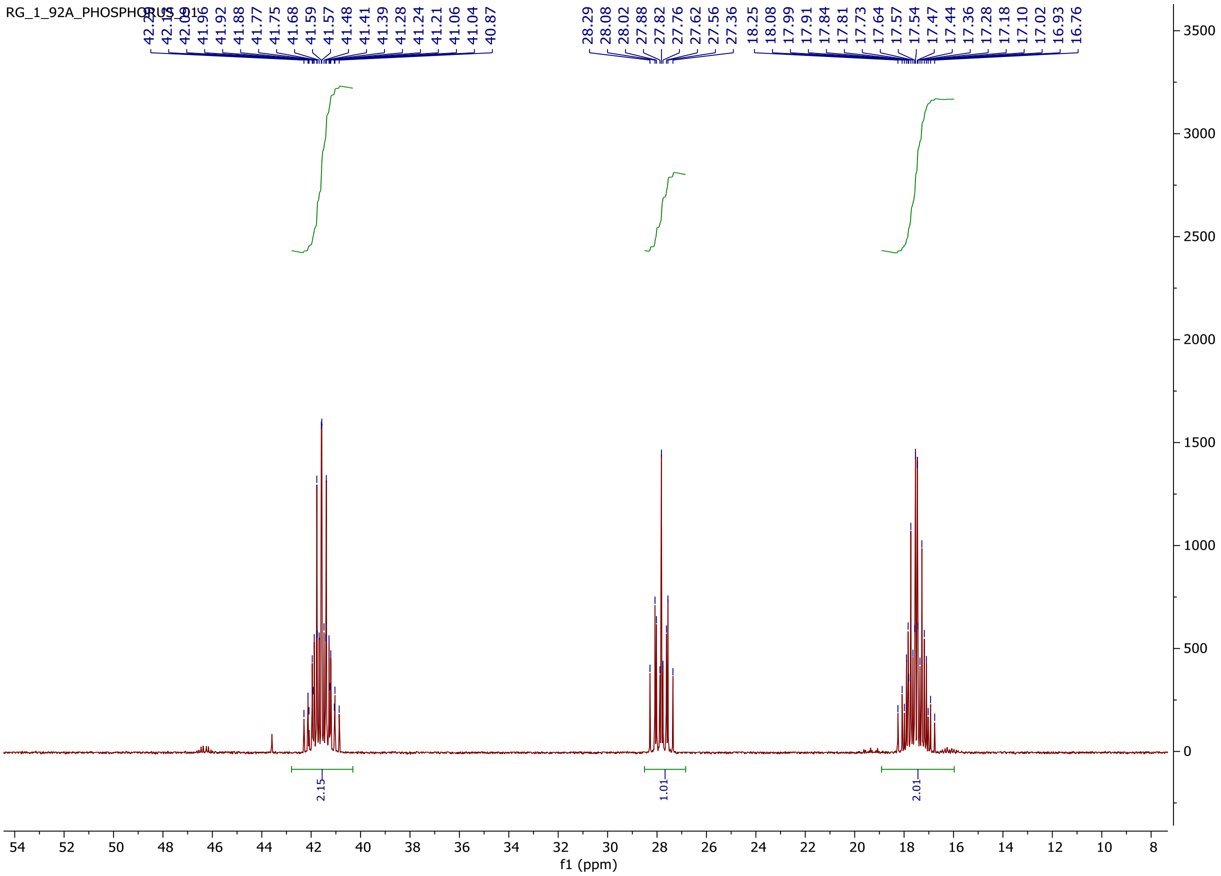

Figure SA.24 $^{31}P\{^1H\}$ NMR of [^{t}SiP$_3$Fe(dmpe)(Cl)][Cl] (**8**) in MeCN-d_3

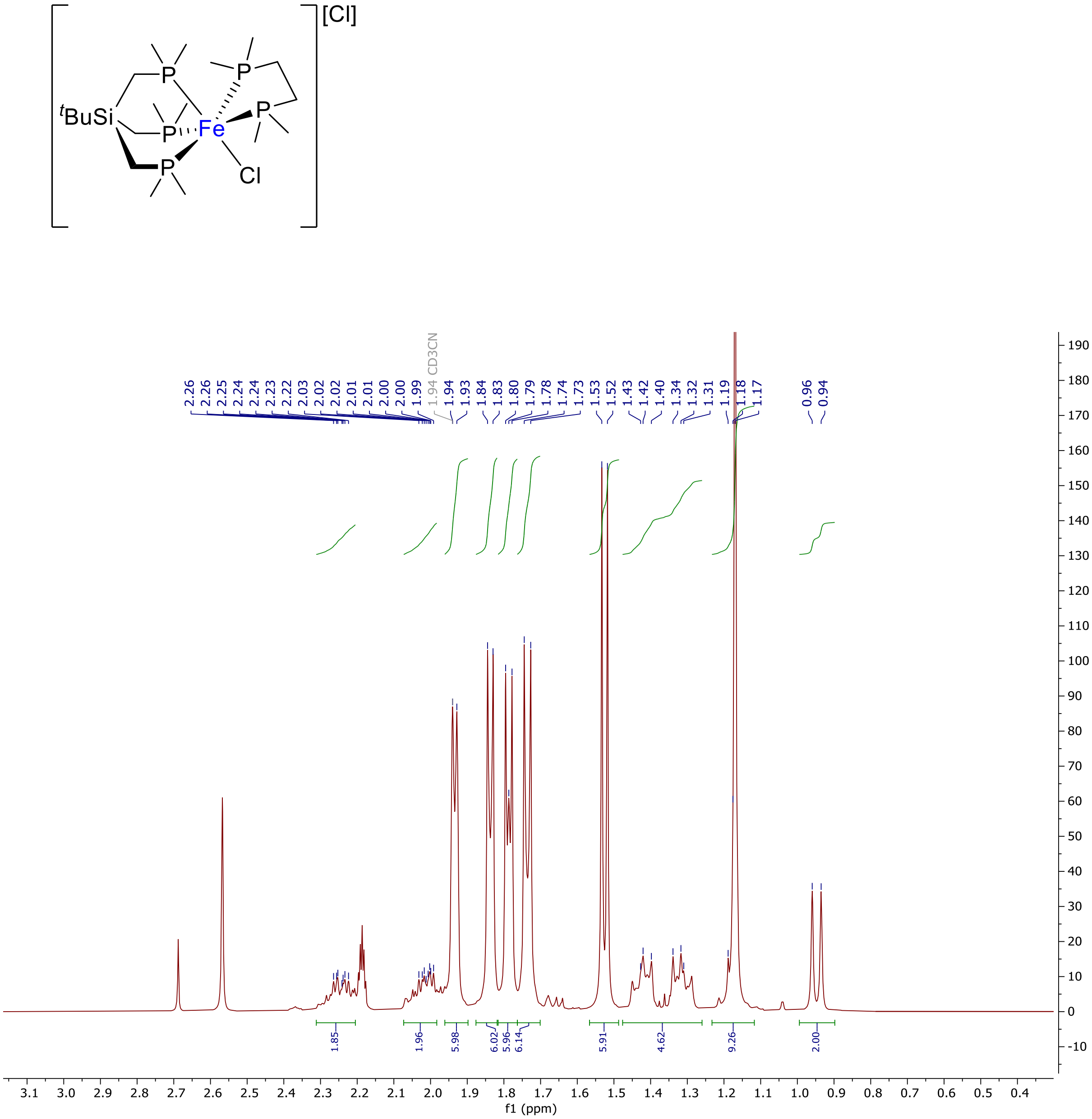

Figure SA.25 ^{1}H NMR of [^{t}SiP$_3$Fe(dmpe)(Cl)][Cl] (**8**) in MeCN-*d*$_3$

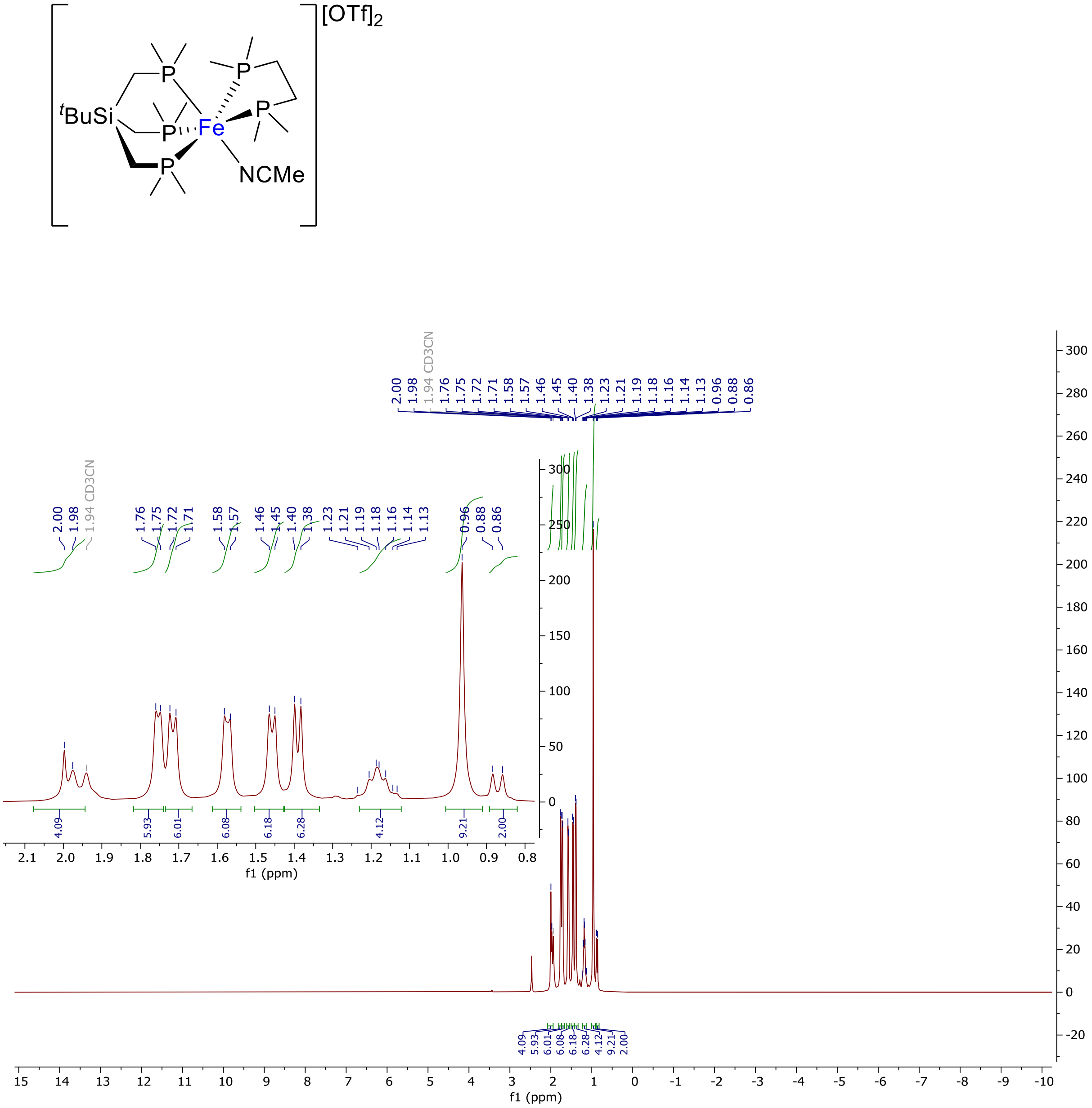

Figure SA.26 ^{1}H NMR of [^{t}SiP$_3$Fe(dmpe)(NCMe)][OTf]$_2$ (**6**) in MeCN-d_3

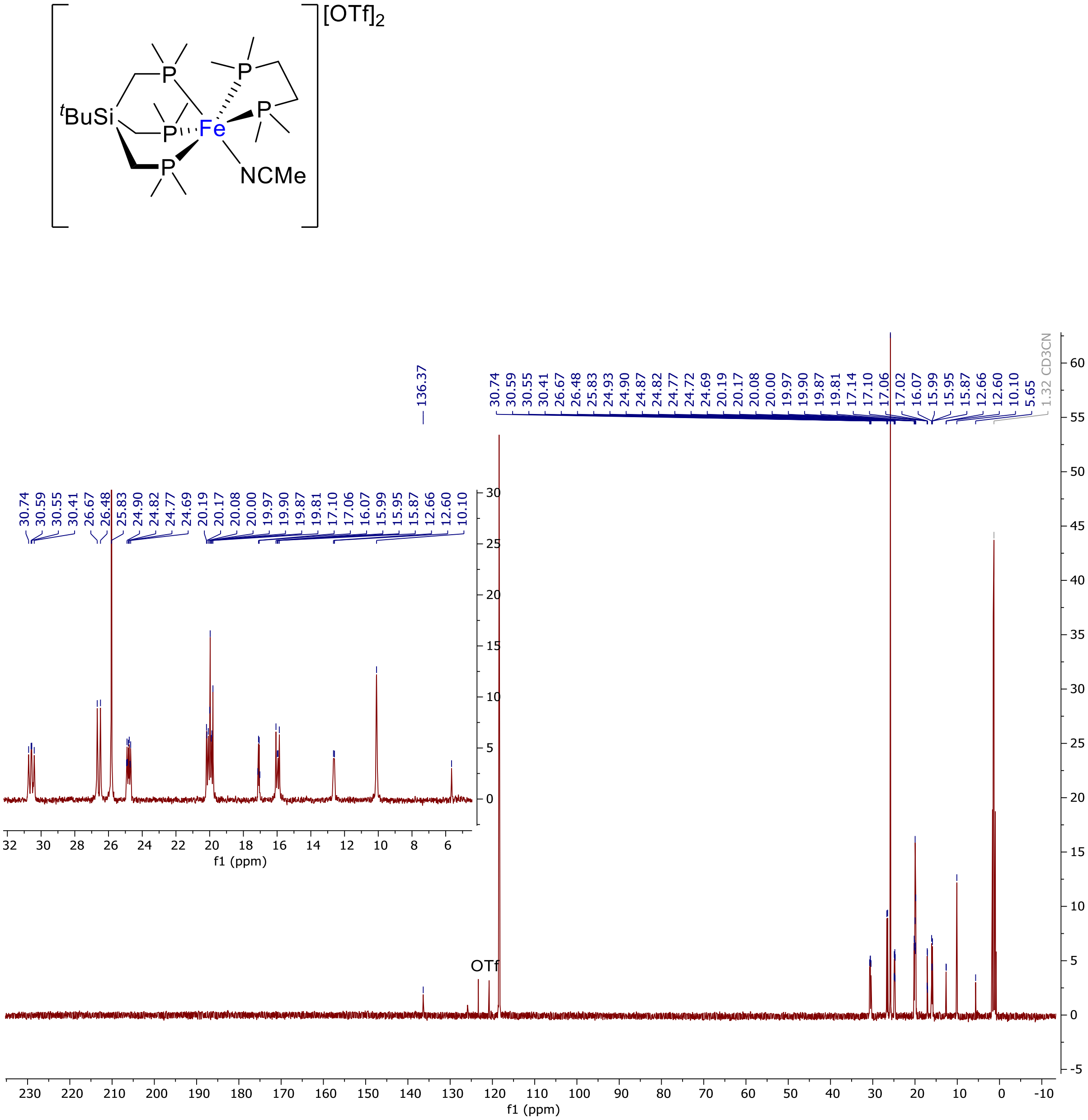

Figure SA.27 ^{13}C NMR of [^{t}SiP$_3$Fe(dmpe)(NCMe)][OTf]$_2$ (**6**) in MeCN-d_3

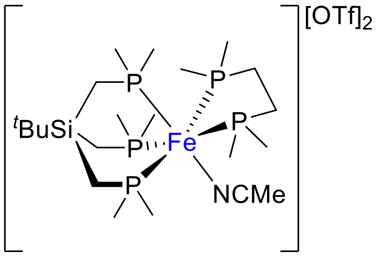

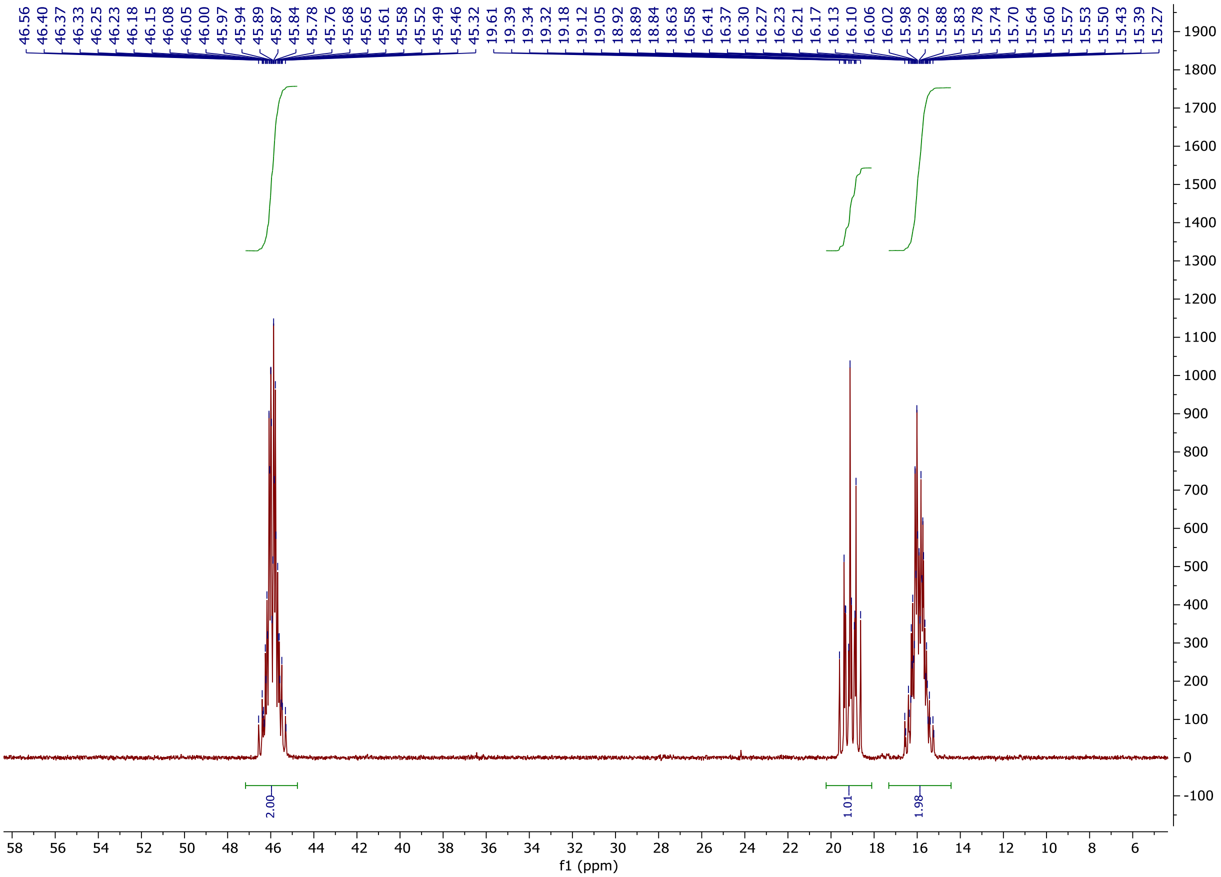

Figure SA.28 ^{31}P{^{1}H} NMR of [^{t}SiP$_3$Fe(dmpe)(NCMe)][OTf]$_2$ (**6**) in MeCN-d_3

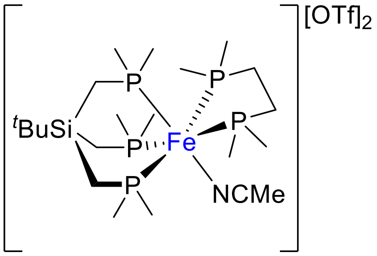

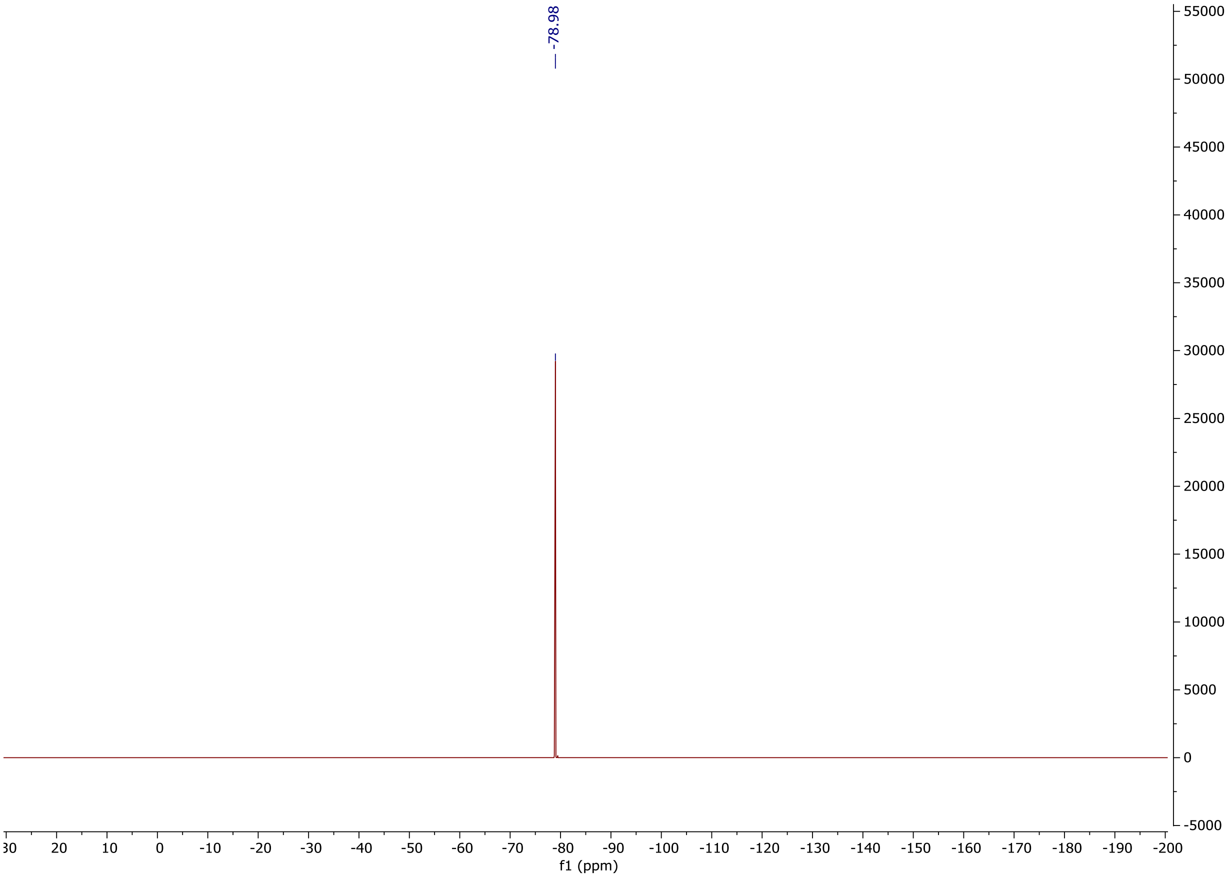

Figure SA.29 ^{19}F NMR of [^{t}SiP$_3$Fe(dmpe)(NCMe)][OTf]$_2$ (**6**) in MeCN-d_3

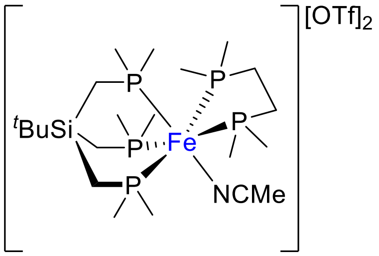

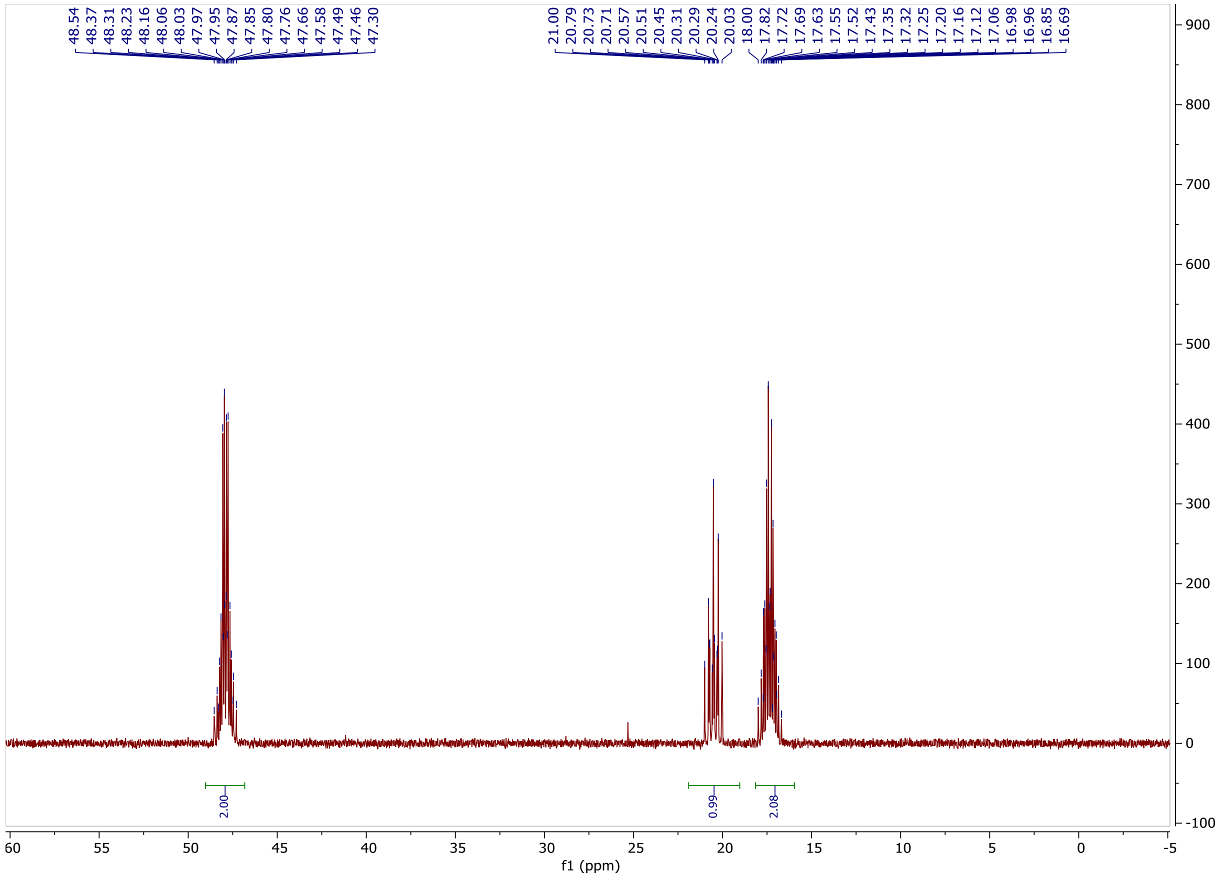

Figure SA.30 $^{31}P\{^{1}H\}$ NMR of [$^{t}SiP_3Fe(dmpe)(NCMe)][OTf]_2$ (**6**) in DMSO-d_6

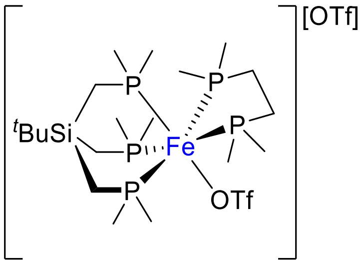

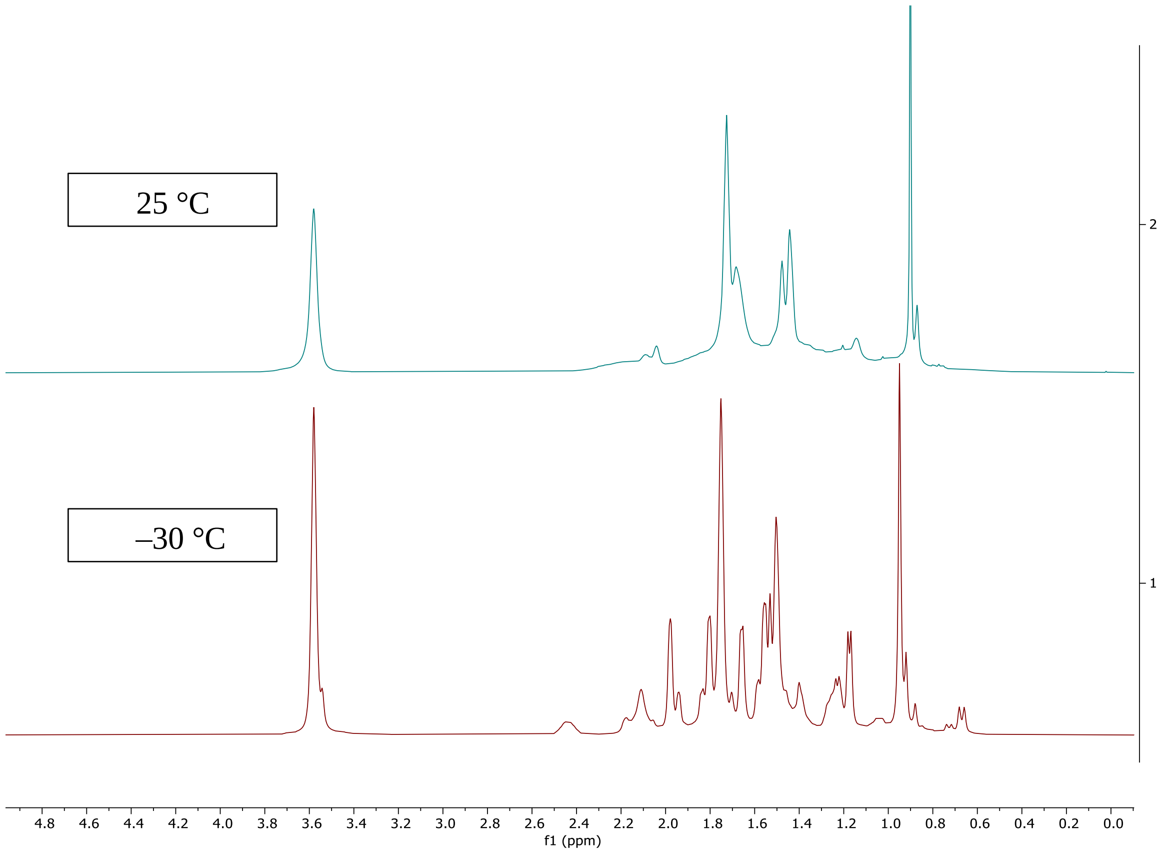

Figure SA.31 ^{1}H NMR of [^{t}SiP$_3$Fe(dmpe)(OTf)][OTf] (**9**) in THF-d_6 at 25 °C (top) and –30 °C (bottom)

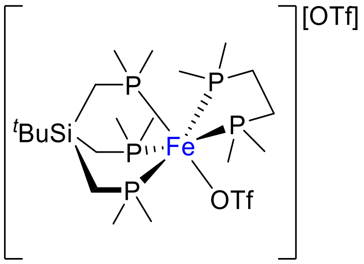

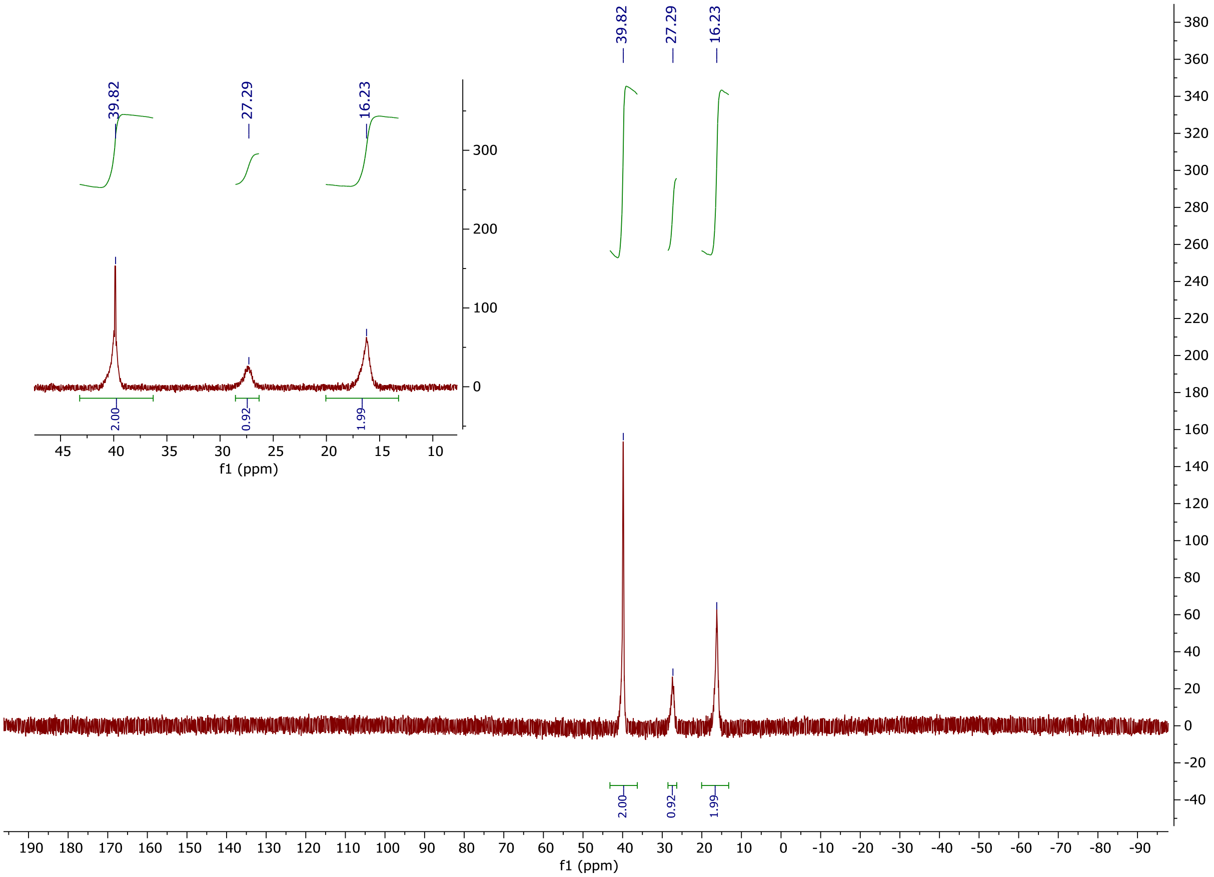

Figure SA.32 ^{31}P{^{1}H} NMR of [^{t}SiP$_3$Fe(dmpe)(OTf)][OTf] (**9**) in THF-d_6

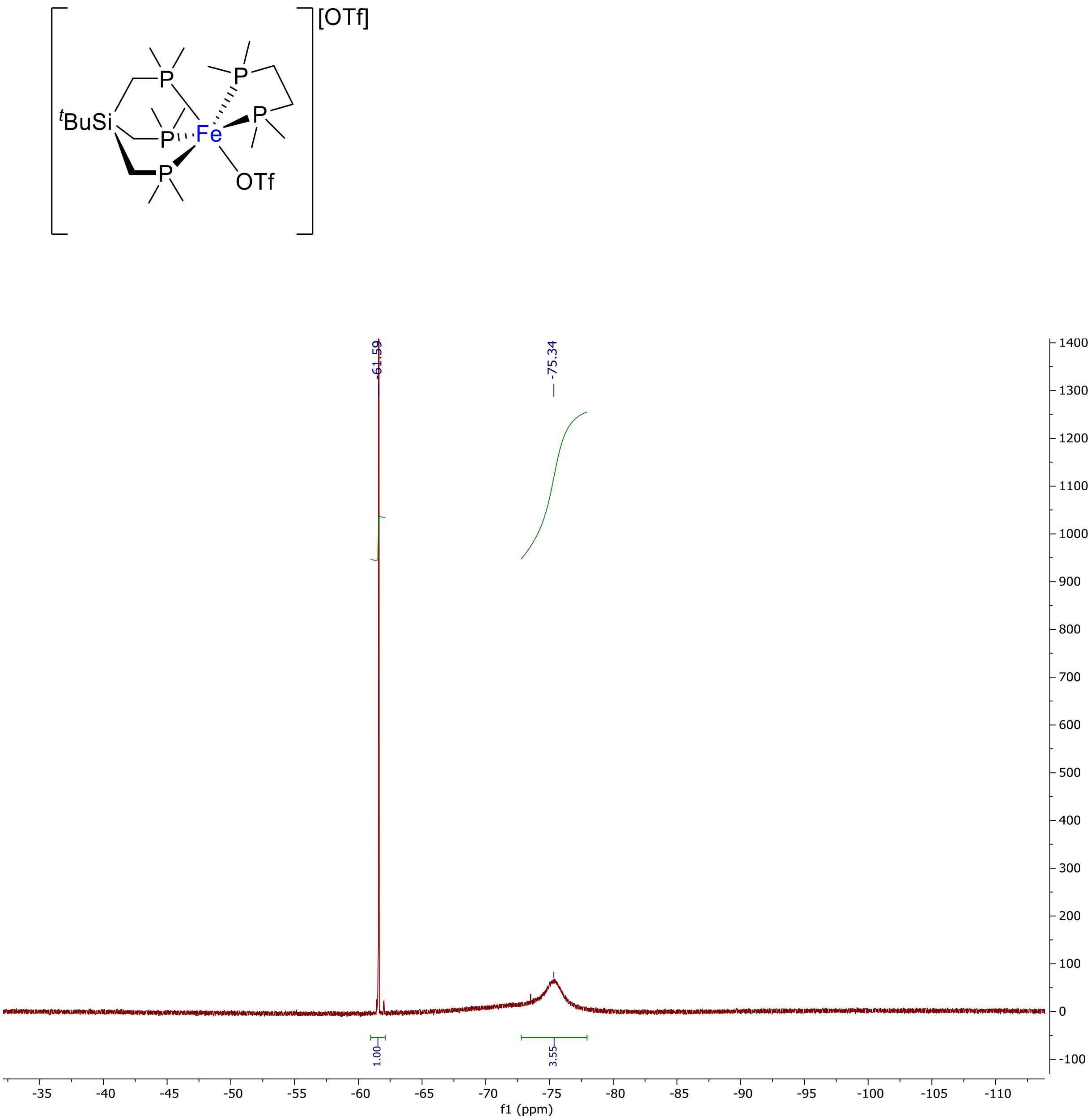

Figure SA.33 ^{19}F NMR of [^{t}SiP$_3$Fe(dmpe)(OTf)][OTf] (**9**) in THF-d_6

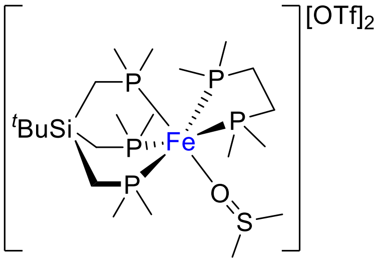

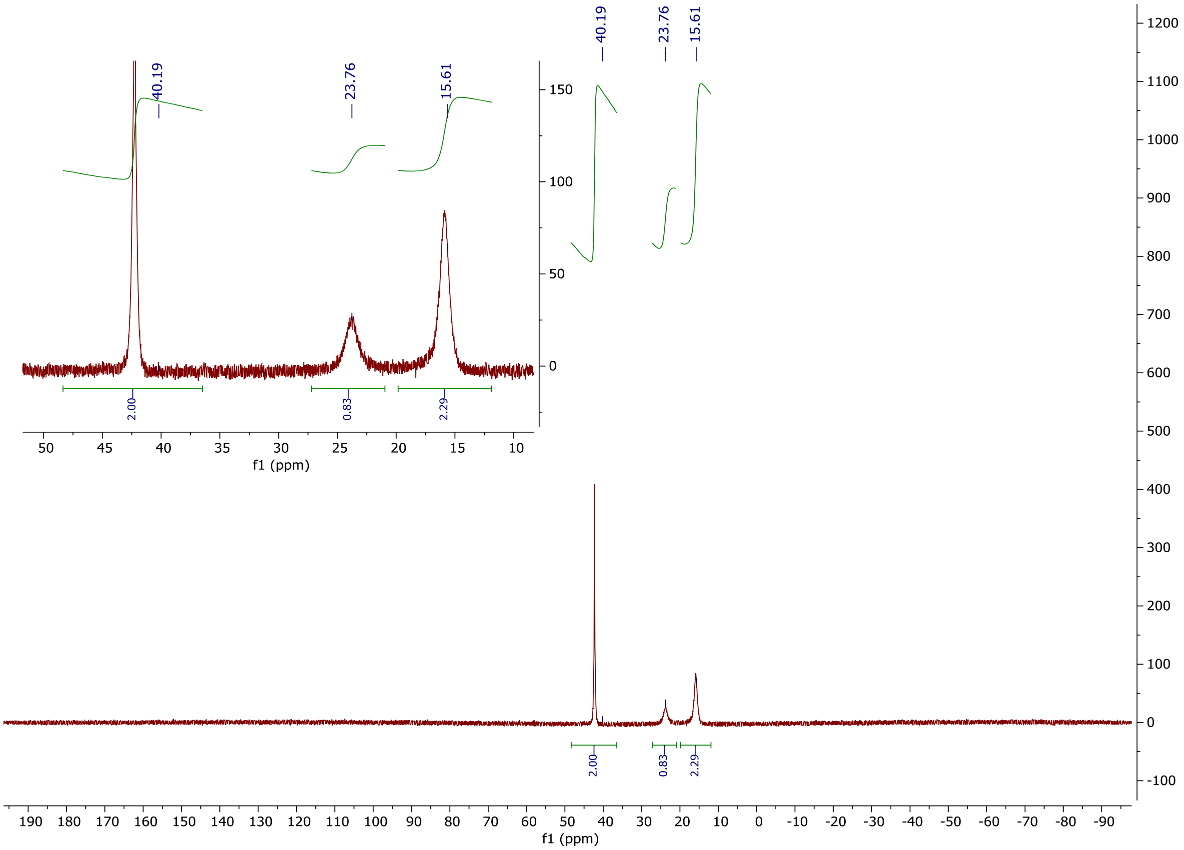

Figure SA.34 $^{31}P\{^1H\}$ NMR of [^{t}SiP$_3$Fe(dmpe)(DMSO)][OTf]$_2$ (**11**) in DMSO-d_6

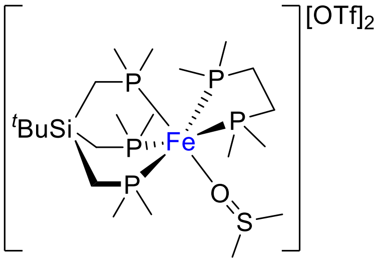

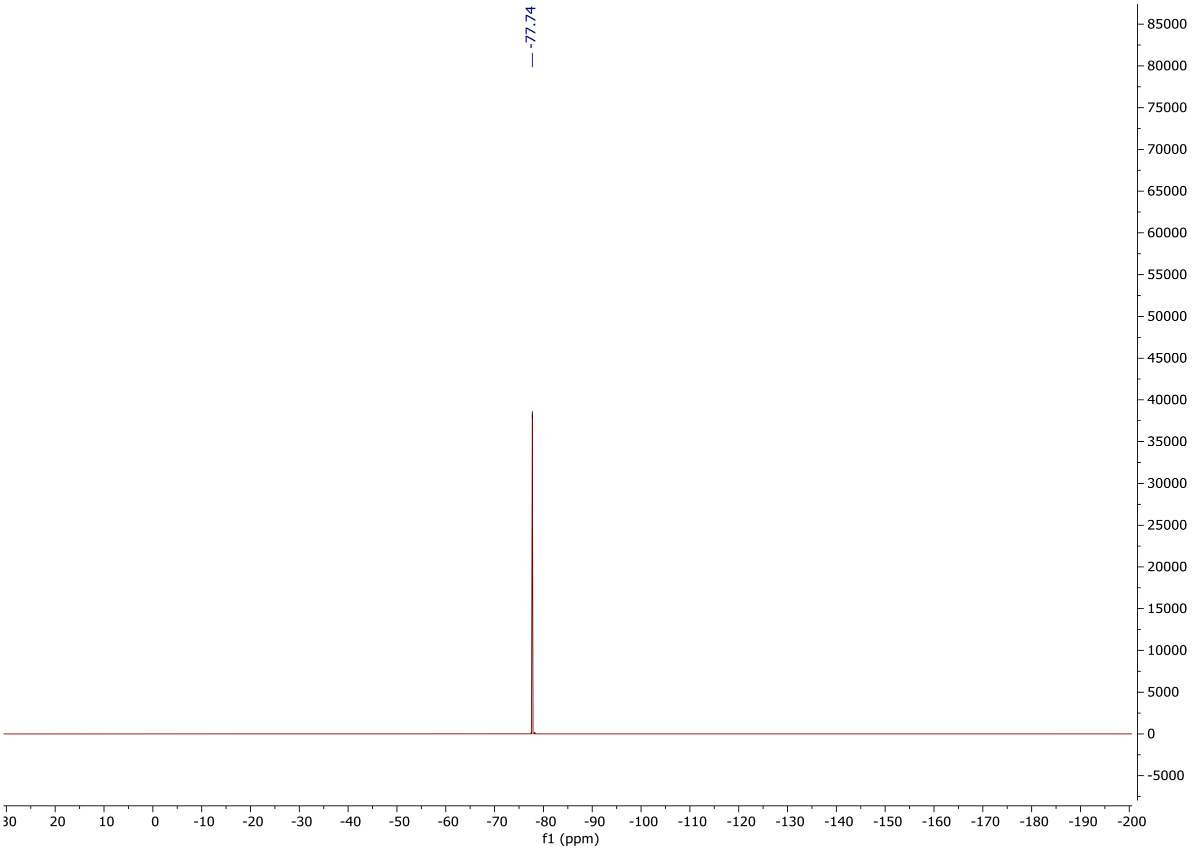

Figure SA.35 ^{19}F NMR of [^{t}SiP$_3$Fe(dmpe)(DMSO)][OTf]$_2$ (**11**) in DMSO-d_6

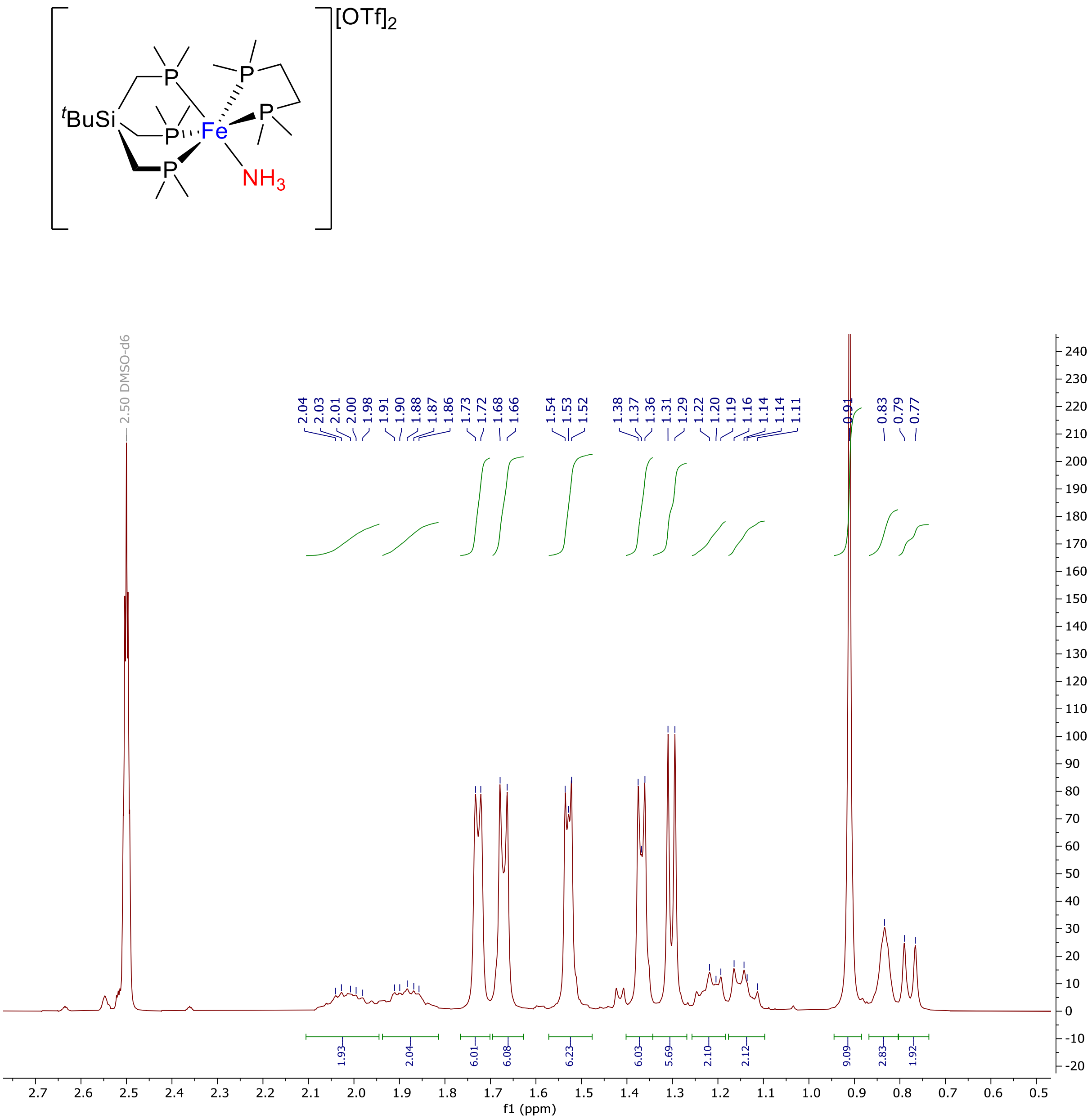

Figure SA.36 ^{1}H NMR of [^{t}SiP$_3$Fe(dmpe)(NH$_3$)][OTf]$_2$ (**7**) in DMSO-d_6

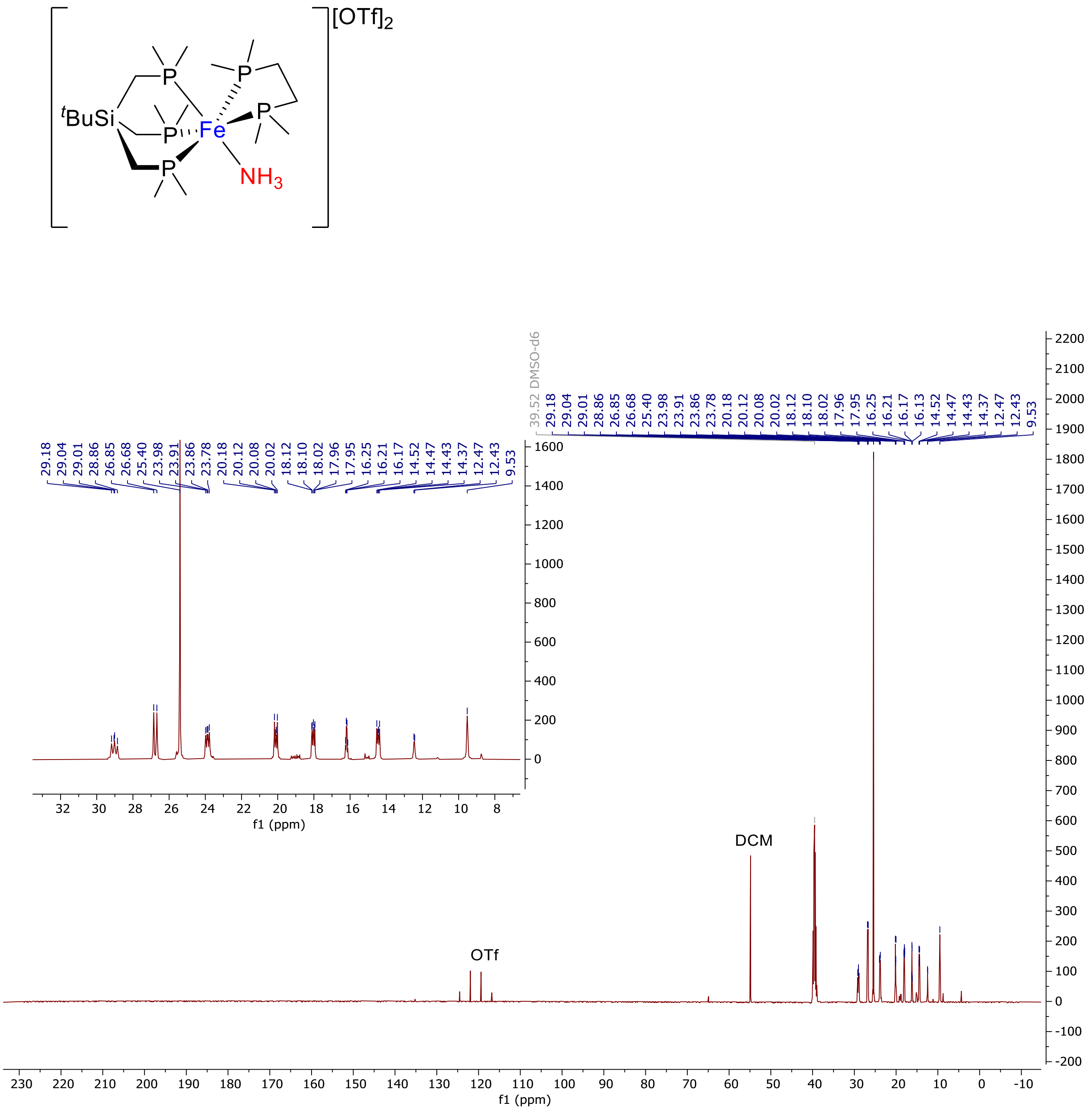

Figure SA.37 ^{13}C NMR of [^{t}SiP$_3$Fe(dmpe)(NH$_3$)][OTf]$_2$ (**7**) in DMSO-*d*$_6$

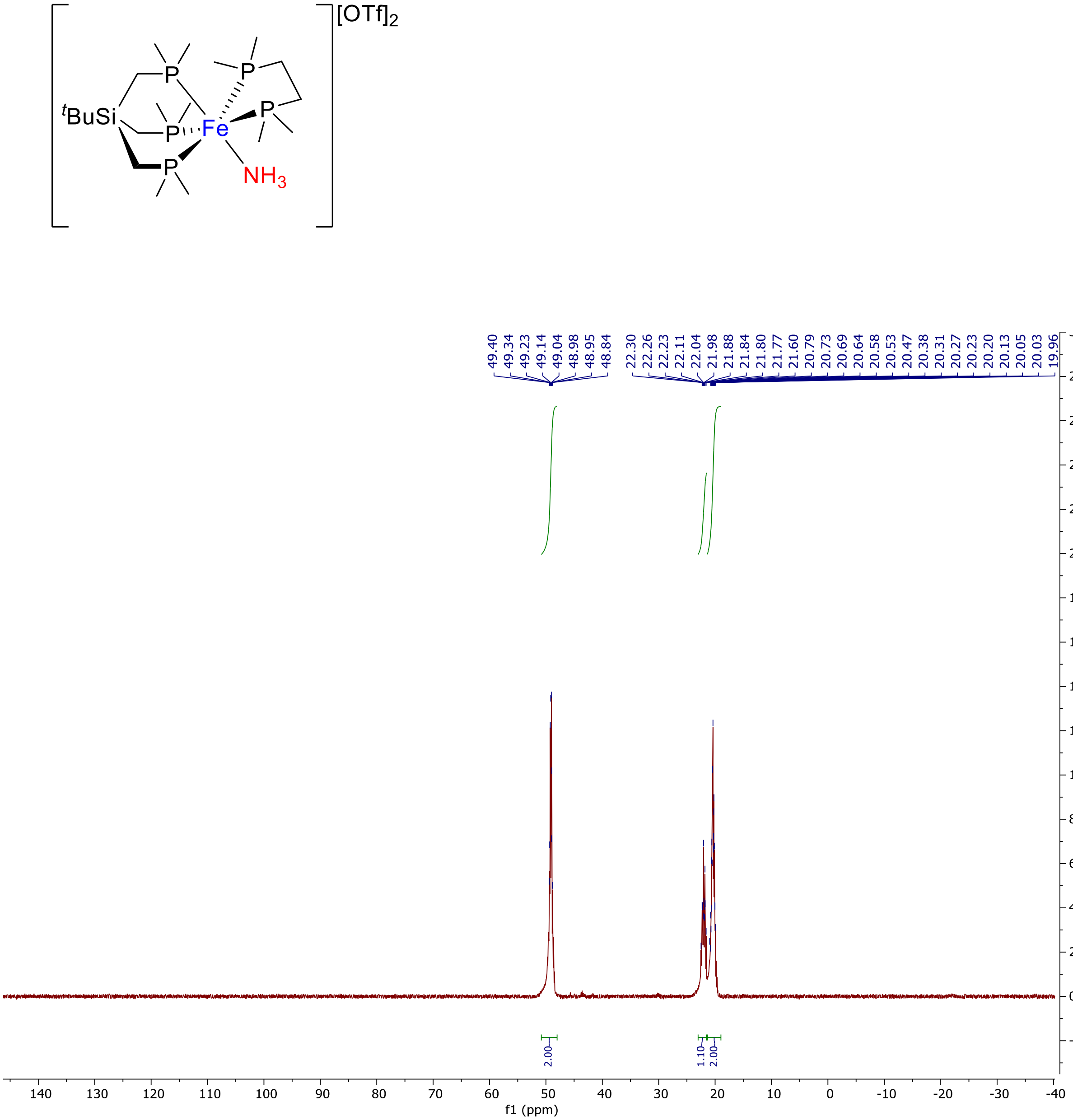

Figure SA.38 $^{31}P\{^{1}H\}$ NMR of [$^{t}SiP_3Fe(dmpe)(NH_3)$][OTf]$_2$ (**7**) in DMSO-d_6

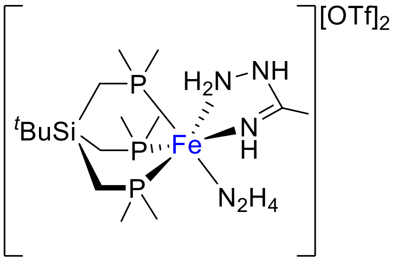

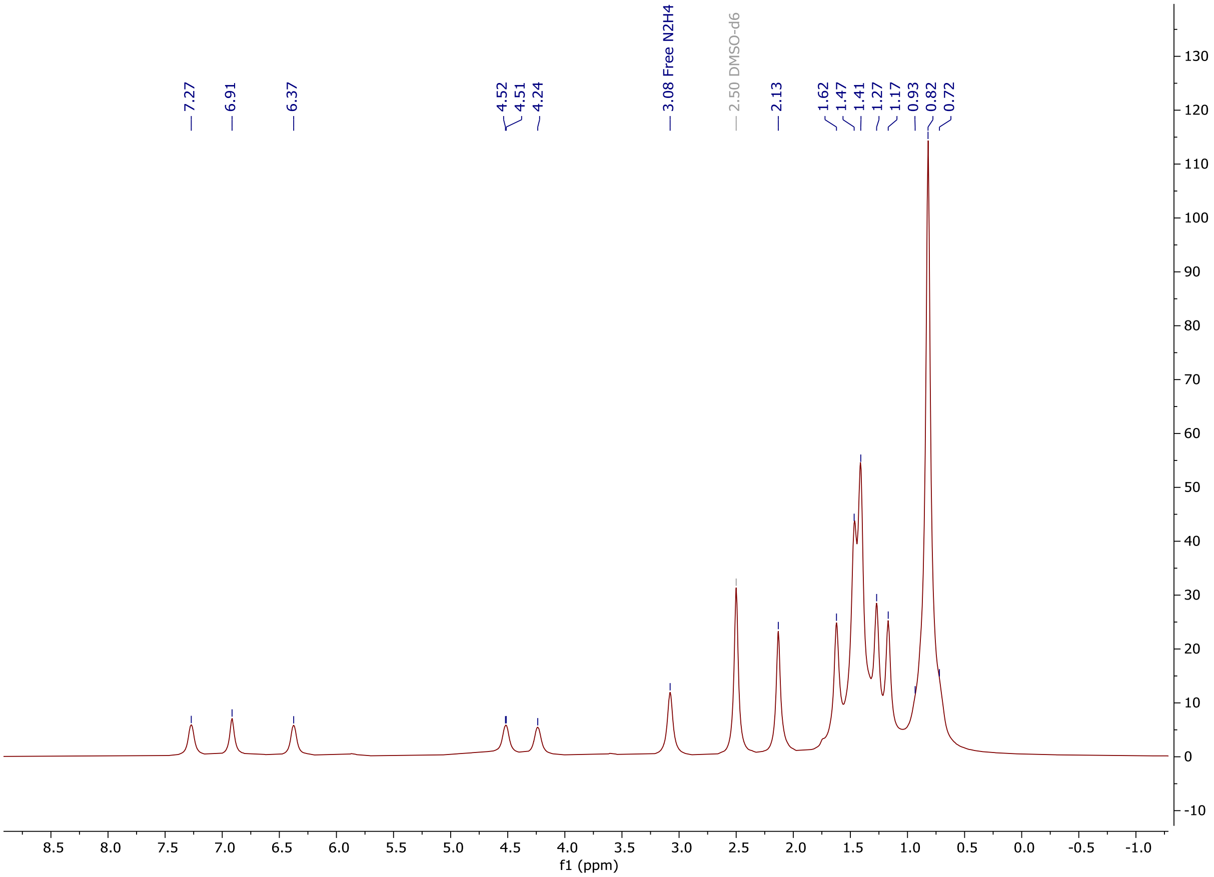

Figure SA.39 ^{1}H NMR of [^{t}SiP$_3$Fe(N$_2$H$_4$)(MeC(NH)NH$_2$NH)][OTf]$_2$ (**10**) in DMSO-d_6

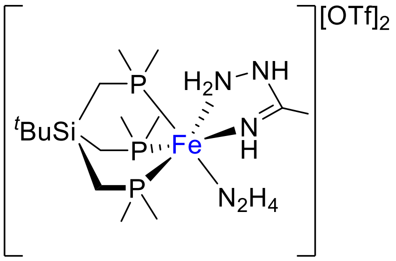

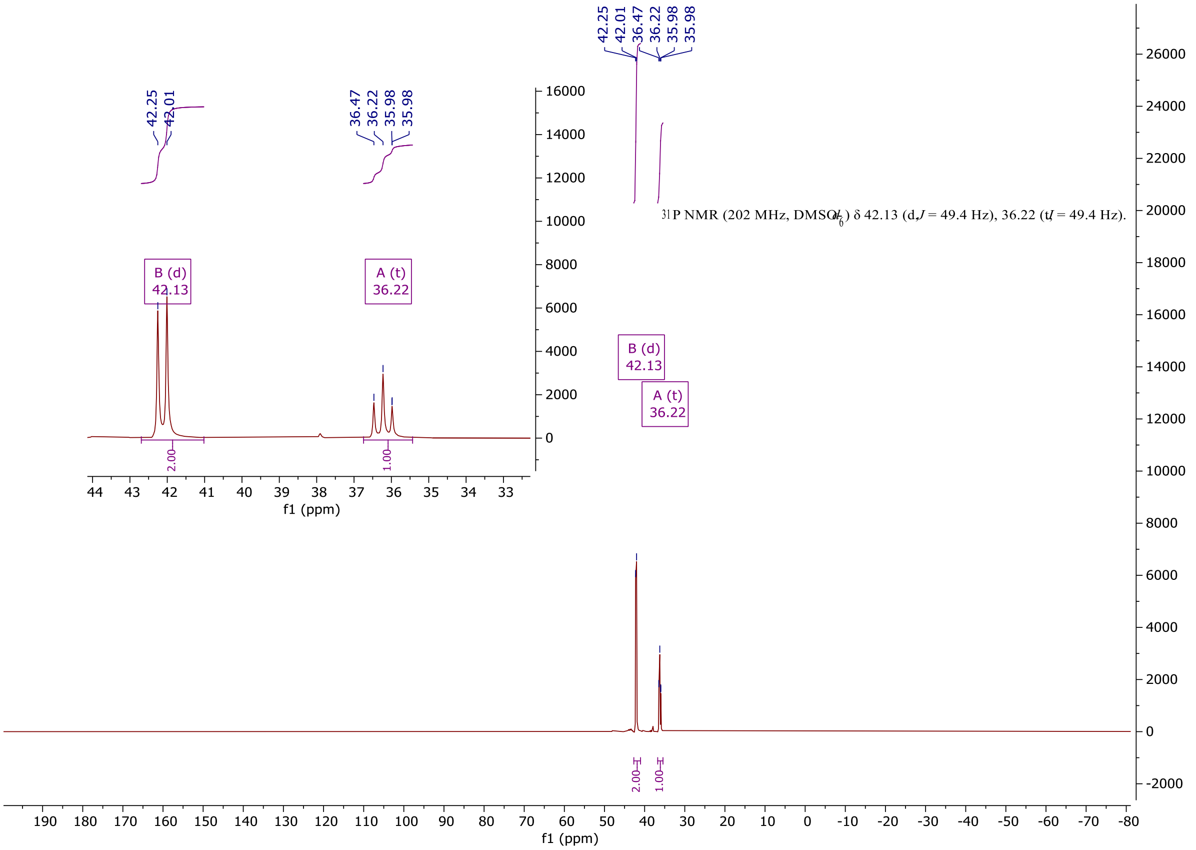

Figure SA.40 $^{31}P\{^{1}H\}$ NMR of [^{t}SiP$_3$Fe(N$_2$H$_4$)(MeC(NH)NH$_2$NH)][OTf]$_2$ (**10**) in DMSO-d_6

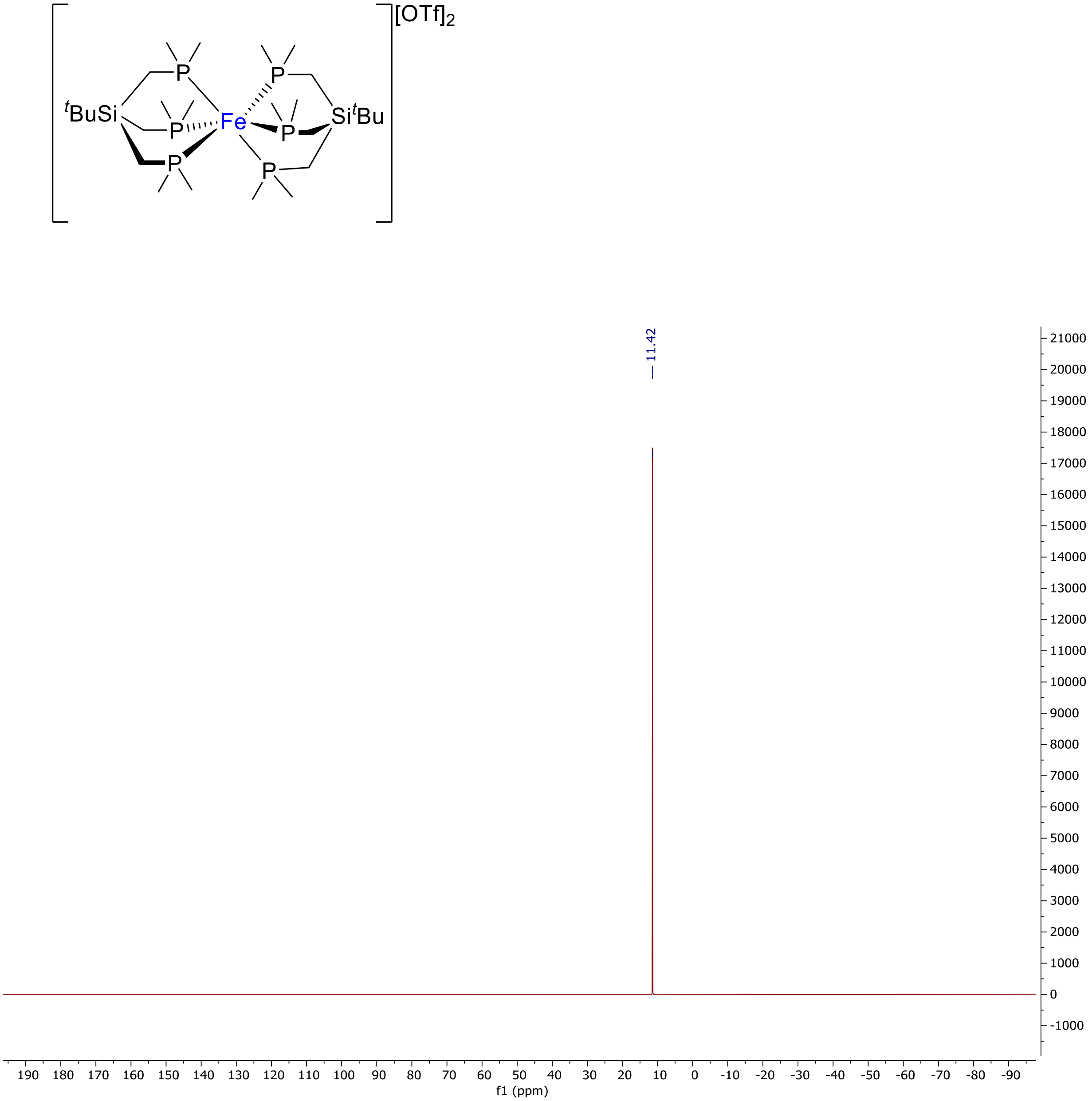

Figure SA.41 $^{31}P\{^{1}H\}$ NMR of $[(^{t}SiP_3)_2Fe][OTf]_2$ (**5**) in DMSO-*d*$_6$

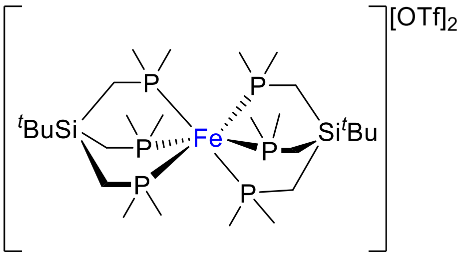

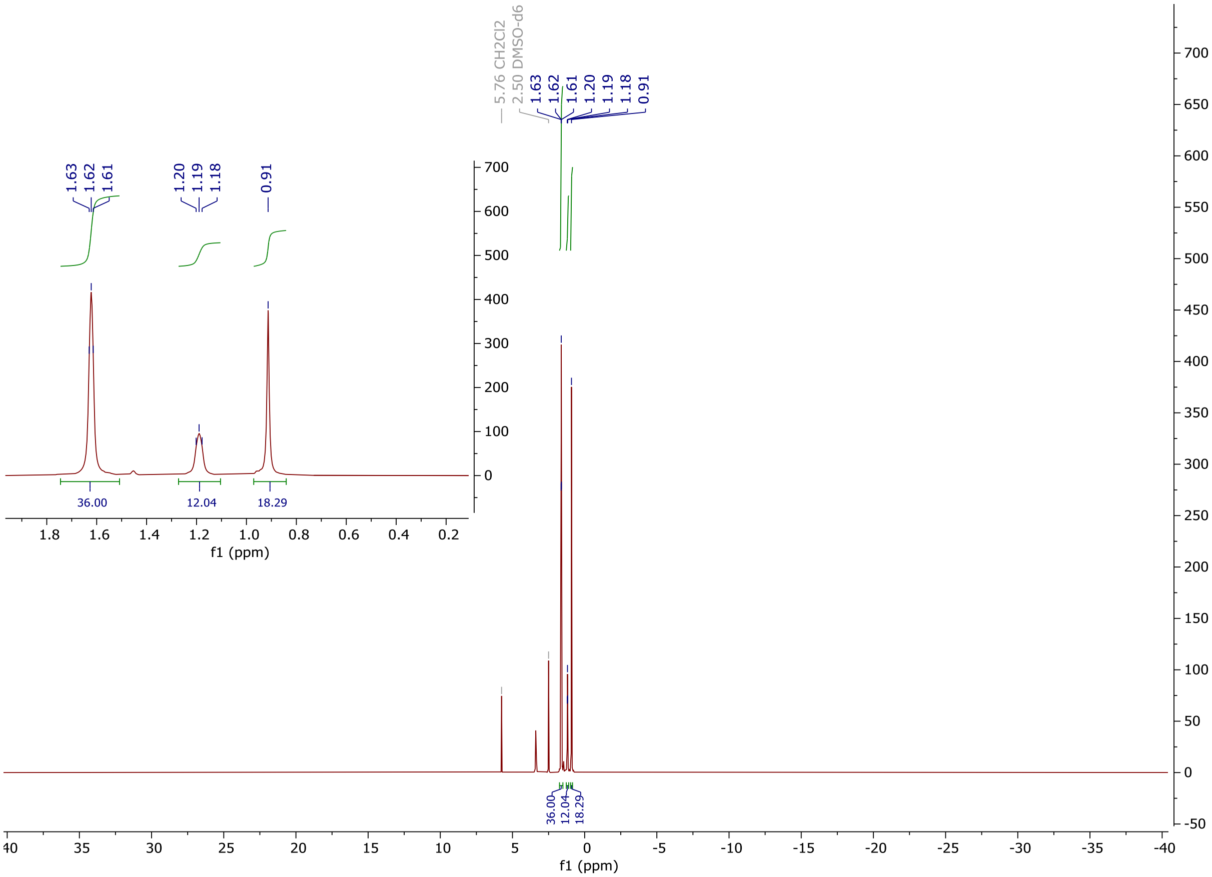

Figure SA.42 ^{1}H NMR of [(^{t}SiP$_3$)$_2$Fe][OTf]$_2$ (**5**) in DMSO-d_6

SA.2 Crystallographic Data

SA.2.1 Crystal Data and Experimental for Complex 2

Crystal structure from crystals provide, they appear twinned, but refinement using the 2 components of the twin is reported here. The second domain is rotated from first domain by 179.9 degrees about the reciprocal axis 0.003 1.000 -0.001 and real axis -0.067 1.000 -0.030. BASF value 0.2829(7).

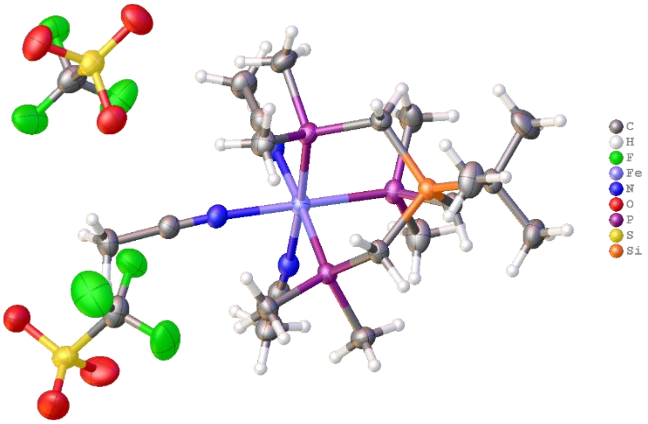

Experimental. Single orange block-shaped crystals of **MRS1018ATW** were used as received. A suitable crystal 0.17×0.12×0.11 mm^3 was selected and mounted on a None on an Bruker APEX-II CCD diffractometer. The crystal was kept at a steady T = 173(2) K during data collection. The structure was solved with the ShelXT (Sheldrick, G.M. (2015). Acta Cryst. A71, 3-8) structure solution program using the Intrinsic Phasing solution method and by using **Olex2** (Dolomanov et al., 2009) as the graphical interface. The model was refined with version 2018/3 of ShelXL (Sheldrick, Acta Cryst. A64 2008, 112-122) using Least Squares minimisation.

Crystal Data. $C_{21}H_{42}F_6FeN_3O_6P_3S_2Si$, M_r = 787.54, triclinic, P-1 (No. 2), a = 10.1234(16) Å, b = 10.4065(17) Å, c = 16.720(3) Å, α = 87.180(2)°, β = 89.315(2)°, γ = 86.376(2)°, V = 1755.7(5) Å^3, T = 173(2) K, Z = 2, Z' = 1, μ(MoKα) = 0.789, 12496 reflections measured, 12496 unique (R_{int} = 0.0460) which were used in all calculations. The final wR_2 was 0.1223 (all data) and R_1 was 0.0460 (I > 2(I)).

Compound	**MRS1018ATW**
CCDC	**1871069**
Formula	$C_{21}H_{42}F_6FeN_3O_6P_3S_2Si$
$D_{calc.}$/ g cm^{-3}	1.490
μ/mm^{-1}	0.789
Formula Weight	787.54
Colour	orange
Shape	block
Size/mm^3	0.17×0.12×0.11
T/K	173(2)
Crystal System	triclinic
Space Group	P-1
a/Å	10.1234(16)
b/Å	10.4065(17)
c/Å	16.720(3)
α/°	87.180(2)
β/°	89.315(2)
γ/°	86.376(2)
V/Å^3	1755.7(5)
Z	2
Z'	1
Wavelength/Å	0.710730
Radiation type	MoK$_\alpha$
Θ_{min}/°	1.219
Θ_{max}/°	25.900
Measured Refl.	12496
Independent Refl.	12496
Reflections with I > 2(I)	9842
R_{int}	0.0460
Parameters	401
Restraints	0
Largest Peak	0.830
Deepest Hole	-0.318
GooF	1.038
wR_2 (all data)	0.1223
wR_2	0.1113
R_1 (all data)	0.0618
R_1	0.0460

SA.2.2 Crystal Data and Experimental for Complex 3

Crystal Structure has two Fe(L)(NH3)3, 4 triflate anions, two waters and one Nitromethane moieties in the asymmetric cell. One of the triflates is disordered.

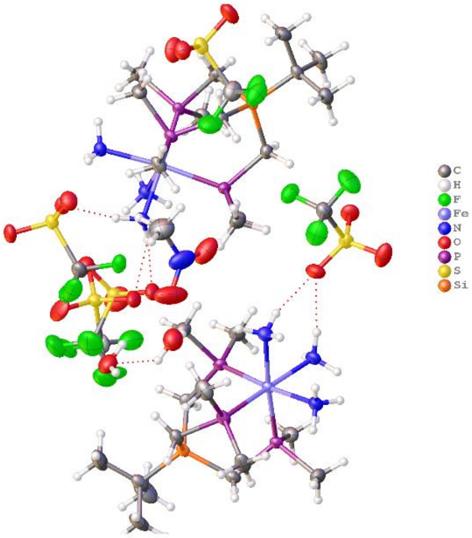

Compound	**MRS820D**
Formula	$C_{31}H_{89}F_{12}Fe_2N_7O_{15}P_6S_4Si_2$
CCDC	2023779
$D_{calc.}$/ g cm^{-3}	1.502
μ/mm^{-1}	7.170
Formula Weight	1510.03
Colour	orange
Shape	plate
Size/mm^3	0.35×0.30×0.06
T/K	100.01(10)
Crystal System	triclinic
Space Group	*P*-1
a/Å	14.3915(3)
b/Å	16.3759(3)
c/Å	16.8383(3)
α/°	72.9448(18)
β/°	64.938(2)
γ/°	70.772(2)
V/Å^3	3338.88(14)
Z	2
Z'	1
Wavelength/Å	1.54184
Radiation type	Cu K$_\alpha$
Θ_{min}/°	2.905
Θ_{max}/°	77.296
Measured Refl's.	49696
Indep't Refl's	13679
Refl's I≥2 σ(I)	11971
R_{int}	0.0702
Parameters	807
Restraints	30
Largest Peak	0.978
Deepest Hole	-0.832
GooF	1.073
wR_2 (all data)	0.1683
wR_2	0.1617
R_1 (all data)	0.0660
R_1	0.0588

Experimental. Single orange plate crystals of **MRS820D** Used as received. A suitable crystal with dimensions 0.35 × 0.30 × 0.06 mm^3 was selected and mounted on a nylon loop with paratone oil on a XtaLAB Synergy, Dualflex, HyPix diffractometer. The crystal was kept at a steady *T* = 100.01(10) K during data collection. The structure was solved with the ShelXT (Sheldrick, 2015) solution program using dual methods and by using Olex2 (Dolomanov et al., 2009) as the graphical interface. The model was refined with ShelXL 2018/3 (Sheldrick, 2015) using full matrix least squares minimisation on $\boldsymbol{F^2}$.

Crystal Data. $C_{31}H_{89}F_{12}Fe_2N_7O_{15}P_6S_4Si_2$, M_r = 1510.03, triclinic, *P*-1 (No. 2), a = 14.3915(3) Å, b = 16.3759(3) Å, c = 16.8383(3) Å, α = 72.9448(18)°, β = 64.938(2)°, γ = 70.772(2)°, *V* = 3338.88(14) Å^3, *T* = 100.01(10) K, *Z* = 2, *Z'* = 1, μ(Cu Kα) = 7.170, 49696 reflections measured, 13679 unique (R_{int} = 0.0702) which were used in all calculations. The final wR_2 was 0.1683 (all data) and R_1 was 0.0588 (I≥2 σ(I)).

SA.2.3 Crystal Data and Experimental for Complex 4

Crystal Structure from crystal provided. The ether co-solvent shown at 50 percent occupancy resides on mirror plane (1 diethyl ether molecule per Fe dimer). The triflate is disordered across the mirror plane; there is one per molecule of triflate per Fe dimer.

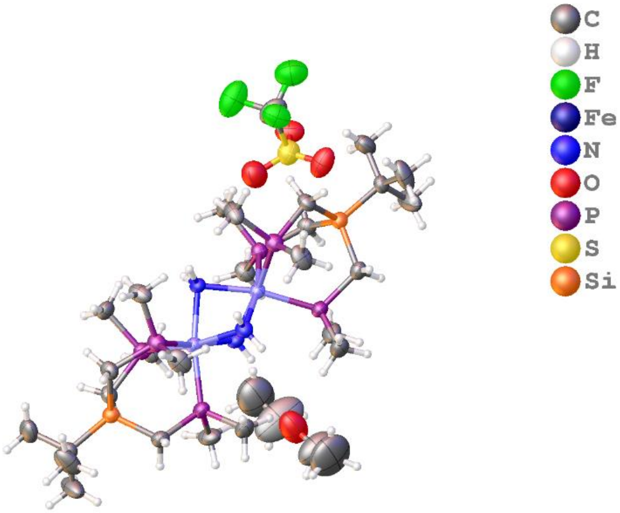

Compound	**MRS1017B**
Formula	$C_{31}H_{82}F_3Fe_2N_3O_4P_6SSi_2$
$D_{calc.}$/ g cm^{-3}	1.320
μ/mm^{-1}	0.898
Formula Weight	1003.75
Colour	red
Shape	parallelogram
Size/mm^3	0.16×0.10×0.04
T/K	173(2)
Crystal System	orthorhombic
Space Group	*Pnma*
a/Å	19.3780(14)
b/Å	25.3037(18)
c/Å	10.3017(7)
α/°	90
β/°	90
γ/°	90
V/Å^3	5051.3(6)
Z	4
Z'	0.5
Wavelength/Å	0.710730
Radiation type	MoK$_\alpha$
Θ_{min}/°	1.610
Θ_{max}/°	25.413
Measured Refl.	31969
Independent Refl.	4760
Reflections Used	2655
R_{int}	0.1284
Parameters	306
Restraints	118
Largest Peak	0.560
Deepest Hole	-0.522
GooF	1.011
wR_2 (all data)	0.1538
wR_2	0.1208
R_1 (all data)	0.1241
R_1	0.0569

Experimental. Single red parallelogram-shaped crystals of (**MRS1017B**) were used as received. A suitable crystal (0.16×0.10×0.04) mm^3 was selected and mounted on a nylon loop with paratone oil on a Bruker APEX-II CCD diffractometer. The crystal was kept at T = 173(2) K during data collection. Using **Olex2** (Dolomanov et al., 2009), the structure was solved with the XT (Sheldrick, 2015) structure solution program, using the Intrinsic Phasing solution method. The model was refined with version of **XL** (Sheldrick, 2008) using Least Squares minimisation.

Crystal Data. $C_{31}H_{82}F_3Fe_2N_3O_4P_6SSi_2$, M_r = 1003.75, orthorhombic, *Pnma* (No. 62), a = 19.3780(14) Å, b = 25.3037(18) Å, c = 10.3017(7) Å, $\alpha = \beta = \gamma = 90^\circ$, V = 5051.3(6) Å^3, T = 173(2) K, Z = 4, Z' = 0.5, μ(MoKα) = 0.898, 31969 reflections measured, 4760 unique (R_{int} = 0.1284) which were used in all calculations. The final wR_2 was 0.1538 (all data) and R_1 was 0.0569 (I > 2(I)).

SA.2.4 Crystal Data and Experimental for Complex 6

Crystal structure was determined even though the crystal turned out to be twinned.

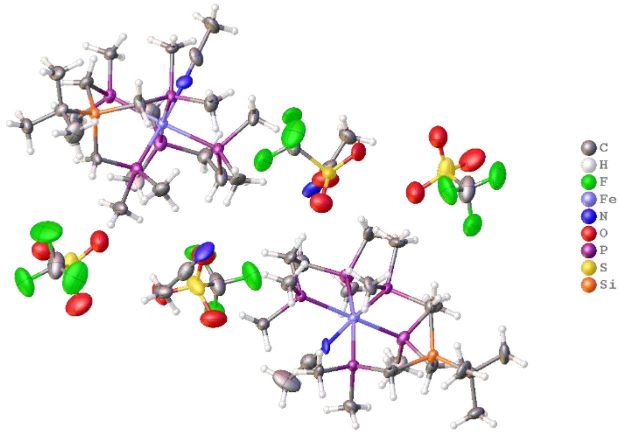

Compound	**MRS1018B**
CCDC	**1872543**
Formula	$C_{25}H_{55}F_6FeN_2O_6P_5S_2Si$
$D_{calc.}$/ g cm^{-3}	1.460
μ/mm^{-1}	0.763
Formula Weight	896.62
Colour	yellow
Shape	needle
Size/mm^3	0.26×0.06×0.04
T/K	173(2)
Crystal System	monoclinic
Flack Parameter	0.48(5)
Hooft Parameter	0.477(14)
Space Group	*Pc*
a/Å	10.6915(16)
b/Å	10.0541(15)
c/Å	38.082(6)
α/°	90
β/°	94.929(2)
γ/°	90
V/Å^3	4078.4(11)
Z	4
Z'	2
Wavelength/Å	0.710730
Radiation type	MoKα
Θ_{min}/°	1.912
Θ_{max}/°	26.069
Measured Refl.	47249
Independent Refl.	15781
Reflections with I > 2(I)	12478
R_{int}	0.0694
Parameters	812
Restraints	68
Largest Peak	1.399
Deepest Hole	-1.168
GooF	1.057
wR_2 (all data)	0.2379
wR_2	0.2235
R_1 (all data)	0.1135
R_1	0.0933

Experimental. Single yellow needle-shaped crystals of **MRS1018B** were used as received. A suitable crystal 0.26×0.06×0.04 mm^3 was selected and mounted on a None on an Bruker APEX-II CCD diffractometer. The crystal was kept at a steady T = 173(2) K during data collection. The structure was solved with the ShelXT (Sheldrick, G.M. (2015). Acta Cryst. A71, 3-8) structure solution program using the Intrinsic Phasing solution method and by using **Olex2** (Dolomanov et al., 2009) as the graphical interface. The model was refined with version 2018/3 of ShelXL (Sheldrick, Acta Cryst. A64 2008, 112-122) using Least Squares minimisation.

Crystal Data. $C_{25}H_{55}F_6FeN_2O_6P_5S_2Si$, M_r = 896.62, monoclinic, *Pc* (No. 7), a = 10.6915(16) Å, b = 10.0541(15) Å, c = 38.082(6) Å, β = 94.929(2)°, $\alpha = \gamma$ = 90°, V = 4078.4(11) Å^3, T = 173(2) K, Z = 4, Z' = 2, μ(MoKα) = 0.763, 47249 reflections measured, 15781 unique (R_{int} = 0.0694) which were used in all calculations. The final wR_2 was 0.2379 (all data) and R_1 was 0.0933 (I > 2(I)).

SA.2.5 Crystal Data and Experimental for Complex 7

Crystal structure of compound shows one THF solvent co-crystallized with the molecule of interest.

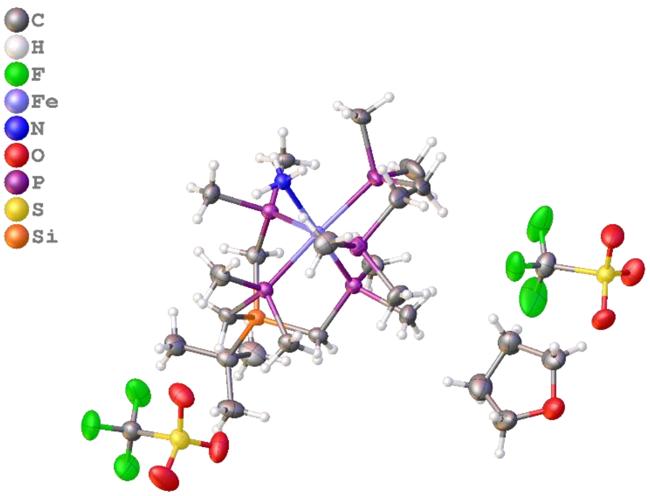

Experimental. Single orange chunk crystals of **tSiP3dmpeFeNH3** used as received. A suitable crystal with dimensions 0.18 × 0.10 × 0.08 mm^3 was selected and mounted on a nylon loop with paratone oil on a Bruker SMART APEX CCD area detector diffractometer. The crystal was kept at a steady T = 173(2) K during data collection. The structure was solved with the **ShelXT** (Sheldrick, G.M. (2015). Acta Cryst. A71, 3-8) solution program using SHELXT and by using **Olex2** (Dolomanov et al., 2009) as the graphical interface. The model was refined with **ShelXL** 2018/3 (Sheldrick, 2015) using full matrix least squares minimisation on $\boldsymbol{F^2}$.

Crystal Data. $C_{25}H_{60}F_6FeNO_7P_5S_2Si$, M_r = 903.65, triclinic, P-1 (No. 2), a = 11.3958(13) Å, b = 12.2488(13) Å, c = 14.9672(16) Å, α = 82.5200(14)°, β = 87.2950(14)°, γ = 83.0945(14)°, V = 2055.3(4) Å^3, T = 173(2) K, Z = 2, Z' = 1, μ(MoKα) = 0.759, 29469 reflections measured, 7559 unique (R_{int} = 0.0767) which were used in all calculations. The final wR_2 was 0.1595 (all data) and R_1 was 0.0556 (I > 2(I)).

Compound	**tSiP3dmpeFeNH3**
CCDC	2000513
Formula	$C_{25}H_{60}F_6FeNO_7P_5S_2Si$
$D_{calc.}$/ g cm^{-3}	1.460
μ/mm^{-1}	0.759
Formula Weight	903.65
Colour	orange
Shape	chunk
Size/mm^3	0.18×0.10×0.08
T/K	173(2)
Crystal System	triclinic
Space Group	P-1
a/Å	11.3958(13)
b/Å	12.2488(13)
c/Å	14.9672(16)
α/°	82.5200(14)
β/°	87.2950(14)
γ/°	83.0945(14)
V/Å^3	2055.3(4)
Z	2
Z'	1
Wavelength/Å	0.71073
Radiation type	MoKα
Θ_{min}/°	1.373
Θ_{max}/°	25.415
Measured Refl's.	29469
Ind't Refl's	7559
Refl's with I > 2(I)	5218
R_{int}	0.0767
Parameters	447
Restraints	0
Largest Peak	1.060
Deepest Hole	-0.431
GooF	1.018
wR_2 (all data)	0.1595
wR_2	0.1361
R_1 (all data)	0.0870
R_1	0.0556

SA.2.6 Crystal Structure and Experimental for Complex 10

Crystal structure of needles crystallized in vial.

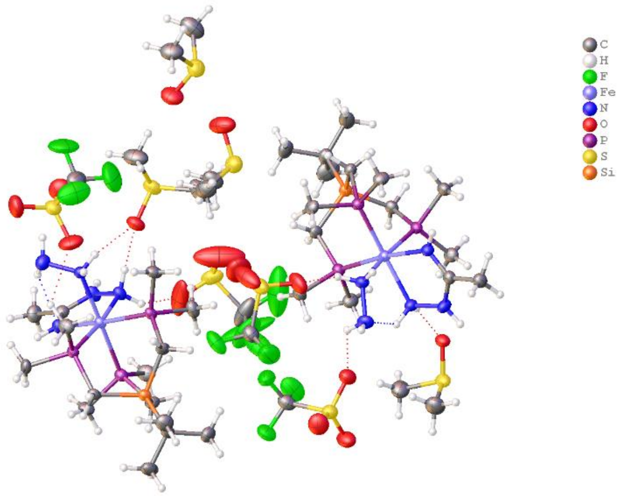

Experimental. Single orange needle-shaped crystals of **MRS1218A** were used as received. A suitable crystal 0.44×0.16×0.07 mm^3 was selected and mounted on a nylon loop with paratone oil on a Bruker APEX-II CCD diffractometer. The crystal was kept at a steady T = 173(2) K during data collection. The structure was solved with the ShelXT (Sheldrick, G.M. (2015). Acta Cryst. A71, 3-8) structure solution program using the Intrinsic Phasing solution method and by using **Olex2** (Dolomanov et al., 2009) as the graphical interface. The model was refined with version 2018/3 of ShelXL (Sheldrick, Acta Cryst. A64 2008, 112-122) using Least Squares minimization.

Crystal Data. $C_{21}H_{56}F_6FeN_5O_8P_3S_4Si$, M_r = 925.79, monoclinic, $P2_1/c$ (No. 14), a = 24.469(3) Å, b = 13.1139(14) Å, c = 26.041(3) Å, β = 96.7260(10)°, $\alpha = \gamma$ = 90°, V = 8298.6(15) Å^3, T = 173(2) K, Z = 8, Z' = 2, μ(MoKα) = 0.781, 66418 reflections measured, 15304 unique (R_{int} = 0.0661) which were used in all calculations. The final wR_2 was 0.1651 (all data) and R_1 was 0.0578 (I > 2(I)).

Compound	**MRS1218A**
CCDC	**1883822**
Formula	$C_{21}H_{56}F_6FeN_5O_8P_3S_4Si$
$D_{calc.}$/ g cm^{-3}	1.482
μ/mm^{-1}	0.781
Formula Weight	925.79
Color	orange
Shape	needle
Size/mm^3	0.44×0.16×0.07
T/K	173(2)
Crystal System	monoclinic
Space Group	$P2_1/c$
a/Å	24.469(3)
b/Å	13.1139(14)
c/Å	26.041(3)
α/°	90
β/°	96.7260(10)
γ/°	90
V/Å^3	8298.6(15)
Z	8
Z'	2
Wavelength/Å	0.710730
Radiation type	MoK$_\alpha$
Θ_{min}/°	1.575
Θ_{max}/°	25.412
Measured Refl.	66418
Independent Refl.	15304
Reflections with I > 2(I)	10808
R_{int}	0.0661
Parameters	923
Restraints	0
Largest Peak	1.569
Deepest Hole	-0.833
GooF	1.032
wR_2 (all data)	0.1651
wR_2	0.1442
R_1 (all data)	0.0869
R_1	0.0578

SA.2.7 Crystal Structure and Experimental for Complex 11

Triflate salt of Complex **11** did not give suitable single crystals. Instead triflate was exchanged by PF_6^- to prepare its corresponding PF_6^- salt which gave suitable single crystals for structure determination.

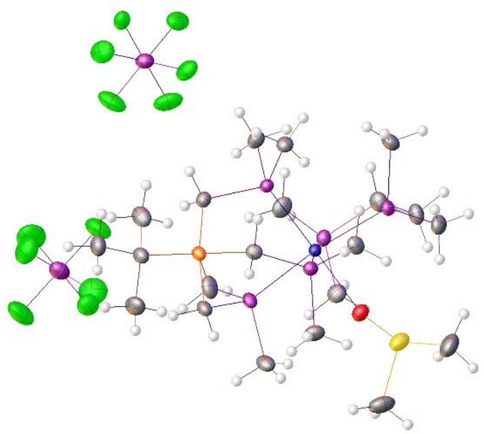

Experimental. Single red plate crystals of **MRS720A** recrystallised from a mixture of DMSO and THF by solvent layering. A suitable crystal with dimensions 0.21 × 0.10 × 0.02 mm^3 was selected and mounted on a nylon loop with paratone oil on a XtaLAB Synergy, Dualflex, HyPix diffractometer. The crystal was kept at a steady T = 99.99(10) K during data collection. The structure was solved with the ShelXT (Sheldrick, G.M. (2015). Acta Cryst. A71, 3-8) solution program using dual methods and by using Olex2 (Dolomanov et al., 2009) as the graphical interface. The model was refined with ShelXL (Sheldrick, Acta Cryst. A64 2008, 112-122) using full matrix least squares minimisation on $\boldsymbol{F}^2$.

Crystal Data. $C_{21}H_{55}F_{12}FeOP_7SSi$, M_r = 884.44, monoclinic, $P2_1/n$ (No. 14), a = 11.09300(10) Å, b = 14.85970(10) Å, c = 22.7442(2) Å, β = 97.9050(10)°, $\alpha = \gamma$ = 90°, V = 3713.50(5) $Å^3$, T = 99.99(10) K, Z = 4, Z' = 1, μ(Cu K_α) = 7.681, 52959 reflections measured, 7758 unique (R_{int} = 0.0462) which were used in all calculations. The final wR_2 was 0.0829 (all data) and R_1 was 0.0328 (I≥2 s(I)).

Compound	**MRS720A**
Formula	$C_{21}H_{55}F_{12}FeOP_7SSi$
CCDC	2020298
$D_{calc.}$/ g cm^{-3}	1.582
μ/mm^{-1}	7.681
Formula Weight	884.44
Colour	red
Shape	plate
Size/mm^3	0.21×0.10×0.02
T/K	99.99(10)
Crystal System	monoclinic
Space Group	$P2_1/n$
a/Å	11.09300(10)
b/Å	14.85970(10)
c/Å	22.7442(2)
α/°	90
β/°	97.9050(10)
γ/°	90
V/$Å^3$	3713.50(5)
Z	4
Z'	1
Wavelength/Å	1.54184
Radiation type	Cu K_α
Θ_{min}/°	3.563
Θ_{max}/°	77.404
Measured Refl's.	52959
Indep't Refl's	7758
Refl's I≥2 s(I)	7285
R_{int}	0.0462
Parameters	412
Restraints	0
Largest Peak	0.604
Deepest Hole	-0.837
GooF	1.034
wR_2 (all data)	0.0829
wR_2	0.0816
R_1 (all data)	0.0350
R_1	0.0328

SA.2.8 Crystal Structure and Experimental for Complex 13

Crystal structure of the best data set is presented here. the data shows the complex and disordered Triflate along with a 50:50 disorder of DMSO/THF solvent molecule. Not all atoms were refined anisotropic.

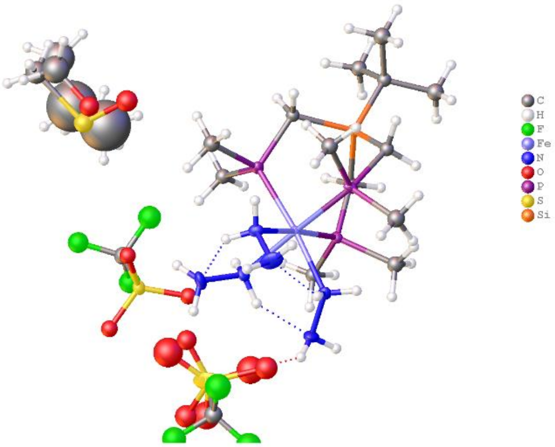

Experimental. Single orange needle crystals of **MRS820C** used as received. A suitable crystal with dimensions 0.12 × 0.08 × 0.06 mm^3 was selected and mounted on a nylon loop with paratone oil on a XtaLAB Synergy, Dualflex, HyPix diffractometer. The crystal was kept at a steady T = 100(2) K during data collection. The structure was solved with the ShelXT (Sheldrick, 2015) solution program using dual methods and by using Olex2 (Dolomanov et al., 2009) as the graphical interface. The model was refined with ShelXL 2018/3 (Sheldrick, 2015) using full matrix least squares minimisation on $\boldsymbol{F}^2$.

Crystal Data. $C_{18}H_{52}F_6FeN_6O_7P_3S_{2.5}Si$, M_r = 835.65, orthorhombic, $Pna2_1$ (No. 33), a = 26.0800(2) Å, b = 13.96248(12) Å, c = 9.81043(8) Å, $\alpha = \beta = \gamma = 90^{\circ}$, V = 3572.38(5) Å^3, T = 100(2) K, Z = 4, Z' = 1, μ(Cu K$_\alpha$) = 7.036, 35587 reflections measured, 5917 unique (R_{int} = 0.0618) which were used in all calculations. The final wR_2 was 0.1697 (all data) and R_1 was 0.0648 ($I \geq 2\,s(I)$).

Compound	**MRS820C**
Formula	$C_{18}H_{52}F_6FeN_6O_7P_3S_{2.5}Si$
CCDC	2026779
$D_{calc.}$/ g cm^{-3}	1.554
μ/mm^{-1}	7.036
Formula Weight	835.65
Colour	orange
Shape	needle
Size/mm^3	0.12×0.08×0.06
T/K	100(2)
Crystal System	orthorhombic
Flack Parameter	0.147(10)
Hooft Parameter	0.143(3)
Space Group	$Pna2_1$
a/Å	26.0800(2)
b/Å	13.96248(12)
c/Å	9.81043(8)
α/°	90
β/°	90
γ/°	90
V/Å^3	3572.38(5)
Z	4
Z'	1
Wavelength/Å	1.54184
Radiation type	Cu K$_\alpha$
Θ_{min}/°	3.389
Θ_{max}/°	77.510
Measured Refl's.	35587
Indep't Refl's	5917
Refl's $I \geq 2\,s(I)$	5776
R_{int}	0.0618
Parameters	272
Restraints	15
Largest Peak	1.576
Deepest Hole	-0.858
GooF	1.028
wR_2 (all data)	0.1697
wR_2	0.1683
R_1 (all data)	0.0660
R_1	0.0648

SA.3 Cartesian Coordinates of the Optimized Iron Complexes

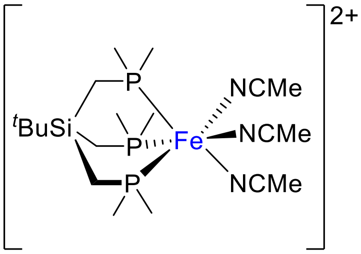

Sum of electronic and thermal Free Energies = –3490.742126 Hartree

Fe	1.17812300	0.00055300	-0.00001800
P	-0.14531200	1.19573800	1.51621000
P	-0.14496400	-1.91168500	0.27650100
P	-0.14644800	0.71543200	-1.79359600
Si	-2.64359000	-0.00176700	0.00036100
C	-0.21432900	2.53304400	-2.04148900
H	-0.64306800	3.04023600	-1.17945200
H	-0.82478800	2.76424400	-2.91535100
H	0.78861700	2.92305700	-2.20704800
C	-0.20926500	0.50108300	3.21402700
H	-0.63248100	-0.50133500	3.22192500
H	-0.82279200	1.13898800	3.85148200
H	0.79413700	0.45466100	3.63410200
C	0.41051100	0.16908700	-3.45335200
H	1.41244900	0.55050500	-3.65144400
H	-0.26632400	0.54823800	-4.22005300
H	0.43518100	-0.91761500	-3.51486300
C	0.40915300	2.90701100	1.87311300
H	1.41171800	2.88979700	2.30105600
H	-0.26781900	3.37920700	2.58619800
H	0.43139700	3.50448100	0.96332600
C	-0.21159600	-3.03263300	-1.17551300
H	-0.64100100	-2.53795000	-2.04436400
H	-0.82106800	-3.90616800	-0.94059400
H	0.79168200	-3.36903800	-1.43151300
C	-1.92291000	-1.63372500	0.65978700
H	-2.04252700	-1.64427600	1.74603100
H	-2.49241800	-2.48854800	0.28669300
C	-1.92417200	0.24422100	-1.74250900
H	-2.04398300	-0.69085200	-2.29510700
H	-2.49478300	0.99462100	-2.29523400
C	-1.92408300	1.38482700	1.08471000
H	-2.04613800	2.33169000	0.55302400

H	-2.49334100	1.48604800	2.01200100
C	-4.54315000	-0.00066500	0.00086300
C	0.41314700	-3.07794500	1.57702400
H	1.41480700	-3.43989000	1.34389300
H	-0.26389400	-3.93138400	1.63112400
H	0.43905500	-2.58976800	2.54966000
C	-5.06302000	1.39983000	-0.38017400
H	-4.73447100	1.71131000	-1.37469200
H	-4.75616000	2.16586500	0.33536700
H	-6.15616500	1.39572200	-0.39456700
C	-5.06368400	-0.36979800	1.40439700
H	-4.73292900	0.33482800	2.17129000
H	-4.75945300	-1.37334600	1.70969000
H	-6.15679700	-0.35235500	1.40853100
C	-5.06565700	-1.03033200	-1.02083200
H	-4.73689400	-2.04765500	-0.79494000
H	-4.76140600	-0.79291000	-2.04260000
H	-6.15878700	-1.04045400	-1.00740500
N	2.38739500	-0.54870700	1.48691400
N	2.38863600	-1.01073500	-1.21878300
N	2.38667100	1.56358400	-0.26687100
C	3.15447800	-1.55678900	-1.87674600
C	3.15387400	-0.84609600	2.28791800
C	3.15211400	2.40686200	-0.40997500
C	4.11142100	3.48147500	-0.58961500
H	4.02530400	3.89802000	-1.59408200
H	3.92643700	4.27334300	0.13762300
H	5.12552600	3.10473600	-0.45035700
C	4.11542300	-1.23062600	3.30536600
H	4.02643900	-0.57586600	4.17341900
H	3.93554600	-2.25954200	3.62004400
H	5.12900000	-1.15484800	2.90974500
C	4.11540000	-2.24941000	-2.71611100
H	4.08163300	-3.32196700	-2.52015000
H	3.88676300	-2.07511200	-3.76846900
H	5.12286800	-1.88614000	-2.50937700

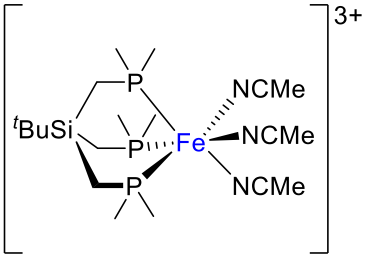

Sum of electronic and thermal Free Energies = –3490.525941 Hartree

Fe	-1.17018000	0.00032200	-0.00011900
P	0.17053100	-1.85157800	0.72043000
P	0.17056500	1.54999300	1.24370100
P	0.17003000	0.30293700	-1.96369800
Si	2.66502100	0.00002500	-0.00030700
C	0.20270500	-1.16018500	-3.05415300
H	0.61805800	-2.03412000	-2.55767400
H	0.82564300	-0.93008600	-3.92066000
H	-0.80037000	-1.39380300	-3.40432500
C	0.20550000	-2.06198600	2.53301700
H	0.62277300	-1.19482600	3.03966600
H	0.82773700	-2.92787000	2.76734100
H	-0.79715700	-2.24652200	2.91243900
C	-0.44258000	1.62002200	-3.06587200
H	-1.44742800	1.38316800	-3.41409400
H	0.22075000	1.68681900	-3.93052700
H	-0.45678900	2.58424400	-2.56223800
C	-0.44239700	-3.46519700	0.13299900
H	-1.44675700	-3.64831600	0.51349000
H	0.22162500	-4.24685800	0.50742000
H	-0.45752200	-3.51186500	-0.95386300
C	0.20486900	3.22548700	0.52105300
H	0.62407900	3.23205700	-0.48243400
H	0.82537600	3.86135900	1.15548500
H	-0.79817400	3.64533900	0.48986400
C	1.92302900	1.06532800	1.40002600
H	2.04708900	0.52995400	2.34431100
H	2.50070600	1.98886000	1.49976800
C	1.92276500	0.67965700	-1.62292000
H	2.04754300	1.76497800	-1.63247800
H	2.49990700	0.30321000	-2.47249500
C	1.92268000	-1.74512900	0.22176600
H	2.04590300	-2.29454200	-0.71446600
H	2.50070900	-2.29409600	0.97089000
C	4.55497500	-0.00032200	0.00001800
C	-0.44260400	1.84700400	2.93501100

H	-1.44738700	2.26705700	2.90338600
H	0.22065500	2.56278400	3.42474400
H	-0.45694200	0.92918800	3.51899400
C	5.06958400	-1.01482900	-1.04284600
H	4.74475200	-0.77751500	-2.05894900
H	4.76968100	-2.04007400	-0.81472400
H	6.16197100	-1.00052200	-1.05254900
C	5.06873800	-0.39693800	1.40009600
H	4.74114300	-1.39460100	1.70295500
H	4.77064600	0.31432300	2.17360400
H	6.16108300	-0.41535900	1.39263500
C	5.07030300	1.40992500	-0.35668700
H	4.74486900	2.17143800	0.35638200
H	4.77190400	1.72487900	-1.35908900
H	6.16267300	1.41091300	-0.33802000
N	-2.36918300	-0.30006900	1.60736800
N	-2.36936000	1.54230300	-0.54400200
N	-2.36793100	-1.24264000	-1.06376700
C	-3.16133300	2.32796700	-0.81789400
C	-3.16071400	-0.45593100	2.42510500
C	-3.15908400	-1.87380800	-1.60709300
C	-4.14879000	-2.67827200	-2.29409200
H	-4.12640000	-2.46670200	-3.36492000
H	-3.94305200	-3.73877300	-2.13537600
H	-5.14423600	-2.44901100	-1.90839300
C	-4.15308500	-0.65045500	3.46242100
H	-4.12796500	-1.68285700	3.81661900
H	-3.95252900	0.01957300	4.30087700
H	-5.14808400	-0.43556700	3.06740300
C	-4.15254000	3.32429000	-1.16934600
H	-4.17877300	4.11058900	-0.41242200
H	-3.90856200	3.76799200	-2.13673300
H	-5.13846800	2.85923200	-1.23179800

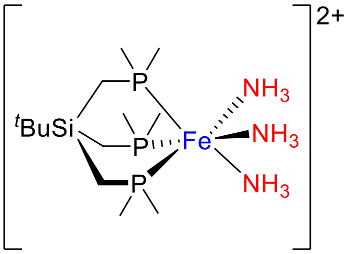

Sum of electronic and thermal Free Energies = –3262.080341 Hartree

Fe	1.81746800	0.00048100	-0.00053500
P	0.48932800	1.85471400	-0.53892000
P	0.49024100	-0.46000800	1.87402200
P	0.49093500	-1.39557500	-1.33465000
Si	-2.01330200	-0.00021900	-0.00109800
N	3.13610300	0.34357500	-1.65993700
H	3.47073900	-0.51158200	-2.09834800
H	3.97653100	0.86759500	-1.42307300
H	2.69617900	0.87041900	-2.40899400
C	0.43656700	-0.95592100	-3.12096400
H	0.03074300	0.04246900	-3.27517200
H	-0.19396700	-1.66458900	-3.65943200
H	1.43231500	-0.99793000	-3.56392600
C	0.43121700	3.17705000	0.73974300
H	0.02096700	2.80766200	1.67799200
H	-0.19684400	3.99975800	0.39556300
H	1.42633200	3.57971200	0.93217500
C	1.01759600	-3.15637700	-1.45810900
H	2.02622400	-3.23591700	-1.86849600
H	0.34427600	-3.70243800	-2.12018200
H	0.99361700	-3.64882000	-0.48513300
C	1.01677400	2.84797400	-1.99788500
H	2.02434500	3.24461500	-1.85860500
H	0.34154400	3.69318300	-2.13783500
H	0.99644500	2.25552700	-2.91352300
C	0.43368300	-2.22807000	2.38176400
H	0.02196100	-2.85670500	1.59408200
H	-0.19278300	-2.34079800	3.26753500
H	1.42932000	-2.59552500	2.63286600
C	-1.29099000	-0.01585600	1.75891400
H	-1.41859800	0.98272000	2.18469000
H	-1.85800100	-0.69043600	2.40517400
C	-1.29095100	-1.51679900	-0.89422700
H	-1.42016000	-2.38512000	-0.24301100
H	-1.85703900	-1.73831200	-1.80232100
C	-1.29146400	1.53203900	-0.86761100

H	-1.41797900	1.40113500	-1.94539600
H	-1.85953800	2.42844200	-0.60696000
C	-3.91120200	-0.00000100	0.00002500
C	1.01718000	0.30945800	3.46254200
H	2.02445500	-0.00964300	3.73770000
H	0.34195800	0.00968600	4.26509300
H	0.99643300	1.39846400	3.40428600
C	-4.43250200	0.19151600	-1.43853800
H	-4.10387100	-0.60354200	-2.11235800
H	-4.12950400	1.14936500	-1.86713100
H	-5.52545700	0.17404900	-1.43855400
C	-4.43015300	1.15073800	0.88570400
H	-4.09989300	2.13136000	0.53433900
H	-4.12691600	1.04201500	1.92934000
H	-5.52309100	1.16136800	0.87102300
C	-4.43142100	-1.34165000	0.55424200
H	-4.10039400	-1.52812100	1.57883600
H	-4.12999400	-2.19155400	-0.06200700
H	-5.52433600	-1.33276800	0.57194600
N	3.14380200	1.26398800	1.12157000
H	4.01803800	0.81314500	1.38502300
H	2.73901100	1.59067200	1.99449500
H	3.41926100	2.10825500	0.62502000
N	3.14334300	-1.60182900	0.53528700
H	2.73136600	-2.52084400	0.40041000
H	3.43104100	-1.58049500	1.51102200
H	4.01102100	-1.61763600	0.00230300

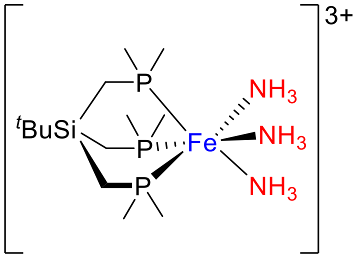

Sum of electronic and thermal Free Energies = –3261.877617 Hartree

Fe	-1.83027400	0.00003600	-0.00027100
P	-0.46986600	1.84781800	-0.76457700
P	-0.47036700	-1.58592800	-1.21753700
P	-0.47113500	-0.26185100	1.98229400
Si	2.02670100	-0.00017900	0.00026800
N	-3.11360200	1.31262800	1.09723400
H	-3.39118500	0.96103300	2.01223300
H	-3.99121400	1.50871300	0.61541500
H	-2.70533600	2.22708800	1.27628400
C	-0.44982700	1.22378400	3.04921500
H	-0.04431700	2.09278800	2.53490000
H	0.18543600	1.01809000	3.91335100
H	-1.44403800	1.46242400	3.42683400
C	-0.44782000	2.02753900	-2.58470000
H	-0.04434800	1.14626800	-3.07927500
H	0.18902300	2.87731300	-2.83948200
H	-1.44165800	2.23667800	-2.98036000
C	-1.05280600	-1.56317300	3.13114000
H	-2.06265200	-1.35974400	3.49152200
H	-0.38964500	-1.57870900	3.99901800
H	-1.01886100	-2.55464800	2.67872300
C	-1.05161300	3.49378100	-0.21309800
H	-2.06166100	3.70404900	-0.56894000
H	-0.38852400	4.25275900	-0.63442100
H	-1.01717600	3.59860700	0.87167200
C	-0.44859000	-3.25242700	-0.46372200
H	-0.04358400	-3.24096900	0.54618300
H	0.18696800	-3.89810300	-1.07343800
H	-1.44270200	-3.69895900	-0.44590600
C	1.28275700	-1.10731500	-1.36873500
H	1.41443600	-0.60013000	-2.32786200
H	1.86090800	-2.03355900	-1.43919500
C	1.28240800	-0.63138700	1.64391600
H	1.41496000	-1.71543600	1.68555700
H	1.85998800	-0.22788800	2.48099600
C	1.28312600	1.73932900	-0.27393500

H	1.41437300	2.31578000	0.64529700
H	1.86160700	2.26394300	-1.04028100
C	3.91527500	-0.00027000	0.00024100
C	-1.05145000	-1.93095300	-2.91905000
H	-2.06155700	-2.34417500	-2.92376000
H	-0.38851100	-2.67550700	-3.36556700
H	-1.01626600	-1.04376400	-3.55197600
C	4.42811200	1.05027700	1.00822000
H	4.10194100	0.84971400	2.03186200
H	4.13212000	2.06765000	0.74279300
H	5.52035800	1.03390100	1.02060200
C	4.42799700	0.34759600	-1.41352500
H	4.10137800	1.33422100	-1.75169200
H	4.13232700	-0.39106500	-2.16188800
H	5.52023300	0.36698500	-1.40549300
C	4.42846800	-1.39836600	0.40585800
H	4.10197900	-2.18464800	-0.27941300
H	4.13307200	-1.67715000	1.41981100
H	5.52070200	-1.40072400	0.38482200
N	-3.11448000	0.29509900	-1.68440200
H	-4.00029600	-0.20438400	-1.60251600
H	-2.71576200	-0.02499400	-2.56393400
H	-3.37659800	1.26581600	-1.84805900
N	-3.11525900	-1.60640800	0.58565100
H	-2.71327800	-2.21369300	1.29605100
H	-3.38393300	-2.22801500	-0.17545000
H	-3.99770900	-1.28629700	0.98523900

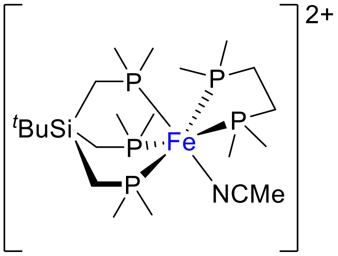

Sum of electronic and thermal Free Energies= -4146.139853 Hartree

Fe	-0.86633700	0.01522800	0.06430500
P	0.53977700	1.94518100	-0.02653400
P	0.49515000	-1.05122600	-1.60568400
P	0.56100100	-0.96288400	1.72324200
P	-2.54243300	-1.74031900	0.12327600
P	-2.51172400	1.09845000	-1.35356000
Si	3.02613900	0.02182200	-0.00766300
C	0.65617200	0.01662500	3.27858900
H	0.94996600	1.04754300	3.09439000
H	1.38423300	-0.43628200	3.95225900
H	-0.31238200	0.01605200	3.77579500
C	0.68026600	2.80787600	-1.64665200
H	1.01641300	2.13714700	-2.43395700
H	1.39390500	3.62875200	-1.56557700
H	-0.27980500	3.22550600	-1.94218800
C	0.15496700	-2.60632500	2.44333700
H	-0.83454100	-2.60011300	2.89848000
H	0.88518600	-2.85349100	3.21533300
H	0.18601400	-3.38647800	1.68584000
C	0.05631800	3.35476800	1.05062800
H	-0.94233800	3.71306900	0.80838800
H	0.76299300	4.17436200	0.91459800
H	0.07401500	3.05813300	2.09810600
C	-3.07159000	2.79192500	-0.90268900
H	-3.25118400	2.87193200	0.16708800
H	-4.00163900	3.01557900	-1.42723500
H	-2.33824200	3.54319700	-1.19038200
C	0.76512200	-2.86731000	-1.44042500
H	1.00725800	-3.16925200	-0.42554600
H	1.58544900	-3.16594700	-2.09374000
H	-0.12232000	-3.40861300	-1.75503400
C	-4.09274300	0.15266900	-1.17421700
H	-4.56627200	0.47056800	-0.24277600
H	-4.77510800	0.42620300	-1.98142100
C	2.24358800	-0.46062900	-1.66701200
H	2.28996000	0.40713100	-2.32820000

H	2.83217900	-1.23892000	-2.15836300
C	2.34240800	-1.17800100	1.29186400
H	2.48162800	-2.19761600	0.92642200
H	2.91945900	-1.11099800	2.21751300
C	2.31161500	1.72202800	0.42702600
H	2.40906000	1.87488500	1.50423400
H	2.88501100	2.52313100	-0.04542000
C	4.92433800	0.01783200	-0.07061800
C	0.04687000	-1.01592000	-3.38842000
H	-0.92323000	-1.48361600	-3.55506100
H	0.79559800	-1.57104300	-3.95530800
H	0.01609200	0.00217900	-3.76823400
C	5.48918700	0.58173100	1.24847500
H	5.19117300	-0.01037700	2.11713700
H	5.18617000	1.61680200	1.42156200
H	6.58192000	0.56993100	1.21658100
C	-2.39766600	1.27143000	-3.18011100
H	-1.49615400	1.80439300	-3.47557500
H	-3.26185800	1.83230100	-3.53851100
H	-2.39711700	0.29771800	-3.66384300
C	-3.56267900	-1.76587400	1.65654700
H	-2.95014300	-1.96833100	2.53354300
H	-4.32276700	-2.54373800	1.58037800
H	-4.06255000	-0.81080100	1.80231400
C	-3.81952700	-1.34600800	-1.15371400
H	-3.43913100	-1.68482900	-2.12070300
H	-4.72972400	-1.91663200	-0.95685900
C	5.40660500	0.89357000	-1.24428300
H	5.08239800	1.93289900	-1.15058400
H	5.06664800	0.51666100	-2.21146800
H	6.49946600	0.90394700	-1.27176600
C	5.43762200	-1.42237200	-0.26783800
H	5.07637200	-1.87119400	-1.19641000
H	5.15935400	-2.07950400	0.55906800
H	6.52959200	-1.42080900	-0.32077300
C	-2.33161800	-3.54466500	-0.15907700
H	-2.03205700	-3.74300700	-1.18538000
H	-3.28781500	-4.04070600	0.01218400
H	-1.59599000	-3.98070300	0.51223000
N	-1.84751800	0.86185900	1.54037000
C	-2.40125500	1.36282000	2.41481100
C	-3.09448300	1.99154000	3.52494400
H	-3.58392000	2.90929300	3.19510000
H	-3.85060400	1.31594900	3.92844300
H	-2.38683500	2.23897600	4.31801400

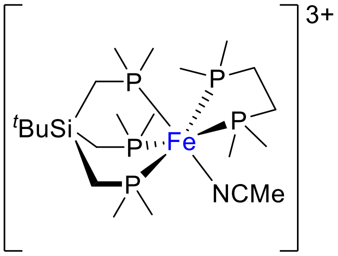

Sum of electronic and thermal Free Energies = –4145.929533 Hartree

Fe	-0.86745500	0.02115800	0.07654800
P	0.60116700	1.99431300	-0.22161600
P	0.51974300	-1.27220500	-1.44859300
P	0.64049700	-0.78938000	1.85935100
P	-2.62538400	-1.77700900	0.22977600
P	-2.58433300	1.01961400	-1.45504700
Si	3.07604000	0.01788900	-0.02645300
C	0.70547900	0.36458200	3.28081500
H	1.03285500	1.36019000	2.99067000
H	1.41009300	-0.02752200	4.01610100
H	-0.27140000	0.43700500	3.75448500
C	0.68842800	2.65246400	-1.93021700
H	1.01975300	1.90260800	-2.64444100
H	1.40096500	3.47925100	-1.94611400
H	-0.27701500	3.03781400	-2.24900000
C	0.15874600	-2.34523400	2.69684700
H	-0.81338600	-2.24410500	3.17664100
H	0.89768400	-2.56389700	3.47033700
H	0.13095400	-3.18482900	2.00649200
C	0.08041600	3.46260000	0.73706300
H	-0.92031700	3.78639500	0.45979200
H	0.77896300	4.27566100	0.53054000
H	0.10481200	3.25513300	1.80521800
C	-3.08321400	2.75458500	-1.14899600
H	-3.25577400	2.94115000	-0.09197200
H	-4.01280800	2.94592400	-1.68866000
H	-2.33780300	3.45687000	-1.51739700
C	0.79248200	-3.03897700	-1.03900700
H	1.08280600	-3.20278900	-0.00627100
H	1.59141800	-3.41103500	-1.68212700
H	-0.09783700	-3.62281700	-1.24787900
C	-4.14824000	0.09089000	-1.15329200
H	-4.59740700	0.47427300	-0.23506100
H	-4.84820200	0.31864900	-1.96056700
C	2.23265900	-0.64149700	-1.60142100
H	2.24772000	0.14526600	-2.35799100

H	2.82366900	-1.46152900	-2.01848700
C	2.39951400	-1.03030400	1.41096700
H	2.55510600	-2.08513300	1.17713600
H	2.98330000	-0.83556900	2.31494600
C	2.35451800	1.75913000	0.23806900
H	2.47306500	2.03287300	1.28874200
H	2.93207900	2.49299300	-0.33108900
C	4.96377100	0.00458600	-0.12898000
C	-0.03450900	-1.42367400	-3.18570000
H	-1.01188300	-1.90080300	-3.24970900
H	0.68423300	-2.04782000	-3.72015000
H	-0.07421100	-0.45528300	-3.67755400
C	5.55049200	0.71834400	1.10692700
H	5.27748600	0.22897200	2.04506400
H	5.25304300	1.76779100	1.16586400
H	6.64152500	0.70217200	1.05108700
C	-2.42681200	0.98406600	-3.27854200
H	-1.51780300	1.47747000	-3.61605000
H	-3.28063300	1.51446100	-3.70442200
H	-2.43529600	-0.03523700	-3.65634600
C	-3.57364000	-1.66681100	1.79547600
H	-2.93879700	-1.85331400	2.65947900
H	-4.36032300	-2.42274800	1.78150600
H	-4.03772900	-0.68991400	1.90547200
C	-3.89184700	-1.40697400	-1.05480100
H	-3.53536700	-1.81018200	-2.00538500
H	-4.80872700	-1.94945500	-0.81150200
C	5.41338000	0.74005000	-1.40876400
H	5.09465000	1.78524100	-1.42824700
H	5.05683900	0.25362900	-2.31955300
H	6.50476200	0.74497700	-1.45970300
C	5.46944900	-1.45248000	-0.16884900
H	5.09147300	-2.00685500	-1.03158200
H	5.21669000	-2.00850600	0.73671700
H	6.55915800	-1.45626200	-0.24769600
C	-2.39412100	-3.58293400	0.05059000
H	-2.11501100	-3.84438200	-0.96774900
H	-3.34835200	-4.06618300	0.26916400
H	-1.65080400	-3.97358100	0.74163100
N	-1.88205600	1.03388800	1.47473300
C	-2.43954900	1.60180500	2.30473300
C	-3.14118900	2.31742000	3.35229800
H	-4.06335300	2.75212300	2.96104000
H	-3.39213700	1.63459900	4.16703200
H	-2.51169900	3.11864000	3.74513000

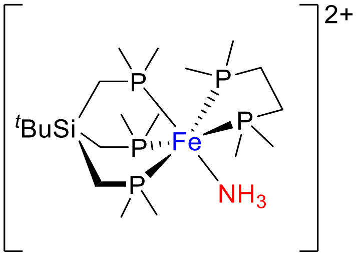

Sum of electronic and thermal Free Energies = –4069.912723

Fe	0.96493100	-0.00001300	-0.32705900
P	-0.53402100	1.76302900	-0.94705900
P	-0.18007600	-0.23398100	1.76594100
P	-0.56011400	-1.61697100	-1.23905900
P	2.72388700	-1.58206100	0.22394100
P	2.66197500	1.61494000	0.30294100
Si	-2.90406900	0.01009400	0.13994100
N	1.83293300	0.08896300	-2.28905900
H	2.01290800	-0.83304200	-2.67205900
H	2.71894700	0.58293900	-2.35105900
H	1.21994600	0.55298000	-2.95205900
C	-0.85810800	-1.41296200	-3.04905900
H	-1.21308100	-0.41495300	-3.29705900
H	-1.61112800	-2.13094200	-3.37605900
H	0.04888600	-1.61198700	-3.62105900
C	-0.56997900	3.25803000	0.12694100
H	-0.78998600	3.00503600	1.16194100
H	-1.33596000	3.94805100	-0.22905900
H	0.38703500	3.77500300	0.09794100
C	-0.13616400	-3.40798200	-1.22405900
H	0.79983100	-3.59600800	-1.74805900
H	-0.92517900	-3.97396100	-1.72305900
H	-0.04517400	-3.77998500	-0.20605900
C	-0.23099900	2.56202000	-2.58205900
H	0.77401300	2.97499300	-2.65105900
H	-0.94297600	3.37704000	-2.72305900
H	-0.38201800	1.86002400	-3.40405900
C	3.11201200	2.93792800	-0.90205900
H	3.23000100	2.56192500	-1.91805900
H	4.06002400	3.38790200	-0.60405900
H	2.36103300	3.72594900	-0.91905900
C	-0.36412300	-1.94197600	2.43494100
H	-0.65814300	-2.66596800	1.68094100
H	-1.11912300	-1.93795500	3.22194100
H	0.57086800	-2.27100200	2.87794100
C	4.27295000	0.70589600	0.43094100

H	4.68094700	0.58788500	-0.57705900
H	4.99296700	1.31487600	0.98094100
C	-1.94506100	0.31106800	1.74794100
H	-1.97503100	1.38106800	1.96494100
H	-2.44407400	-0.17491900	2.58994100
C	-2.27911500	-1.63292300	-0.57205900
H	-2.32713500	-2.38792200	0.21594100
H	-2.94212400	-1.98690500	-1.36505900
C	-2.32603200	1.35407800	-1.06705900
H	-2.53504100	1.01908400	-2.08505900
H	-2.89500700	2.27709400	-0.93005900
C	-4.78506900	0.01814600	0.39994100
C	0.41994700	0.58000200	3.30294100
H	1.42793700	0.24997400	3.54994100
H	-0.23906100	0.31002000	4.12894100
H	0.41697600	1.66300200	3.20494100
C	-5.49907100	-0.05983400	-0.96405900
H	-5.25209600	-0.97184100	-1.51405900
H	-5.27004700	0.79515900	-1.60405900
H	-6.58207100	-0.06480400	-0.81405900
C	2.68100200	2.59494000	1.85794100
H	1.77701900	3.19096500	1.96694100
H	3.53902100	3.26791600	1.84494100
H	2.77098400	1.94293700	2.72394100
C	3.63586800	-2.25708600	-1.23305900
H	2.98785100	-2.87606900	-1.85405900
H	4.46085100	-2.88310900	-0.89105900
H	4.05989000	-1.46709800	-1.85305900
C	4.06791300	-0.65309800	1.08894100
H	3.77091600	-0.53709000	2.13394100
H	4.98889600	-1.24112400	1.08694100
C	-5.20403300	1.31715800	1.11794100
H	-4.94700800	2.21215000	0.54594100
H	-4.75603100	1.40714500	2.10994100
H	-6.28803300	1.32918800	1.25394100
C	-5.19810200	-1.19284300	1.25994100
H	-4.72910200	-1.18385600	2.24694100
H	-4.96312900	-2.14384900	0.77794100
H	-6.27910200	-1.17581300	1.42394100
C	2.63284500	-3.09605900	1.26194100
H	2.41785200	-2.84405300	2.29694100
H	3.59983100	-3.60108600	1.23394100
H	1.87482600	-3.79003800	0.90594100

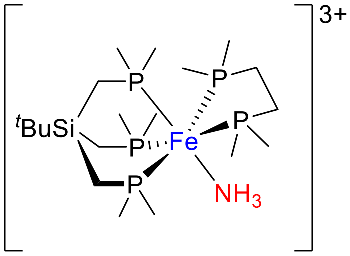

Sum of electronic and thermal Free Energies = –4069.709733 Hartree

Fe	0.97400400	0.01338800	-0.35042600
P	-0.59577300	1.86587600	-0.86774800
P	-0.21263900	-0.42328800	1.75376200
P	-0.63893500	-1.55664000	-1.37653300
P	2.81171200	-1.60848400	0.19606800
P	2.74676200	1.63972200	0.37354600
Si	-2.95285100	0.01273900	0.15367300
N	1.83647900	0.21112900	-2.27375000
H	2.00189400	-0.69220700	-2.70997600
H	2.73197700	0.69038600	-2.30550300
H	1.23142400	0.72021700	-2.91232500
C	-0.90058000	-1.20978100	-3.16117200
H	-1.28331600	-0.20650000	-3.33661100
H	-1.63358900	-1.92010400	-3.54780700
H	0.01371900	-1.34818900	-3.73828000
C	-0.56209100	3.26188500	0.31911600
H	-0.76579100	2.93889300	1.33728000
H	-1.32707400	3.98457400	0.02958500
H	0.40021500	3.76796100	0.29797000
C	-0.14327100	-3.31976800	-1.43950700
H	0.78029100	-3.45183400	-2.00231900
H	-0.92891800	-3.88429100	-1.94568500
H	-0.01414600	-3.73611600	-0.44320200
C	-0.24862500	2.71334200	-2.45852600
H	0.76205800	3.11751300	-2.49619000
H	-0.94802300	3.54523200	-2.56418300
H	-0.40757900	2.05323200	-3.31233100
C	3.14482300	3.01344600	-0.77790000
H	3.26986600	2.68640200	-1.80982400
H	4.08762800	3.46465500	-0.46193800
H	2.38203700	3.78956000	-0.75067100
C	-0.41635900	-2.17783500	2.24509600
H	-0.80272200	-2.80655100	1.44938000
H	-1.12055800	-2.20925800	3.07806800
H	0.52478800	-2.59152800	2.59169700
C	4.33613100	0.70171800	0.43776600

H	4.73209100	0.61835900	-0.57735600
H	5.06535100	1.29091600	0.99870100
C	-1.93787900	0.18894800	1.75727100
H	-1.93331300	1.24039300	2.05110700
H	-2.44558900	-0.34030900	2.56864700
C	-2.33598700	-1.57847500	-0.69049400
H	-2.40804100	-2.40312700	0.02111100
H	-3.00515700	-1.83865200	-1.51554400
C	-2.36791100	1.43224000	-0.97201500
H	-2.60090000	1.17538300	-2.00787200
H	-2.93379500	2.34204300	-0.75321100
C	-4.81879500	0.01769200	0.45419900
C	0.49578800	0.27020100	3.29109200
H	1.50314200	-0.10488400	3.46843400
H	-0.13488100	-0.04078200	4.12631100
H	0.51417200	1.35664000	3.26762200
C	-5.55845600	0.04544100	-0.89980000
H	-5.33641800	-0.82686500	-1.51935000
H	-5.33998100	0.94529400	-1.47923800
H	-6.63666900	0.03793200	-0.72359000
C	2.71195900	2.50184600	1.98789900
H	1.80032100	3.08039900	2.12018800
H	3.56064200	3.18727200	2.02656700
H	2.80534600	1.79688200	2.81030600
C	3.65499400	-2.21127400	-1.32272600
H	2.98861600	-2.81420600	-1.93934000
H	4.49185100	-2.84667400	-1.02793200
H	4.06031600	-1.39871900	-1.92435100
C	4.14049300	-0.67333300	1.06337200
H	3.86203200	-0.59183500	2.11666900
H	5.06392700	-1.25665700	1.03098300
C	-5.20160900	1.26680300	1.27549800
H	-4.95325300	2.20009500	0.76400200
H	-4.73490300	1.27938700	2.26311300
H	-6.28210800	1.27688300	1.43697300
C	-5.21922900	-1.25269700	1.23310300
H	-4.73069100	-1.32172000	2.20841000
H	-5.01090100	-2.16908600	0.67634100
H	-6.29498400	-1.23704500	1.42320400
C	2.69247600	-3.14334000	1.18484500
H	2.51037800	-2.91923000	2.23364500
H	3.65025400	-3.66280600	1.11745800
H	1.91728600	-3.81181700	0.81764900

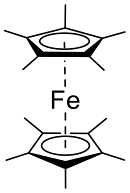

Sum of electronic and thermal Free Energies = –2043.920375 Hartree

Fe	-0.00008700	-0.00001100	-0.00000300
C	1.70164700	1.16130700	0.36370500
C	1.70136900	0.70350500	-0.99249900
C	1.70055700	-0.72780200	-0.97617200
C	1.69965500	-1.15469200	0.39005300
C	1.70041900	0.01289300	1.21819200
C	1.80741400	2.58722100	0.80947400
C	1.80751400	1.56720000	-2.21126800
C	1.80632900	-1.61966700	-2.17468900
C	1.80223900	-2.57057700	0.86728800
C	1.80541500	0.03046600	2.71200700
C	-1.70080500	-0.81354100	-0.90613300
C	-1.70034200	0.61011000	-1.05494400
C	-1.70040600	1.19168700	0.25309200
C	-1.70139400	0.12754200	1.21021000
C	-1.70146000	-1.11181500	0.49382500
C	-1.80499400	-1.81307000	-2.01636700
C	-1.80509500	1.35961700	-2.34732800
C	-1.80363400	2.65297700	0.56392200
C	-1.80663000	0.28288800	2.69597700
C	-1.80805400	-2.47661800	1.10130700
H	2.85490200	0.03546500	3.02875600
H	1.33652400	0.91553600	3.14364900
H	1.33863400	-0.84555500	3.16428400
H	2.85114400	-2.87265000	0.96906300
H	1.33331100	-2.70809800	1.84237500
H	1.33363300	-3.26928200	0.17284500
H	2.85600700	-1.81130500	-2.42615100
H	1.33567100	-2.58884200	-2.00494200
H	1.34223300	-1.17530300	-3.05624600
H	2.85716900	1.74490000	-2.47276900
H	1.33428400	1.10690600	-3.07953500
H	1.34539600	2.54375500	-2.06083400
H	2.85701500	2.88998400	0.90140900
H	1.33737200	3.27204600	0.10271100
H	1.34216500	2.74569900	1.78331600
H	-2.85789700	-2.76653200	1.22605600
H	-1.33711300	-3.23880100	0.47921400

H	-1.34433900	-2.52115800	2.08771600
H	-2.85420400	-2.02472000	-2.25329000
H	-1.33516700	-1.45533600	-2.93328600
H	-1.33767200	-2.76331800	-1.75418000
H	-2.85455500	1.52026300	-2.62054700
H	-1.33595900	2.34242500	-2.28769600
H	-1.33878900	0.81939400	-3.17230500
H	-2.85265900	2.96428500	0.63026400
H	-1.33481000	2.90156900	1.51678900
H	-1.33520400	3.26745500	-0.20616200
H	-2.85608600	0.31537100	3.01112100
H	-1.33809700	-0.54673600	3.22675700
H	-1.33908900	1.20507300	3.04378700

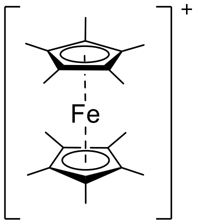

Sum of electronic and thermal Free Energies = – 2043.757440 Hartree

Fe	0.00023600	0.00014700	0.00005200
C	1.73983500	0.46668300	-1.11705100
C	1.74986400	-0.92259000	-0.76565800
C	1.73593000	-1.01795000	0.66430400
C	1.71882400	0.31279300	1.19687300
C	1.72088000	1.23065700	0.09572600
C	1.83586300	1.01994100	-2.50104800
C	1.86083000	-2.06694300	-1.71932000
C	1.82550600	-2.27959200	1.45929000
C	1.78578800	0.67971300	2.64328300
C	1.79032400	2.71982700	0.19466100
C	-1.73199100	-0.92448200	0.79642600
C	-1.71799500	-1.06615500	-0.62981500
C	-1.72402600	0.24615900	-1.20565400
C	-1.74292100	1.19900800	-0.13535000
C	-1.74694900	0.47588400	1.10175000
C	-1.81885200	-2.04050500	1.78573200
C	-1.78501000	-2.35466400	-1.38217800
C	-1.79911300	0.56471000	-2.66297800
C	-1.84308700	2.68187600	-0.28395100
C	-1.85350200	1.07537000	2.46568600
H	2.83678800	3.04193300	0.19704700
H	1.30313100	3.20899000	-0.64804300
H	1.33616600	3.08896800	1.11374900
H	2.83177500	0.77396700	2.95313900
H	1.30114300	1.63430200	2.84538500
H	1.32733400	-0.07763100	3.27822800
H	2.87612800	-2.52085400	1.65162600
H	1.33203500	-2.19073200	2.42641800
H	1.39095100	-3.12701300	0.93003600
H	2.91647600	-2.30095600	-1.89250300
H	1.38858700	-2.96937800	-1.33288900
H	1.41846700	-1.83589400	-2.68780700
H	2.88791600	1.10831200	-2.79140900
H	1.35095700	0.37638400	-3.23424900
H	1.39567300	2.01386000	-2.57392500
H	-2.90713000	1.15141800	2.75406100

H	-1.35438400	0.46952000	3.22102700
H	-1.43528100	2.08054100	2.50207600
H	-2.86900000	-2.29178500	1.96751800
H	-1.32830600	-2.94437200	1.42601100
H	-1.38040700	-1.77150600	2.74609000
H	-2.83054900	-2.61656200	-1.57490400
H	-1.28407300	-2.29258100	-2.34765800
H	-1.34423900	-3.17721700	-0.81983900
H	-2.84691200	0.63515300	-2.97295200
H	-1.32696200	1.51802700	-2.89756000
H	-1.33254300	-0.20748900	-3.27388300
H	-2.89624100	2.98182800	-0.28947700
H	-1.36066200	3.21004700	0.53783600
H	-1.40417800	3.02844300	-1.21887500

SUPPORTING INFORMATION (B) FOR CHAPTER 4

SB.1 NMR Spectra

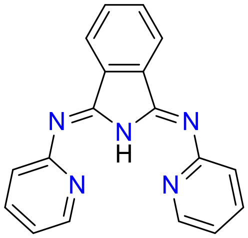

Hbid

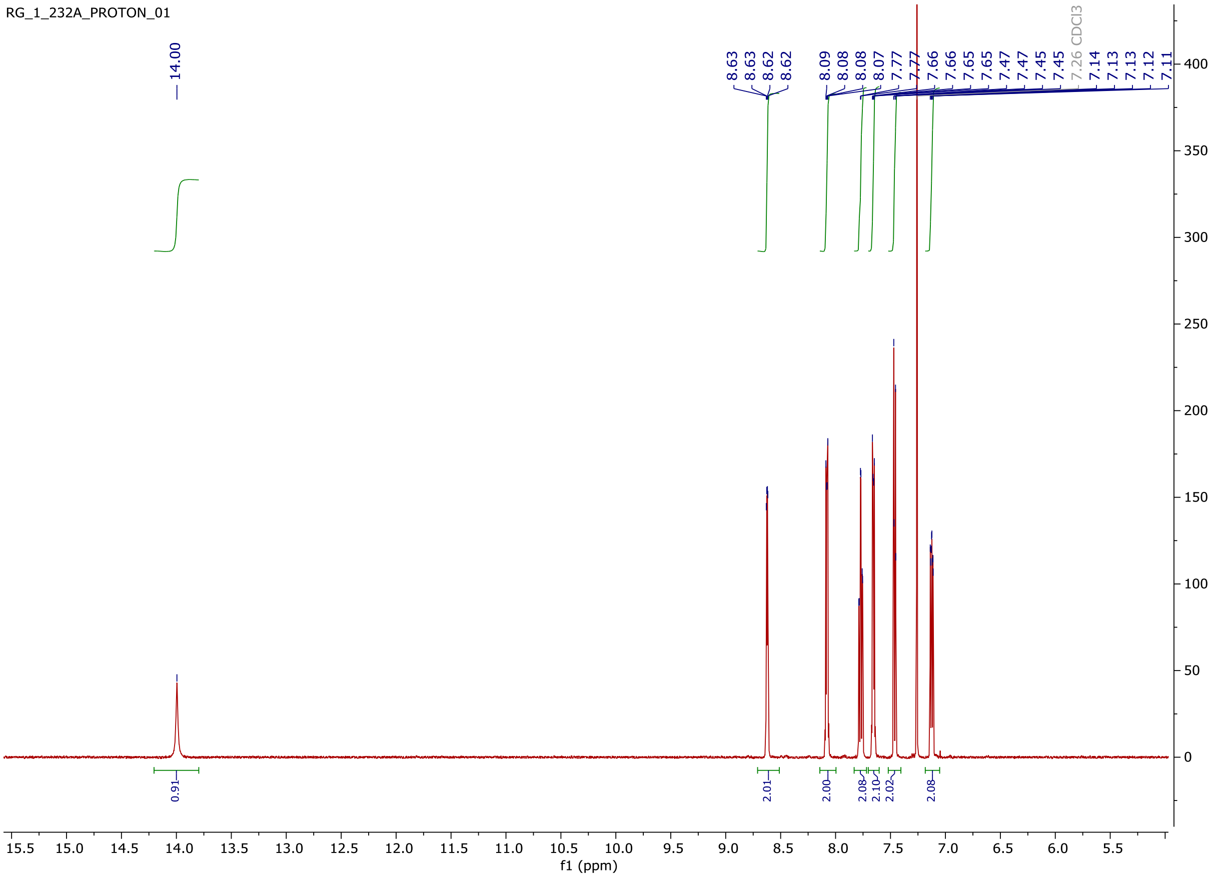

Figure SB.1 ^{1}H NMR of Hbid in $CDCl_3$

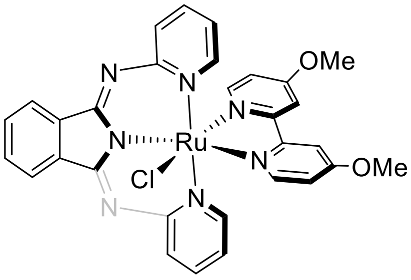

Complex **1**

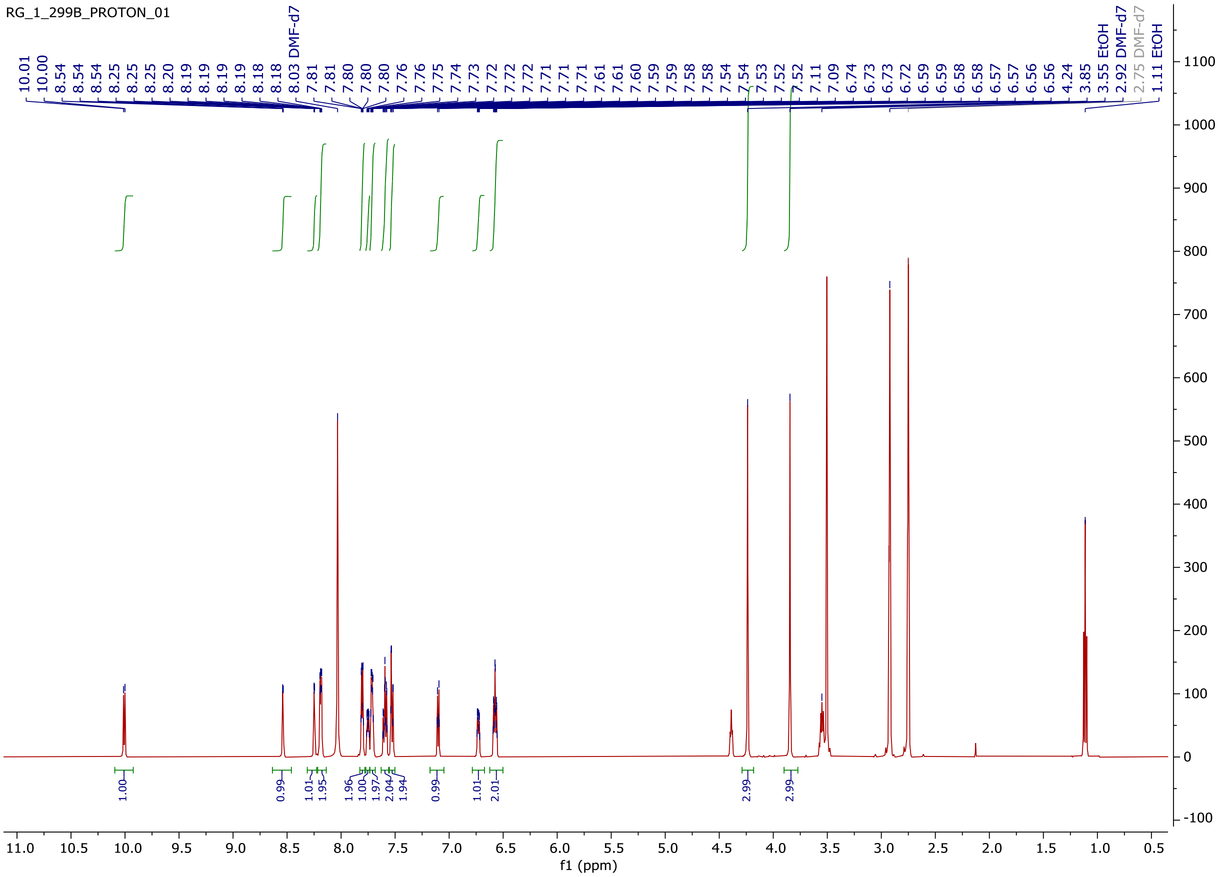

Figure SB.2 ^{1}H NMR of Ru(bid)(bpy’)Cl (**1**) in DMF-d_7

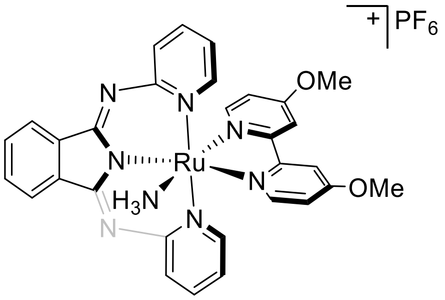

Complex **2**

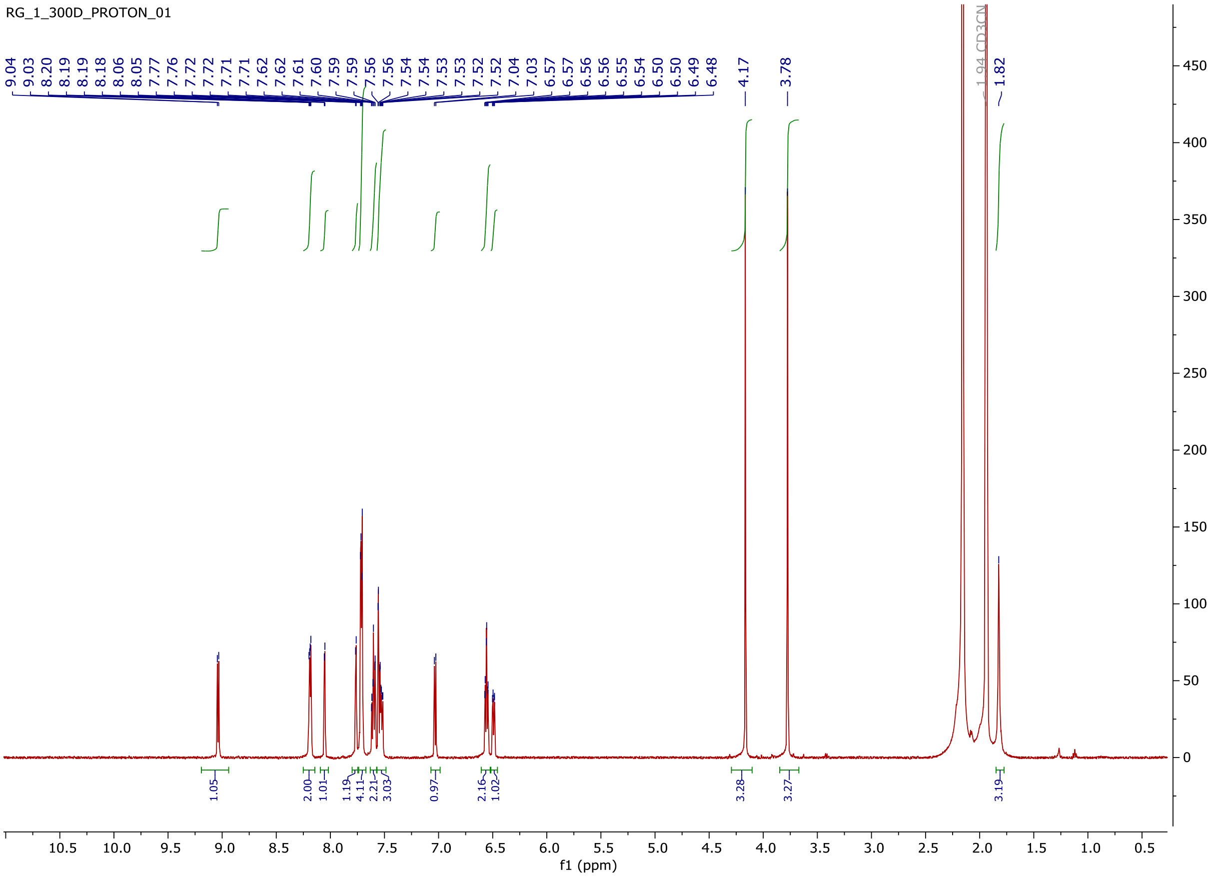

Figure SB.3 ^{1}H NMR of [Ru(bid)(bpy')NH$_3$][PF$_6$] (**2**) in MeCN-d_3

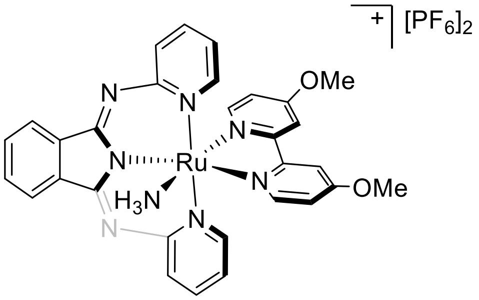

Complex **3**

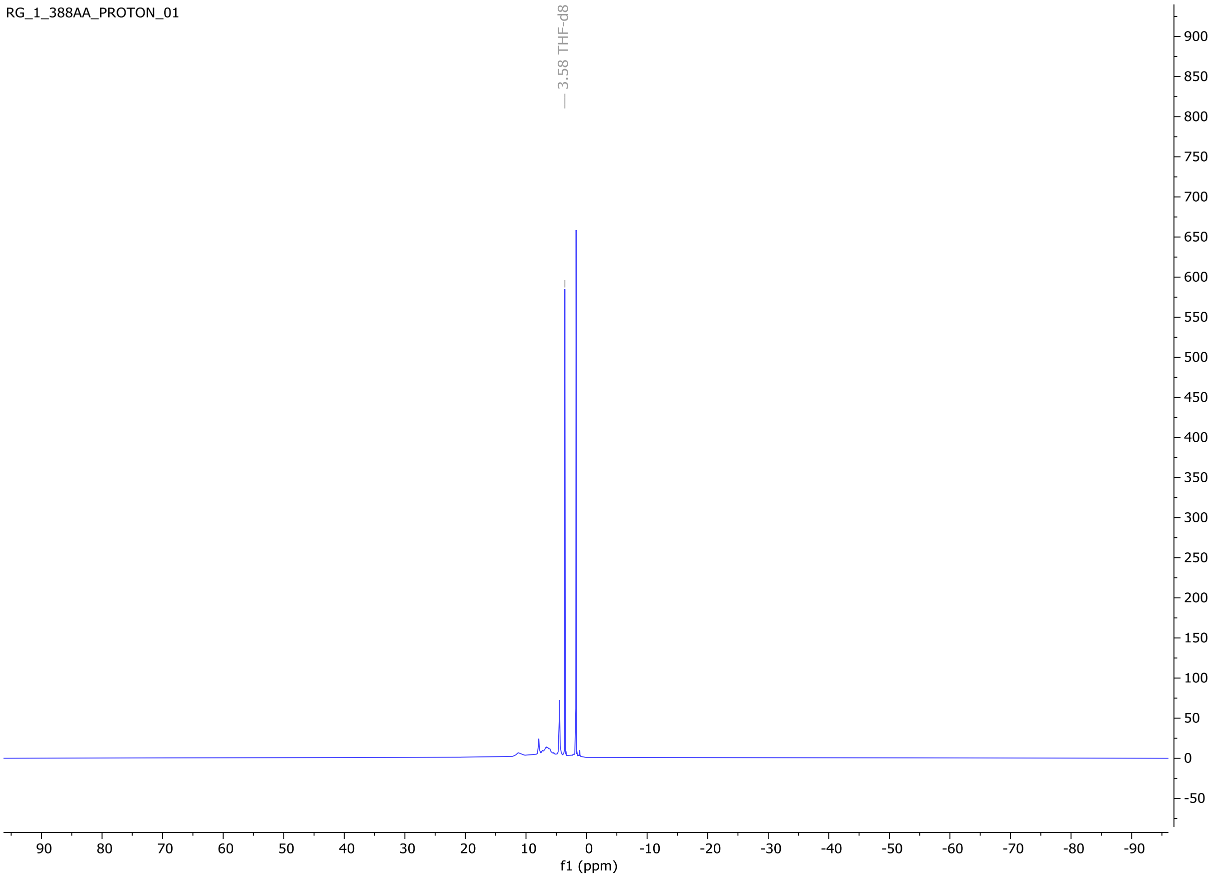

Figure SB.4 ^{1}H NMR of [Ru(bid)(bpy')NH$_3$][PF$_6$]$_2$ (**3**) in THF-d_6 at t = 0 h (vertically zoomed out spectrum)

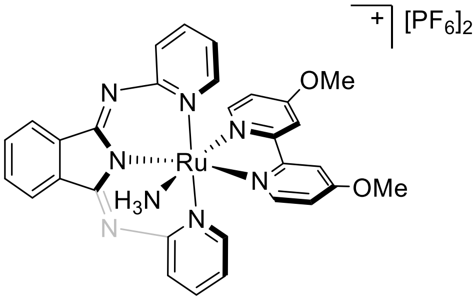

Complex **3**

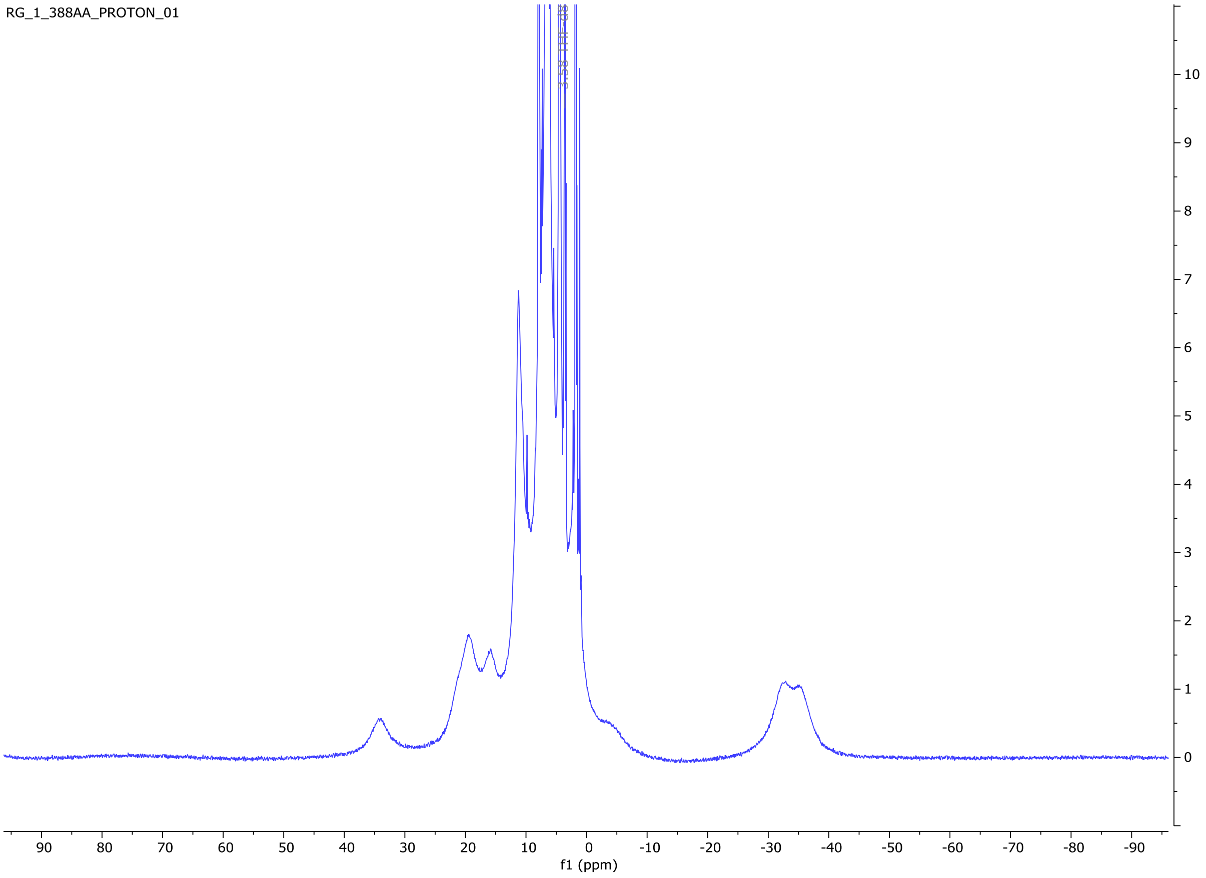

Figure SB.5 ^{1}H NMR of [Ru(bid)(bpy’)NH$_3$][PF$_6$]$_2$ (**3**) in THF-*d*$_6$ at t = 0 h (vertically zoomed in spectrum)

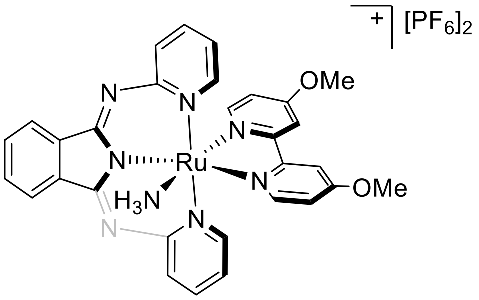

Complex **3**

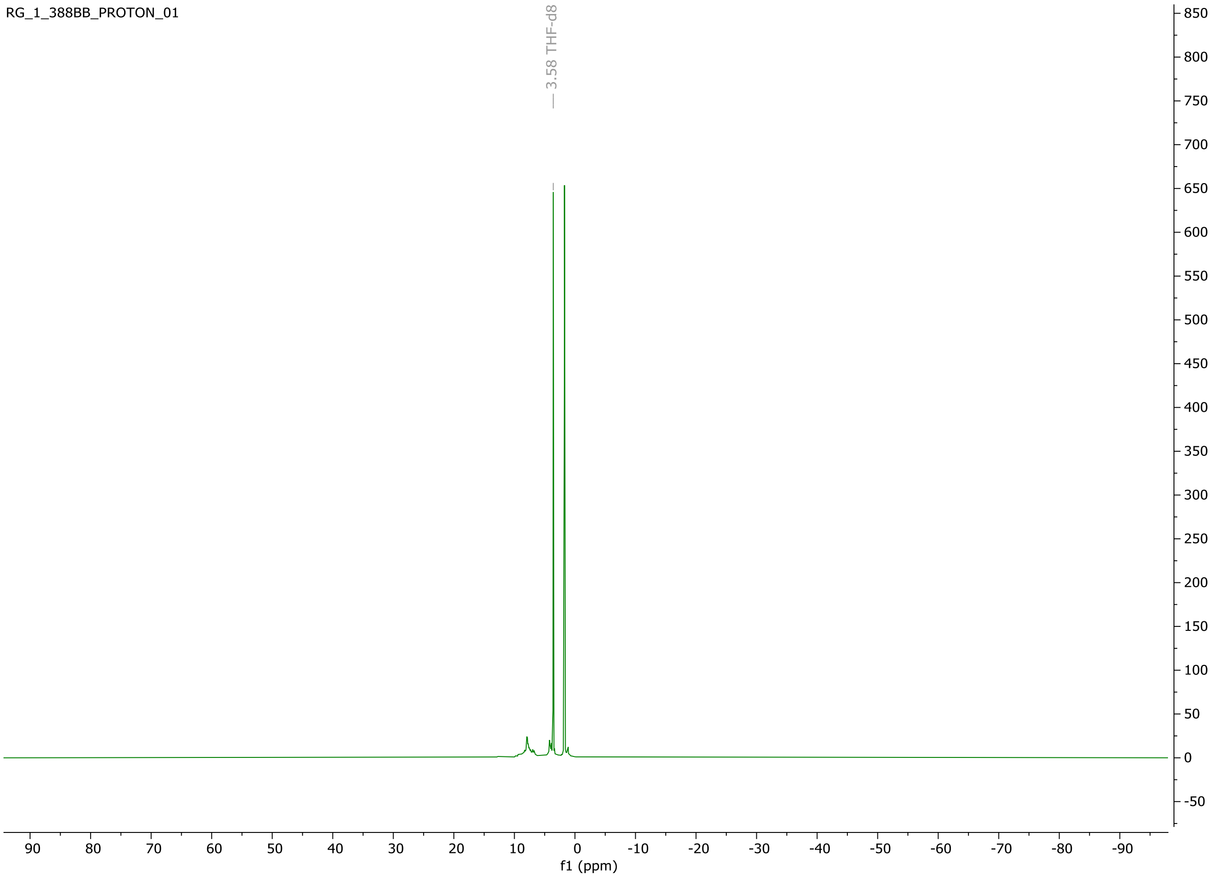

Figure SB.6 ^{1}H NMR of [Ru(bid)(bpy')NH$_3$][PF$_6$]$_2$ (**3**) in THF-d_6 at t = 20 h (vertically zoomed out spectrum)

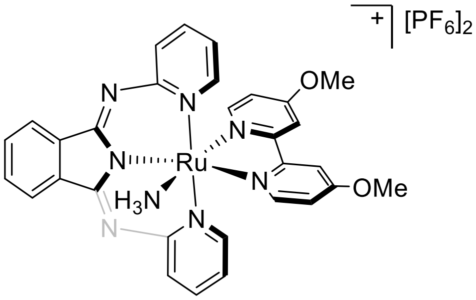

Complex **3**

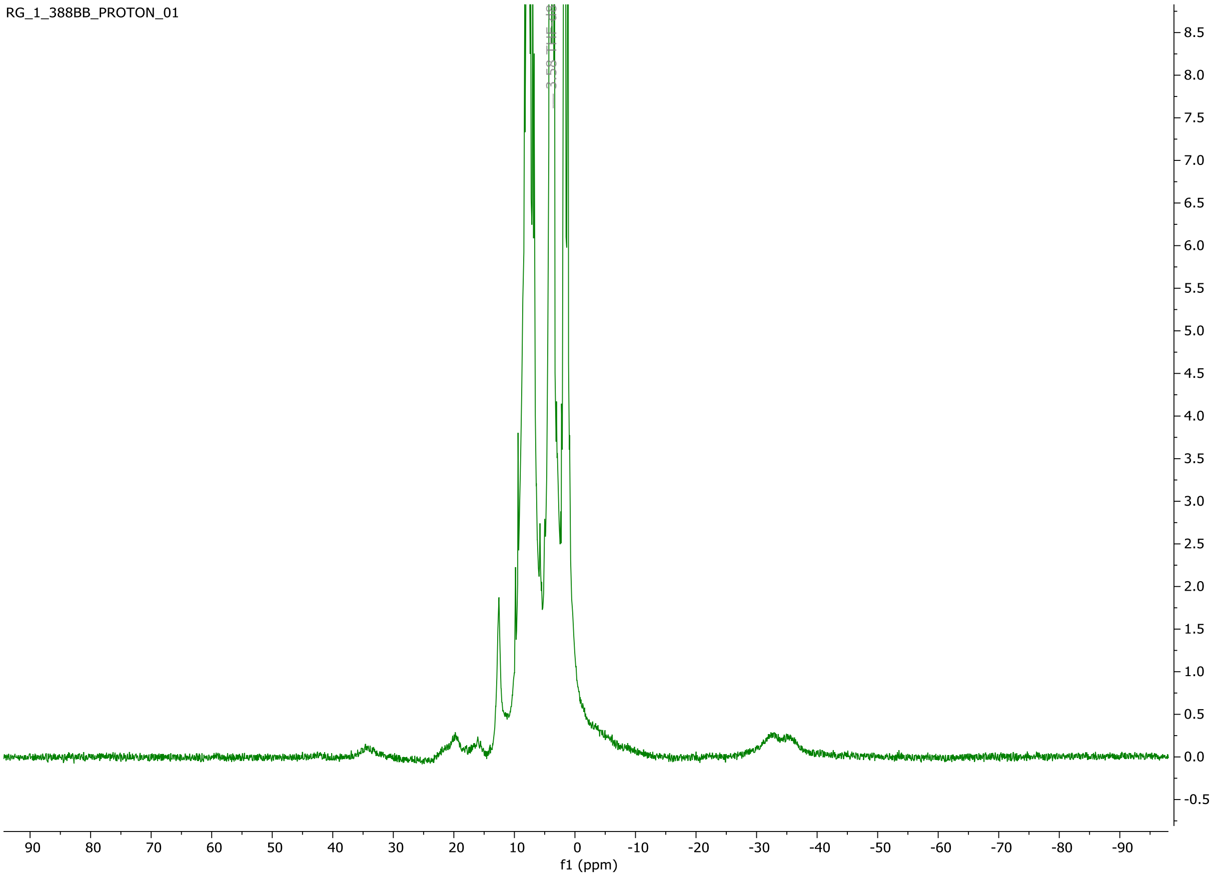

Figure SB.7 ^{1}H NMR of [Ru(bid)(bpy')NH$_3$][PF$_6$]$_2$ (**3**) in THF-*d*$_6$ at t = 20 h (vertically zoomed in spectrum)

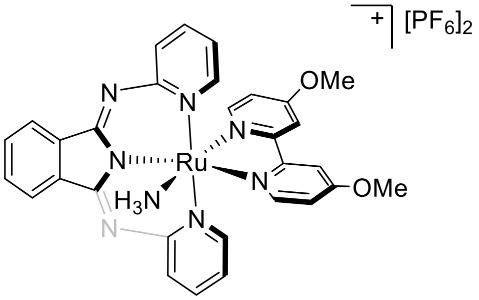

Complex **3**

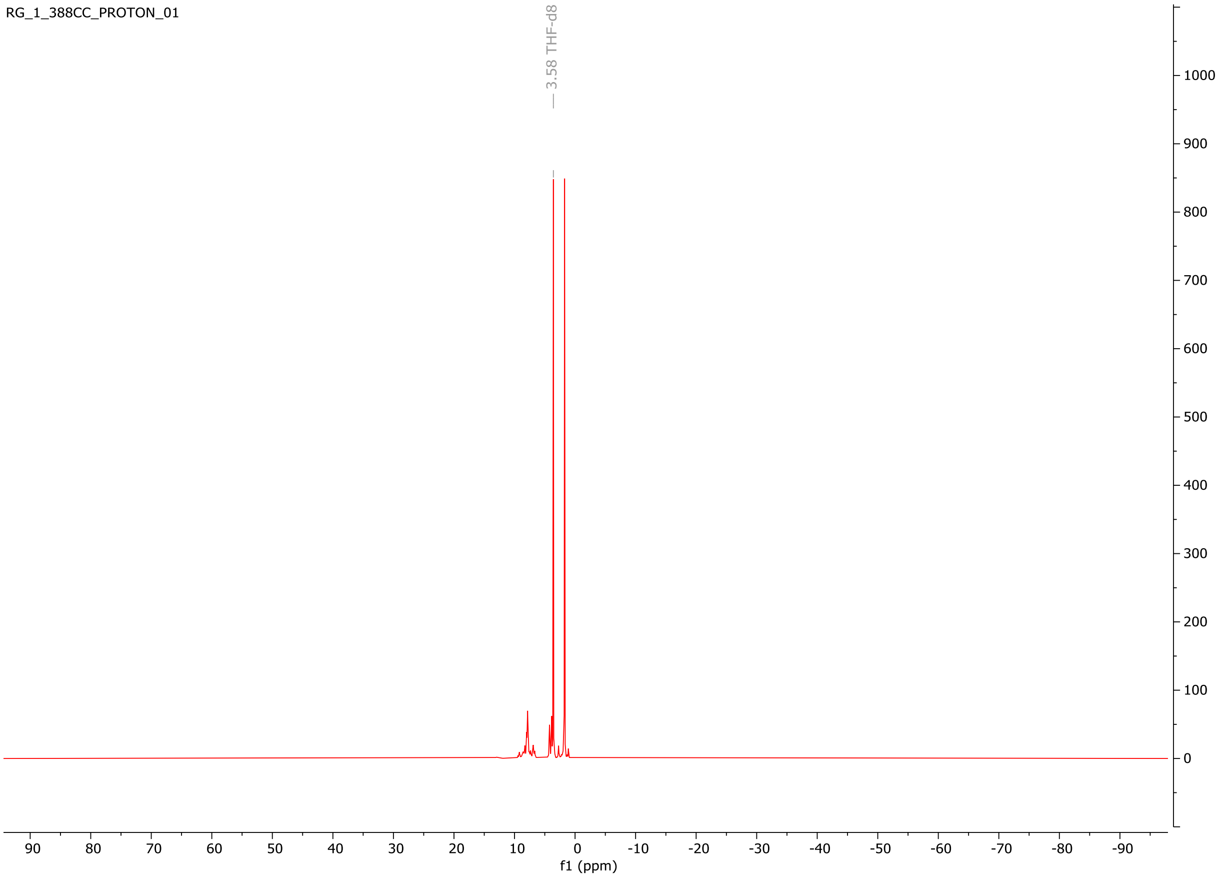

Figure SB.8 ^{1}H NMR of [Ru(bid)(bpy’)NH$_3$][PF$_6$]$_2$ (**3**) in THF-*d*$_6$ at t = 96 h (vertically zoomed out spectrum)

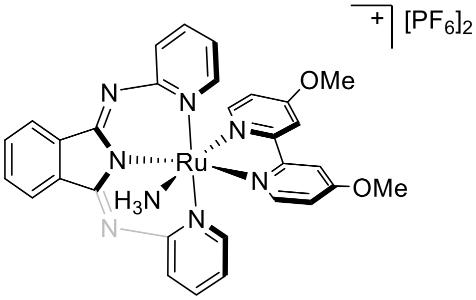

Complex **3**

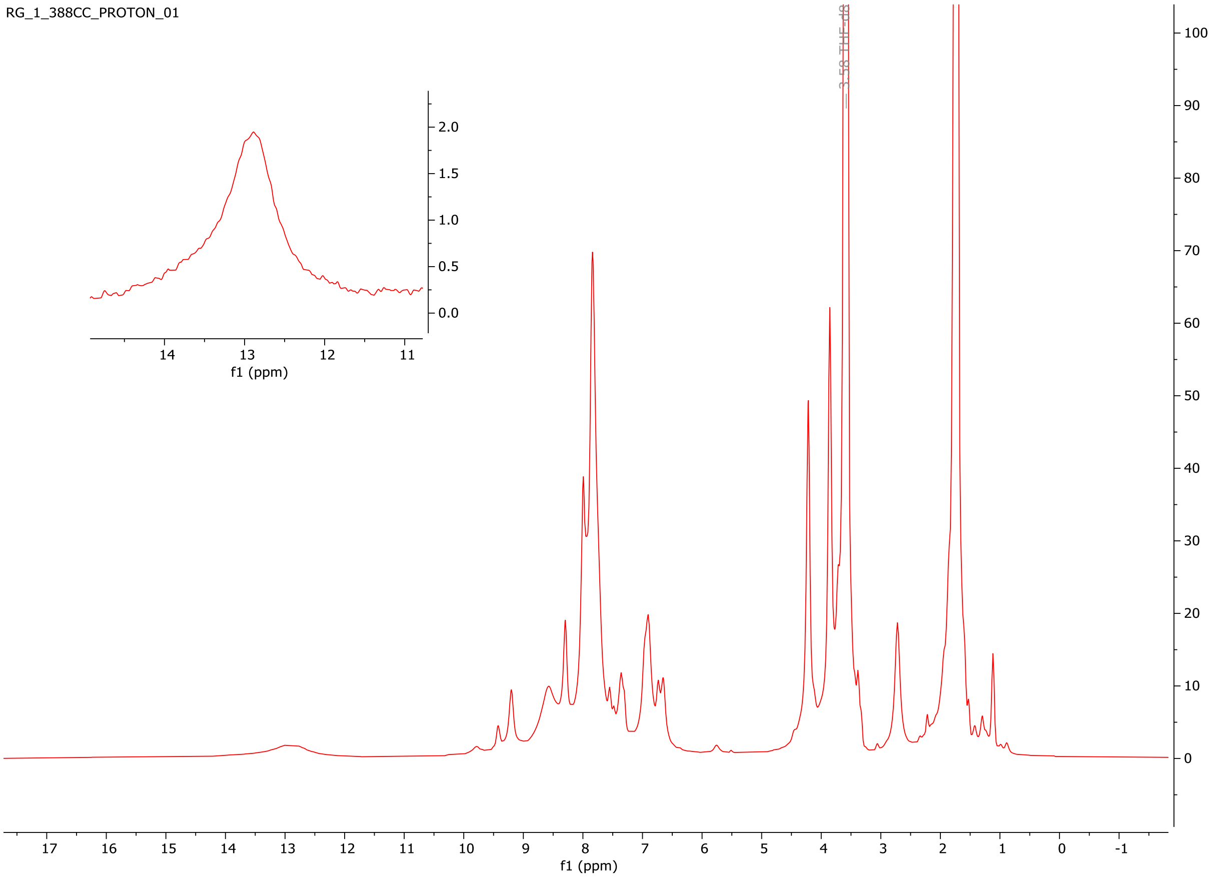

Figure SB.9 ^{1}H NMR of [Ru(bid)(bpy')NH$_3$][PF$_6$]$_2$ (**3**) in THF-d_6 at t = 96 h (vertically zoomed in spectrum)

SB.2 Crystallographic Data

SB.2.1 Crystal Data and Experimental for Complex 2

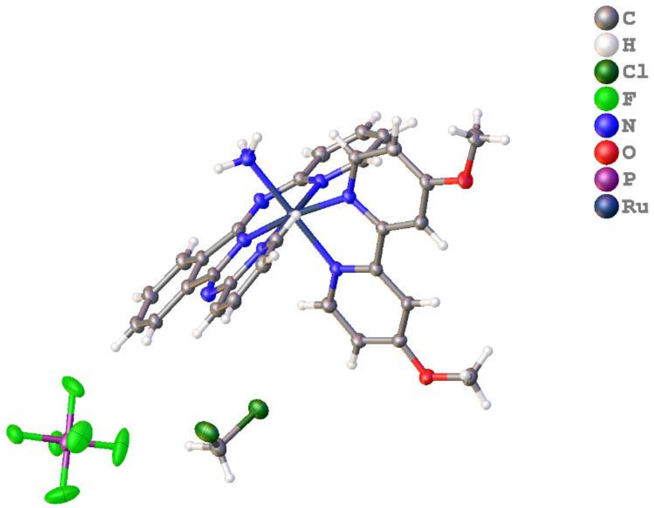

Compound	**Complex 2**
CCDC	**1993356**
Formula	$C_{31}H_{29}Cl_2F_6N_8O_2PRu$
$D_{calc.}$/ g cm^{-3}	1.712
μ/mm^{-1}	6.413
Formula Weight	862.56
Colour	blue
Shape	plate
Size/mm^3	0.26×0.13×0.04
T/K	100.00(10)
Crystal System	triclinic
Space Group	P-1
a/Å	10.7072(2)
b/Å	12.3824(3)
c/Å	14.0815(3)
α/°	107.399(2)
β/°	102.504(2)
γ/°	100.944(2)
V/Å^3	1673.05(7)
Z	2
Z'	1
Wavelength/Å	1.54184
Radiation type	Cu K$_\alpha$
Θ_{min}/°	3.439
Θ_{max}/°	71.029
Measured Refl's.	26574
Ind't Refl's	6310
Refl's with I > 2(I)	5901
R_{int}	0.0526
Parameters	474
Restraints	0
Largest Peak	0.732
Deepest Hole	-1.171
GooF	1.065
wR_2 (all data)	0.1062
wR_2	0.1010
R_1 (all data)	0.0390
R_1	0.0360

Experimental. Single blue-plate crystals of Complex **2** used as received. A suitable crystal with dimensions 0.26 × 0.13 × 0.04 mm^3 was selected and mounted on a nylon loop with paratone oil on a XtaLAB Synergy, Dualflex, HyPix diffractometer. The crystal was kept at a steady T = 100.00(10) K during data collection. The structure was solved with the **ShelXT** (Sheldrick, G.M. (2015). Acta Cryst. A71, 3-8) solution program using dual methods and by using **Olex2** (Dolomanov et al., 2009) as the graphical interface. The model was refined with **ShelXL** (Sheldrick, Acta Cryst. A64 2008, 112-122) using full matrix least squares minimisation on $\boldsymbol{F}^2$.

Crystal Data. $C_{31}H_{29}Cl_2F_6N_8O_2PRu$, M_r = 862.56, triclinic, P-1 (No. 2), a = 10.7072(2) Å, b = 12.3824(3) Å, c = 14.0815(3) Å, α = 107.399(2)°, β = 102.504(2)°, γ = 100.944(2)°, V = 1673.05(7) Å^3, T = 100.00(10) K, Z = 2, Z' = 1, μ(Cu K$_\alpha$) = 6.413, 26574 reflections measured, 6310 unique (R_{int} = 0.0526) which were used in all calculations. The final wR_2 was 0.1062 (all data) and R_1 was 0.0360 (I > 2(I)).

SB.2.2 Crystal Data and Experimental for Complex 4

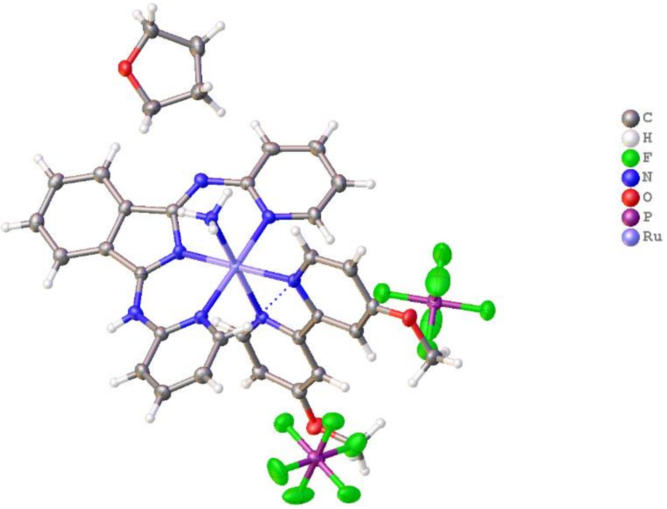

Experimental. Single red needle-shaped crystals of complex **4** used as received. A suitable crystal with dimensions 0.11 × 0.06 × 0.02 mm^3 was selected and mounted on a nylon loop with paratone oil on a XtaLAB Synergy, Dualflex, HyPix diffractometer. The crystal was kept at a steady T = 99.9(3) K during data collection. The structure was solved with the **ShelXS** (Sheldrick, 2008) solution program using direct methods and by using **Olex2** 1.3 (Dolomanov et al., 2009) as the graphical interface. The model was refined with **ShelXL** 2018/3 (Sheldrick, 2015) using full matrix least squares minimisation on $\boldsymbol{F^2}$.

Crystal Data. $C_{34}H_{36}F_{12}N_8O_3P_2Ru$, M_r = 995.72, monoclinic, $P2_1$ (No. 4), a = 9.35985(18) Å, b = 15.3882(4) Å, c = 13.4460(3) Å, β = 91.9032(17)°, $\alpha = \gamma$ = 90°, V = 1935.58(7) Å^3, T = 99.9(3) K, Z = 2, Z' = 1, μ(Cu K$_\alpha$) = 5.023, 21661 reflections measured, 7474 unique (R_{int} = 0.0486) which were used in all calculations. The final wR_2 was 0.0889 (all data) and R_1 was 0.0348 (I≥2 s(I)).

Compound	**Complex 4**
Formula	$C_{34}H_{36}F_{12}N_8O_3P_2Ru$
CCDC	2101754
$D_{calc.}$/ g cm^{-3}	1.708
μ/mm^{-1}	5.023
Formula Weight	995.72
Color	red
Shape	needle-shaped
Size/mm^3	0.11×0.06×0.02
T/K	99.9(3)
Crystal System	monoclinic
Flack Parameter	-0.011(5)
Hooft Parameter	-0.014(4)
Space Group	$P2_1$
a/Å	9.35985(18)
b/Å	15.3882(4)
c/Å	13.4460(3)
α/°	90
β/°	91.9032(17)
γ/°	90
V/Å^3	1935.58(7)
Z	2
Z'	1
Wavelength/Å	1.54184
Radiation type	Cu K$_\alpha$
Θ_{min}/°	3.289
Θ_{max}/°	80.105
Measured Refl's.	21661
Indep't Refl's	7474
Refl's I≥2 s(I)	7185
R_{int}	0.0486
Parameters	544
Restraints	1
Largest Peak	0.438
Deepest Hole	-0.765
GooF	1.068
wR_2 (all data)	0.0889
wR_2	0.0880
R_1 (all data)	0.0365
R_1	0.0348

SUPPORTING INFORMATION (C) FOR CHAPTER 5

SC.1 NMR Spectra

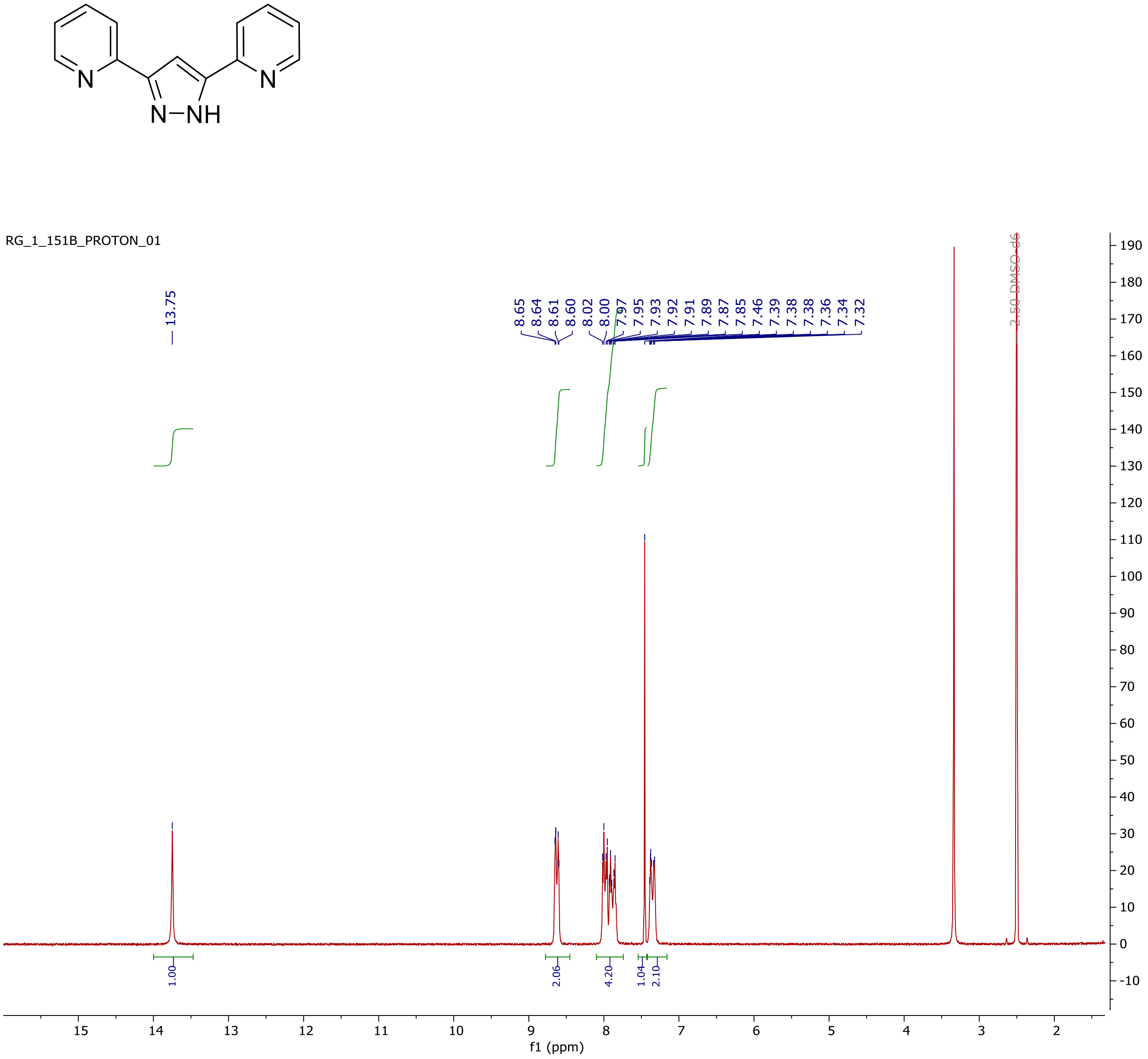

Figure SC.1 ^{1}H NMR of Hbpp in DMSO-d_6

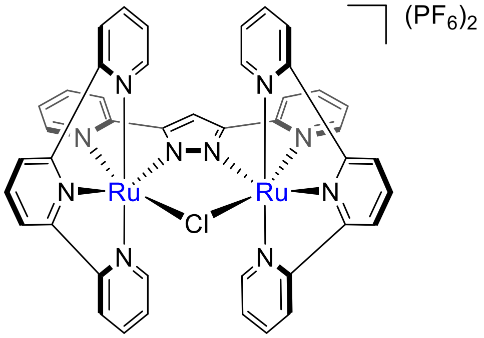

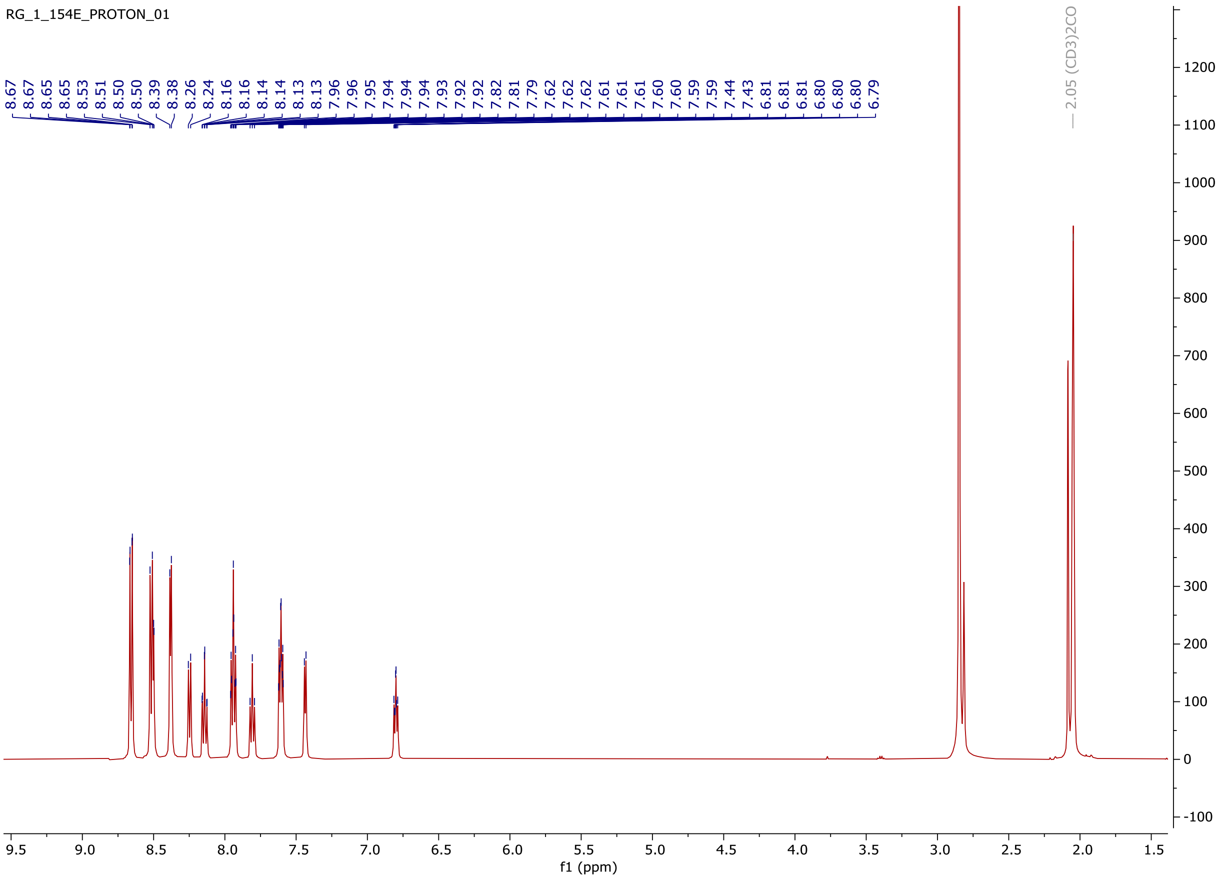

Figure SC.2 ^{1}H NMR of [Ru$_2^{II}$(μ-Cl)(bpp)(trpy)$_2$][PF$_6$]$_2$ (**1**) in acetone-d_6

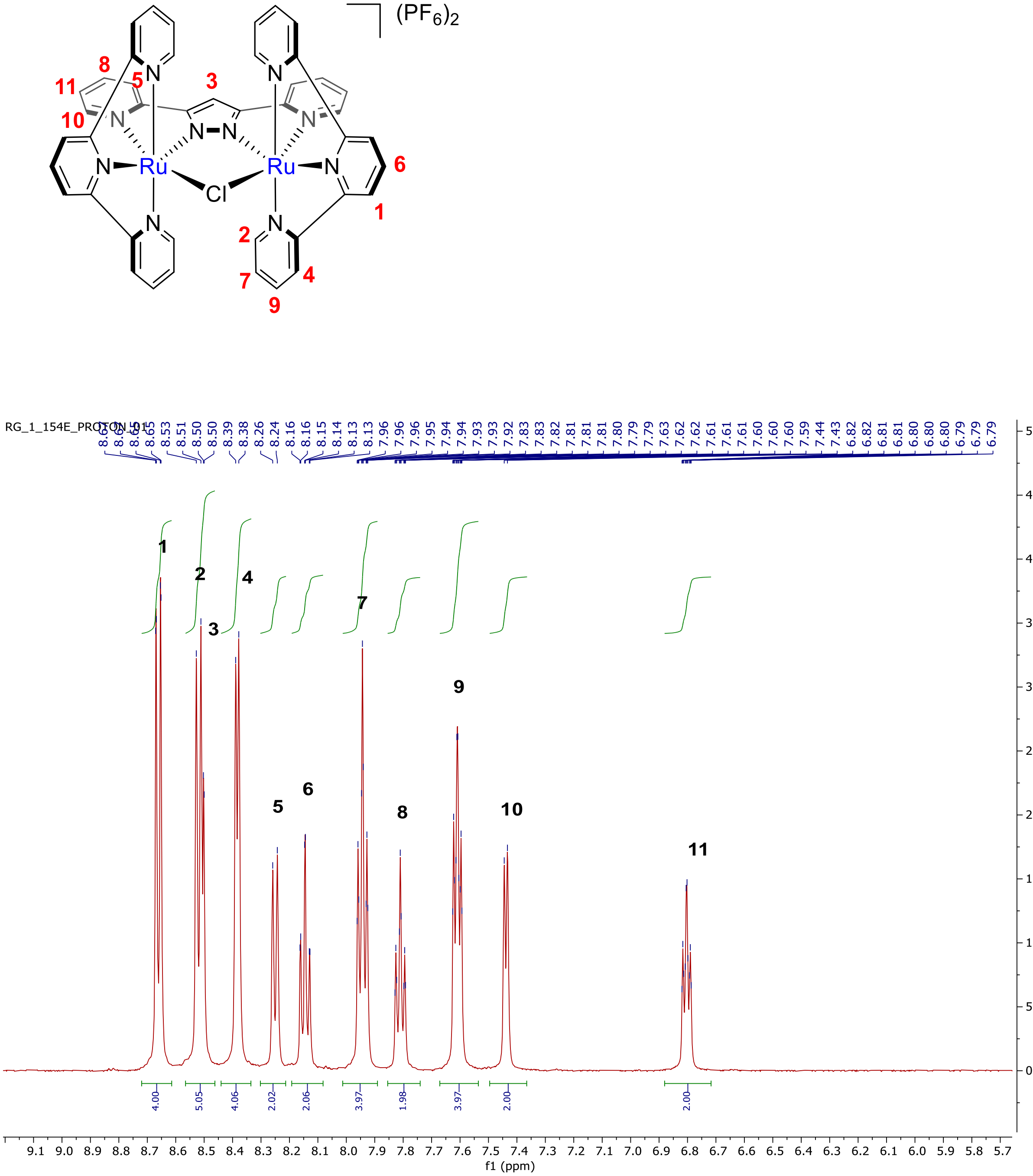

Figure SC.3 ^{1}H NMR of $[Ru_2^{II}(\mu\text{-}Cl)(bpp)(trpy)_2][PF_6]_2$ (**1**) in acetone-*d₆* (aromatic region)

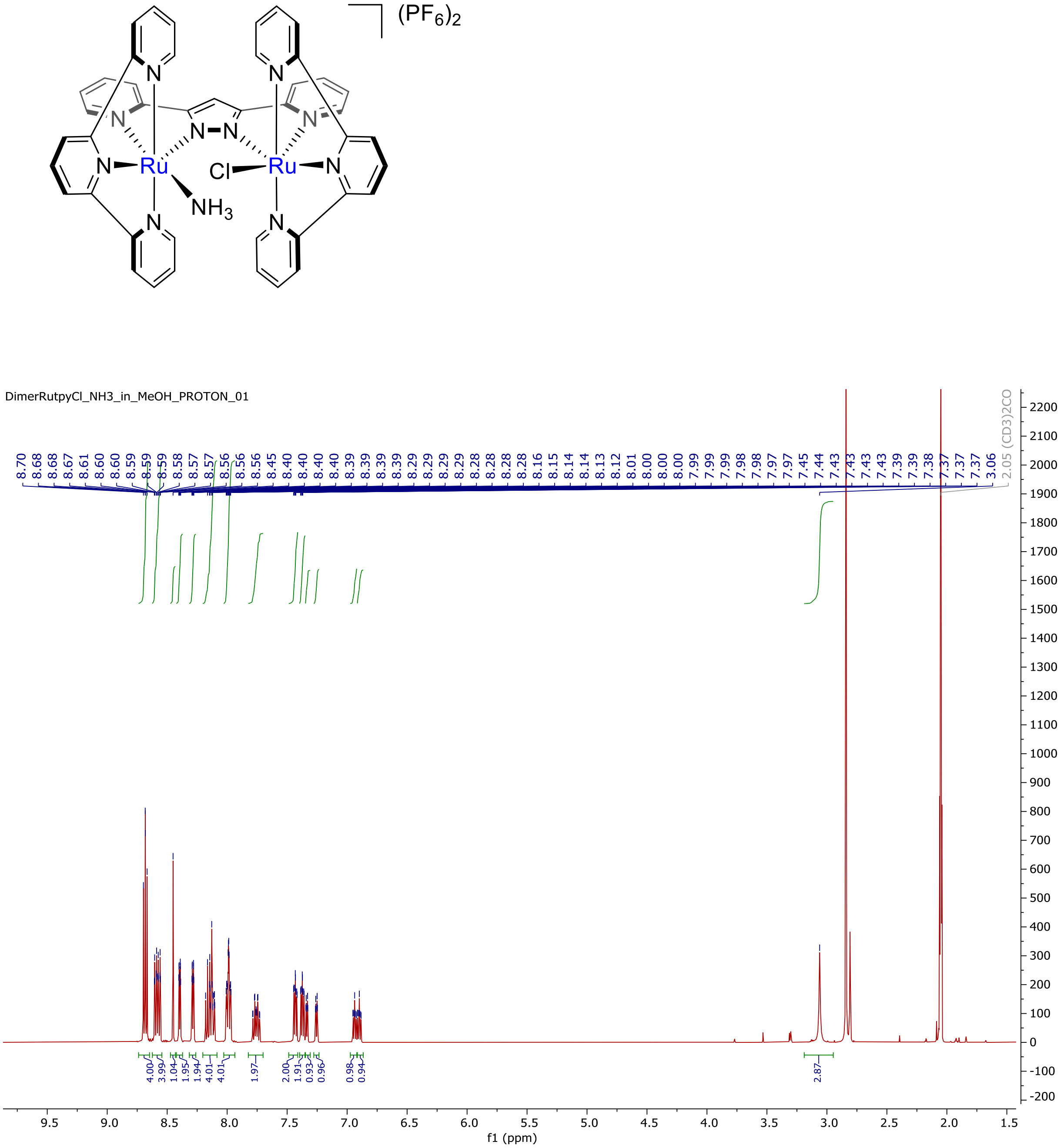

Figure SC.4 ^{1}H NMR of $[Ru_2^{II}(NH_3)Cl(bpp)(trpy)_2][PF_6]_2$ (**2**) in acetone-d_6

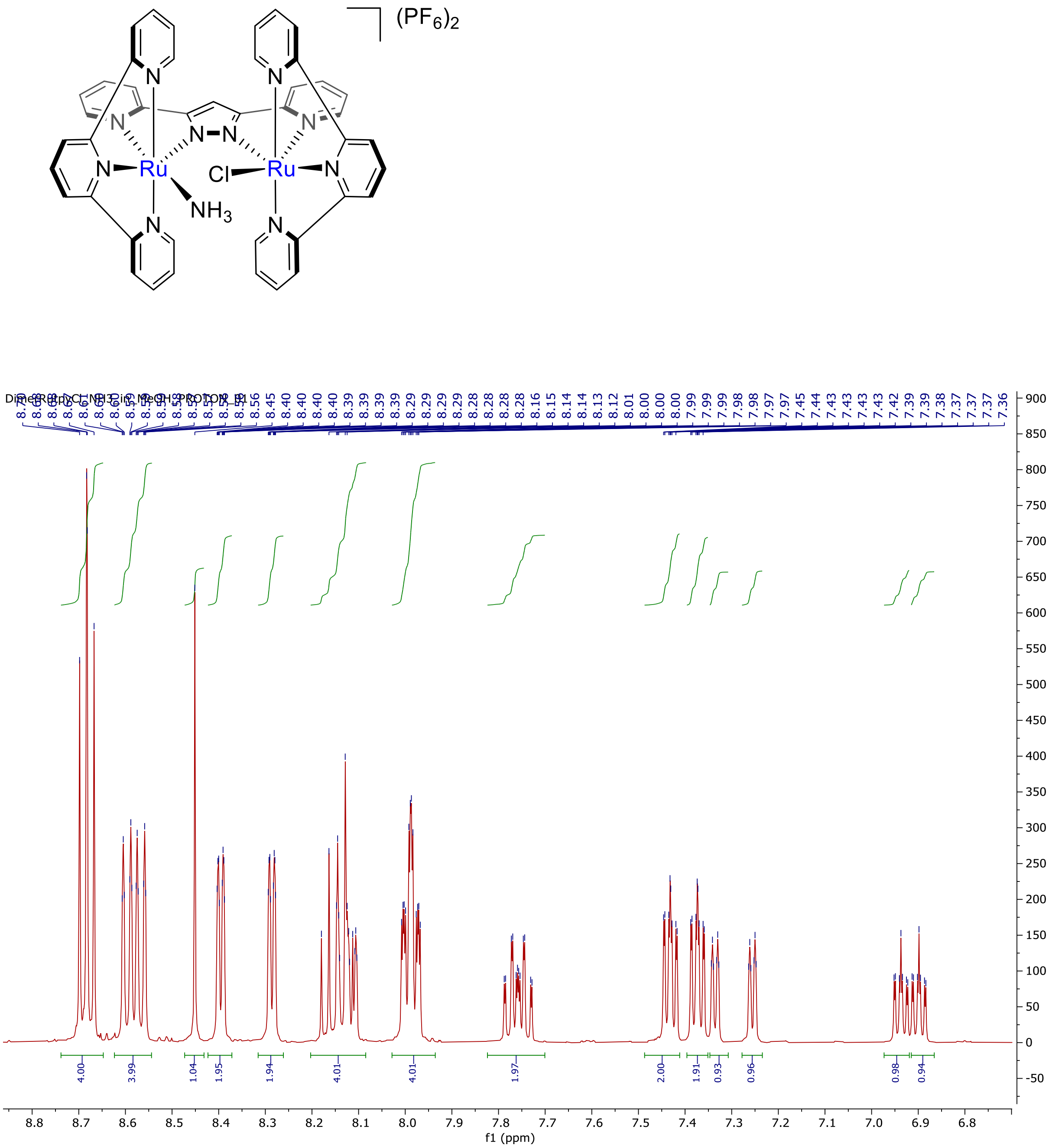

Figure SC.5 ^{1}H NMR of $[Ru_2^{II}(NH_3)Cl(bpp)(trpy)_2][PF_6]_2$ (**2**) in acetone-d_6 (aromatic region)

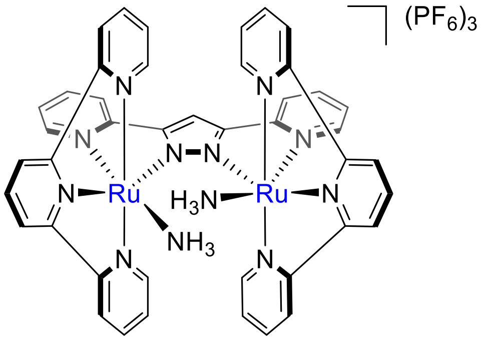

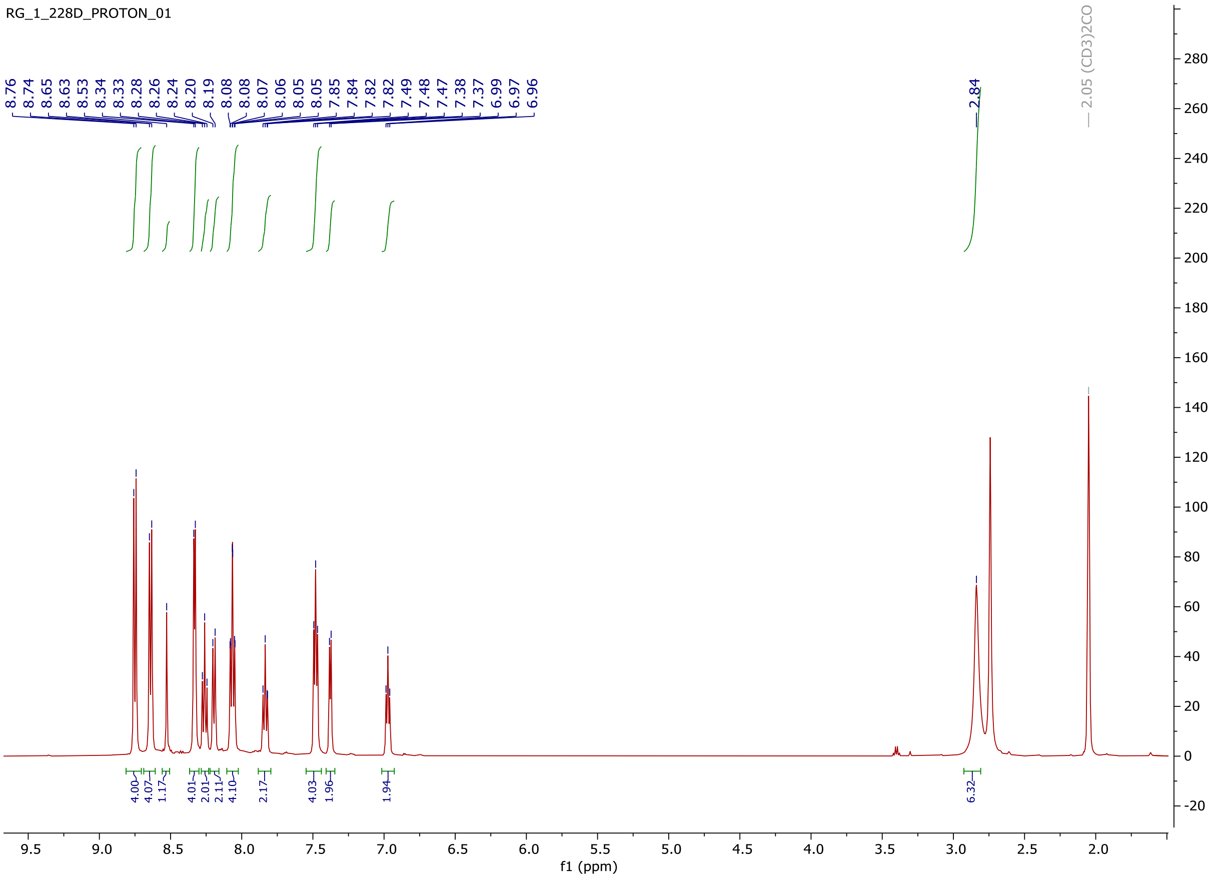

Figure SC.6 ^{1}H NMR of $[Ru_2^{II}(NH_3)_2(bpp)(trpy)_2][PF_6]_3$ (**3**) in acetone-d_6

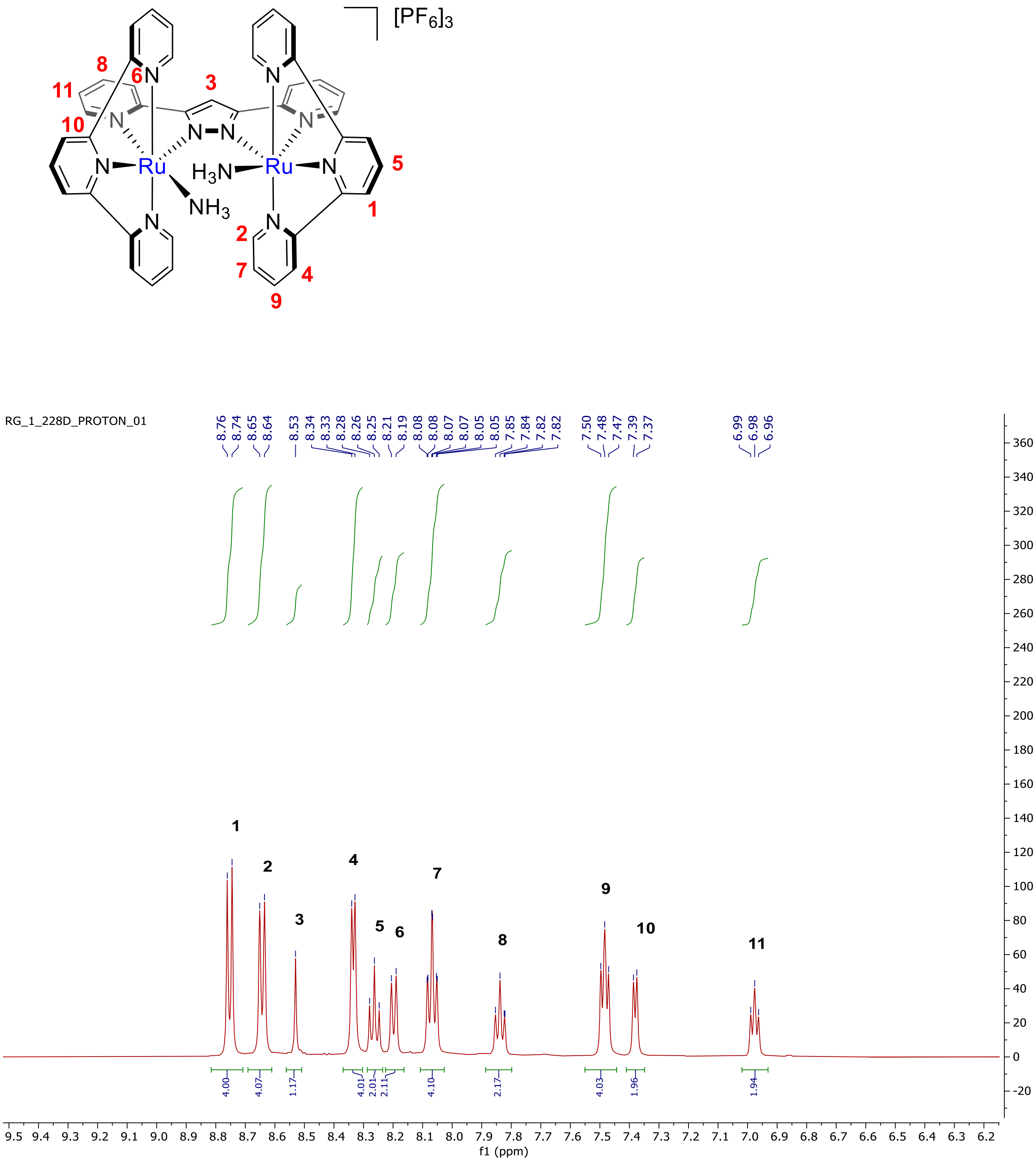

Figure SC.7 ^{1}H NMR of [Ru$_2^{II}$(NH$_3$)$_2$(bpp)(trpy)$_2$][PF$_6$]$_3$ (**3**) in acetone-*d$_6$* (aromatic region)

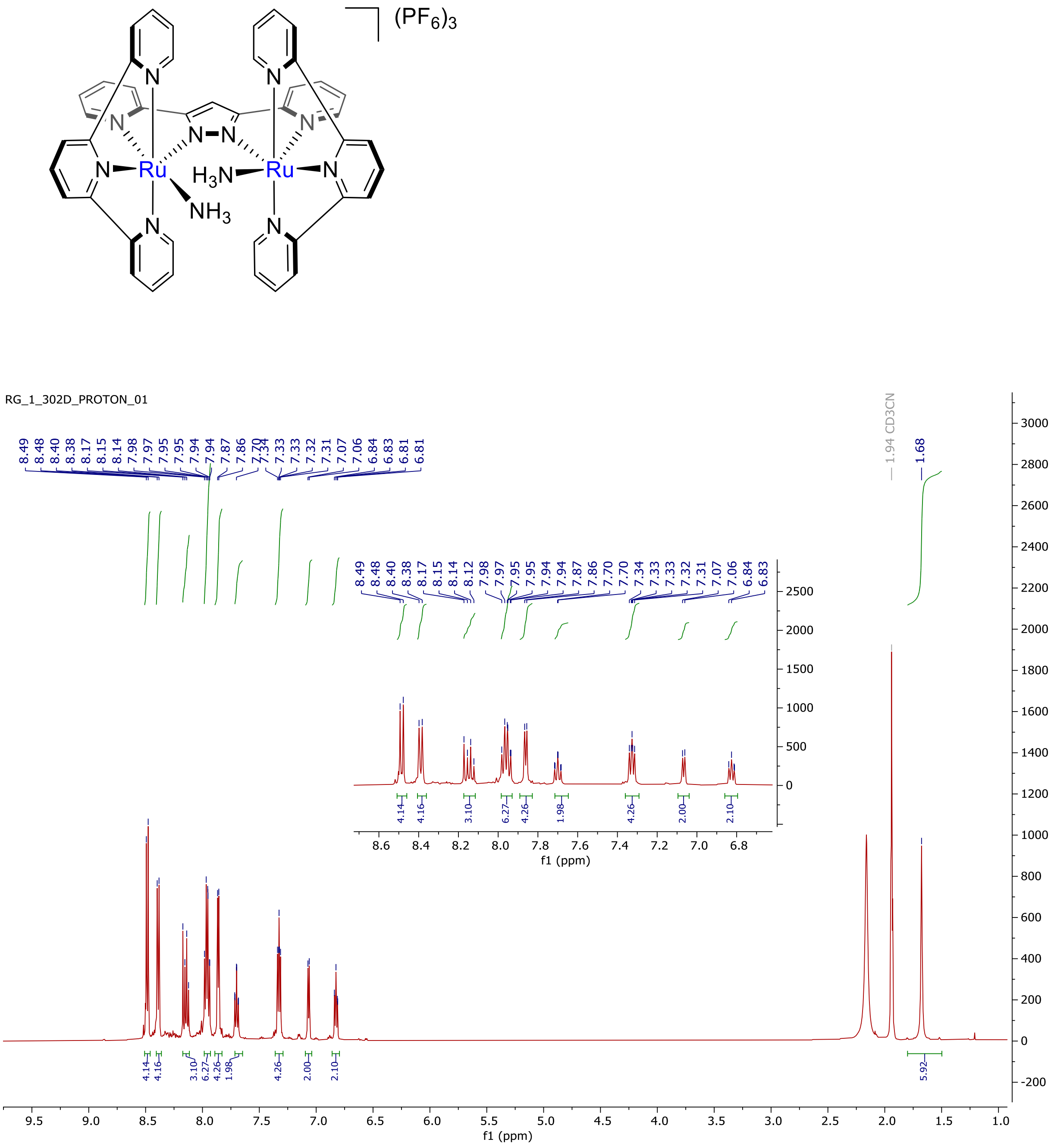

Figure SC.8 ^{1}H NMR of [Ru$_2^{II}$(NH$_3$)$_2$(bpp)(trpy)$_2$][PF$_6$]$_3$ (**3**) in MeCN-d_3

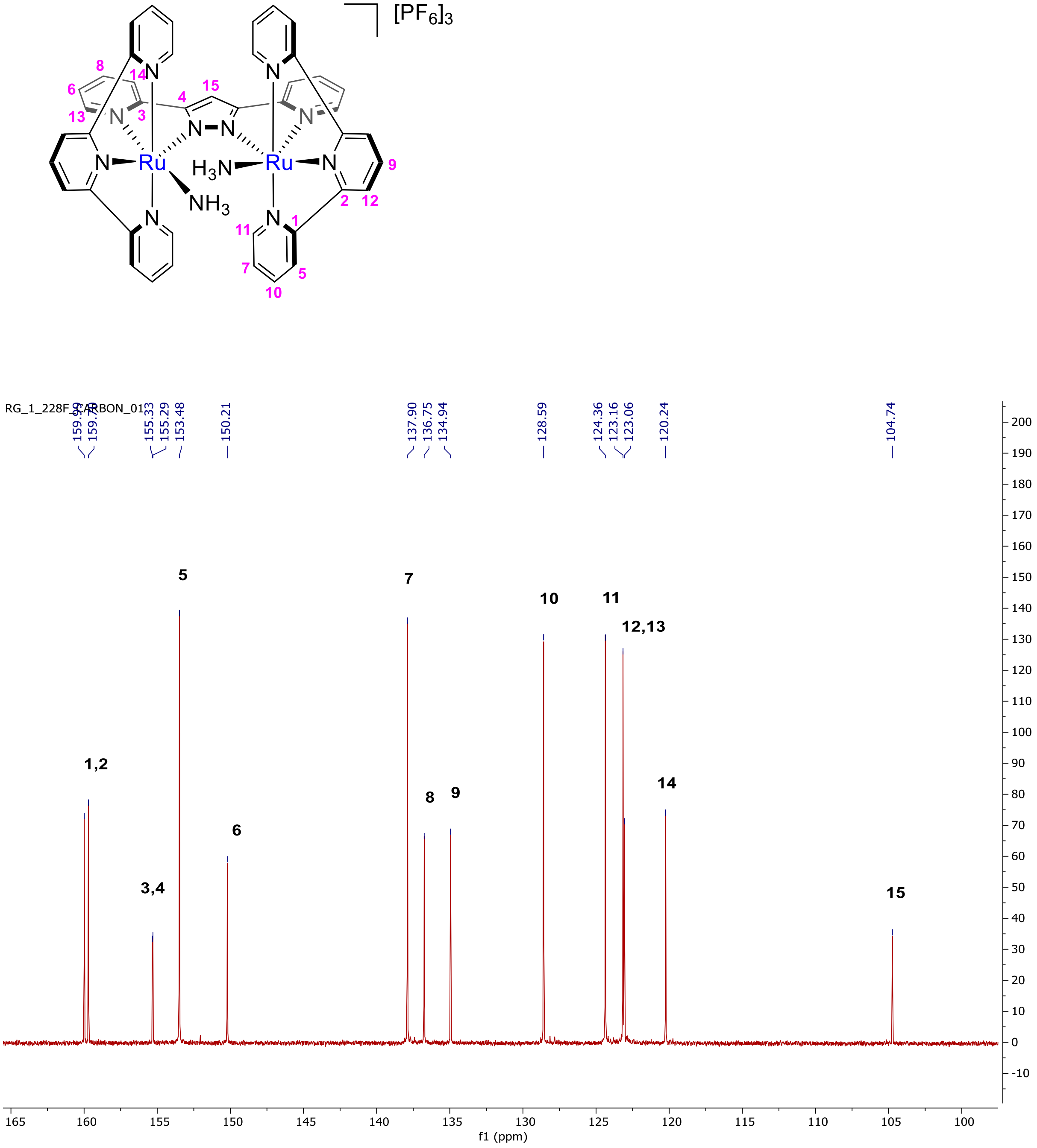

Figure SC.9 ^{13}C NMR of [$Ru_2^{II}(NH_3)_2$(bpp)(trpy)$_2$][PF_6]$_3$ (**3**) in acetone-d_6

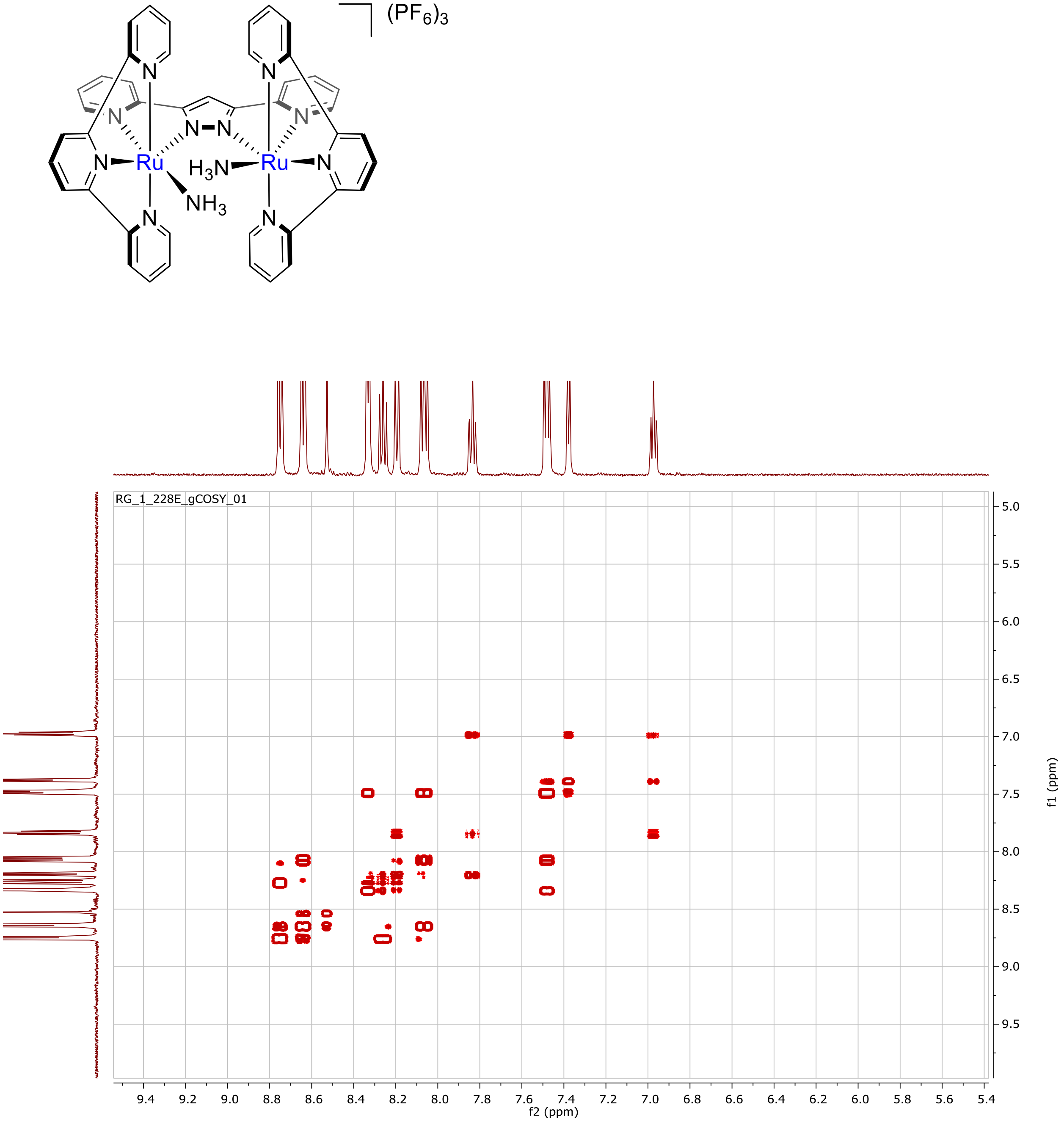

Figure SC.10 gCOSY NMR of [Ru$_2^{II}$(NH$_3$)$_2$(bpp)(trpy)$_2$][PF$_6$]$_3$ (**3**) in acetone-*d*$_6$

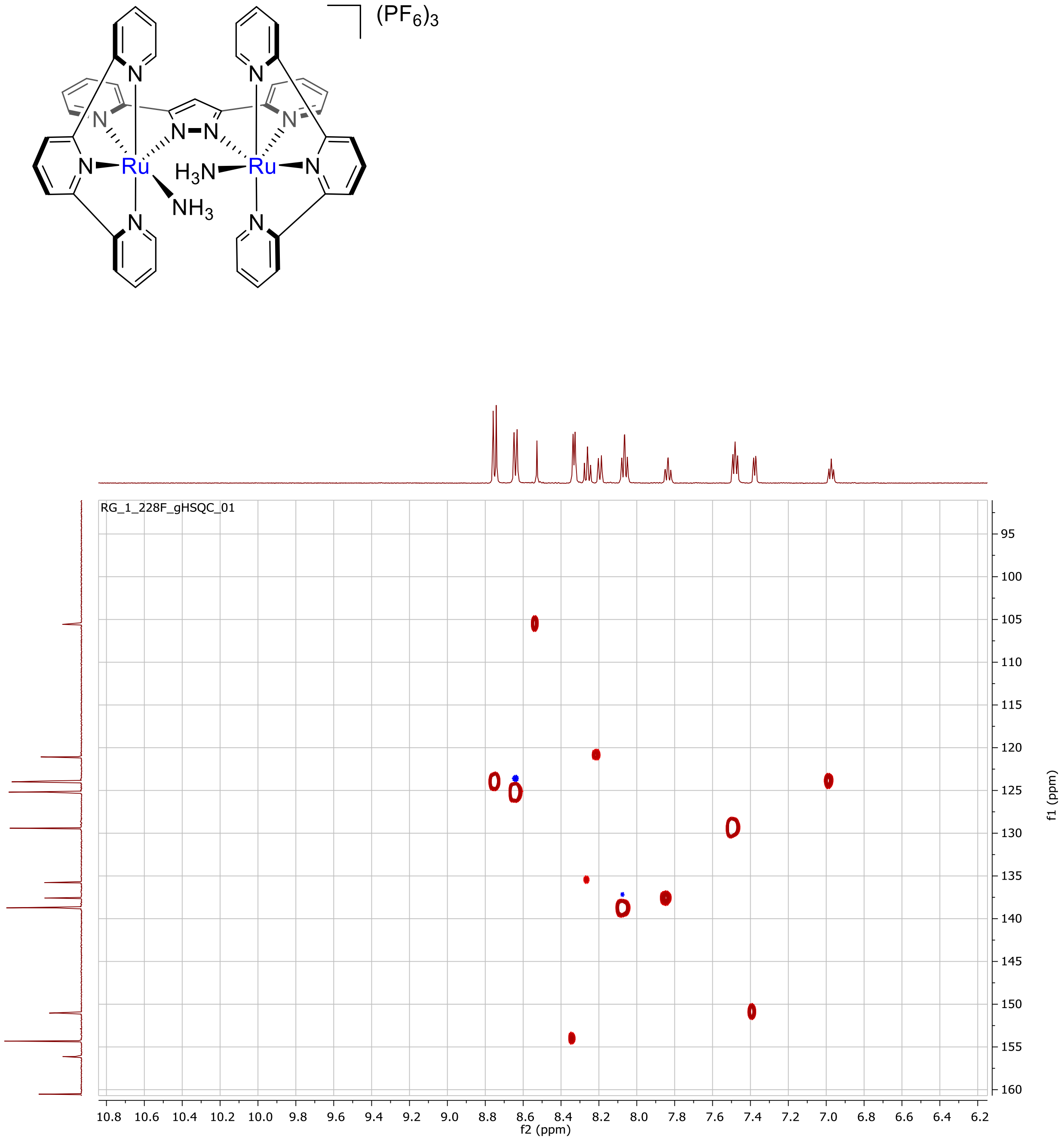

Figure SC.11 gHSQC NMR of [Ru$_2^{II}$(NH$_3$)$_2$(bpp)(trpy)$_2$][PF$_6$]$_3$ (**3**) in acetone-*d*$_6$

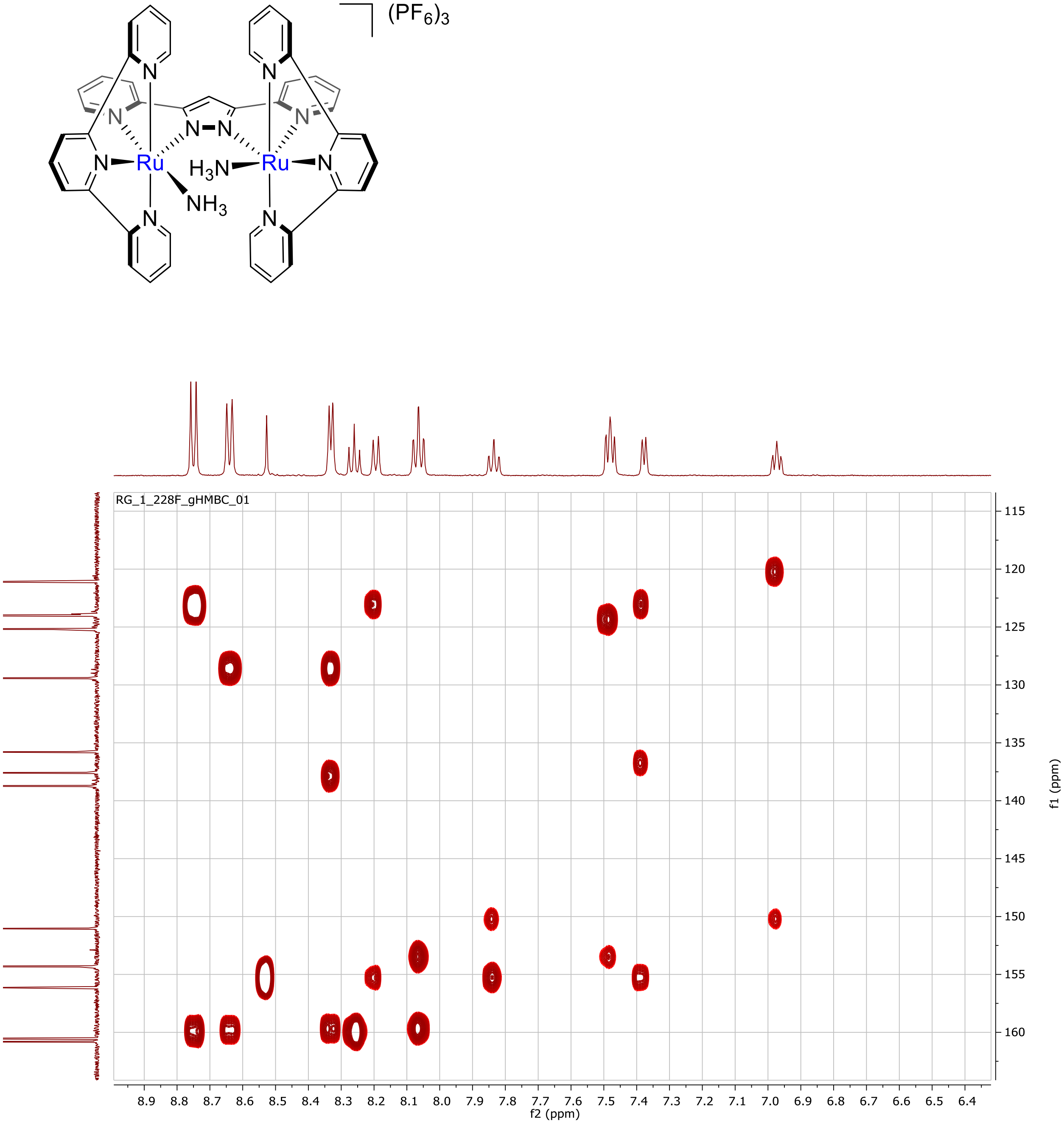

Figure SC.12 gHMBC NMR of of [Ru$_2^{II}$(NH$_3$)$_2$(bpp)(trpy)$_2$][PF$_6$]$_3$ (**3**) in acetone-d_6

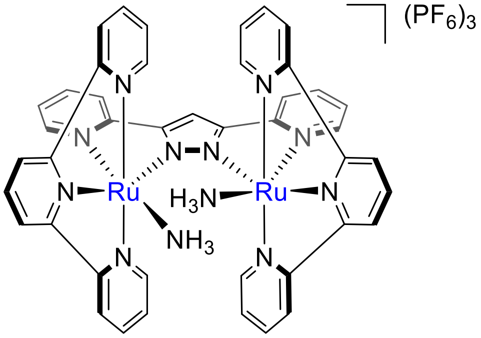

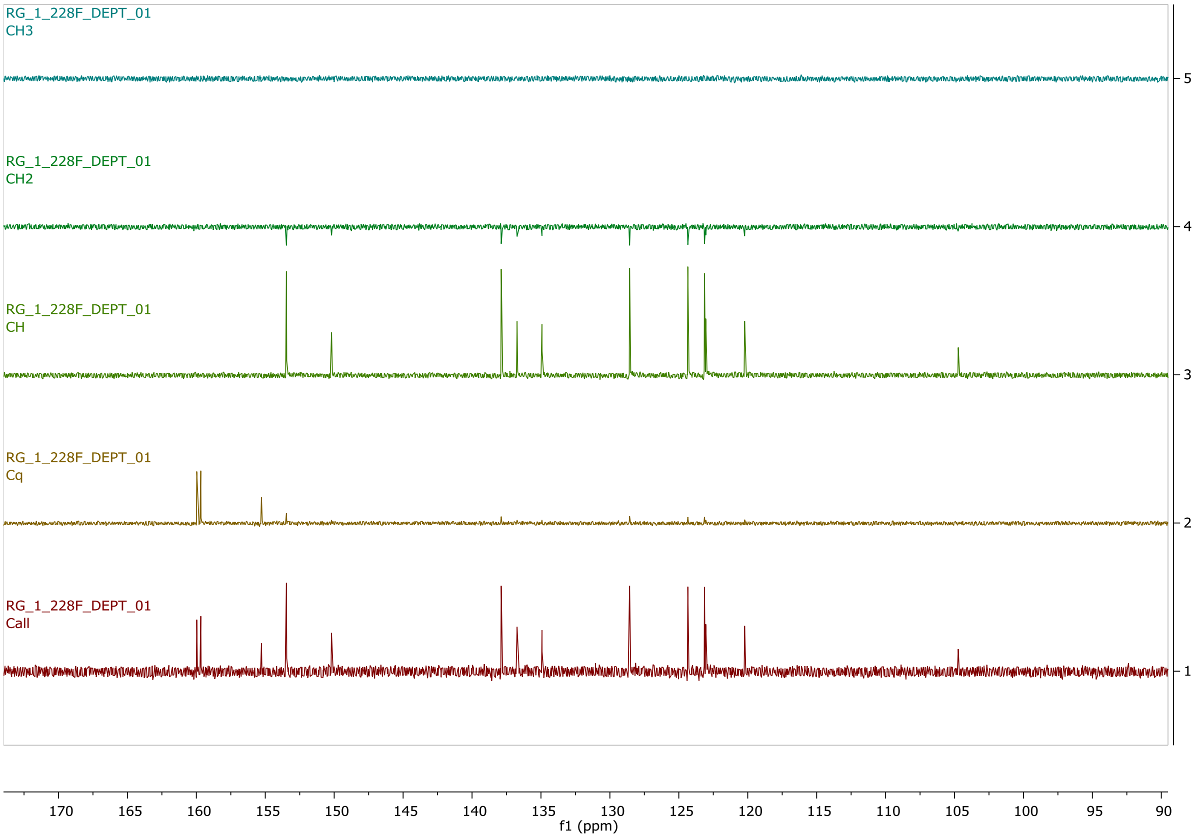

Figure SC.13 DEPT NMR of [Ru$_2^{II}$(NH$_3$)$_2$(bpp)(trpy)$_2$][PF$_6$]$_3$ (**3**) in acetone-*d*$_6$

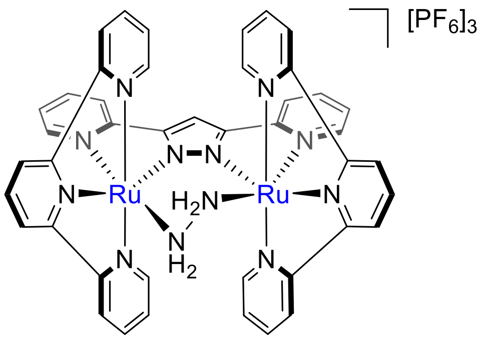

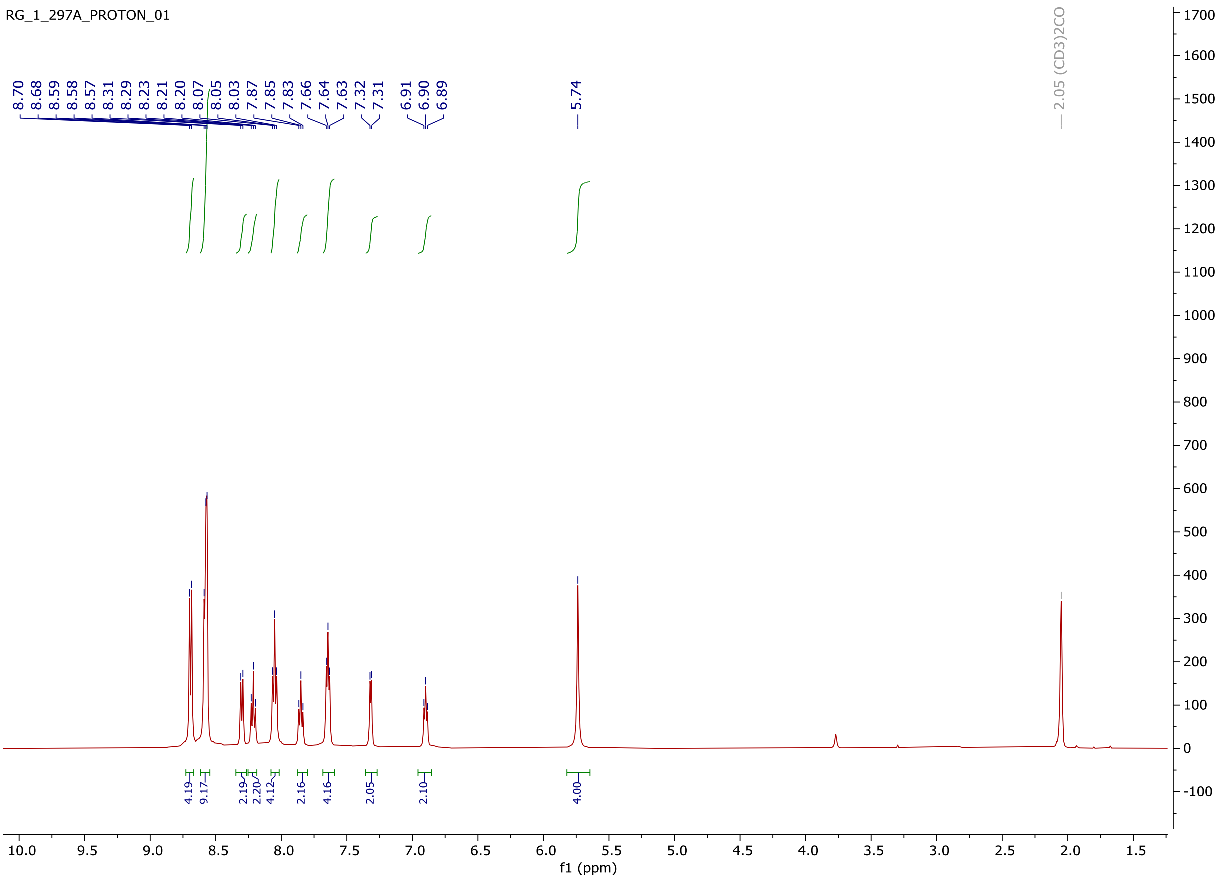

Figure SC.14 ^{1}H NMR of [Ru_2^{II}(μ-N_2H_4)(bpp)(trpy)$_2$][PF_6]$_3$ (**4**) in acetone-d_6

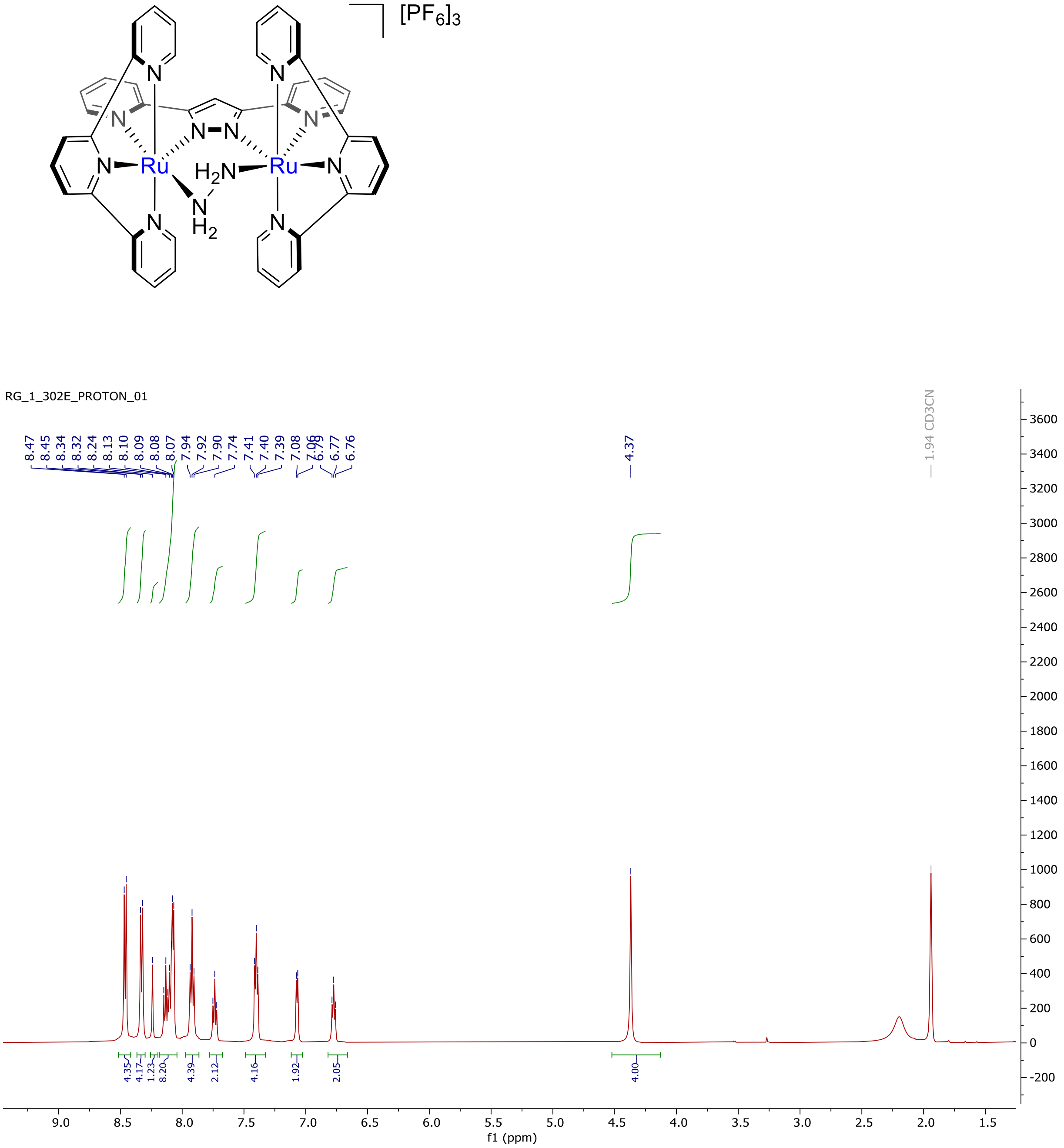

Figure SC.15 ^{1}H NMR of $[Ru_2^{II}(\mu\text{-}N_2H_4)(bpp)(trpy)_2][PF_6]_3$ (**4**) in MeCN-d_3

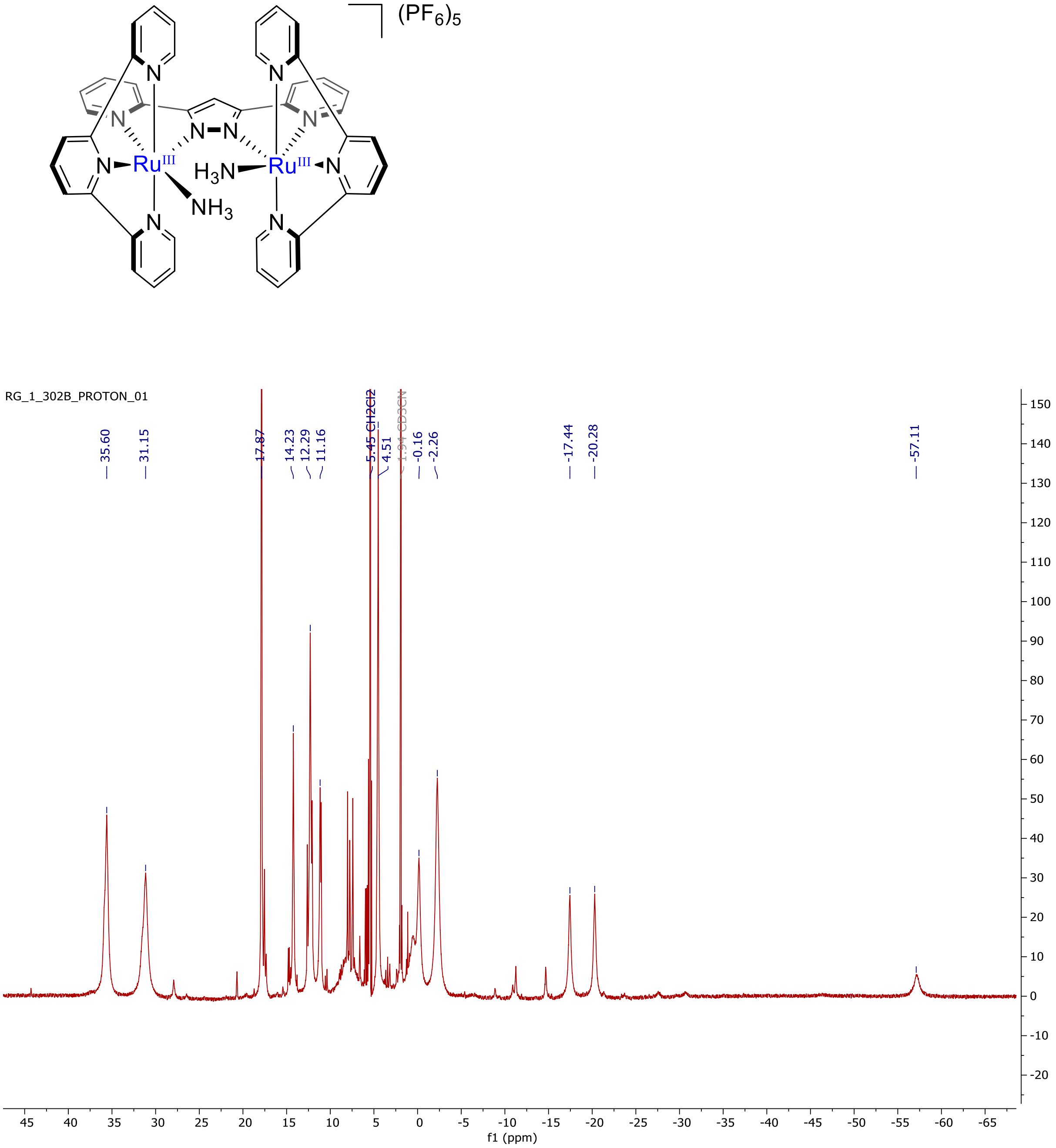

Figure SC.16 ^{1}H NMR of [Ru$_2^{III}$(NH$_3$)$_2$(bpp)(trpy)$_2$][PF$_6$]$_5$ (**3b**) in MeCN-*d*$_3$

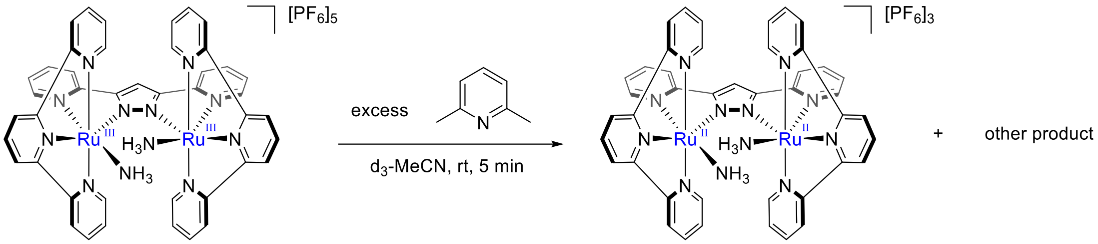

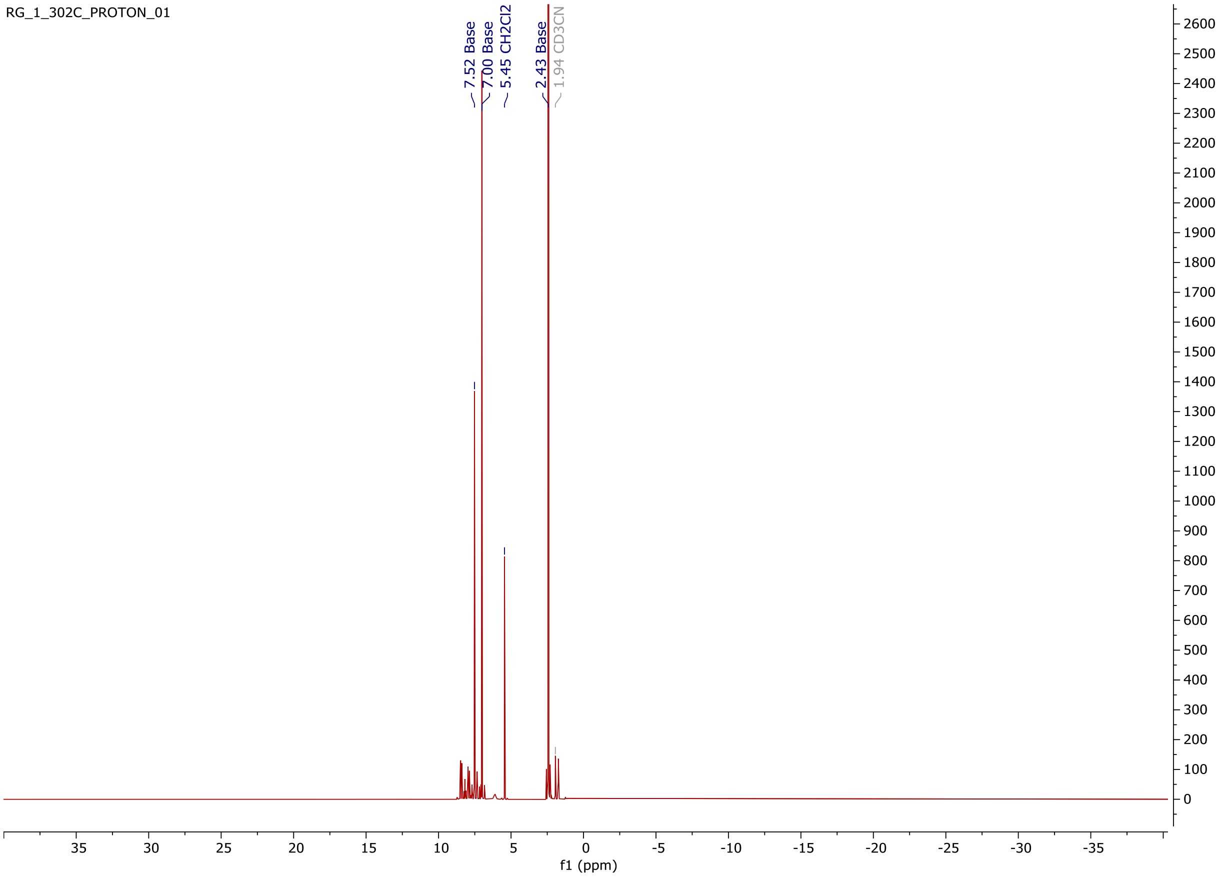

Figure SC.17 ^{1}H NMR of the products of the reaction of **3b** with 2,6–dimethylpyridine in MeCN-*d$_3$*

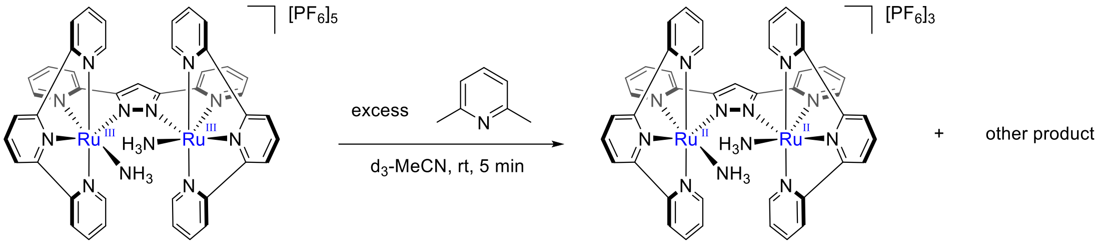

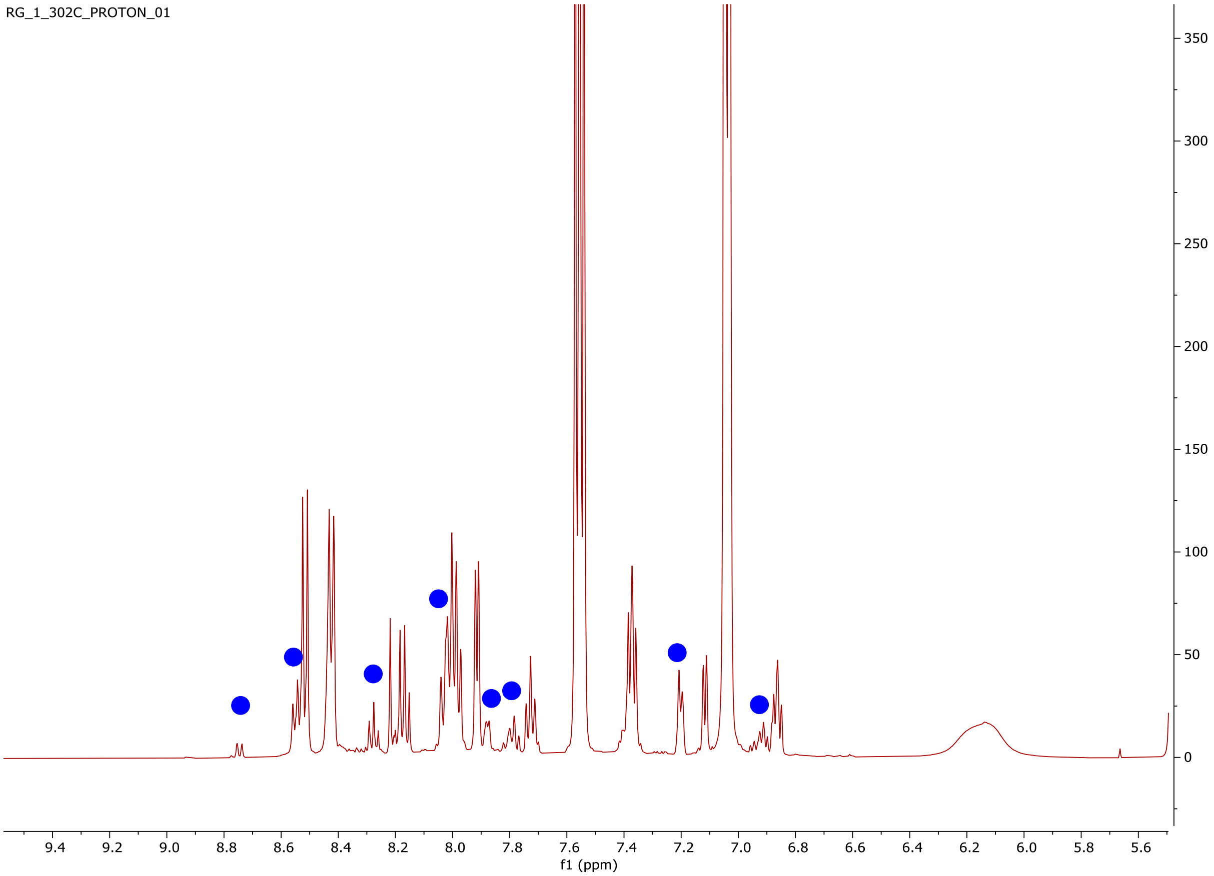

Figure SC.18 ^{1}H NMR of the products of the reaction of **3b** with 2,6–dimethylpyridine in MeCN-*d*$_3$ (aromatic region). Blue dots are the peaks of the unidentified product(s)